AS-CAST AUSFERRITIC DUCTILE IRON MATERIALS OBTAINED BY A CONTROLLED COOLING PROCESS

DOCTORAL THESIS

Urko de la Torre Ugarte

University of Deusto

Supervisor: Dr. Pablo García-Bringas

Co-Supervisor: Dr. Susana Méndez Bóveda

2022/01

AS-CAST AUSFERRITIC DUCTILE IRON MATERIALS OBTAINED BY A CONTROLLED COOLING PROCESS

DOCTORAL THESIS

Urko de la Torre Ugarte

University of Deusto

The supervisor: Dr. Pablo García-Bringas

The co-supervisor: Dr. Susana Méndez Bóveda

The Ph.D. student: Urko de la Torre Ugarte

Dedicated to my grandmother who passed away during the development of this work and to my children Oinatz and Izadi who were born on this period

Batek goserikan diraueino
ez gara gu asetuko
beste bat loturik deino
ez gara libre izango

Martxa baten lehen notak
Joxan Artzek idatzita ta Mikel Laboak musikatuta

ACKNOWLEDGMENTS

I would like to thank my colleagues Rodolfo and Susana for their dedication and scientifical and psychological support during the development of this work. Without them, this work would have never come into existence. On the other hand, you both are welcome for having given you the opportunity to combine beer, taloak and/or tacos and science, an unbeatable triangle.

Thanks to Jon Garay and Jontxu for their help and their hard work during the experimental trials.

I would also like to express my gratitude to my supervisors for having given me the freedom to develop this work and to lead it through the path that I considered convenient.

Furthermore, my appreciation to our former responsible, Ramón Suárez, because his was the idea of the present work.

Additionally, special thanks to our former CEO Pedro Intxausti, because he friendly pushed me and the institution so that I could carry out my PhD.

Moreover, I would like to thank Azterlan for giving me the opportunity to develop this thesis and for supporting me to finish the work.

Finally, I would like to thank my family, my wife, parents, aunt, grandparents, sister, mother-in-law, brother in-law and children for their help and support during the path that life represents and of course for their contribution to become what I am.

TABLE OF CONTENTS

ABSTRACT

Within the framework of the spheroidal graphite cast irons, the ADI materials are the ones that present the best mechanical properties. Due to their excellent strength/ductility relationship, they can replace forged steel in some applications and due to their optimal strength/weight ratio, even aluminium alloys. These materials base their exceptional mechanical properties on their ausferritic microstructure.

This ausferritic microstructure is conventionally obtained applying a heat treatment process called austempering to the as-cast foundry castings. This is an aspect that hinders the market expansion of the ADI materials, because it implies a cost increase, an energy consumption growth, and a lead time extension, together with a complexity increase due to the co-work between the foundry and the heat treater.

Trying to overcome this handicap, on the present research work, the obtention of spheroidal graphite iron castings with an as-cast ausferritic microstructure is approached, acting on the cooling process, without the need of a subsequent heat treatment. This way, the negative aspects that the austempering heat treatment can involve could be overcome.

To that aim, the technology necessary to face an engineered cooling process was studied. The practical basis of the actions taken during the cooling process so that an as-cast ausferritic microstructure could be achieved, was to perform them as simple as possible, trying to facilitate the future industrial application of the methodology. For this reason, air cooling was defined as the way to avoid the pearlitic nose and an insulating medium was considered to maintain a constant temperature during the isothermal transformation, step that allows the formation of a fully ausferritic microstructure.

Together with the necessary technology, the main process parameters were studied, and their optimal working ranges were defined. These parameters include:

Alloying elements: The minimum necessary alloy content to evict pearlite formation was specified. Nickel, molybdenum, and copper were used to this purpose, being these three the main alloying elements for the ADI materials and three of the elements that most strongly affect the austemperability of the alloy.

Shakeout temperature: The influence on the final microstructure and on the mechanical properties of the shakeout temperature was studied. This is the moment at which the accelerated cooling rate due to the air-cooling starts, once the castings are extracted from the sand mould.

Austempering temperature and time: These are the parameters that have a major influence on the ausferrite formation and consequently on the mechanical properties. A deep study of the kinetics of the ausferrite formation was performed, defining the temperature (upper or lower ausferrite), and holding time effect on the ausferritic microstructure and on the mechanical properties. The processing window in terms of time was defined.

Having defined the technology and the optimal working ranges of the main process parameters for an engineered cooling process, an advanced characterization of the material was performed. Dynamical properties, low temperature performance and corrosion behaviour were analysed and seen if they agree with the conventionally obtained ADI materials results.

The former analyses were carried out considering standard cast samples. The next step was to produce a technology demonstrator prototype. A steering knuckle was chosen for that purpose. A high and a low section size were studied, and their final microstructure defined. This was related to the mechanical properties.

Finally, trying to approach the industrial application of the as-cast ausferritic technology, a mathematical model was developed. This model establishes if a specific casting, with certain thickness differences, can be produced through a controlled cooling process and if it is possible to obtain fully ausferritic microstructures on all its sections. If the technology application is feasible for that casting, then the minimum alloy content and the optimal shakeout and austempering temperatures are defined for the different sections. The austempering temperature is related to the ultimate tensile strength and hardness, so that its optimal value is defined based on the desired mechanical properties.

Resulted from all the developed experiments, the as-cast method to obtain an ausferritic matrix in ductile iron castings was proved to be a valid methodology to produce cast parts as an alternative to conventionally austempered ADI materials. This technology is now ready to be industrially applied.

ABBREVIATIONS

α	Alpha iron or ferrite
ADI	Austempered ductile iron
AF/ α_{AC}	Acicular ferrite
AF_S	Acicular ferrite formation start temperature
bcc	Base centred cubic
bct	Body centred tetragonal
γ	Gamma iron or austenite
CCT	Continuous cooling transformation
CGI	Compacted graphite iron
CR	Cooling rate
CR_{min}	Minimum cooling rate to avoid the pearlitic nose
DIL	Dilatometry samples
E	Elongation
ECP	Electrochemical potential
E_{corr}	Corrosion potential
fcc	Face centred cubic
HBW	Brinell hardness
I_{corr}	Corrosion current density
LAF	Lower acicular ferrite
LGI	Lamellar graphite cast iron or grey iron
LOM	Light optical microscopy
MCI	Malleable cast iron
M_f	Martensite formation finish or end temperature
M_s	Martensite formation start temperature
N	Nodule count
OCP	Open circuit potential
QDIL	Quenching dilatometry samples
RA/ γ_{HC}	Reacted or high carbon austenite
RE	Rare Earths

SEM	Field emission gun scanning electron microscopy
SGI	Spheroidal graphite cast iron or ductile iron
SSS	Solid solution strengthened
TA	Thermal analysis cups
t_{AUS}	Time passed after reaching the AF_S temperature
T_{etd}	Eutectoid transformation temperature
t_{ISO}	Time passed on the isothermal stage
T_{loss}	Temperature loss in the insulating medium
T_{shkout}	Shakeout temperature
TM	Thermal modulus
T_{temp}	Austempering, tempering or isothermal transformation temperature
TTT	Temperature-Time transformation
UAF	Upper acicular ferrite
UTS	Ultimate tensile strength
YS	Yield strength

LIST OF FIGURES

LIST OF TABLES

1. INTRODUCTION

Cast iron defines a group of ferrous alloys, which presents a higher carbon content than 2.06 % and lower than 6.67 % in weight or mass[1]. This is the main difference they present with steel, which is the other main member of the iron-based alloys. Steel presents a lower carbon content than 2.06 %[2]. Due to this fact, cast iron solidifies with a eutectic and thus it presents two differentiated phases, that are, graphite or iron carbides (Fe_3C) and the metallic matrix. On the other hand, steel, due to its lower carbon content is only made up of the metallic matrix, because all the carbon content present in the alloy is dissolved in the metallic phase[3]. This can be seen on the iron carbon diagram shown in Figure 1[4]. The dotted red lines define the stable diagram and the continuous black lines, define the metastable one.

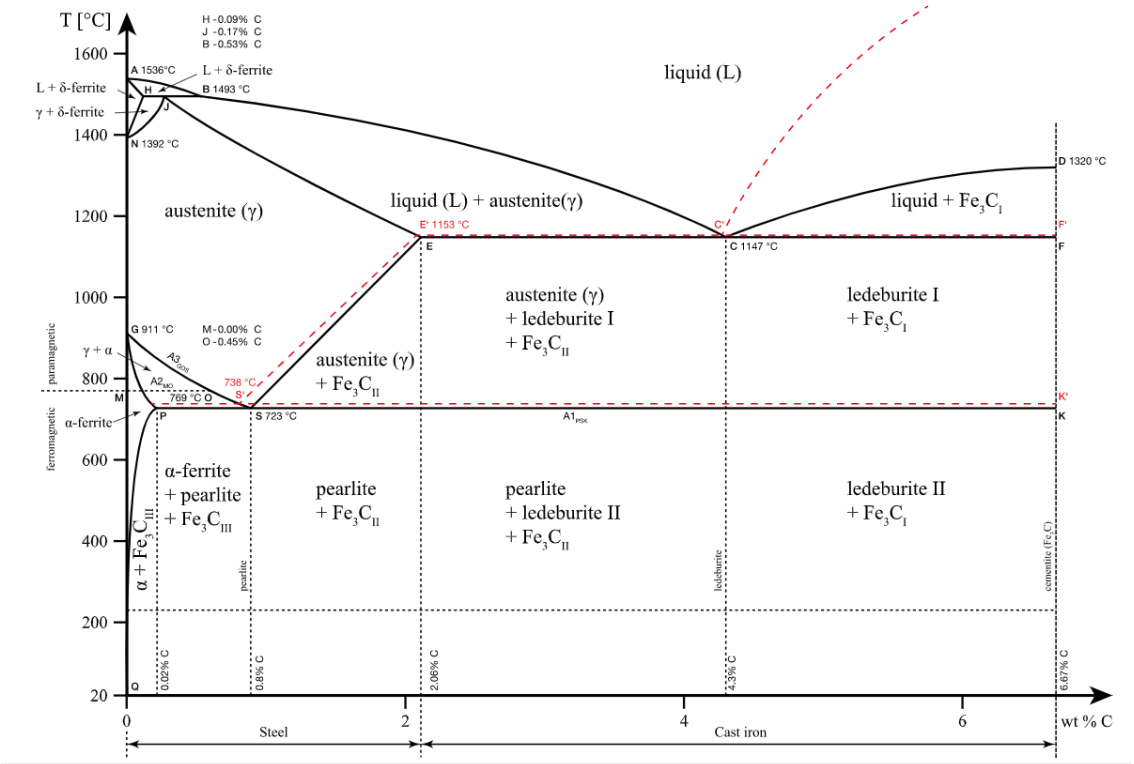

Figure 1. Iron-carbon stable and metastable diagram by Caesar[4].

The chemical composition, conditioning of the melt, cooling rate and other important processing variables make that cast iron solidifies in accordance with the thermodynamically stable iron-graphite system or with the metastable iron-cementite system[5].

If the solidification process takes place following the metastable diagram, no graphite is formed, and all the carbon is present both dissolved in the metallic phase and as iron carbides. These iron carbides, also called cementite, are a compound with a metallic character and the formula Fe_3C, which crystallizes in the orthorhombic system. They are formed in weight by 6.67 % carbon and 93.33 % iron. That is why cast iron presents a maximum of 6.67 % carbon, when all the carbon forms iron carbides. These alloys are called white cast iron (WCI). Iron carbides are very hard and brittle and with a high abrasion resistance. The name white iron comes from the white colour that presents its fracture surface due to the brittleness created by the carbide formation and absence of graphite.

If the solidification process takes place following the stable diagram, then the carbon precipitates as graphite[6]. Graphite formation in iron-based materials offers advantages regarding a multitude of properties. On the one hand, the graphite gives the material enhanced mechanical properties compared with white iron and on the other hand, a lower contraction compared with white iron and steel. The solidification shrinkage of the metallic phase or austenite is counteracted by the graphite expansion and thus, the feeding systems can be minimized increasing the production yield of the material. Additionally, the machinability is improved since graphite acts as a lubricant and leads to discontinuous chips. Moreover, vibrations are damped, and the weight is reduced by approximately 8 % compared to steel because the graphite presents a lower density than the metallic phase.

In addition to the carbon, the main alloying element of the cast iron is silicon. It can be said that for cast iron in general, considering an industrial production, carbon is in between 2.0-4.0 % and silicon in a range between 0.8-3.0 % for white cast iron and between 1.2-3.0 % considering graphitic cast iron, although for the latest solid solution strengthened ductile iron alloys it could be industrially increased up to 4.3 % and it was seen that it could be further increased to 5.2 %[7]. This would make a ternary Fe-C-Si alloy, nevertheless, the solidification and subsequent cooling of cast iron alloys is normally explained by the simpler carbon-iron binary diagram, shown in Figure 1. Figure 2[8] shows the most typical working ranges for carbon and silicon contents for different iron-based alloys. It is seen, how the cast iron presents a higher carbon and silicon content than steel. The silicon content influences the carbon content that the austenite can dissolve, for this reason, it can happen that the alloys with a carbon content lower than 2.06 % solidify with a eutectic, and thus be also considered as cast iron. Another characteristic that is contributed by the silicon addition, is that this element is a graphite promoter, so that the stable solidification behaviour is benefited.

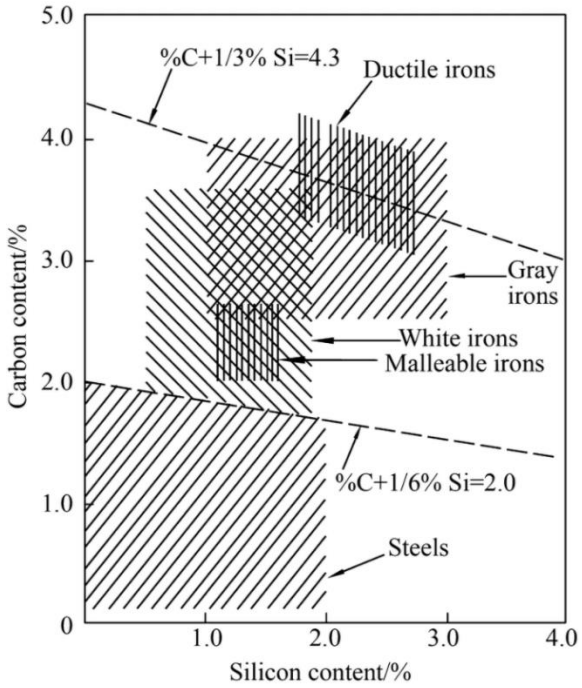

Figure 2. Carbon and silicon contents for the different iron-based alloys by Waiman[8].

Considering the carbon and silicon as the main alloying elements in cast iron, apart from graphite and cementite precipitation, there is another important criterion to make a classification of cast iron, and that is the carbon equivalent. The carbon equivalent can be calculated using the Equation 1[9], Equation 2[10] or Equation 3[11], depending on the literature source.

Equation 1. $\%\ C_{eq} = \%\ C + 0.30\ \%\ Si + 0.33\ \%\ P - 0.015\ \%\ Mn + 0.26\ \%\ S$

Equation 2. $\%\ C_{eq} = \%\ C + 0.28\ \%\ Si + 0.303\ \%\ P + 0.007\ \%\ Mn + 0.092\ \%\ Cu$

Equation 3. $\%\ C_{eq} = \%\ C + 0.31\ \%\ Si + 0.331\ \%\ P - 0.028\ \%\ Mn + 0.076\ \%\ Cu$

It is seen, that in any of the calculation ways, the main contributors to the carbon equivalent are carbon and silicon contents. Based on the carbon equivalent, the cast iron alloys can be classified in three big groups, hypoeutectic, eutectic, and hypereutectic.

The alloy is considered hypoeutectic when the carbon equivalent is lower than 4.30 %, eutectic when it equals 4.30 % and hypereutectic, when it is higher than that value. This will affect the solidification behaviour[12].

When the alloy is hypoeutectic, as seen in Figure 1, then the solidification starts by austenite precipitation. Afterwards, the liquid fraction gets carbon enriched while more austenite precipitates, because the austenite is not able to dissolve all the carbon content present in the alloy. The chemical composition of the liquid fraction follows the liquidus line, till the liquid reaches the eutectic composition of 4.30 % carbon equivalent. At this point, the eutectic solidification occurs, at which graphite or cementite and austenite precipitate at the same time forming a coupled eutectic compound.

When the alloy is eutectic, then the solidification takes place by means of eutectic coupled compounds of austenite and graphite or cementite from the beginning to the end of the solidification[13].

On the hypereutectic case, due to the high carbon equivalent, then the solidification starts by graphite or cementite precipitation. The carbon amount into the liquid phase decreases following the liquidus line, until the liquid reaches the eutectic composition and then, the eutectic solidification starts.

The present work deals with graphitic cast iron, solidified following the stable Fe-C diagram and the alloy is targeted to be of eutectic composition.

2. BACKGROUND

2.1. TYPES OF CAST IRON

Cast iron can be white (WCI) or graphitic, depending on how the carbon precipitates. If the solidification takes places following the metastable Fe-C diagram, then all the carbon present in the liquid melt precipitates as iron carbides. On the other hand, if the solidification takes place following the stable Fe-C diagram, then all the carbon present in the liquid melt precipitates as graphite. On this case, the material is called graphitic cast iron. For graphitic cast iron, the graphite can adopt different forms and thus, based on the graphite morphology, several types of cast iron can be identified: grey or lamellar graphite cast iron (LGI), compacted graphite cast iron (CGI), ductile or spheroidal graphite cast iron (SGI) and malleable cast iron (MCI)[14 15]. Some micrographs of these graphite morphologies as well as the carbide formation in WCI are shown in Figure 3. These micrographs were obtained by optical microscopy on the left column at 100 magnifications and scanning electron microscopy on the centre and right columns, with different magnifications.

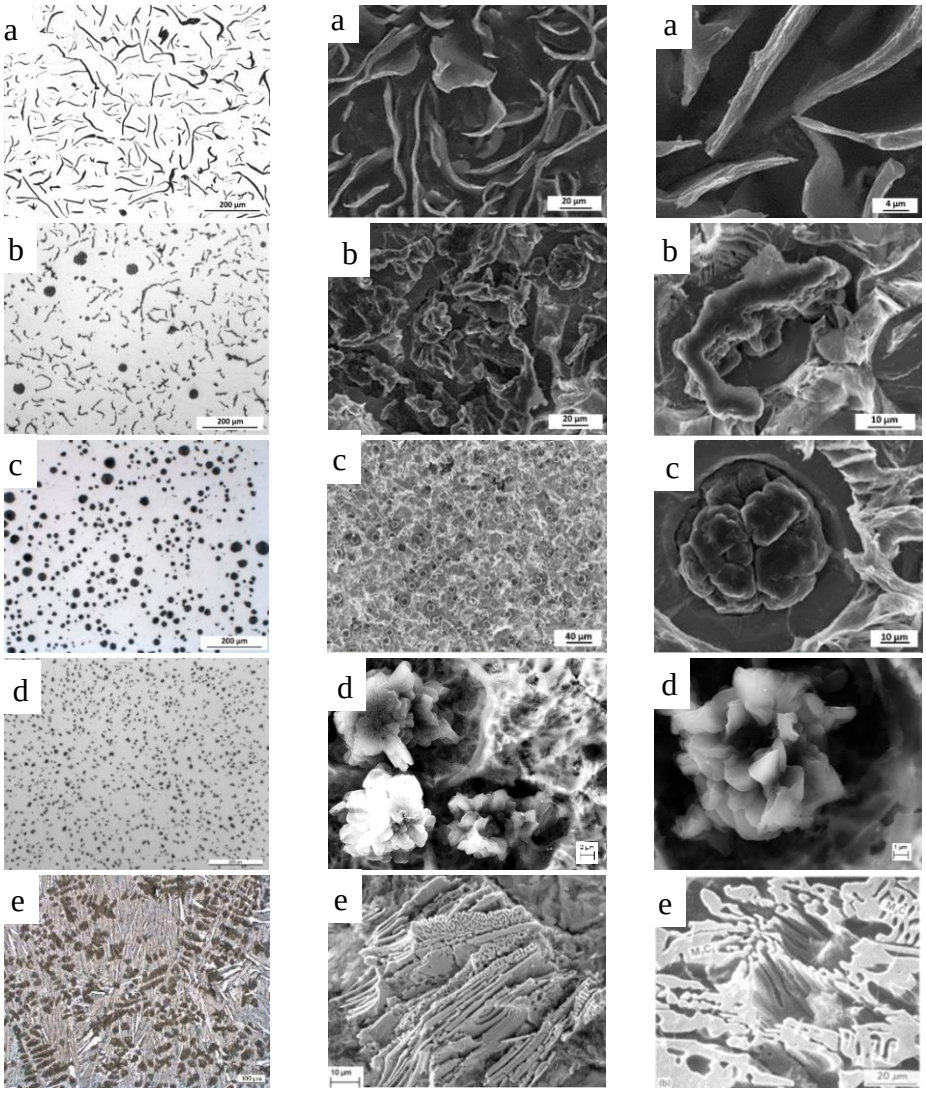

Figure 3. Carbon precipitation morphology of different cast irons a) LGI, b) CGI, c) SGI, d) MCI and f) WCI.

The different graphite shapes of the graphitic cast iron alloys are gathered into the ISO 945-1 standard[16]. These different types are shown in Figure 4, at 100 magnifications.

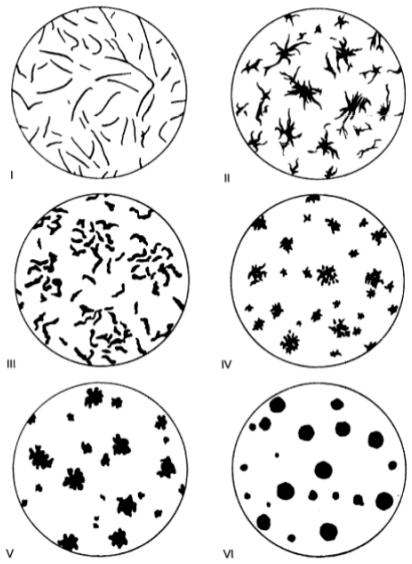

Figure 4. Main graphite shapes in cast iron alloys. Standard ISO 945-1[16].

Type I corresponds to LGI, type III to CGI, type IV to MCI and type V and VI to SGI. Type II is not a conventionally industrially produced graphite shape.

2.1.1. Spheroidal Graphite or Ductile Cast Iron (SGI)

SGI is the material among the cast iron family, that presents the best mechanical properties. The optimization of the mechanical properties compared to the other cast irons is due to the spheric form of the graphite particles. The graphite precipitates as independent spheroids surrounded by the metallic matrix. The precipitation of the graphite particles as nodules instead of the natural lamellar form is obtained by means of the so called spheroidization or nodulization treatment. Conventionally, this treatment is industrially carried out adding a certain quantity of an alloy containing controlled amounts of magnesium, calcium, cerium and lanthanum. The main utilized nodulizing element is the magnesium and its content is habitually in between 0.025-0.040 %[17].

While the graphite lamellae act as stress concentration points in the metallic matrix, the spheroidal form of the graphite hinders the creation of cracks, offering SGI the increased ductility that gives this material its name. Additionally, this material can present a high toughness and fatigue resistance[18].

Regarding the ISO 945-1[16] standard and the graphite shapes shown in Figure 4, the graphite particles are classified as spheroidal or nodular graphite when they are type V and VI. The nodularity or spheroidization index, which shows the proportion of spheroidal graphite particles in a cast iron sample, is a parameter used to control the correct spheroidal form of the graphite. The calculation of the nodularity is explained in the standard ISO 945-4[19], where it is defined as shown in Equation 4. Normally, the nodularity is required to be >85 % for SGI, but in some safety applications it can be required as >90 %.

Equation 4. Nodularity % = (Area Type VI + Area Type V) / total area of graphite * 100

Another important parameter regarding the graphite shape, is its size[20]. The size is linked to the moment during the solidification at which the graphite particle precipitates. The earlier stage of the solidification that the particle nucleates, the bigger it will be at the end of the solidification due to the longer time to grow that it has compared to particles precipitated later. The graphite particle size is designated by numbers from 1 to 8 in accordance with the ISO 945-1[16]. 8 is the smallest particle size and 1 is the biggest. On this behalf, smaller graphite size and thus higher nodule count, leads to a lower microshrinkage tendency of the alloy, because the small graphite particles are assumed to precipitate on the last stages of the solidification process, and they help to counteract the metallic contraction when the feeding system is not able to feed the castings due to the high solid fraction at those stages.

In addition to the shape of the particles and their size, it is also important their number, which is referred as graphite particle count or nodule count and it defines the number of graphite particles per unit of area[21]. The higher this value, the better metallurgical quality, that it describes, because it means that the nucleation potential for the graphite was high and thus higher graphite particle count.

The mechanical properties of SGI present a wide range of resistance and ductility and based on this wide range of combinations, the applications can be very varied, like for instance: holders and housings for the brake system, crankshafts, differential cases, steering knuckles and manifolds for the automotive sector, hubs, gear boxes, housing supports and frames for the wind energy sector, in addition to parts for the heavy vehicle industry, valves, construction, agriculture, railway and industrial machinery among many others.

As it will be next further explained, the mechanical properties of SGI depend on their microstructure. Among the different SGI families, the Austempered Ductile Iron or ADI family is the one that presents the best mechanical properties, based on their ausferritic microstructure. The present work is focused on this material family.

2.1.2. Lamellar Graphite Cast Iron (LGI)

LGI, also called grey iron, represents the family of cast iron materials in which the graphite precipitates with a flake or lamellar form. The term grey iron comes from the colour that shows its fracture surface due to the presence of graphite. It is the most widely produced cast material on a weight basis, because it presents a relatively low cost, good wear resistance, a high thermal conductivity and vibration damping capacity, as well as a good machinability and low contraction tendency[2223]. Their main applications are machinery bases, die structural elements, internal combustion engines cylinder blocks, brake discs, weights and counterweights, exhaust manifolds etc.

The flake like graphite morphology, gives lamellar iron its good properties, but also, its presence leads to a very low ductility and the tensile strength is limited compared to other cast irons. This graphite shape is referenced as type I in the ISO 945-1[16] and is shown in Figure 4.

Lamellar shape is the natural form of the graphite, that is, if no extra treatment is performed to the liquid melt, then the graphite will grow acquiring a flake form with interconnected lamellae[24].

The lamellar graphite morphology is defined in the standard ISO 945-1[16] as type A, B, C, D and E. Normally, type A lamellar graphite is sought.

2.1.3. Compacted Graphite Cast Iron (CGI)

CGI is an intermediate material in between lamellar and spheroidal cast iron, combining a high thermal conductivity, together with a noteworthy mechanical resistance[25]. This type of cast iron is also known as vermicular graphite iron and is characterized by clusters of a worm-like shape graphite particles, coarser and shorter than the lamellae present in grey iron. Considering the ISO 945-1[16] standard and the graphite shapes shown in Figure 4, the graphite particles are classified as compacted graphite when they are type III.

The most usual way of preparing CGI, consists of undertreating a melt with usual spheroidizing elements, namely magnesium and rare earths. However, the range of residual spheroidizing elements for getting the proper graphite morphology is quite limited and highly sensitive to casting conditions[26]. Due to this narrow working range and the difficult implementation to an industrial environment, CGI has not evolved as expected.

Their main applications are for components in which heat transfer and mechanical loading are needed like cylinder blocks and heads for internal combustion engines[27].

2.1.4. White Cast Iron (WCI)

The main characteristic of WCI is that the carbon precipitates from the liquid melt as iron carbides Fe_3C. This is a metastable phase, and it is characterized by a very high hardness and brittleness. There is no graphite present on these alloys. The high hardness of these materials involves a very low toughness and thus they present a lack of machinability.

This leads to applications for parts that are subjected to high wear stresses and no ductility is required, such as, grinding bodies or interior sleeves of concrete mixers[28]. Additionally, they are used as a base material for the manufacture of malleable cast iron parts.

2.1.5. Malleable Cast Iron (MCI)

This is a cast iron that is produced on a first step as WCI and then heat treated, so that the carbon contained in the cementite is transformed into graphite. This graphite presents a spheroidal form, uniformly dispersed and with an irregular shape, which is called temper carbon. Taking into consideration the ISO 945-1[16] standard and the graphite shapes shown in Figure 4, the graphite particles are classified as temper carbon when they are type IV.

The heat treatment applied to the white iron consists of an annealing performed at a temperature high enough that the decomposition of the iron carbides is enabled, conventionally in the range 900-970 ºC. Afterwards, the cooling process is divided in two steps. The first step down to a temperature in between 740-760 ºC is performed as fast as possible. The second step will define the microstructure and thus the mechanical properties, so the cooling rate must be adapted to the desired metallic phase. At low cooling rates, the austenite formed during the austenitizing step at high temperature transforms into ferrite. Increasing the cooling rate, more pearlite will form[29].

The ductility and toughness of malleable iron is close to that of ductile iron. For this reason and considering that the production of malleable cast iron due to the heat treatment, is more expensive and laborious than that of ductile iron, this material is in disuse. Nevertheless, it is still a very useful material to produce very thin section components, because the carbide precipitation is targeted. For this reason, their main applications are pipe fittings and valve parts for pressure services, diesel pistons, steering gear housings, carriers, compressor crankshafts etc.

2.2. MECHANICAL PROPERTIES

The mechanical properties of the cast iron materials present a very wide range. The morphology of the graphite is one of the key points that will define these properties. Thus, SGI, LGI, CGI and MCI cannot be considered as one group and they should be treated separately, since the different graphite shapes that they present will influence the mechanical properties stronger than any other variables.[30] For this reason, there are different standards that define the minimum requirements that each material must meet.

Considering the main graphitic cast irons, SGI requirements are defined in the EN 1563[31] standard, special grades of ductile iron called ADI (Austempered ductile Iron) are defined in the EN 1564[32] standard, LGI in the EN 1561[33] standard and CGI in the ISO 16112[34] standard.

2.2.1. Tensile Test

In order to determine the mechanical properties, the most usual test is a tensile test, which, involves straining a specimen in tension to fracture. The result of this test provides the values of the ultimate tensile strength (UTS), the yield strength (YS) and the elongation (E). How to carry out a tensile test, is defined in the ISO 6892[35] standard. The E is the increase in the gauge length. The UTS is the stress corresponding to the maximum force and the YS, a key parameter for the design of the components, is the stress corresponding to the point reached during the test at which plastic deformation occurs without any increase in the force. This is the stress value at which the functionality of the component is compromised and thus from a design point of view, should never be reached.

In Figure 5 are shown the UTS and YS relationship with the E defined in the above-mentioned standards. These values are obtained after applying a tensile test to specimens machined from samples cast separately. Among the SGI materials from the standard EN 1563[31], two groups have been separated, the conventional ones with no special reference which are marked with circles and the solid solution strengthened materials, referenced as SSS marked with squares. These alloys were introduced into the standard in the edition of 2012.

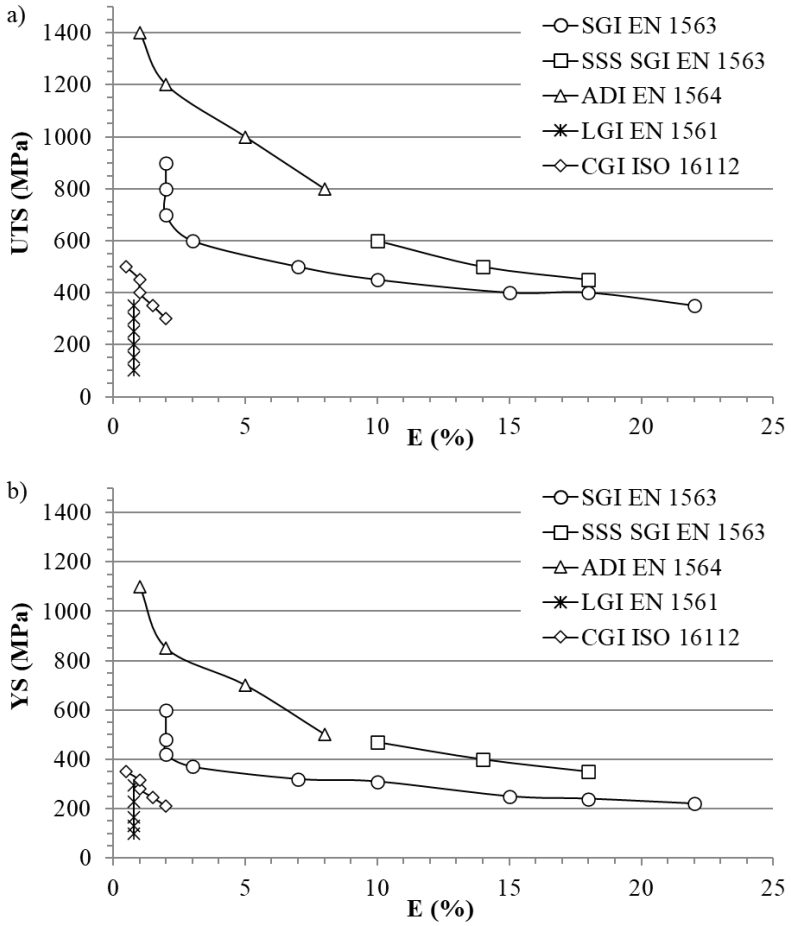

Figure 5. a) UTS and E and b) YS and E evolution for the main cast iron materials[31,32,33,34].

These values are tabulated in Table 1, together with the designation of each material.

Table 1. Mechanical requirements for graphitic cast irons[31,32,33,34].

Cast Iron Type	Standard	Designation	UTS (MPa)	YS (MPa)	E (%)
SGI	EN 1563	EN-GJS-350-22	350	220	22.0
		EN-GJS-400-18	400	240	18.0
		EN-GJS-400-15	400	250	15.0
		EN-GJS-450-10	450	310	10.0
		EN-GJS-500-7	500	320	7.0
		EN-GJS-600-3	600	370	3.0
		EN-GJS-700-2	700	420	2.0
		EN-GJS-800-2	800	480	2.0
		EN-GJS-900-2	900	600	2.0
SSS SGI		EN-GJS-450-18	450	350	18.0
		EN-GJS-500-14	500	400	14.0
		EN-GJS-600-10	600	470	10.0
ADI	EN 1564	EN-GJS-800-8	800	500	8.0
		EN-GJS-1000-5	1000	700	5.0
		EN-GJS-1200-2	1200	850	2.0
		EN-GJS-1400-1	1400	1100	1.0

Table 1 (Cont.) Mechanical requirements for graphitic cast irons[31,32,33,34].

Cast Iron Type	Standard	Designation	UTS (MPa)	YS (MPa)	E (%)
LGI	EN 1561	EN-GJL-100	100	--	0.8
		EN-GJL-150	150	98	0.8
		EN-GJL-200	200	130	0.8
		EN-GJL-250	250	165	0.8
		EN-GJL-300	300	295	0.8
		EN-GJL-350	350	228	0.8
CGI	ISO 16112	EN-GJV-300	300	210	2.0
		EN-GJV-350	350	245	1.5
		EN-GJV-400	400	280	1.0
		EN-GJV-450	450	315	1.0
		EN-GJV-500	500	350	0.5

It is seen that SGI presents optimized mechanical properties compared to CGI and LGI. As said before, these differences are based on the shape of the graphite particles. Nevertheless, it is very important to point out, that for the different cast irons, if the graphite morphology is the desired one and no degenerations are present, then the mechanical properties are defined by the metallic matrix or the microstructure.

LGI shows very low elongation and limited resistance, but their attractive as a material relies on their high thermal conductivity, low contraction tendency, vibration damping capacity and their low manufacturing cost. The natural precipitation form of the graphite as interconnected lamella makes that the strength is decreased compared to SGI and CGI. Additionally, the ductility of the material is very limited and independent of the UTS requirement, the elongation specification remains at a minimum of 0.8 %. Nevertheless, there are other factors like for instance the ratio between primary austenite precipitation and eutectic reaction that also affect the mechanical properties of grey iron[36].

CGI, with their worm like graphite shape, intermediate between a nodular and lamellar shape, presents improved mechanical properties compared to the LGI, but lower ones compared to SGI[37]. Nevertheless, these materials maintain a high thermal conductivity compared to the SGI, and that is their main functional attractive.

Focusing on the SGI materials, which are the target of this work, three different groups have been made. The conventional ductile iron materials referenced as SGI present an increasing resistance as the elongation decreases, reaching UTS values of 900 MPa for an elongation of 2 %. On the other side, resistances of 350 MPa and elongations of up to 22 % can be obtained. These alloys present ferritic, pearlitic or ferritic/pearlitic microstructures and the ratio of these two phases is the cause of this evolution[38]. These phases are better explained on the next section, but the ferrite presents a higher ductility and lower resistance than the pearlite [39], so if a higher elongation is sought, then the matrix should be more ferritic[40] and for a higher resistance, pearlitic matrixes are sought[41].

The SSS SGI materials, are strengthened by an increase on the silicon content[42]. These materials have the characteristic that they present a fully ferritic matrix, but as a consequence of a higher silicon content, this ferrite is harder and thus exhibits a higher resistance at the expense of a lower ductility. For this reason, they can compete with the SGI ferritic-pearlitic materials, presenting a higher resistance for the same elongation. Additionally, the ratio YS/UTS is higher for these alloys than the conventional ones, increasing from 60-70 % to 75-80 %. These materials are recently increasing their market niche and are displacing the conventional ductile iron in some applications, because in addition to the optimized mechanical properties, they present a very good machinability[43].

The ADI materials or Austempered Ductile Iron, the target of this work, are the SGI materials that present by far the best mechanical properties[44,45]. Compared to the other cast iron materials, the mechanical properties improvement is substantial and as can be seen in Figure 6, they can even compete with steel in terms of resistance and elongation[46]. This improvement in the mechanical properties, is based on an ausferritic microstructure, which is made up of reacted austenite and acicular ferrite. Conventionally, this microstructure is obtained applying a heat treatment which is called austempering. After austenitizing the as-cast microstructure, an isothermal quench is applied in the range between 250 and 450 ºC and the temperature maintained constant for a given time, so that the ausferritic reaction can evolve.

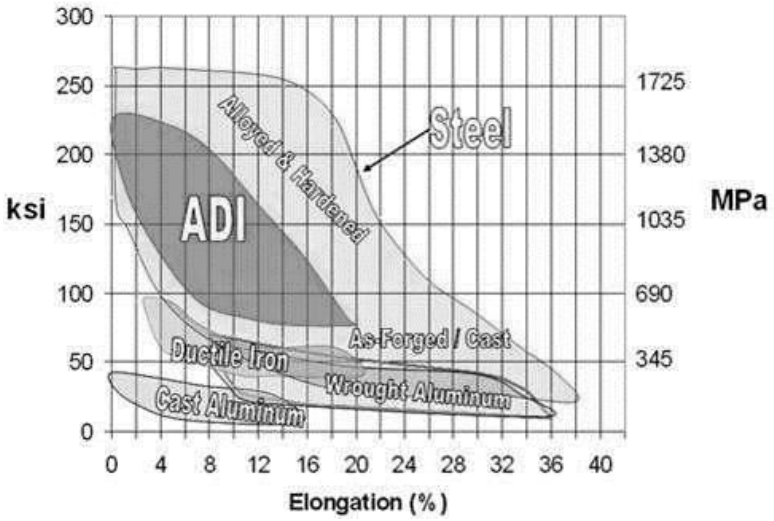

Figure 6. UTS and E relationship for different metallic alloys.

Taking into account the lower density of SGI compared to steel due to the presence of graphite (up to 10 % less), ADI offers an optimal strength to weight ratio. At the same time, this advantage makes that ADI costs 20 % less per unit weight than steel and 50 % less than aluminium as shown in Figure 7[47]. Thus, ADI materials offer engineering and design advantages that make them attractive for a wide range of applications, including automotive light vehicles and heavy trucks, railway, agriculture, construction, and mining.

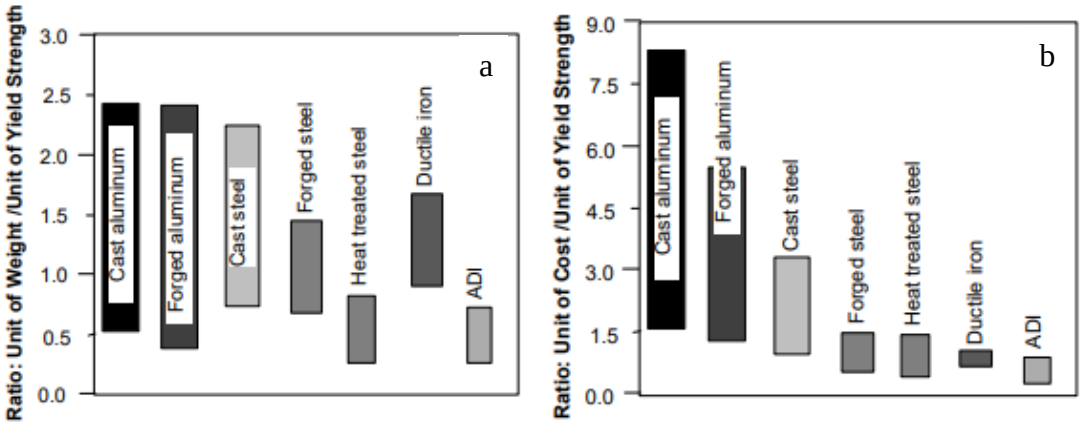

Figure 7. Relative weight (a) and cost (b) per unit of YS for different metallic materials by Hayrynen [47].

2.2.2. Hardness

Hardness represents a simple, easy and fast way of defining the mechanical properties and thus it is a common process control test in cast iron foundries. It is not defined in the standards as a requirement, but as illustrative values. Only for the LGI can be a requirement if the material is demanded taking into account the hardness. For cast iron, the hardness is normally measured using the Brinell hardness (HBW) test, whose methodology is defined in the standard ISO 6506-1[48]. In graphitic cast iron, the graphite can influence the hardness measurement and for this reason, it is needed a measuring methodology that presents a large size of indentation, so that, both the graphite particles and the metallic matrix are considered together. The minimum and maximum values for the hardness that are defined in the standards, are shown in Figure 8, as their evolution with the E.

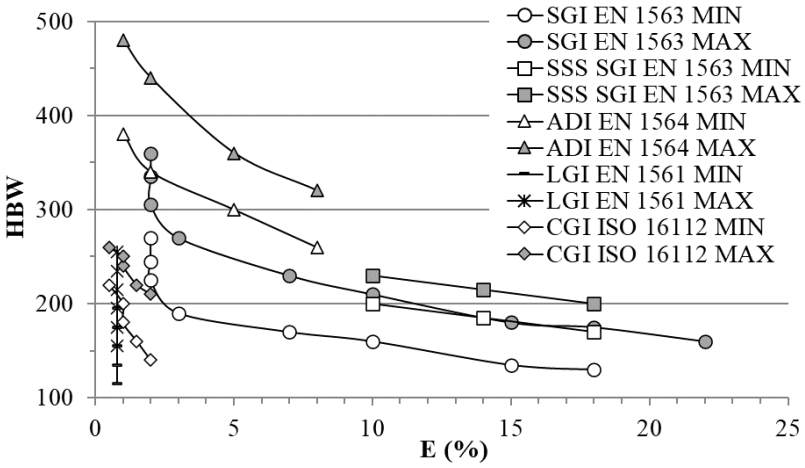

Figure 8. Hardness ranges for the different graphitic cast irons[31,32,33,34].

These values are tabulated in Table 2.

Table 2. Standardized values for the hardness of graphitic cast iron[31,32,33,34].

Cast Iron Type	Standard	Designation	HBW
SGI	EN 1563	EN-GJS-350-22	<160
		EN-GJS-400-18	130-175
		EN-GJS-400-15	135-180
		EN-GJS-450-10	160-210
		EN-GJS-500-7	170-230
		EN-GJS-600-3	190-270
		EN-GJS-700-2	225-305
		EN-GJS-800-2	245-335
		EN-GJS-900-2	270-360
SSS SGI		EN-GJS-450-18	170-200
		EN-GJS-500-14	185-215
		EN-GJS-600-10	200-230
ADI	EN 1564	EN-GJS-800-8	260-320
		EN-GJS-1000-5	300-360
		EN-GJS-1200-2	340-440
		EN-GJS-1400-1	380-480
LGI	EN 1561	EN-GJL-HB155	<155
		EN-GJL-HB175	115-175
		EN-GJL-HB195	135-195
		EN-GJL-HB215	155-215
		EN-GJL-HB235	175-235
		EN-GJL-HB255	195-255
CGI	ISO 16112	EN-GJV-300	140-210
		EN-GJV-350	160-220
		EN-GJV-400	180-240
		EN-GJV-450	200-250
		EN-GJV-500	220-260

The hardness follows the same tendency as the resistance, the higher the elongation, the lower the hardness. It is seen the strengthening effect of the silicon for a ferritic matrix, because the SSS SGI materials present a higher hardness that the ferritic-pearlitic SGI materials for the same elongation. Additionally, the ADI materials present the highest hardness among the graphitic cast iron, which is in good agreement with the highest resistance that they exhibit.

2.2.3. Impact Resistance

In addition to the tensile test data, some of the SGI grades present an impact resistance requirement. This requirement is only demanded for the grades that present the highest toughness, that are, the non-strengthened ferritic alloys and the ausferritic one with the highest ductility. How these values are obtained is described in the standard ISO 148-1[49]. This standard defines the specimen dimensions, type of the notch that presents the specimen (U or V), the force that is applied for the test etc. The test consists of breaking the specimen notched in the centre and supported at each end by one impact from a swinging pendulum. The standard requirements are shown in Table 3. These values correspond to tests performed on specimens machined from independently cast samples. The values of the SGI materials correspond to a sample presenting a thickness lower than 30 mm. The specimens are V notched.

Table 3. Impact resistance requirement for SGI[31,32].

Cast Iron Type	Standard	Designation	Impact Resistance. V Notched (J)					
			(23 ± 5) ºC		(-20 ± 2) ºC		(-40 ± 2) ºC	
			Av. 3 Tests	Ind.	Av. 3 Tests	Ind.	Av. 3 Tests	Ind.
SGI	EN 1563	EN-GJS-350-22 RT	17	14	--	--	--	--
		EN-GJS-350-22 LT	--	--	--	--	12	9
		EN-GJS-400-18 RT	14	11	--	--	-	--
		EN-GJS-400-18 LT	--	--	12	9	--	--
ADI	EN 1564	EN-GJS-800-8	10	9	--	--	--	--

Depending on the application, the material presents a requirement at room or low temperature. The softer ferritic grades can be applied for this low temperature applications, but the ADI material has a defined requirement only at room temperature. The lower the resistance of the material, and the higher the ductility, the impact resistance increases[50]. In terms of toughness, the ADI materials are the SGI materials that present the highest values[51,52].

The low or room temperature requirements are based on the ductile to brittle transition temperature. This temperature is strongly affected by the silicon content, increasing it dramatically when the silicon increases[53]. For this reason, the SSS SGI materials do not present any impact resistance requirement, because at room temperature they are in the brittle zone [42].

2.2.4. Fatigue Resistance

Another important physical property for a metallic material, is the fatigue resistance or fatigue strength. Fatigue is the damage that can lead a component to failure due to repeated or cyclic loading at levels even considerably below the YS. A fatigue failure is directly related to the stress level and number of applied cycles, so the fatigue resistance is analysed applying different levels of cyclic stress to a specimen, and then measuring the number of cycles that were applied until failure. If there is no failure after a certain number of cycles, normally above 10^6, depending on the application and functionality of the component, then it is supposed that for that stress level, the material will not fail under cyclic fatigue. The maximum stress level reaching that number of cycles at a fatigue test is defined as the fatigue limit. The results of this test are plotted on a S-N curve, being the vertical axis the stress and the horizontal axis the number of cycles to failure. How to carry out a fatigue test is defined in the standard ISO 1099[54].

The fatigue resistance, as well as other physical properties, is dependent of the graphite shape, and thus LGI, CGI and SGI should be studied separately. Additionally, fatigue strength is dependant of the microstructure of the material. Data of fatigue resistance for the different cast iron materials are not standardized, but they have been deeply studied. LGI presents the lower fatigue limit among the graphitic cast irons, as it happens with the UTS and YS[55], CGI improves the fatigue resistance compared to LGI [56] and SGI presents the highest fatigue strength among the cast iron materials[57]. On the work from Rausch eta al[58] there is a comparison of the fatigue resistance for the materials EN-GJL-270, EN-GJV-450 and EN-GJS-700. These results are shown in Figure 9. It is seen, how as the UTS and YS increase, the fatigue strength also increases.

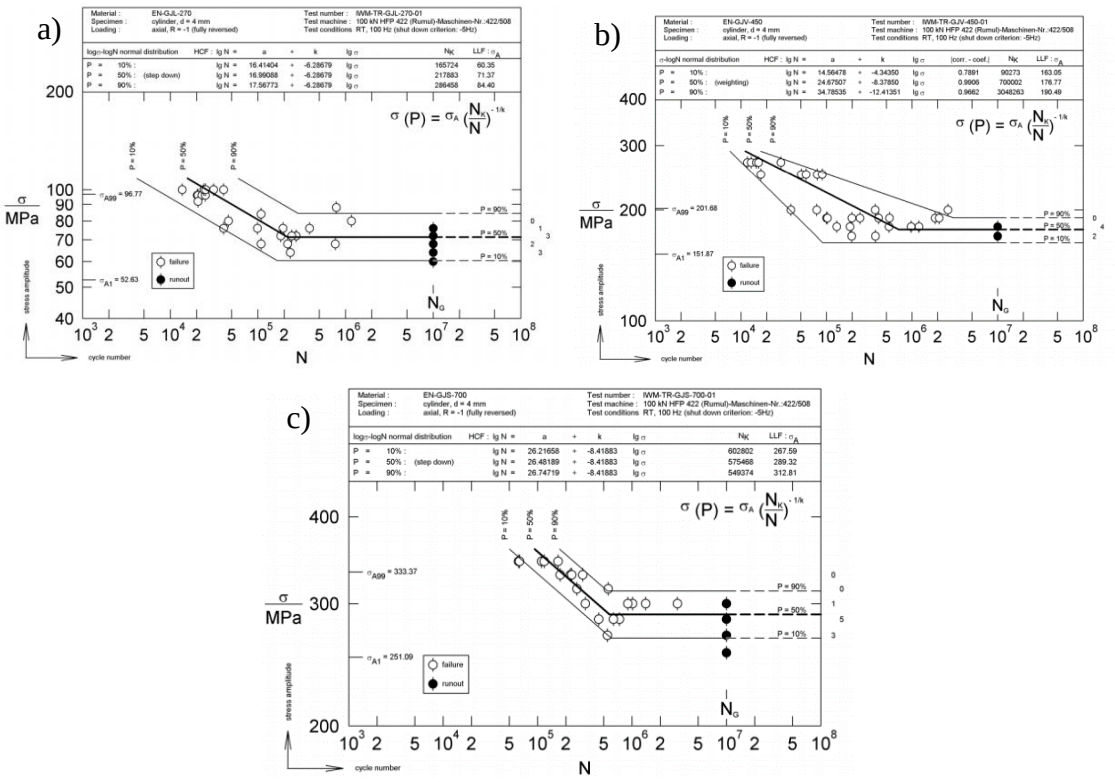

Figure 9. S-N curves for different cast irons a) EN-GJL-270, b) EN-GJV-450 and c) EN-GJS-700 from the work by Rausch eta al.[58].

Considering the SGI materials, in the work from Luo et al [57] there is a comparison of their fatigue strength considering the microstructure or the metallic matrix. These results are shown in Figure 10.

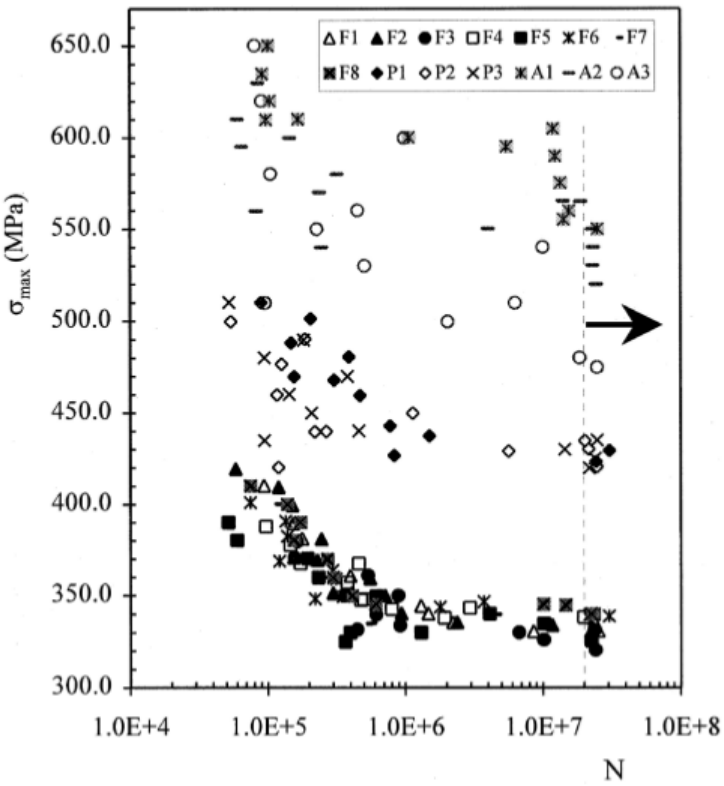

Figure 10. S-N curves for different SGI materials F (Ferritic), P (Pearlitic) and A (ADI) from the work by Luo et al.[57]

It is seen that a ferritic matrix presents the lowest fatigue resistance among the SGI materials and the ADI materials the highest one. This is in good accordance with the tensile test values and corroborates the optimal properties of the ADI materials[59,60].

2.3. SOLID-TO-SOLID TRANSFORMATION

Solid to solid transformation involves a phase transformation in the solid state, in which if a crystalline material or element exists in two or more polymorphic or allotropic forms, then it transforms from one form to another. These transformations define the final microstructure or the phases that made up the metallic matrix of a metallic material at room temperature. At the same time, this microstructure defines the mechanical properties of the material. For this reason, it is a key point of this work to investigate these solid-to-solid transformations that take place during the cooling process of a metallic material.

2.3.1 Transformations of iron carbon alloys

In the case of pure iron, at atmospheric pressure, it can have two allotropic forms as a function of temperature. α-iron is stable between room temperature and 910 ºC and has a bcc structure, while at higher temperatures and up to 1392 ºC, pure iron acquires a fcc structure constituting the so-called γ-iron. From 1392 ºC, iron acquires again a stable bcc structure, giving rise to δ-iron. The change in crystal structure can occur through two distinct transformation mechanisms and thus phase transformations could be divided in two groups as proposed by Buerger[61]: reconstructive and displacive. On the one hand, if sufficient atomic mobility is favoured, then the crystal structure fcc of γ-iron may undergo a complete rebuild to the bcc form of α-iron. In this case, many bonds have to be broken and new ones formed, altering the atomic arrangement of the original crystal which are then rearranged or rebuilt into a new pattern. This is the case of a reconstructive transformation. However, if the fcc phase is rapidly cooled to a very low temperature, well below 910 ºC, the atomic mobility is not sufficient to enable reconstructive transformation. On this case, the driving force for the transformation increases with the undercooling, which allows the formation of a new crystal structure through a deformation of the original pattern by the coordinated movement of atoms through the interface. This type of transformation is called displacive and the phase transition involves the distortion of bonds rather than their destruction and the structural changes are smaller than for reconstructive reaction. It is a diffusionless transformation. This is the case of martensite formation[62]. Figure 11 shows the nature of the different transformations that take place for an iron-carbon alloy. It is seen, that at high temperatures, the transformations are reconstructive, because the atoms have easier to move, while at lower temperatures this movement is more restricted and thus the displacive transformations take advantage.

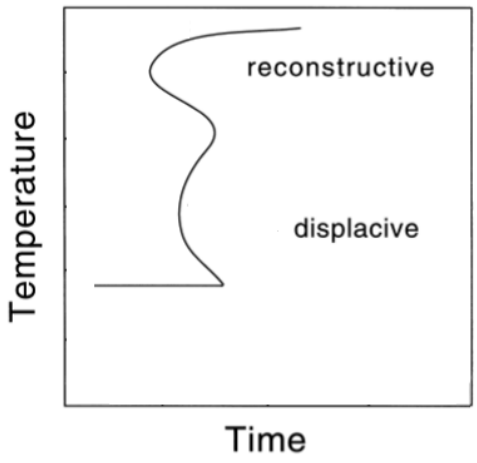

Figure 11. Nature of the different phase transformation in Fe-C alloys.

The addition of carbon modifies the structure and the temperature range of stability of the iron phases as seen in the Fe-C diagram (Figure 1). The solid solution of carbon in γ iron is called austenite (also γ), and the carbon atoms are distributed in interstitial positions of the fcc lattice. The addition of carbon stabilizes the austenite at temperatures below 910 ºC, down to 723 ºC for an alloy with a carbon content of 0.77 %. This composition of iron and carbon is called eutectoid, and the corresponding temperature is called the eutectoid temperature. On the other hand, the solid solution of carbon in iron α constitutes the so-called ferrite (also α), with a maximum carbon solubility equal to 0.02 % by mass. In the Fe-C equilibrium diagram (Figure 1) it is observed that, at the eutectoid temperature, the degree of enrichment of austenite is such that it decomposes into a laminar structure, made up of ferrite and cementite, called pearlite. The transformation from austenite to ferrite or pearlite is a reconstructive one.

An important concept for the solid-state transformations in cast iron, is the partitioning of the substitutional elements during these transformations. In iron carbon alloys, carbon acts as an interstitial solute and the other alloying elements as substitutional ones[63]. Diffusivity of interstitial solute is much higher than that of the substitutional ones. If it is considered that no partitioning of the substitutional elements exists, then an isopleth section of the Fe-C diagram for the silicon content of the studied alloy could be used for the description of the eutectoid transformation.

2.3.2. Thermodynamic and kinetics concepts for phase transformation

Phase transformations are affected by thermodynamic and kinetic factors. Thermodynamic theory defines what is possible to spontaneously happen in nature. Nevertheless, it does not give information about the rate at which a reaction or transformation takes place. Hence, it is not possible to thermodynamically define the mechanism that a transformation has followed from the initial to the final state. This is studied by the kinetic theory[64].

Thermodynamical equilibrium, at which no changes will occur independent of the time passed, is the state of less Gibbs free energy of a system. The Gibbs free energy is a parameter that explains the stability of a compound or a phase. If this parameter is negative, then the compound or phase is stable, and it is possible for it to spontaneously form. The more negative this energy becomes, the stability of the compound or the phase increases. These equilibrium conditions are displayed by the phase or equilibrium diagrams, in this particular case the Fe-C diagram shown in Figure 1. These diagrams show which phases are stable for a given pressure, temperature, and chemical composition conditions, considering the less energy of the whole system. Nevertheless, it can happen that a situation represents a local minimum of the free energy of the system, but not the lowest minimum. This is called a metastable equilibrium, which does not exclude the existence of lower minimums.

While thermodynamic theory is essential to understand any phase transformation, it does not explain how the transformation is performed. Kinetics theories explain how the nucleation and growth of a phase takes place. These kinetics aspects are dealt with Continuous Cooling Transformation (CCT) or Temperature-Time Transformation (TTT) diagrams[65]. CCT diagrams are performed cooling a sample at a constant rate from a fully austenitic microstructure for the Fe base alloys and then analysing its final microstructure at room temperature. They define, for a given cooling rate which is the obtained microstructure. TTT diagrams study the kinetics of isothermal transformations. They display the required time for a fully austenitic matrix to transform to other phases at a constant temperature. They determine when a transformation begins and when it ends. They are useful diagrams for isothermal phase transformation processes, as it is the case of the ausferritic reaction. Both diagrams can be defined using dilatometry techniques or thermal analysis. In Figure 12 an example of TTT and CCT diagrams developed for SGI by Gazda[66] are shown.

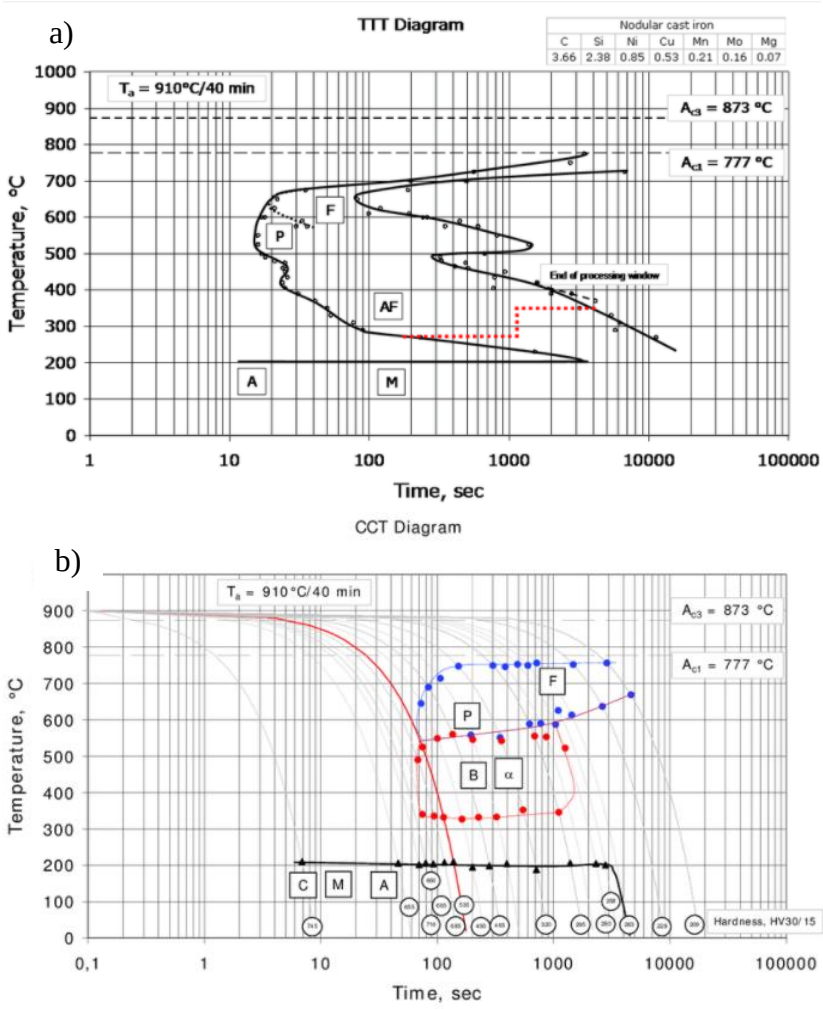

Figure 12. Example of a) TTT and b) CCT diagrams developed for SGI by Gazda[66], being F: Ferrite, P: Pearlite, AF, Ausferrite, A: Retained Austenite, M: Martensite, B: Bainite and C: Carbides.

2.3.3. Microstructure classification for graphitic cast irons

Considering graphitic cast irons, the microstructure or the metallic matrix formed after the solid-to-solid transformation, can be made up of different phases that are next described[67 68]:

- AUSTENITE: This metallic phase, also called gamma iron (γ), has a Face Centred Cubic (fcc) crystallographic structure. Each unit cell presents an atom at each one of the eight corners of a cube and another atom at the centre of every face of the cube. It is an interstitial solid solution of carbon in iron, being its maximum carbon solubility of 2.06 % at 1147 ºC as seen in the Fe-C diagram (Figure 1). For cast iron, the metallic matrix is fully austenitic just after the solidification and for conventional alloys, it is not thermodynamically stable at room temperature. Nevertheless, increasing the carbon content dissolved by this phase can make it stable at room temperature. There are also austenite stabilizer elements, like for instance nickel, manganese and nitrogen. The stabilization of the austenite is because the eutectoid transformation temperature at which the austenite changes, goes below room temperature. This phase presents a high toughness.

- FERRITE: This metallic phase, also called alpha iron (α), has a Base Centred Cubic (bcc) crystallographic structure. Each unit cell presents an atom at each one of the eight corners of a cube and one in the centre of the cube. This is the product of a stable eutectoid reaction and is the softest phase of the ones present in cast iron. Thus, it presents a high machinability. It is an interstitial solid solution of carbon in iron. Its carbon solubility is very low, being its maximum 0.02 % at 723 ºC and 0.008 % at room temperature (Figure 1). On the other hand, it dissolves different quantities of silicon, manganese, copper etc. and these elements, mainly silicon, can modify its properties. Silicon is a substitutional solute in the bcc structure of the ferrite, and it hardens this phase.

  To promote the formation of ferrite, low cooling rates are sought, because then the cooling process is closer to the stable eutectoid transformation. If the casting geometry does not allow a sufficiently low cooling rate to promote a fully ferritic microstructure, an annealing heat treatment can be applied. Another way to favour the formation of ferrite is by adding ferrite promoter elements like silicon, cobalt or boron.

- PEARLITE: This is a dual phase structure. It consists of alternate layers of ferrite and iron carbide (Fe_3C). Its carbon solubility is of 0.77 %, which is the eutectoid composition of the Fe C diagram (Figure 1). This is the product of a metastable eutectoid reaction and the presence of carbides combined with ferrite, gives this structure higher resistance than ferrite, but at the expense of a lower ductility. The thickness of the carbide and ferrite layers defines its properties, being those optimized by a finer pearlite in which the thickness of those layers is very fine.

Pearlite formation is promoted by a high cooling rate because this way the cooling process is moved away from the stable eutectoid reaction and the metastable favoured. If the casting geometry does not allow a sufficiently high cooling rate to promote a fully pearlitic microstructure, a normalizing heat treatment can be applied. Additionally, the addition of certain elements like copper, tin, antimony, manganese etc. favours the pearlite formation.

- AUSFERRITE: This is a dual phase microstructure, which is made up of acicular ferrite or ferrite needles and carbon enriched austenite or reacted austenite. The formation of this phase takes place when, parting from an austenitic microstructure, the temperature is maintained constant in a range in-between 250-450 ºC. To that aim, it is conventionally applied an austempering heat treatment, which, after the austenization, consists in an isothermal quench to the desired temperature. To achieve this phase, the eutectoid transformation must be supressed by a rapid cooling and then the martensite formation avoided by maintaining a constant temperature in the ausferritic transformation range (250-450 ºC), always above the martensite formation start temperature (M_S). Depending on the temperature, the ausferrite can be upper or lower. Upper ausferrite is formed at higher temperatures (350-450 ºC) and its morphology is thicker and coarser, while lower ausferrite is formed at lower temperatures (250-350 ºC) and it is finer.

  The ausferritic formation is promoted by the addition of elements that increase the hardenability of the material, that is, that prevent the eutectoid transformation, like for instance molybdenum, nickel, copper, and manganese. Additionally, a minimum maintaining time is needed at the ausferrite formation temperature range, so that the transformation can evolve and be completed. However, too long maintaining time can lead to the formation of bainite, which should be avoided.

- MARTENSITE: This is a supersaturated solid solution of carbon in iron and its crystallographic structure is a Body Centred Tetragonal (bct) form. It is usually obtained by a rapid cooling of austenite, without any atomic diffusion, but by a sudden diffusionless shear process and the consequent deformation of the parent lattice into that of the martensite. Its formation is thus promoted by the prevention of the eutectoid transformation. During the rapid cooling, the formation of martensite starts at the M_S and ends at the martensite formation end or finish temperature (M_f). This temperature range is not very wide, being usually around 150 ºC, and together with the rapid cooling, the transformation can be considered to happen almost instantaneously. Martensite has an acicular appearance in form of needles and is a very hard phase, whose hardness can be of over 700 Brinell. The machinability of this phase is extremely low. The martensite formed after the rapid cooling, also called, quenching, is very brittle and for this reason, it is advisable a tempering heat treatment, so that the internal stresses formed during the quenching are eased. After the tempering process, the martensite is called tempered martensite.

Martensite formation is promoted by very high cooling rates, normally achieved by a quenching heat treatment. The addition of elements that increase the hardenability of a material, such as molybdenum and nickel favour also the formation of martensite, because they help to avoid the eutectoid transformation.

- BAINITE: This is the phase that is obtained if the time during the isothermal transformation period to obtain ausferrite is prolonged. Then, the carbon enriched austenite cannot dissolve more carbon and it starts to decompose into ferrite and small iron carbides. The combination of ferrite needles and carbides makes up the bainitic phase. This is a phase that in steels is formed directly during the isothermal transformation, because they usually present a lower silicon content than cast iron. The higher silicon content in cast iron hinders the formation of iron carbides and thus the formation of bainite is delayed to what is called stage II of the ausferritic reaction. This is a non-desirable and detrimental phase because the precipitation of carbides lowers the ductility of the material.

In Figure 13 the different microstructures that can be the product of the solid-state transformations for SGI are shown. These micrographs were obtained by optical microscopy after etching the samples with the reactant Nital 5 %. Different magnifications were used for the sake of clarity.

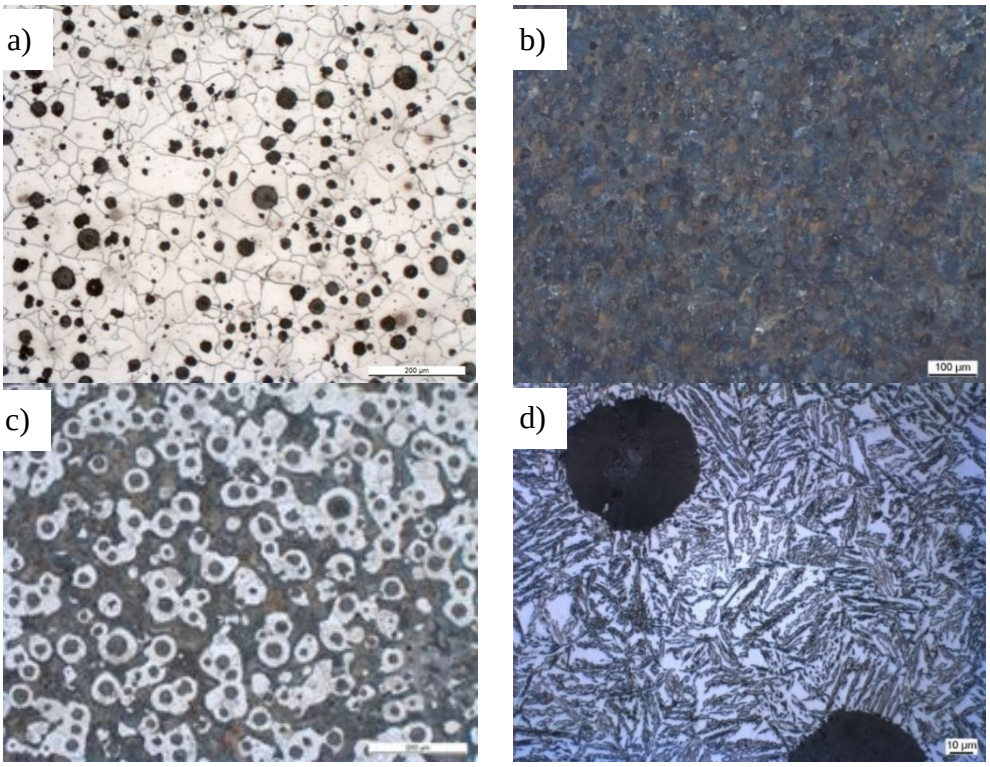

Figure 13. Solid-to-solid transformation products for SGI a) Ferrite 100x, b) Pearlite 100x, c) Ferrite/Pearlite 100x, d) Upper Ausferrite 500x, e) Lower Ausferrite 500x and f) Martensite 500x.

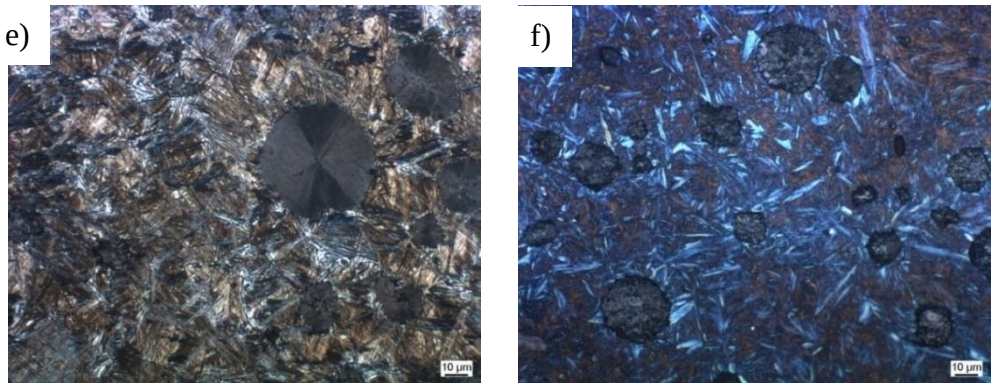

Figure 13. (Cont.) Solid-to-solid transformation products for SGI a) Ferrite 100x, b) Pearlite 100x, c) Ferrite/Pearlite 100x, d) Upper Ausferrite 500x, e) Lower Ausferrite 500x and f) Martensite 500x.

The solid-state transformation defines the final microstructure of the cast iron components. The mechanical properties are directly dependent of this microstructure. Figure 14 shows the relationship between the UTS and E from the standards for SGI shown in Figure 5 and the microstructures that are needed to fulfil these requirements (Figure 13).

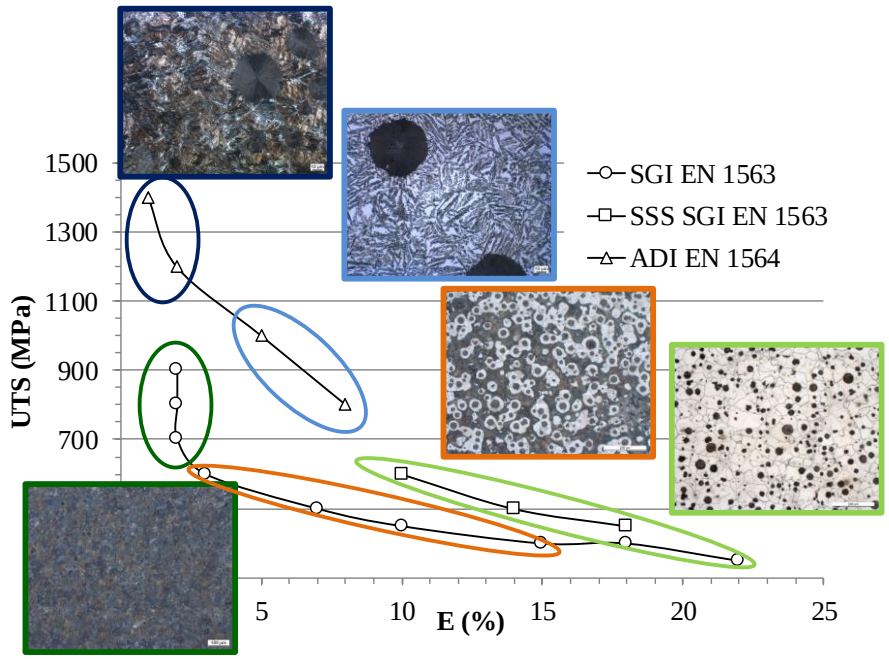

Figure 14. Relationship between microstructure and UTS and E for SGI[31,32].

It is seen that a fully ferritic microstructure as the softest phase, presents the lowest resistance and the highest elongation. A fully pearlitic microstructure presents higher resistance at the expense of a much lower ductility. Ferritic-pearlitic microstructures remain in between them.

The optimal mechanical properties for SGI, are shown by fully ausferritic microstructures, that are characteristic of the ADI materials. Upper ausferrite is more ductile and softer than the lower one, which presents the highest resistance for the ductile iron family. The present work deals with the ausferritic microstructures.

3. STATE OF THE ART

3.1. SOLIDIFICATION

Cast iron materials define their graphitic structure during the solidification, being the product of this process graphite and austenite for a stable solidification process and carbides and austenite for a metastable solidification, as defined in the Fe-C phase diagram (Figure 1).

In this work, SGI is studied. Consequently, only a stable solidification is considered, during which spheroidal or nodular graphite is formed together with the austenite[69]. The precipitation of iron carbides during the solidification has a detrimental impact on the mechanical properties and therefore it is considered as a defect.

It has been stated that, for cast iron, if the graphite morphology is the desired one, then the mechanical properties will be defined by the microstructure or the metallic matrix. Besides, the mechanical properties as a function of the graphite shape have been presented and shown, the crucial impact that the graphite shape presents on the mechanical properties. Nodular or spheroidal graphite is the graphite shape that provides cast iron with the best mechanical properties (Figure 5).

To promote a fully spheroidal graphite shape during solidification[70], after the raw materials have been melted in the furnace and the chemical composition adjusted, a nodulizing treatment is performed to the liquid melt before pouring. Magnesium is the main element used for spheroidization[71].

As magnesium is a very reactive element, it is not added in a pure state to the liquid melt, but as a form of a FeSiMg alloy, having these alloys contents of around 45 wt.% Si and a defined Mg content, conventionally, in between 3 and 12 wt.%. These alloys have a certain content of calcium (1-2 wt.%) in order to increase the efficiency of the nodulization. The responsible for the nodular shape of the graphite is the active or free magnesium, that is, the one that is not combined with oxygen or sulphur[72]. As calcium is a more reactive element with oxygen and sulphur than magnesium, it helps to increase the reaction yield and reduce the reactivity of the reaction, because it combines with oxygen and sulphur before magnesium does. Thus, less Mg addition is needed. Moreover, the FeSiMg alloys present rare earths[73], normally in a proportion of 2 times cerium and one time lanthanum. Cerium is an element that also promotes the spheroidization of the graphite and the addition of Ce and La helps to avoid the formation of degenerated graphite[74]. After this treatment a nodularity, as expressed in Equation 4, higher than 90 % is sought.

In addition to the nodulization treatment, inoculation is another main step of the liquid melt preparation of SGI. It consists of a late addition of a FeSi product, containing 75 % of silicon, with small additions of other elements like barium, aluminium, bismuth, zirconium, cerium etc[75]. Inoculation is applied to promote a stable solidification and avoid iron carbide formation[76]. The effect the inoculation has on the liquid melt, is the formation of nuclei that favour graphite nucleation. Thus, the nucleation capacity of the liquid melt is enhanced, and the metastable solidification hindered. The addition of the inoculant product creates some compounds in the liquid melt that act as nucleation sites for the graphite particles during the solidification[77].

Another parameter that influences the graphite nucleation and growth is the solidification time[78]. The solidification time is influenced by the section size or thermal modulus (TM) of the casting. It is given by the geometry and mould positioning of the part. The TM will be the concept used on this work to account for the section size of the casting. It is based on Chvorinov's classic rule[79] (solidification time is proportional to the geometrical modulus of a casting) combined with the solidification time obtained from the simulation software that apply heat transfer equations during liquid to solid transition[80]. Being a geometrical concept, the TM is normally expressed in length units. When the TM of a casting increases, the solidification time increases and, for ductile iron, the risk of microstructural defects, such as microshrinkage, graphite degenerations and high segregation, resulting in undesirable phases at the grain boundaries, increases[81]. Moreover, the higher the solidification time, the lower the nodule count, which combined with the previously mentioned phenomena, decreases the mechanical properties[82]. In Figure 15 it is shown an example of the section size influence in the solidification time.

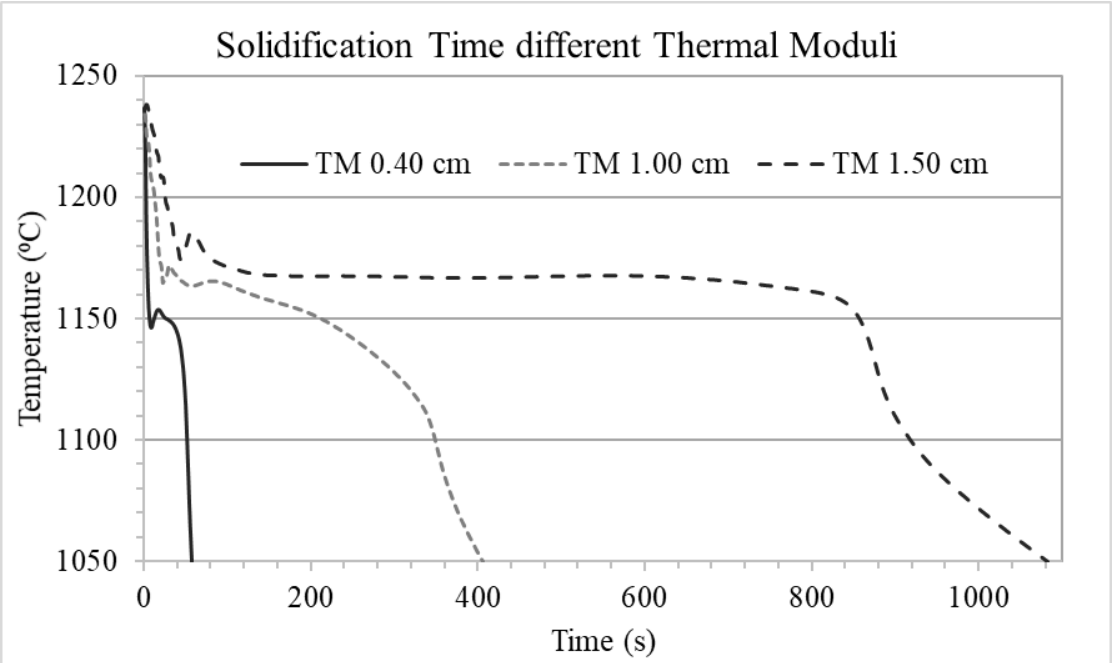

Figure 15. Section size influence on the solidification time.

The solidification process of ductile iron has been extensively studied[83] and is not the aim of the present work. Nevertheless, the influence of nodulization, inoculation and section size on the solidification and thus on the mechanical properties must be considered.

3.2. EUTECTOID TRANSFORMATION

Conventionally, SGI components present a mixed ferritic-pearlitic microstructure as seen in Figure 13. Due to the cooling conditions, the transformation takes place away from equilibrium conditions, which would be represented by a fully ferritic microstructure. This way, the transformation occurs successively in the stable (ferrite) and metastable (pearlite) diagram. The formation of ferrite and pearlite compete at intermedium cooling rates. Ferrite is favoured at lower cooling rates and pearlite becomes predominant at higher cooling rates[84].

Considering a ferritic and/or pearlitic microstructure, the final metallic matrix is defined during the eutectoid transformation. This transformation could be described assuming that there is no substitutional solute redistribution during the reaction[85]. This transformation occurs[86] as the austenite starts to decompose following the stable system and ferrite halos start to grow symmetrically around the graphite spheroids, because the graphite particles act as carbon sinks to which the carbon dissolved in the austenite diffuses. Thus, the austenite is impoverished in carbon and the ferrite formation, phase that presents a very low carbon dissolution, is allowed. The austenite transformation proceeds without any partitioning of substitutional solutes, having the ferrite the same chemical composition as the parent phase (apart from the carbon content), so the transformation is governed by carbon diffusion and redistribution. Afterwards, the ferrite grows by the transfer of carbon from the remaining austenite to the graphite nodules, which diffuses through the ferrite halo. In Figure 16 is shown a scheme of this growth suggested by Lacaze et al.[86] and the corresponding radial distribution of carbon. This process is slowed as the thickness of the halos increases. Hence, as the cooling process advances, the temperature can decrease sufficient, so that, the driving force for the pearlite formation is high enough for the pearlite to nucleate and grow following the metastable system. The needed undercooling for pearlite formation is higher than that of the ferrite. Therefore, pearlite appears at the austenite ferrite interface and grows as spherical colonies in the parent austenite. The grow of pearlite is faster than that of ferrite, so when the pearlite starts to form, the ferrite has little time to keep on growing. These transformations are reconstructive.

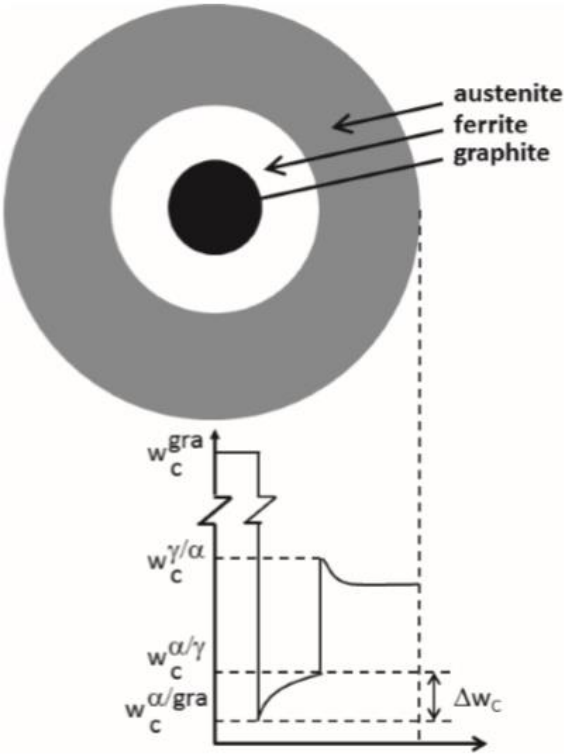

Figure 16. Ferrite formation scheme and the corresponding radial distribution of carbon by Lacaze et al.[86].

On the other hand, when the microstructure is fully pearlitic (Figure 13), the growth of the pearlite is not related to the graphite nodules, since only short-range redistribution between ferrite and cementite is needed at the austenite-pearlite interface. Accordingly, pearlite is thought to nucleate at austenite grain boundaries, or what is the same, on the last to freeze areas during the solidification, where the pearlite promoting elements have accumulated[87]. Pearlite is thought, as well as ferrite, to have the same chemical composition as the austenite parent phase, excluding long range diffusion of substitutional atoms.

The stable eutectoid transformation and thus a fully ferritic microstructure (Figure 13) is only expected to occur under certain cooling conditions that are close to an equilibrium situation, that is, low cooling rates. Otherwise, the transformation takes place away from the stable situation, and nucleation and growth kinetics of pearlite are favoured[88].

The cooling rate is one of the key parameters in order to define the final microstructure of cast iron. The higher the cooling rate, the lower the ferrite content and the eutectoid transformation start temperature. This means that a higher undercooling is needed from the equilibrium conditions to start the eutectoid transformation as the cooling rate increases. This was studied by Sertucha et al.[89], being their results shown in Figure 17. This fact promotes the pearlite formation, because the lower the transformation temperature, the lower the carbon diffusivity that governs the ferrite formation. When the transformation temperature decreases below the Curie temperature of the ferrite (769 ºC, as seen in Figure 1), then the carbon diffusion coefficient is strongly decreased. In addition, it is seen, that above a given cooling rate value, the undercooling for pearlite formation is lower than for ferrite formation, which promotes a fully pearlitic microstructure.

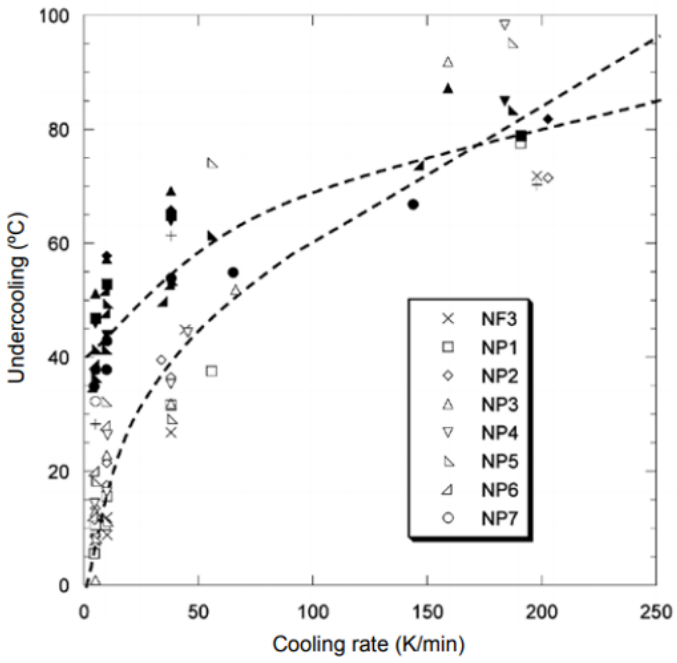

Figure 17. Evolution of the undercooling for ferritic (open symbols and crosses) and pearlitic (solid symbols and plus signs) reactions by Sertucha et al.[89].

Another important factor to define the final microstructure, is the alloying elements. To promote a pearlitic microstructure, pearlite promoting elements are added to the melt, being the industrially most used one's copper, manganese, and tin. On the other hand, to promote a ferritic microstructure, silicon is the main ferrite stabilizer, while cobalt and boron also present a ferritizing effect. The effect of these elements is thought to be that they modify the formation start temperature of both the stable and metastable eutectoid. Depending on their effect on the ferrite and pearlite formation temperature, they will promote one phase formation or the other.

Besides, if another phase that is not ferrite and/or pearlite is desired, then the eutectoid transformation must be avoided. As well as to promote a ferritic or pearlitic microstructure, the avoidance of the eutectoid transformation can be made by two different approaches: acting on the cooling rate and adding alloying elements.

Regarding the cooling rate, this should be increased if the hindering of the eutectoid transformation is sought. As seen in Figure 12-a on the CCT diagram, the formation of pearlite starts below a certain cooling rate. This threshold cooling rate value below which pearlite is formed and above which the eutectoid transformation is avoided is defined by the tip on lower times that presents the elliptical form that defines the formation of pearlite, which is also known as the pearlitic nose. The slope tangent to this ellipse represents this cooling rate threshold value. If the cooling rate is above that threshold level, then depending on the cooling process at lower temperatures, the final microstructure will be ausferritic, bainitic, or martensitic. Conventionally, these high cooling rates are achieved by quenching treatments.

Considering the addition of alloying elements, it can modify the cooling rate threshold value at which the austenite starts to decompose during the eutectoid transformation. This effect is called hardenability, because it facilitates the obtention of martensite, which is the hardest phase in cast iron. The most used elements to increase the hardenability in cast iron are nickel, molybdenum, copper, and manganese. An example of this effect is shown in Figure 18 for the case of molybdenum, as proposed by Gumienny et al.[90]. It is seen, how in spite of not changing the cooling rate, the addition of molybdenum moves the pearlitic nose to longer times. This way, considering a casting that presents on a given section the cooling rate shown in Figure 18, then if no addition of molybdenum is made, the microstructure will be ferritic-pearlitic, but with the molybdenum addition, the eutectoid transformation is avoided, and the final microstructure will be defined by the cooling process below that temperature range.

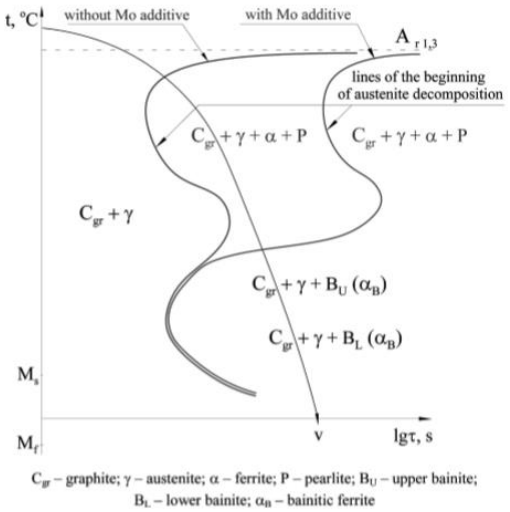

Figure 18. Influence of molybdenum on the pearlitic nose of cast iron by Gumienny et al.[90].

Therefore, if the eutectoid transformation is avoided, the austenitic phase will remain and then comes the final part of the cooling process which will define the microstructure. At lower temperatures than the eutectoid transformation temperature range, as it is seen in Figure 12 and Figure 18, it is the ausferritic nose, which defines the formation of ausferrite. This is going to be next described.

On the other hand, if after avoiding the eutectoid transformation, the cooling rate is high enough to avoid the ausferritic nose, then the microstructure will be martensitic. This is usually obtained by means of a quenching process directly from the fully austenitic microstructure at high temperature, down to room temperature.

3.3. AUSFERRITIC TRANSFORMATION

An ausferritic microstructure, is made up of acicular ferrite (AF) or ferrite needles (α_{AC}) and carbon enriched austenite or reacted austenite (RA) (γ_{HC}) as seen in Figure 19.

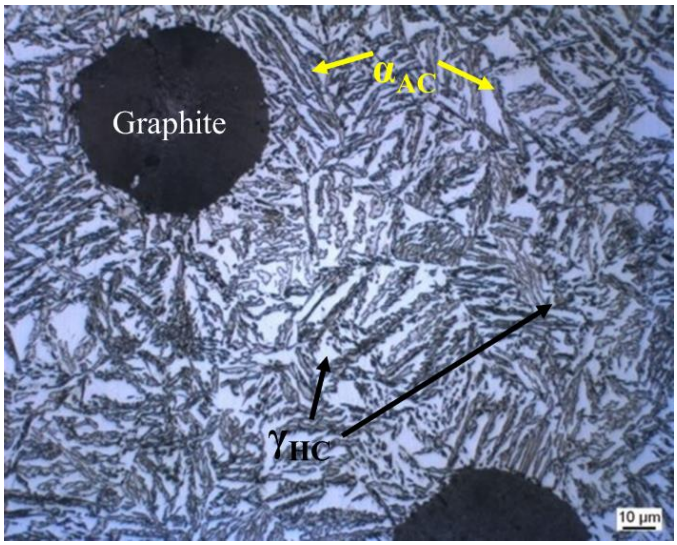

Figure 19. Micrograph of an ausferritic microstructure in SGI. 500x.

Ausferrite is formed during the cooling process of a cast iron, at lower temperatures than the eutectoid transformation, more precisely, in between 250 and 450 ºC[91]. To achieve a fully ausferritic microstructure, the eutectoid transformation must be avoided. Additionally, some time must be given for the reaction to be completed at the ausferrite formation temperature.

Austenite transformation during cooling is widely documented for steels[92], while this process for cast iron is a more complex one and has been less studied. Formation of bainite in steel is a similar process to the ausferrite formation in cast iron and was first discovered, thus its documentation is wider[93]. This phase could be seen as the predecessor of the ausferrite because the acicular morphology is similar in both microstructures. Nevertheless, the ausferritic transformation differs significantly from the bainite formation in steel.

Parting from the parent austenite, the ausferrite formation starts with the formation of carbon supersaturated AF. This excess of carbon, just after the AF formation, is partitioned to the surrounding austenite and thus the austenite is carbon enriched during this process[94]. This high carbon austenite is called reacted austenite (RA). If the temperature is maintained constant for a long time, the reaction evolves, and once the austenite is not able to dissolve more carbon, then it starts to decompose into ferrite and iron carbides. This can lead to an elongation drop, because the cementite apparition lowers the ductility and the toughness of the material. This decomposition being detrimental for the mechanical properties, it occurs at very long transformation times and should be avoided. The ausferrite formation could then be defined as a two-stage reaction[95], as shown in Figure 20[96]:

1- Austenite transforming to AF and to RA.

2-Further austenite decomposition to ferrite and cementite.

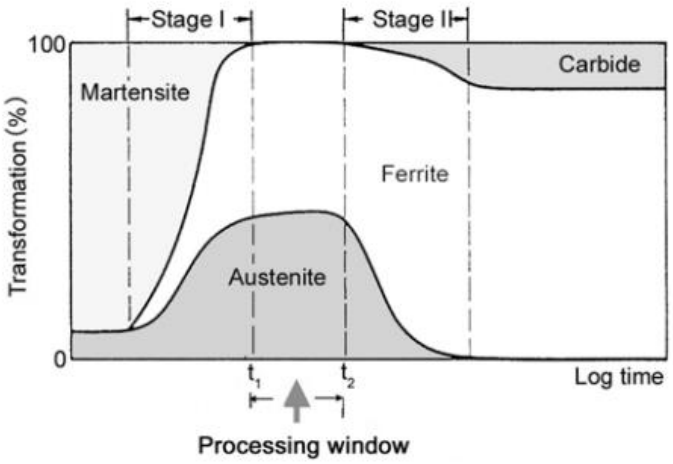

Figure 20. Ausferrite formation as a two-stage reaction by Harding[96].

The silicon content of cast iron hinders the precipitation of iron carbides and that is the main difference between the ausferrite in cast iron and bainite in steel, because cementite does not form from the beginning[97]. In Figure 21, is shown a section of a Fe-C-Si diagram together with the free energy curves of the ferrite (α), austenite (γ) and cementite (Fe_3C), to illustrate the thermodynamical explanation for the two stages reaction.

As iron carbide formation is a sluggish process, the system follows the metastable equilibrium relationship, which is defined by the tangent line between the minimum of the ferrite and austenite free energy curves. In Figure 21 is seen, that an austenite obtained at the austenitizing temperature T_1, presents a dissolved carbon content of around 0.8 %.

When this austenite is quenched to the ausferrite formation temperature represented by T_A, then the free energy of the system is the one of the point "a". When the transformation starts and AF starts to form (stage I), the free energy of the system lowers to point "b", where there is a metastable equilibrium between ferrite and austenite. As the reaction evolves, and if time is provided, then the RA will decompose into ferrite and cementite (stage II), dropping the free energy of the system to the point "c". The time passed between the stage I and stage II is called the time processing window of the heat treatment, because the ausferrite transformation is complete and the optimal mechanical properties are then achieved, before the austenite decomposition into carbides and ferrite starts. This time window is significant enough so as to be able to avoid the formation of carbides during the heat treatment.

The high carbon content of the austenite makes the austenite stable at room temperature, because it lowers its Gibbs free energy (Figure 21[97]) and thus, the martensite formation start temperature (M_S) decreases to temperatures considerably below room temperature. Below that temperature, martensite forms by a displacive mechanism[62]. This transformation is very rapid and there is no need of a temperature arrest.

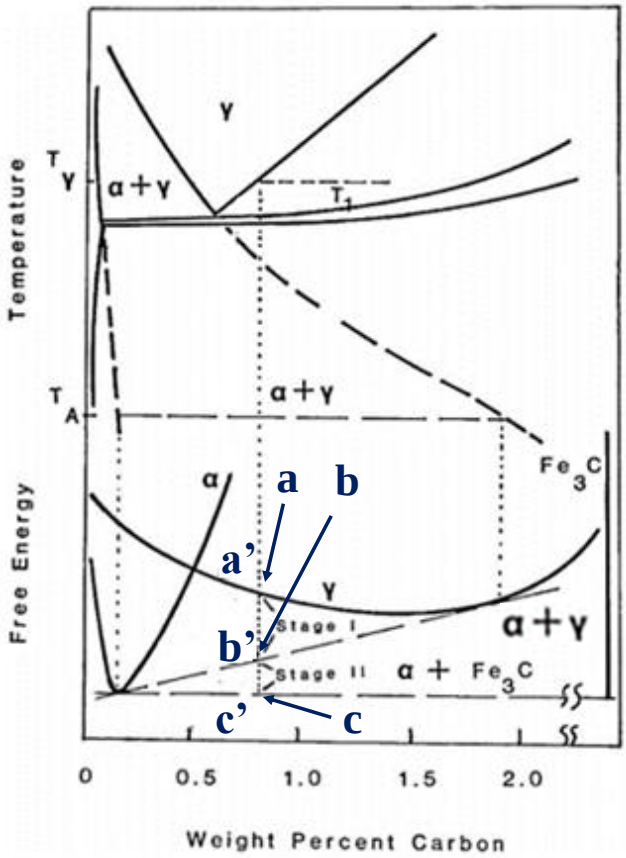

Figure 21. 2.4 % Si isopleth of the Iron-Carbon-Silicon phase diagram together with the free energy representation at the ausferrite transformation temperature by Rouns et al.[97].

At low transformation temperatures (below 350 ºC), the slow diffusion of carbon, may result in carbide formation together with the AF from the beginning of the reaction[98]. On this case, the reaction takes place following the above mentioned two stages, but the difference is that on the first stage, small carbide precipitation takes place together with the AF. Afterwards, during the second stage, the RA transforms into carbides and ferrite. There is no clear agreement on the scientific community, whether this happens, or the reaction takes place the same way as explained above.

The formation of ausferrite in ductile iron, as well as bainite in steels is generally accepted to be a displacive mechanism [99,100]. The AF or bainite is formed when the conditions for nucleation and growth are satisfied. This means that enough free energy is available to ensure a detectable nucleation rate. In addition to that, the chemical free energy change for transformation must exceed the stored energy of the transformation product due to the displacive mechanism of the transformation. The growth of an AF or bainite subunit or platelet is considered diffusionless, that is, the austenite transforms into a carbon supersatured AF subunit, without carbon diffusion between the phases. The formed AF plate retains the chemical composition of the parent austenite phase. However, soon afterwards, the excess of carbon on the ferrite needles is partitioned into the surrounding austenite. The nucleation of the AF plates takes place preferentially at graphite/austenite interfaces and at austenite grain boundaries[101]. Once the first subunits are nucleated and grown, new plates can also nucleate in this formerly formed subunits. The plates of AF, surrounded by RA, form what is called a sheaf. Transformation ceases before the austenite achieves its equilibrium composition given by the A_{e3} curve on the phase diagram, an effect called incomplete reaction phenomenon[102]. The reaction actually stops when the carbon concentration of the austenite reaches the T_0 curve, which describes the locus of all points on the phase diagram where austenite and ferrite of the same chemical composition have equal free energies, as seen in Figure 22[93]. When the free energy of the austenite becomes lower than that of the ferrite, then diffusionless growth becomes thermodynamically impossible. Taking into account the stored energy of the AF (400 J mol^{-1}), the $T^{0'}$ curve can be defined[99].

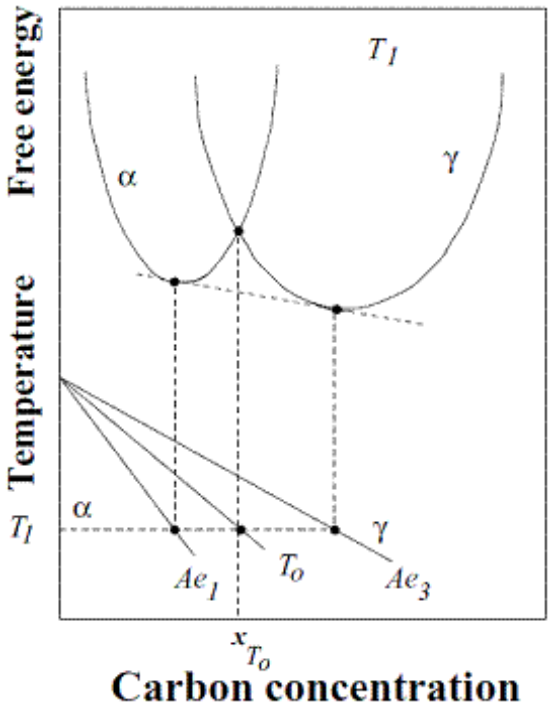

Figure 22 Schematic illustration of the origin of the T_0 curve on the phase diagram by Bhadeshia[93]. γ and α refer to austenite and ferrite respectively.

On the other hand, the diffusive mechanism states that an AF plate grows by carbon diffusion through the ferrite-austenite interface[103]. At the end of the reaction, the carbon concentration of the austenite is then defined by the equilibrium composition given by the A_{e3} curve.

The main experimental evidence to support the displacive theory, is that the austenite carbon concentration after the ausferrite formation is closer to the T_0 curve than that of the A_{e3} curve[104].

Assuming the incomplete reaction phenomenon, and that no reaction overlaps with the ausferrite formation (no carbide precipitation is considered), then the maximum volume fraction of AF or ferrite needles V_α can be calculated using the lever rule shown in Equation 5 [105].

Equation 5 $$V_\alpha = \frac{x_{T_0} - x_\gamma}{x_{T_0} - x_\alpha}$$

where x_γ is the average carbon content of the austenite at the beginning of the isothermal transformation, x_α is the carbon content of the AF and x_{T0} is the carbon content given by the T_0 curve.

Depending on the isothermal transformation temperature, the AF will be upper acicular ferrite (UAF) for high isothermal temperatures (350-450 ºC) or lower acicular ferrite (LAF) for low isothermal temperatures (250-350 ºC). As seen in Figure 23, UAF is thicker and coarser with a feathery morphology, while LAF is finer and presents a more acicular morphology. The UAF is softer than the LAF and thus the mechanical properties at higher isothermal transformation temperature, present higher ductility and lower resistance than at lower isothermal temperatures[106].

Increasing the isothermal temperature, implies at the same time a higher RA quantity and lower AF content[107]. As seen in Figure 22, as the transformation temperature decreases, the T_0 curve displaces to higher carbon contents. This carbon content increase that the austenite can dissolve at lower temperatures, makes that more AF can be formed till the reaction stops and thus less RA.

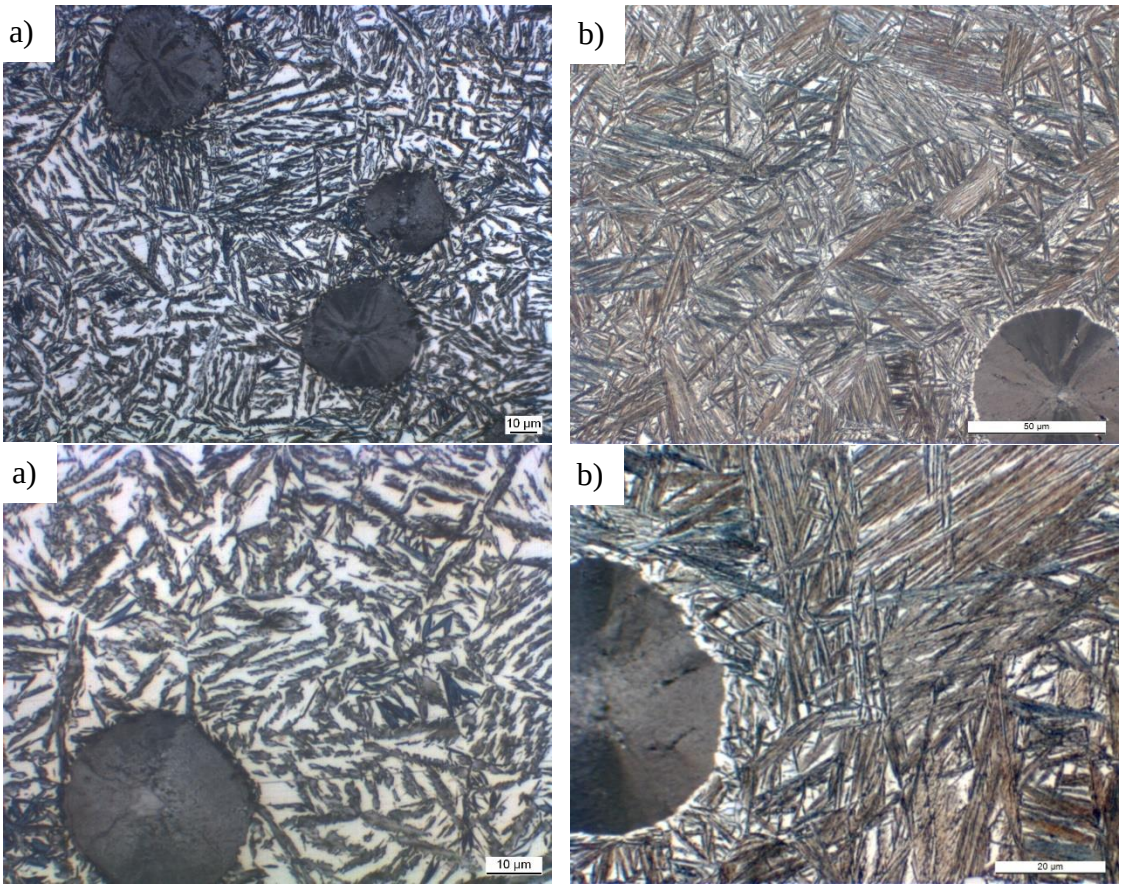

Figure 23. Micrographs of a) upper ausferrite and b) lower ausferrite. 500x upper row, 1000x lower row.

The transformation time is also decisive in order to obtain the desired microstructure[108]. If this time is not enough to achieve a complete reaction, the stage I is not completed and then, the remaining parent austenite will transform into martensite when cooling to room temperature. This is because the M_S decreases as the carbon content dissolved in the austenite increases (Figure 24[108]). If this carbon content is not high enough, then the M_S is above the room temperature and during the final cooling, the unreacted austenite transforms into martensite.

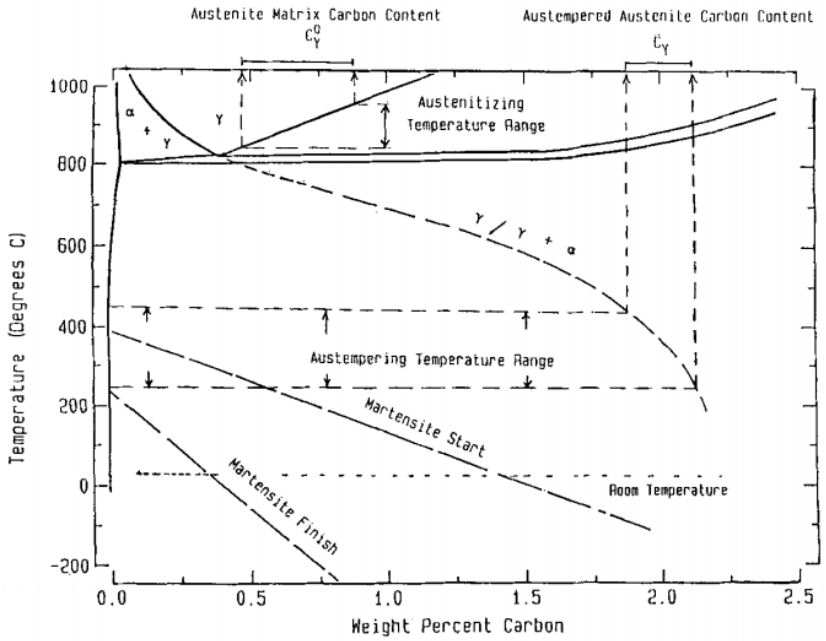

Figure 24. 2.5 % Si isopleth of the Iron-Carbon-Silicon phase showing metastable γ/(α+γ) and M_s and M_f temperatures by Rundman et al.[108].

3.4. AUSTEMPERING HEAT TREATMENT

ADI materials and their ausferritic microstructure are conventionally produced applying an austempering heat treatment to the as-cast obtained foundry product. This heat treatment is made up of an austenitizing step followed by an isothermal quench. The temperature time diagram of the austempering is shown in Figure 25[109]. The aim of this treatment is to obtain a fully ausferritic microstructure which is the one that gives the ADI materials their excellent mechanical properties, presenting high resistance values combined with a high ductility and a high fatigue limit[110].

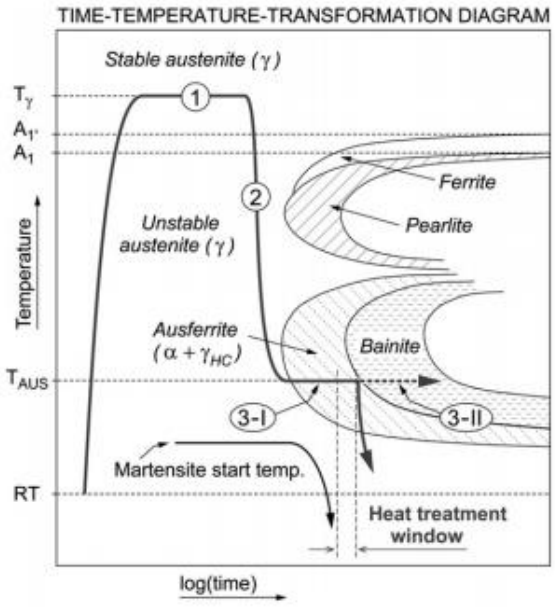

Figure 25. Time-Temperature diagram of an austempering heat treatment by Meier et al.[109].

Following the steps defined in Figure 25, the austempering heat treatment starts by an austenitizing step (1). During the austenitizing, the as-cast microstructure of the castings, a ferritic and/or pearlitic matrix, is transformed into austenite. To that aim, the castings are heated above the A_{e3} temperature, when the austenite becomes stable. Some time is needed at that temperature, which is usually in the range 850-950 ºC, for the complete transformation and homogenization of the carbon dissolved in the austenite[111]. During this temperature arrest, the austenite is carbon enriched by carbon diffusion from the graphite particles. The austenite carbon content after the austenitizing step ($C_{\gamma 0}$) is influenced by the austenitizing temperature (T_{γ}) and the chemical composition of the alloy. This relationship is frequently simplified as expressed in Equation 6[112]:

Equation 6. $C_{\gamma 0}= (T_{\gamma}/420)-0.17(\%\ Si)-0.95$

The time needed to reach a homogenized austenite depends on different variables. On the one hand, a higher austenitizing temperature accelerates the formation of austenite[113]. On the other hand, the chemical composition also affects the austenitizing time, having the silicon content a negative effect. Furthermore, the as-cast microstructure of the casting has also an influence, the pearlite promoting a faster austenitizing step than the ferrite[114]. The austenitizing time to achieve a uniform carbon dissolution in austenite can vary from less than 30 minutes for a pearlitic thin wall castings to over 3.5 hours for a ferritic thick wall casting[98].

Once the microstructure is fully austenitic and its chemical composition homogenised, then a rapid cooling is applied (step (2)). The target is to avoid the pearlitic nose and, in this manner, to have a fully austenitic microstructure when the ausferrite formation temperature is reached[115]. Below the A_{e3} temperature, the austenitic phase becomes unstable. For this reason, the cooling rate must be high and thus a quenching process is applied on this step.

The ausferrite formation takes place above the M_S temperature and up to 450 ºC. A temperature maintenance is needed in that range to allow the formerly explained ausferritic transformation to develop. This is referenced as step (3) in Figure 25. Industrially, the temperature arrest, called tempering or austempering temperature is limited to the range 250-400 ºC[116].

During the temperature arrest, the austenite parent phase transforms into AF and carbon enriched austenite during the so-called stage I of the reaction (step (3-I)), forming ausferrite. If the time is prolonged, then the stage II starts, during which the previously RA is decomposed in ferrite and iron carbides (step (3-II)), forming bainite [95, 96].

What is sought during the third step, is to get a fully ausferritic microstructure, that is, to complete the stage I of the reaction, and avoid the start of the stage II. The time between the end of the first stage and the beginning of the second stage is called, the processing window[108], as shown in Figure 20.

Once the stage I of the reaction has been finished and the castings have their fully ausferritic microstructure, they are air cooled to room temperature.

During the austenization step, it is important to maintain a controlled atmosphere, so that the castings are not oxidized[117] and decarburized[118]. At temperatures above 650 ºC, the rate at which these phenomena occur, increases substantially. If the castings are in contact with oxygen, oxidation of the surface can happen, creating iron oxides at the surface, compound which is very detrimental. A severe oxidation is called scaling. These compounds are very hard, and they hinder importantly the machining. Additionally, the contact with the oxygen, makes that the carbon present as graphite on the surface of the castings, combines with the oxygen producing carbon monoxide, promoting a decarburization of the casting surface. The longer the time passed at the austenitizing temperature, the deeper the oxidized and decarburized layer.

On an industrial, scale the protective atmosphere for the austenization can be made up of inert gases (nitrogen, argon or helium), hydrogen or of endothermic atmospheres that can be a mixture of the formers with carbon monoxide or carbon dioxide and trace amounts of water vapour. Additionally, the heat treating could be performed in vacuum, or the castings could be coated, but these two solutions are quite expensive so that to be applied for the ADI materials[119].

After the austenization step, the rapid cooling process followed by a temperature arrest is called an isothermal quenching. This is normally performed introducing the castings after the austenization step into a molten salt bath[120]. This bath is at the desired transformation temperature. The castings must be taken from the austenization furnace to the salt bath rapidly to avoid oxidation. Once in the salt bath, the castings have no contact with the atmosphere, so oxidation and decarburization are avoided.

The heat transmission in a salt bath is performed mainly by conduction in a high thermal conductivity medium. Consequently, the cooling rate is higher than radiation or convection. Nevertheless, the cooling rate in a salt bath is slower than quenching the castings in oil or in water, but this helps to prevent distortion or crack problems[121].

The salt bath conventionally used for the austempering treatment is made up of KNO_3, $NaNO_2$ and $NaNO_3$ in different proportions. The melting point of the salt bath must be below the transformation temperature.

During these second step of the austempering heat treatment, the concept of hardenability or austemperability is very important[122]. Hardenability refers to the ability of an iron-based alloy to form a fully martensitic microstructure. This implies that the eutectoid transformation as well as the ausferritic or bainitic transformations have been avoided. Austemperability is limited to avoid the eutectoid transformation, so that, the ausferritic or the bainitic transformations can take place. This is represented on a CCT curve by the needed cooling rate to avoid the pearlitic nose (Figure 12 and Figure 18).

The austempering treatment conditions define the mechanical properties of the material as will be next described.

3.4.1 Temperature and time influence

As explained before, the main two steps of the austempering heat treatment are the austenitizing step and the austempering or tempering step.

The major influence of the austenitizing step on the final microstructure, is through its effect on the dissolved carbon content that presents the parent austenite phase[98].

Decreasing the austenitizing temperature, the austempering kinetics are accelerated[123]. As seen in Figure 21, as the austenitizing temperature increases, the carbon content dissolved by the austenite increases for a cast iron material. Thus, the free energy of the austenite parent phase at the tempering temperature decreases. This implies that the driving force for the ausferrite formation increases as the austenitizing temperature decreases (points "a' " - "b' " in Figure 21). Nevertheless, decreasing the austenitizing temperature, reduces the austemperability of the alloy[124].

A decrease in the austenitizing temperature, reduces the time for completion of the stage I of the ausferritic transformation[125]. The higher driving force of lower austenitizing temperatures, implies that the carbon partitioning on the austenite after the AF is formed occurs more rapidly. This reduces the heat treatment time. This effect does not influence the stage II. Besides, higher austenitizing temperature increases the austenite fraction and, consequently, reduces the AF fraction for the same tempering temperature[126]. Moreover, the carbon content of the austenite present in the ausferrite increases at higher austenitizing temperatures, due to the higher initial carbon content of the parent austenite[127].

All these results are given, considering a fully austenitizing time. The time required for a fully austenization is the one needed to reach an austenitic phase with the maximum solubility of carbon given by the Fe-C-Si diagram. This time is a function of different variables.

The microstructure of the as-cast casting has a large influence on the time needed to reach a homogeneous fully austenitic matrix. The transformation parting from a pearlitic matrix is faster than parting from a fully ferritic one[128].

The silicon content of the alloy influences negatively the austenitizing time. This element increases the A_{e1} transformation temperature and thus it slows down the austenitizing kinetics.

Furthermore, a higher austenitizing temperature increases the transformation rate, so the time need to achieve a homogeneous fully austenitic microstructure is reduced[129].

This leads to, as expressed before, austenitizing times to achieve a uniform carbon dissolution in austenite from less than 30 minutes to over 3.5 hours [98].

In Figure 26, the evolution of the ultimate tensile strength (UTS) and yield strength (YS), with the austenitizing is shown. Data from the literature were gathered [116, 127, 130], and the same austempering temperature (T_{temp}) and the same austempering time (120 minutes) were considered, to be able to analyse the pure effect of the austenitizing temperature. The austenitizing time was in all cases 120 minutes.

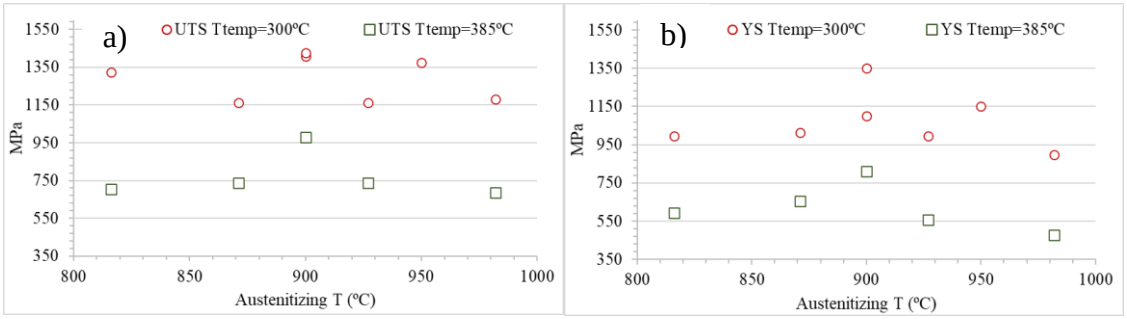

Figure 26. Austenitizing temperature influence on the a) UTS and b) YS for the same austempering conditions[116, 127, 130].

It is seen, that for a given austempering temperature, the UTS and YS are in a comparable range for the different austenitizing temperatures. This is because the austempering step is the one who determines the final microstructure morphology and thus the mechanical properties.

In addition to the austenitizing, the other main step of an austempering heat treatment is the isothermal transformation of the parent austenite to the targeted ausferrite. This step is called austempering or tempering and it is the step that majorly influences the mechanical properties of the material, as seen in Figure 26.

Austempering temperature defines the morphology of the AF of the ausferrite, as well as its content. The isothermal transformation temperature range is usually 250-450 ºC[91], although industrially, the range 250-400 ºC is the most usually applied one.

As explained before, the isothermal transformation temperature determines if the AF presents an UAF or LAF morphology. For high isothermal temperatures (350-450 ºC), the morphology is UAF and LAF for low isothermal temperatures (250-350 ºC) [130]. Figure 23 shows an example of upper and lower ausferrite. UAF is thicker and coarser, while LAF is finer. Moreover, at high austempering temperatures, there is a higher austenite amount, and it is also thicker than the austenite at lower austempering temperature.

Upper ausferrite presents a higher ductility and lower resistance than at lower isothermal temperatures[106, 131, 132], alongside a higher impact energy[133] and a higher fracture toughness[134]. Together with this, the hardness decreases at higher transformation temperatures and the fatigue limit increases as the austempering temperature increases [135, 136].

The relationship of the UTS, YS and elongation (E) with the austempering temperature is shown in Figure 27. Data from the literature were considered[116, 124, 127, 130, 131, 132, 133, 134]. Austempering times longer than 60 minutes were considered, so that a fully transformation of austenite into ausferrite is taken into account, without the negative influence of martensite apparition. The values defined on the standard EN 1564[32] (Table 1) for the ADI materials are added.

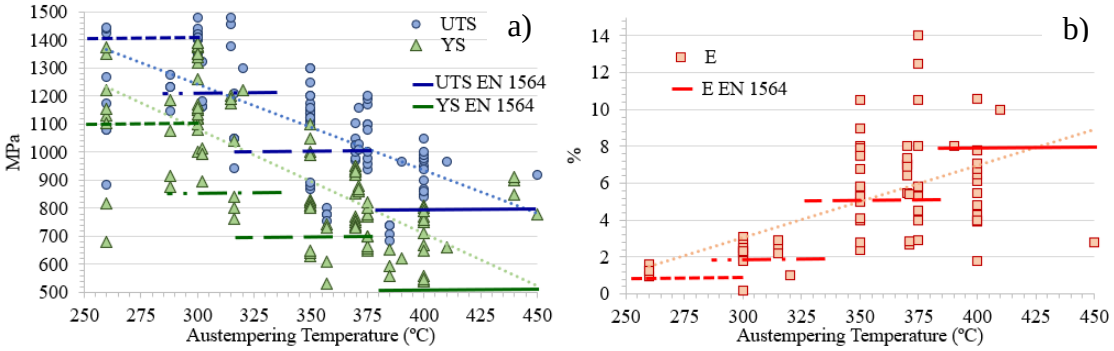

Figure 27. Evolution of the a) UTS and YS and b) E with the austempering temperature[116, 124, 127, 130, 131, 132, 133, 134].

It is observed, that depending on the ADI grade that is targeted, the austempering temperature must be defined accordingly. For the most ductile grades, the most difficult specification to meet is that of the E.

This mechanical properties' evolution with the austempering temperature is due to the nature of the obtained microstructure. The change in the AF shape, together with the austenite content difference, are responsible for that evolution.

The AF and the RA contents are defined by the Equation 5. The austenite content for a complete transformation is the rest that it is not AF. As seen in Figure 22, the carbon content defined by the T_0 curve increases as the austempering temperature decreases. Introducing a higher value of x_{T0} in the Equation 5, for the same x_γ, then the AF volume increases[107]. This means, that the RA content drops as the austempering temperature decreases, if the other process parameters are maintained constant. Accompanied by this content decrease, the carbon dissolution in the RA increases at low austempering temperatures. This fact promotes the stability of this phase.

The higher the RA content, the higher the ductility, impact strength and toughness of the ausferritic microstructure[137].

The shape of the AF changes with the austempering temperature. For higher isothermal transformation temperatures, the ferrite needles are coarser. The ausferritic microstructure also coarsens as the austempering temperature increases. Finer ferrite needles and finer ausferritic microstructure is obtained at low austempering temperatures[138].

Austempering time influences the grade of evolution of the reaction. As seen in Figure 20, the ausferrite transformation can be defined in two stages. During the first stage, the parent austenite coming from the austenitizing step and subsequent quenching to the austempering temperature, decomposes into AF and RA. During this stage, the ferrite needles are formed and the carbon that they reject, is partitioned through the austenite. This process increases the carbon content dissolved by the austenite and thus its stability at room temperature. If the austempering time is prolonged too long, then the stage II of the reaction starts. During the second stage, the RA decomposes into ferrite and carbides.

What is sought during the austempering treatment, is that the stage I of the reaction is fully completed and that the second stage has not begun. The time between the end of the first stage and the start of the second stage is what is called the processing window for the ADI materials[139]. If the first stage is not finished, then some of the austenite is not carbon enriched and thus, unstable at room temperature. This austenite is called unreacted or untransformed austenite. During the last cooling to room temperature, it will partially transform into martensite. This is a very hard and brittle phase, that negatively affects the ductility and the toughness of the material.

On the one hand, the time needed for the second stage to commence is quite long and thus, easy, not to enter on this stage. This must be avoided because the precipitation of carbides lowers the mechanical properties. The reaction that takes place during the second stage is undesirable, since it leads to an embrittlement of the structure and reduces considerably the ductility and toughness of the alloy.

On the other hand, a minimum time needed for the completion of the first stage must be ensured during the isothermal step, since a not complete ausferrite transformation leads to martensite formation. Martensite is a very hard phase, that hinders the ductility of the ADI materials[140].

The key for the room temperature stability of the austenite, is its carbon content. When the dissolved carbon content in the austenite increases, the stability of the austenite increases and thus, the M_S decreases (Figure 24). If the M_S is below the room temperature, then the austenite is stable at that temperature. The austenite to martensite transformation, occurs when the driving force of the reaction (free energy change between austenite and martensite) reaches a critical value at the M_S [141]. An increase of the carbon content present in the austenite reduces the free energy change between the austenite and the martensite, and thus the driving force is not enough, and the transformation does not take place.

In Figure 28 it is shown the evolution of the UTS, YS and E with the austempering time for different austempering temperatures. The data were gathered from the literature[116, 124, 127, 130, 131, 132].

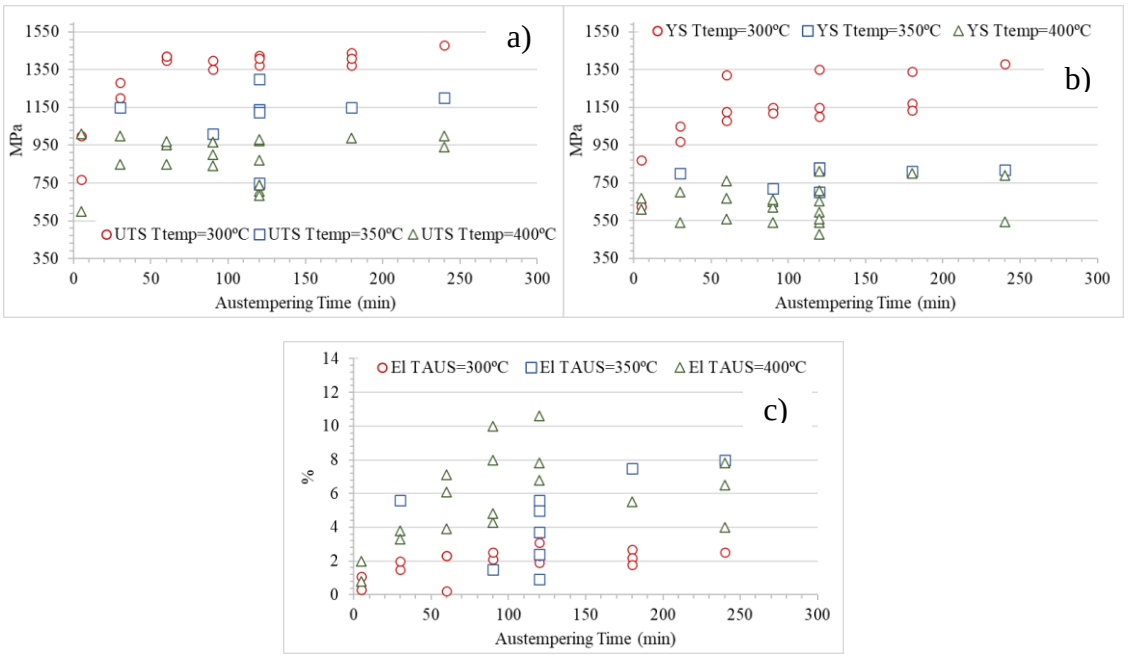

Figure 28. Evolution of the a) UTS, b) YS and c) E with the austempering time for different austempering temperatures[116, 124, 127, 130, 131, 132].

It is seen that a minimum time is needed to reach the maximum values of the resistance and the ductility of the material. This is related to the stage I transformation rate or the ausferrite formation kinetics. For a complete ausferritic microstructure to be formed, time is needed for the reaction to develop. If the reaction is not fully developed, then the carbon content dissolved by the austenite could be not enough to make it stable at room temperature, leaving some unreacted austenite. Consequently, during the late air cooling to room temperature after the austempering step, some of the unreacted austenite will transform to martensite. This martensite is the reason of the low E at the early stages of the reaction.

3.4.2 Alloying elements influence

Alloying elements influence the austempering heat treatment and thus the final microstructure in two different ways:

1- Displacing the pearlitic nose to longer times. This means that the eutectoid transformation is hindered during the quenching to the tempering temperature. This concept is called austemperability and reflects the ability of the alloy to have a fully austenitic microstructure at the beginning of the ausferritic reaction[142]. Therefore, it is possible to obtain a fully ausferritic microstructure without pearlite formation.

2- Modifying the kinetics of the ausferritic transformation. The time needed to perform the stage I and when the onset of the stage II occurs can be altered adding different alloying elements. This causes a variation in the processing window. On this behalf, they affect, on the one hand, the carbon dissolution in the parent austenite formed during the austenitizing step as expressed in Equation 6. On the other hand, they segregate during the solidification process, creating a heterogeneous chemical composition distribution in the parent austenite phase. Both effects influence the driving force for the ausferritic transformation, affecting consequently the transformation time[143].

The mostly used alloying elements in ADI production are nickel, molybdenum, copper, and manganese.

Considering austemperability, this can be modified changing the austenitizing and tempering temperatures. Higher austenitizing temperature and lower austempering temperature increase the austemperability. Nevertheless, this influences the final microstructure. Formerly on this work, it was seen, that the austempering temperature is the most important parameters to define the mechanical properties of the alloy. For this reason, this variable is defined depending on the mechanical properties or the ADI material that is sought. Besides, a higher austenitizing temperature, apart from a higher energy consumption during the heat treatment, it involves a lower driving force for the ausferrite formation, and thus a narrowing of the processing window. For these reasons, industrially, the most common way to influence the austemperability, is by adding alloying elements.

The concept of austemperability, was numerically defined by Voight et al.[98] as shown in Equation 7. This equation describes the maximum bar diameter (D_C) in mm that can be obtained without pearlite apparition for the considered alloy. Bar diameters higher than that are not feasible to produce without pearlite formation.

Equation 7. $Dc = 124\ C\gamma_0 + 27\ \%\ Si + 22\ \%\ Mn + 16\ \%\ Ni - 25\ \%\ Mo - 1.68 \times 10^{-4}\ T_{temp}^2 + (-127)\ (\%\ Mn * \%\ Mo) + 88\ (\%\ Ni * \%\ Mo) + 62\ (\%\ Cu * \%\ Mo) + 12\ (\%\ Cu * \%\ Ni) + 11\ (\%\ Mn * \%\ Cu) - 20\ (\%\ Mn * \%\ Ni) - 137$

Being $C\gamma_0$ the austenite carbon content after the austenitizing step defined by Equation 6 and T_{temp} the austempering temperature.

For each chemical composition, the austemperability as a function of the cooling rate is expressed by the Continuous Cooling Transformation (CCT) diagrams as seen in Figure 12-b. The cooling rate includes the effect of the section size of the casting and the cooling media, since it is a combination of both.

Alloying elements influence the as-cast structure of ductile iron due to segregation phenomena. Segregation is the heterogeneous distribution of an element from the first zones that solidify to the last to freeze areas or the zones that solidify the last. It is commonly accepted, that the graphite promoting elements segregate at the first to freeze areas and the carbide promoters segregate to the last to freeze areas[144]. In Figure 29 it is shown the segregation profile by Yescas[145] of the main alloying elements in ductile iron or SGI. The first areas that solidify are the graphite particles and the last to freeze areas are the ones that are the furthest from the graphite nodules.

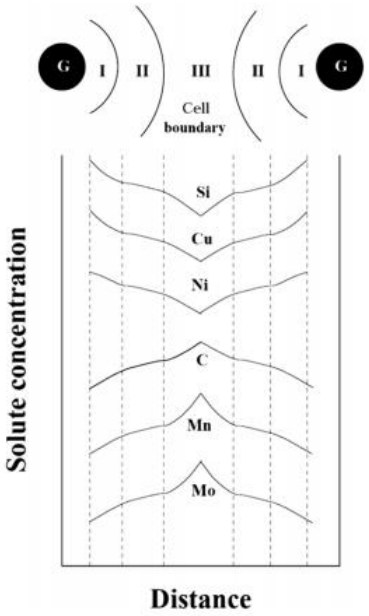

Figure 29. Segregation profile of the main alloying elements in SGI by Yescas[145].

It is seen, how silicon, nickel and copper segregate negatively. This means that their concentration is higher at the zones surrounding the graphite nodules. On the contrary, carbide promoters like manganese and molybdenum segregate positively. This means that their concentration is higher at the zones far from the graphite spheroids or the grain boundaries.

Segregation is more severe when the solidification time is longer, that is, for heavy section castings. The processing of the liquid melt, can be optimized to reduce the segregation phenomena, like for instance, enhancing the effectivity of the inoculation. In SGI, the liquid melt treatment optimization is reflected in a higher nodule count. Higher solidification times lead to lower nodule counts, but this effect can be partially counteracted by the metallurgy. The higher the nodule count implies a lower segregation phenomenon because it means a refining of the structure[146].

The effect of segregation on the austempering treatment, is that the different chemical composition profiles imply different transformation responses. If the segregation phenomena increase, then the ausferritic transformation on the last to freeze areas can be retarded and blocky unreacted austenite pools can be formed, which will partially transform to martensite during the last cooling to room temperature[147].

Regarding the transformation kinetics of the ausferritic reaction, next are summarized the main effects of these elements:

Nickel: This is an austenite stabilizer element and after molybdenum and manganese, the most powerful element that increases austemperability in ADI materials. It segregates negatively and is a graphite promoter. Consequently, hinders the precipitation of carbides. It increases the driving force for the start of the ausferritic transformation stage I[148], nevertheless, it shows no special impact on the processing window.

Molybdenum: This is the element that increases the most the austemperability. It is a carbide promoting element due to its strong positive segregation. For this reason, its content should not be higher than 0.30 %, because then, the risk of carbide precipitation at the grain boundaries would be too high. It slows the stage II reaction during the tempering stage, so it opens the processing window[149].It has no special impact on the driving force of the stage I and it has no considerable delaying effect on this stage of the transformation[150].

Copper: This is the main pearlitizer element used in SGI. It is the least expensive of the alloying elements that increases austemperability and thus, although its effect is weaker than that of Mo, Mn, and Ni, it is extensively used in ADI production. The effect on the ausferrite reaction, is that it reduces the transformation rate during the stage I[151].

Manganese: It segregates very strongly on the last to freeze areas and is a carbide stabilizer element. For this reason, its content must be limited to 0.80 %, otherwise, carbide precipitation is very likely to happen. It delays the onset of the stage I[152]. Additionally, due to the strong segregation, it reduces the processing window in the last to freeze zones. Even though it is a powerful austemperability increaser (the second after Mo), its strong segregation profile limits its use.

The addition of some elements together, affects the behaviour of the others[153,154]. For instance, adding negatively segregating elements like silicon and nickel, reduces the effect of positively segregating elements like manganese and molybdenum. For this reason, the addition of different elements at the same time is of interest. Nevertheless, it must be well studied which elements are added together. Nickel and copper additions decrease the transformation rate of the ausferrite formation, and thus the transformation time becomes larger[155]. Nevertheless, the addition of manganese and molybdenum together delays even more the ausferrite formation[156].

3.5. APPLICATIONS OF THE ADI MATERIALS

The mechanical properties shown by the ADI materials make them interesting for a wide group of different applications. The main markets are the automotive sector, including light vehicles and heavy trucks, railroad, agriculture and construction and mining. In Figure 30 are shown the main market applications of the ADI materials in North America the year 2001[157].

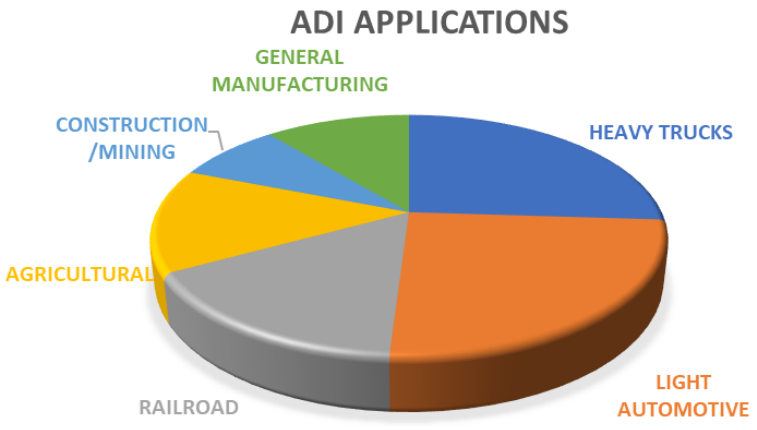

Figure 30. North American ADI market distribution in 2001 by Hayrynen et al.[157].

It is seen that the transportation industry dominates the ADI production (26 % heavy trucks, 25 % light vehicle and 16 % railroad). Agricultural application with 14 %, general manufacture with 11 % and construction and mining with 8 % are the following main sectors.

The application of the ADI changes depending on its grade[32]. The ADI grades which present the lowest resistance, but the highest ductility and toughness, are used in suspension system and dynamic applications. On the other hand, the harder grades, are used in applications in which wear resistance is the most demanding property during the lifetime of the component[158].

Regarding the automotive sector, gears, engine brackets, differential case covers, suspension lift kits, truck steering knuckles, truck steering arm, truck trailer wheel hub and many other components are performed[159,160].

Another automotive component that is currently produced in ADI is the crankshaft[161],[162]. For this component, ADI replaced forged steel. This involves an important weight and cost reduction. Nevertheless, this component has not been developed in ADI as expected and some projects were dropped in favour of steel.

An example of the competitivity of the ADI materials, was performed by Branderberg et al.[163]. In Table 4 are shown the results of this study. Conventional ductile iron, steel and ADI were compared for a given crankshaft application.

Table 4. Results of the study performed by Branderberg et al.[163] with crankshaft produced in different materials.

	ADI	Steel	Ductile Iron
UTS (MPa)	1083	910	903
YS (MPa)	827	738	538
E (%)	13.7	23.2	10.8
Fatigue Strength (MPa)	427	400	324
Impact Energy Unnotched (J)	141	325	75
HBW	300	226-266	262-277

Seeing these mechanical properties, ADI was chosen for this crankshaft. The strength and wear resistance needed for this application were achieved and due to manufacturability, cost and weight saving reasons it was preferred to steel. Moreover, a better noise, vibration and harshness (NVH) properties were obtained, so the engine was quieter.

Concerning the railroad sector, some components of the railway changing system are performed in ADI, as well as the components of the brake system, wheels, suspension parts, covers and others[164,165,166].

About the agricultural sector and earth moving components for mining and construction, the main advantage of the ADI materials is their high wear resistance together with a high toughness[167]. For this reason, ADI presents a better behaviour for these components than quenched and tempered steel[168].

3.6. CONTROLLED COOLING

Recently, for cast iron materials, one of the research developments that is gaining importance, is the control of the cooling process of the cast component, which is also known as engineered cooling[169]. The aim of controlling the cooling process, is to take advantage of the energy that the castings present after the solidification and, by changing the cooling conditions, obtaining the desired microstructure in as-cast conditions. This way, there is no need of a subsequent heat treatment.

For this, an early shakeout at a high temperature is necessary and afterwards, to act on the cooling rate of the different sections of a component, increasing or decreasing the cooling rate, depending on the desired microstructure[170].

Additionally, in order to obtain the desired microstructure in as-cast conditions, the actions on the cooling process are applied together with alloying elements, that is, acting on the chemistry of the liquid melt. As explained before, the alloying elements are added to increase the hardenability or the austemperability of the material[171]. The effect of the alloying elements on the cooling rate needed to obtain different microstructures is described by Temperature-Time Transformation (TTT) or Continuous Cooling transformation (CCT) diagrams[172] as shown in Figure 12.

Most of the controlled cooling process developments were performed to obtain fully ausferritic microstructures as-cast, because this is the microstructure that presents the best mechanical properties.

The obtention of ausferritic microstructures by means of engineered cooling, was first approached in 1985 by Janowak et al.[173]. This work was based on adding alloying elements like nickel, copper, and molybdenum to increase the austemperability of the material. During the cooling process, after a hot temperature shake out, air cooling was applied. Afterwards, the temperature was maintained constant using an insulating material. The target of this research was to see if ausferritic microstructures could be obtained by means of a simple controlled cooling process. The tested castings were standard Y2 blocks. They alloyed with 3.3 % C, 2.3 % Si, 1.5 % Ni, 1.0 % Cu and 0.5 % Mo. The engineered cooling process was performed by shaking out the sand mould at 870 ºC and then, air cooling the casting to the austempering temperature of 370 ºC. The casting was then introduced into a container of an insulating material for 120 minutes. The temperature of the casting after the austempering step was of 345 ºC. Finally, the casting was taken out from the insulating material and air cooled to room temperature. The results were positive, as shown in Table 5. Nevertheless, this idea was not further developed.

Table 5. Mechanical properties obtained by an engineered cooling process by Janowak et al.[173].

UTS (MPa)	YS (MPa)	E (%)	HBW
876	504	7.9	269

Yoo et al.[174] using a permanent model and cylindrical shape castings attempted to obtain ausferritic microstructures in SGI. The shakeout temperature was of 870 ºC and the castings immediately quenched to the austempering temperature of 340 and 360 ºC using a salt bath. The austempering time was 120 minutes. The chemical composition was 3.81-3.82 % C, 3.01-3.07 % Si, 0.05-1.08 % Cu, 0.065-1.03 % Ni and 0.001-0.300 % Mo. The mechanical properties obtained are shown in Table 6.

Table 6. Mechanical properties obtained by an engineered cooling process by Yoo et al.[174].

T_{temp} (ºC)	UTS (MPa)	YS (MPa)	E (%)
340	996	809	8.12
360	1029	702	9.01

Afterwards, further attempts to obtain ausferritic microstructures were performed by Meena et al.[175]. In this case, the investigation was performed using a permanent mould and a continuous casting heat treatment process. The cooling process is more complex than the one used by Janowak eta al.[173]. After solidification, the castings were shaken out at 1000-1010 ºC and austenitized in a muffle furnace at 930 ºC for 90 minutes. Afterwards, the castings were cooled in a fluidized bed at room temperature to the temperature range in between 400-500 ºC, and then transferred to another fluidized bed at 380 ºC for 60, 90, 120 and 150 minutes. Finally, the castings were air cooled. The chemical composition used was 3.44 % C, 2.56 % Si, 0.76 % Cu, 0.71 % Ni and 0.20 % Mo. The castings were rectangular blocks of 182 x 29 x 16 mm^3. The mechanical properties of the samples austempered at 60 and 90 minutes met the standards of the ADI materials.

4. OBJECTIVES

Cast iron materials present a very interesting option for design engineers for a wide range of applications. Among the cast iron materials, SGI presents the best mechanical properties in terms of UTS, YS, E, impact resistance and fatigue strength. More precisely, among these SGI materials, ADI or Austempered Ductile Iron is the alloy family that presents the optimal mechanical properties, making them a real alternative even for applications or components that are currently manufactured in steel and even aluminium and magnesium components[176].

Nevertheless, one of the most relevant advantages of cast iron and by extension of SGI is their application in the as-cast condition, without the need of a subsequent heat treatment, because they are a very cost competitive material family.

The fact that ADI materials are currently produced by means of an austempering heat treatment, hinders their development and the broadening of their market. The application of a heat treatment implies an added difficulty to the product soundness due to the variability of the treatment itself. It implies an added energy consumption, with its negative effect on the environmental aspects and carbon footprint of the components produced this way, as well as a cost increase. Furthermore, the lead time is increased due to the extra process needed after the as-cast state. Moreover, the austempering heat treatment is not a simple treatment and it requires an exhaustive control of the different steps (austenitizing and austempering) to get the desired microstructure. All these points go against the competitivity of the ADI materials.

The main objective of the present work is the obtention of an ausferritic microstructure in SGI in as-cast conditions, by means of a controlled cooling or engineered cooling process directly after the solidification and consequently, avoiding the application of a heat treatment.

The main target is that the as-cast ausferritic ductile iron products meet the standards of the conventionally obtained ADI components.

In addition to that main target, the following objectives are sought:

On the one hand, the feasibility of the methodology is a very important target. This is studied, to guarantee its applicability. On the other hand, another objective is to ensure that the standards of the ADI materials are fulfilled, considering statical, as well as dynamical properties, low temperature, and corrosion behaviour. For this, an advanced characterization of the obtained material is carried out. The objective is to obtain an industrially feasible methodology and a product that meets the quality standards. For this reason, in addition to standard samples, technology demonstrator prototypes are produced, to ensure, that the technology is applicable to real castings.

The definition of the optimal working ranges of the main process variables is another targeted objective. The alloying content, shakeout temperature and tempering temperature and time are evaluated to that aim.

The ausferritic transformation is deeply studied to analyse the effect of the controlled cooling process parameters on the mechanical properties. The objective is to deepen on the knowledge of the ausferrite formation kinetics and see if there is any difference linked to the absence of the austenitizing step.

The industrial application of the technology is another important objective of the present work. For this reason, the working limits of the methodology are studied, and a model is developed to check if a casting manufacture is feasible by means of this new technology. The target is to have an industrial tool, capable of helping the foundry to apply a controlled cooling process in the industrial production and adjust it for the different references they produce. This way, the ausferritic as-cast methodology would be ready to be industrially applied.

5. EXPERIMENTAL PROCEDURE

The present work is focused on SGI with a eutectic chemical composition. Carbon and silicon contents were maintained constant, and the used alloying elements were copper, nickel and molybdenum. The target was to avoid the influence of major alloying elements like carbon and silicon and focus on the effect of the elements that affect the austemperability and the ausferritic transformation. The manganese was maintained on a low range to avoid the negative effects of its segregation.

The trials were carried out in Fundación Azterlan placed in Durango (Basque Country). Figure 31 shows a general view of the melting shop during the temperature measurement of the prepared melt in the furnace before the tapping process.

Figure 31. General view of the melting shop in Fundación Azterlan facilities.

The melts were prepared in a medium frequency induction furnace (250 Hz, 100 kW) of 100 kg in capacity. The raw materials were low-alloyed steel scrap, low-alloyed pig iron and returns of a ferritic SGI. Graphite and FeSi75 were used to adjust the carbon and silicon contents in the furnace. Moreover, high purity nickel and copper and FeMo were used to adjust the nickel, copper, and molybdenum contents. The chemical composition of the used raw materials is shown in Table 7.

Table 7. Chemical composition of the raw materials used in the furnace.

Raw material	%C	%Si	%Mn	%Cu	%Ni	%Mo	%P	%S	%Cr	%Al
Low alloyed steel scrap	0.005-0.007	0.002-0.004	0.14-0.17	--	--	--	0.003 - 0.005	0.004-0.007	--	--
Low alloyed pig iron	4.09-4.16	0.12-0.15	0.013-0.020	--	--	--	0.019 - 0.025	0.005-0.008	0.027-0.034	--
Ferritic SGI returns	3.5-3.75	2.20-2.50	<0.25	<0.05	--	--	<0.030	0.003-0.008	--	--
Graphite	>99.0	--	--	--	--	--	--	<0.03	--	--
FeSi75	0.09-0.16	74.0-75.7	--	--	--	--	--	--	--	0.76-1.14
Cu	--	--	--	>99.0	--	--	--	--	--	--
Ni	--	--	--	--	>99.9	--	--	--	--	--
FeMo	0.02-0.03	0.66-2.05	--	--	--	64.2-65.9	0.03-0.05	0.03-0.04	--	--

After melting, the composition was checked and adjusted according to the required carbon, silicon, nickel, copper, and molybdenum contents.

The transfer of the melt from the furnace to the ladle was made at a temperature between 1500-1530 ºC.

The nodulization treatment was carried out following the sandwich methodology adding 1.20 % (by weight with respect to the total weight of the ductile iron alloy) of a FeSiMg alloy with the chemical composition shown in Table 8. The FeSiMg was positioned at the bottom of the ladle on the side designed for that purpose and covered with steel scrap (2.0-2.5 wt.%) to retard the reaction, before tapping the melt form the furnace, as shown in Figure 32.

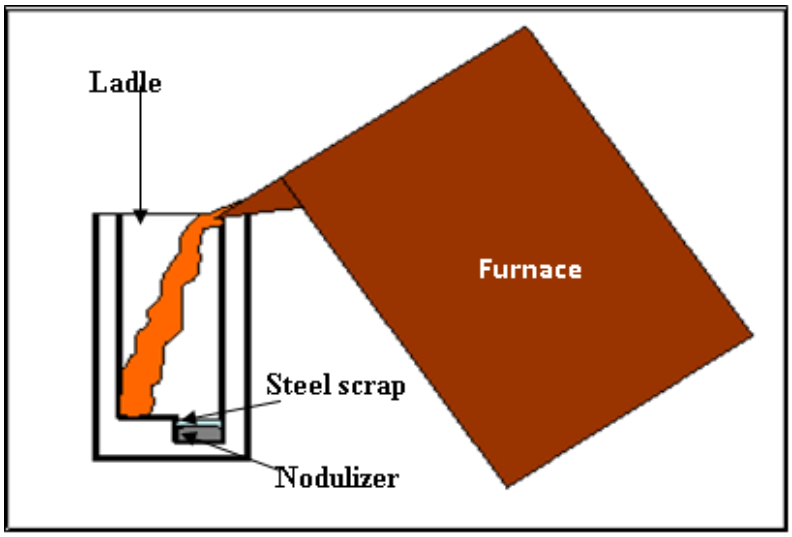

Figure 32. Nodulizing treatment by means sandwich methodology.

The inoculation was performed in mould using 0.20 % (by weight with respect to the total weight of the ductile iron alloy) of a FeSi alloy, whose chemical composition is shown in Table 8. The chosen inoculation product was defined based on the casting that was to be poured as will be explained later.

Table 8. Chemical composition of the used nodulizer and inoculants.

Raw material	Grain size (mm)	%Si	%Mg	%Ca	%Al	%RE	%Zr	%Ba	%Bi
FeSiMg	2-20	45.5-46.6	6.0-6.5	0.97-1.01	0.17-0.76	0.87-1.01	--	--	--
Inoculant A	0.20-0.50	69.9-72.1	--	1.38-1.62	0.85-0.93	0.37-0.39	0.12-0.20	0.34-0.38	0.46-0.49
Inoculant B	Solid block	68.0-76.0	--	0.30-1.50	3.20-4.50	--	--	--	--

The chemical composition was measured from a coin shape chill. The carbon and sulphur contents were measured by combustion techniques using a LECO C and S analyser (Figure 33-a), a C-S 744 equipment. The other elements were analysed by spark spectrometry (Figure 33-b) on a Spectrolab M10 equipment.

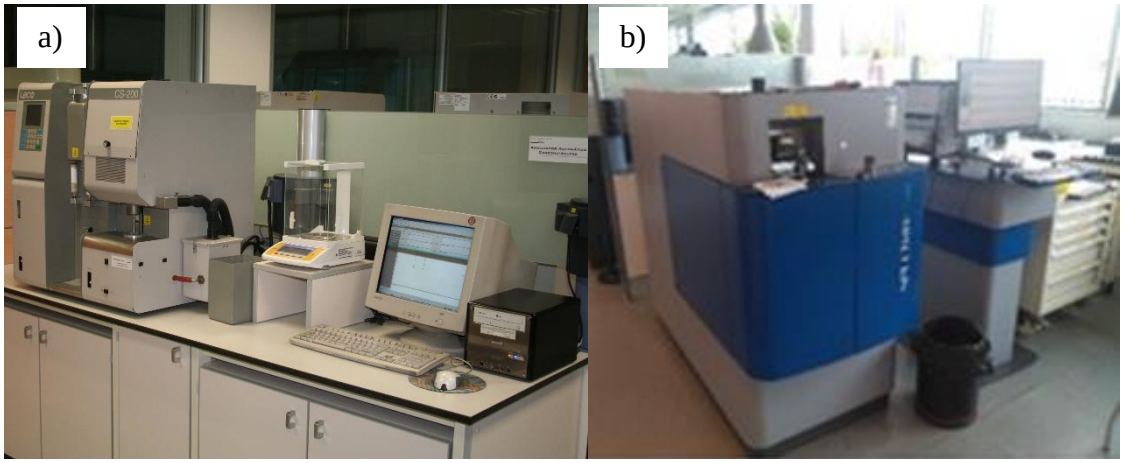

Figure 33. a) C-S analyser and b) spark spectrometer used to measure the chemical composition.

In a first series of experiments, CCT (Continuous Cooling Transformation) diagrams were performed modifying the Cu, Ni and Mo quantities. To achieve different cooling rates (CR) to develop these diagrams, cylinders and plates of different sizes were poured (Figure 34).

The plates' surface size was constant and of 100 x 60 mm^2 and from 10 to 80 mm in thickness, varying each 10 mm. The plates with a thickness between 10 and 40 mm and the ones presenting a thickness from 50 to 80 mm were poured in separated moulds.

The cylinders were, with the height equal to the diameter, of 24, 38, 48, 60, 72 and 90 mm. The four smallest cylinders and the two biggest ones were poured in separated moulds. Despite being in the same pattern, they were divided in two moulds, to make easier the manipulation during the engineered cooling process. The cavities that were not used were filled with sand, so that only the desired cavities were filled with metal.

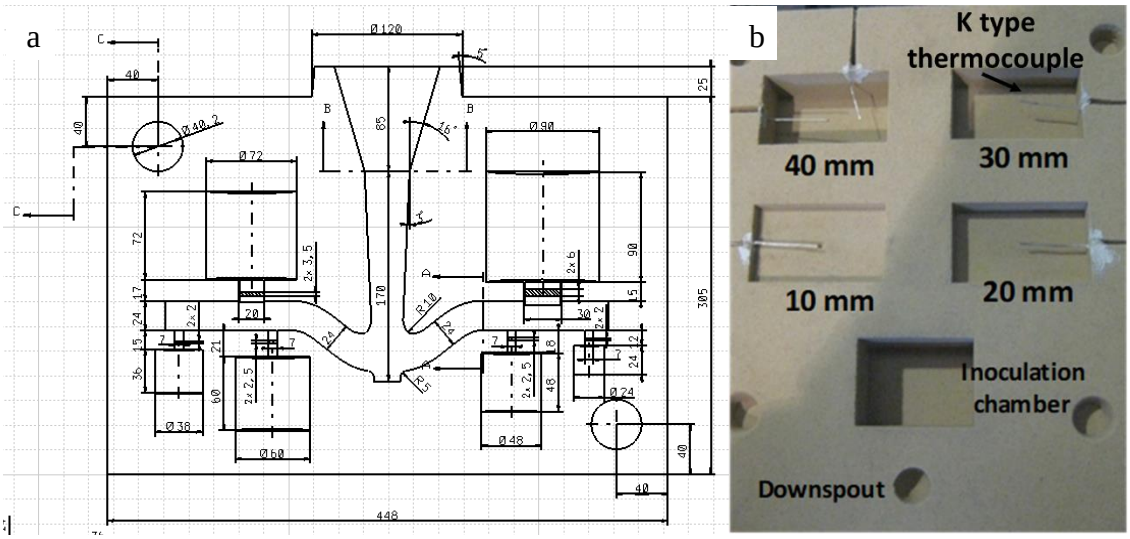

Figure 34. Examples of some a) cylinders and b) plates moulds to obtain samples with different CR.

The thermal modulus (TM) range of these castings calculated by the simulation software QuikCAST® is between 0.40 cm and 1.50 cm and is shown in Table 9. Examples of the cylinders and plates distribution in the mould are shown in Figure 34. A K type thermocouple was inserted in the centre of each cavity to be able to record their thermal evolution. These castings were inoculated by means of the inoculant B (Table 8) 0.20 wt.% (by weight with respect to the total weight of the casting and filling and feeding systems) placed in the downspout or downsprue of the moulds.

In addition to the plates and the cylinders, on the first series of experiments, keel blocks Y2 (Figure 35), as per the standard EN 1563[31] were poured in order to analyse both the microstructure and the mechanical properties of the material. A type K thermocouple was inserted in the centre of the samples, so that the solidification and subsequent cooling process could be recorded. The inoculation of these Y2 blocks was performed using the inoculant product referenced as A in Table 8, placing 0.20 wt.% in the bottom of the mould. This inoculant was used, to promote its dissolution and increase the inoculation efficiency, as the keel block moulds do not have a downsprue.

Besides the Y2 blocks, in order to evaluate the effect of the TM or the section size, on the microstructure and mechanical properties evolution, Y1 and Y3 blocks (Figure 35), as per the standard EN 1563[31] were poured on further trials. Y1 blocks present a section size on the bottom of 12.5 mm, Y2, 25 mm and Y3, 50 mm. Additionally, thermal analysis cups (TA) were poured, which present a lower TM than the Y blocks. In Figure 35 is shown the different TM of each casting predicted by the simulation software QuikCAST®.

To study the ausferrite transformation kinetics, dilatometry samples (DIL) machined from the Y2 blocks were studied. These are cylindrical samples measuring Ø 10 mm and 8 mm height. Additionally, for the CCT diagram development, quenching dilatometry (QDIL) samples were machined from the Y2 blocks, when, due to a low alloy content, a very high CR was needed to avoid the pearlitic nose. These are cylindrical samples and measure 4 mm Ø and 10 mm height.

In Table 9 are shown the TM values of all the studied castings. With this TM range (0.15-1.75 cm) it is considered to cover the section size range that present the main components produced in ADI.

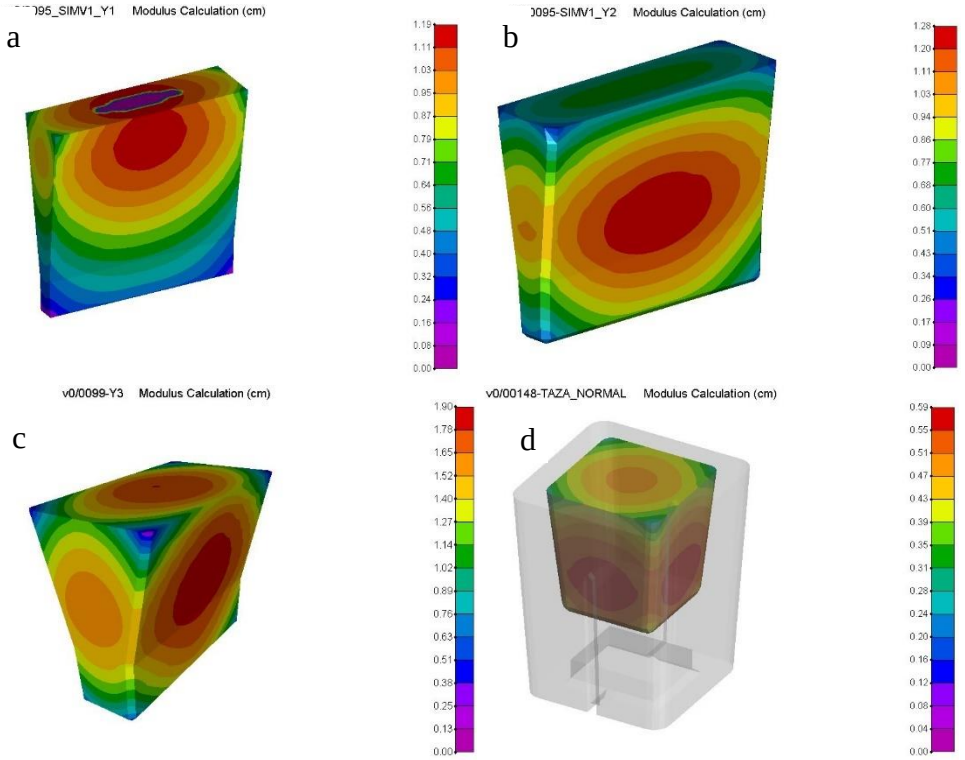

Figure 35. TM of the different castings predicted by the software QuikCAST®. a) Y1, b) Y2, c) Y3, d) TA.

Once the controlled cooling process was defined from the experiments on the keel blocks, steering knuckles were poured as a technology demonstrator prototypes. The purpose was to verify that the methodology is also reliable for real castings, presenting different section thicknesses, with high quality standards as specified by the automotive industry. For this reason, steering knuckles were produced following the engineered cooling methodology defined on the first steps of this work. This casting is shown in Figure 36. This is a safety component for the automotive sector, the part that attaches the wheel to the suspension and steering components. It is manufactured in an SGI ferritic material, because a high ductility is needed for its functionality and the 400 MPa UTS that presents this microstructure is enough for design aspects.

The experimental procedure performed for the steering knuckles was the same as for the keel blocks with two differences. On the one hand, two type K thermocouples were inserted in a thin and a thick sections as shown in Figure 36 and on the other hand, the inoculation was carried out in mould using 0.20 wt.% of the inoculant referenced as B in Table 8. The TM of both analysed sections were simulated by the software QuikCAST® and they are shown in Table 9. The results of the simulation are shown in Figure 37.

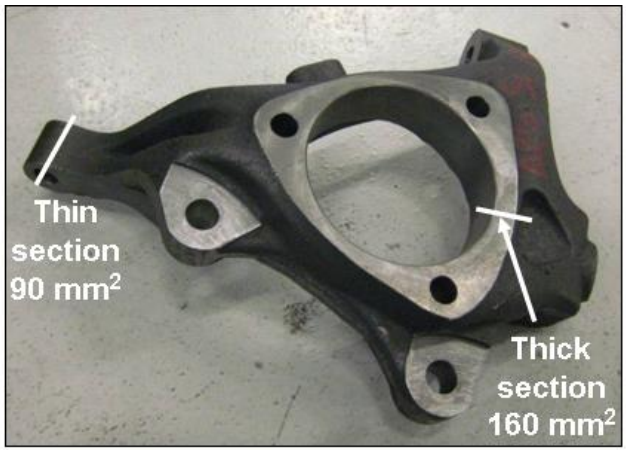

Figure 36. Illustration of the thin and the thick sections recorded for the steering knuckle.

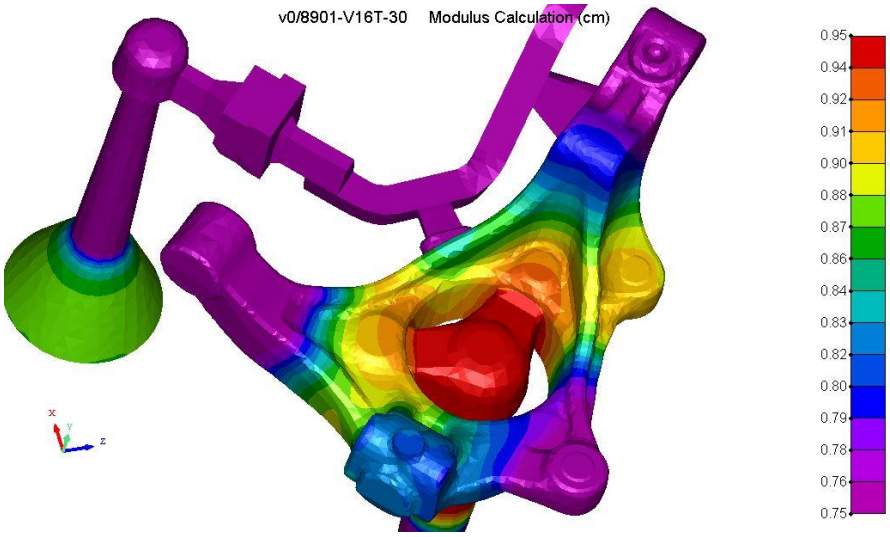

Figure 37. TM simulation of the steering knuckle by the software QuickCAST®.

Table 9. TM of the produced samples.

Sample	TM (cm)	Sample	TM (cm)	Sample	TM (cm)
DIL	0.15	Plate 10 mm	0.39	Cylinder Ø 24 mm	0.40
QDIL	0.07	Plate 20 mm	0.65	Cylinder Ø 38 mm	0.63
TA	0.55	Plate 30 mm	0.83	Cylinder Ø 48 mm	0.80
Y1	0.70	Plate 40 mm	0.97	Cylinder Ø 60 mm	1.00
Y2	1.11	Plate 50 mm	1.07	Cylinder Ø 72 mm	1.20
Y3	1.75	Plate 60 mm	1.15	Cylinder Ø 90 mm	1.50
Steering knuckle Thin	0.65	Plate 70 mm	1.22		
Steering knuckle Thick	0.83	Plate 80 mm	1.28		

The moulds for all the studied castings were produced in chemically bonded sand.

To apply an engineered cooling process to the different castings, a high temperature shakeout was performed by mechanical means. The sand that could be stuck to the surface of the castings was also removed by mechanical means.

The applied cooling media to the castings was air cooling. This decision was taken based on the simplicity of the methodology.

The temperature arrest to provoke the ausferrite formation, was applied by two different means. First, the samples were introduced into a heat treatment furnace, which was at the temperature defined for the ausferrite formation. This furnace is shown in Figure 38-a. The furnace enables having a constant temperature, nevertheless, it implies an energy consumption. For this reason, another methodology was studied, introducing the castings in a reusable insulating medium called expanded perlite. The main properties of this material are shown in Table 10 and an example of its utilization is shown in Figure 38-b.

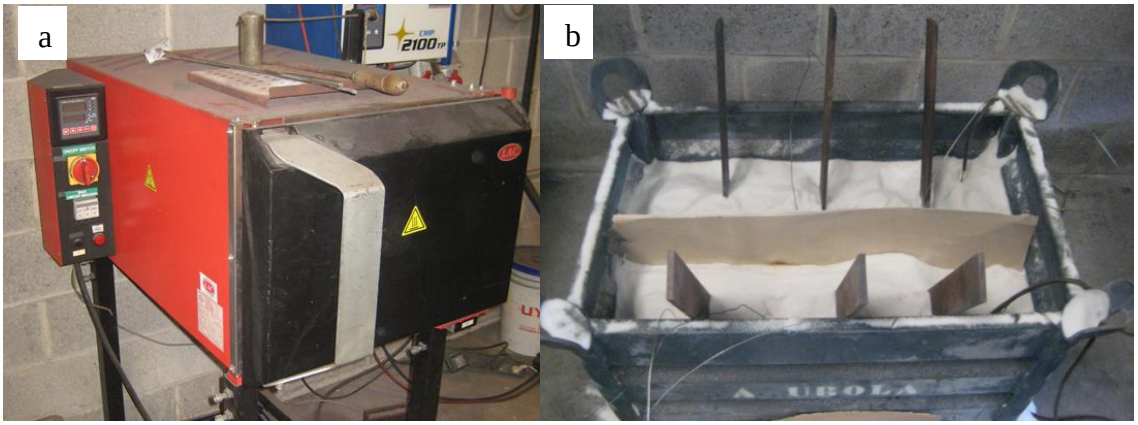

Figure 38. Different media to maintain a constant temperature in the castings. a) Furnace, b) Reusable insulating material.

Table 10. Main characteristics of the insulating medium used to maintain a constant temperature.

Thermal conductivity	0.04-0.06 W/mK
Mesh size	<5 mm
Density	40-120 Kg/m^3

Different austempering temperatures and times were tried, to study the evolution of the microstructure and mechanical properties with them.

The castings were maintained in the furnace or in the insulating medium for the defined temperature and time during the ausferrite formation and afterwards air cooled till room temperature.

An example of the thermal evolution of an engineered cooling process for the different Y blocks is shown in Figure 39.

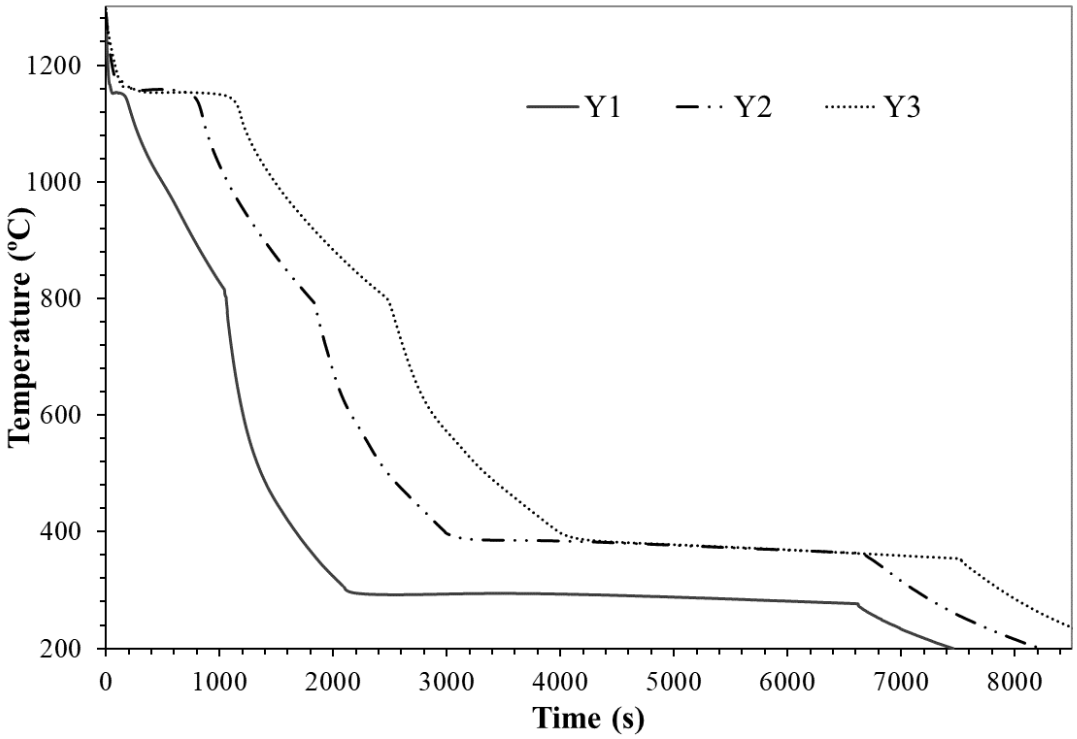

Figure 39. Thermal evolution of an engineered cooling process for the different Y blocks.

Furthermore, to study the kinetics of the ausferritic reaction, interrupted cooling experiments were performed with the Y blocks and the TA samples following the same cooling process (early shakeout and air cooling), but quenching the samples in water once reached the temperatures of 550, 525, 500, 450, 400 and 300 °C.

In the case of the dilatometry tests, the samples followed a thermal evolution using a thermomechanical analyser equipment Q400 TMA, shown in Figure 40-a. The samples were heated up at 20 °C/min rate to an austenitizing step at 900 °C for 40 minutes, afterwards air cooled till the isothermal temperature and there maintained during 1, 2, 5, 10, 15, 20, 30, 50 and 180 minutes. Finally, air cooled to room temperature. On this case, due to the impossibility of performing an as-cast cycle, the air cooling was maintained to obtain equivalent CR than for the Y blocks and the TA samples.

The quenching dilatometry tests were performed using a L78 R.I.T.A. (Linseis) quenching dilatometer shown in Figure 40-b. The samples were heated up at 20 °C/min rate from room temperature to 900 ºC and maintained at that temperature for 40 minutes. Afterwards, they were cooled at a CR up to 350 ºC/min down to room temperature. The high CR was obtained cooling the samples in a helium atmosphere. To be able to record such a high CR with a high accuracy, the thermocouples were welded to the sample. The thermocouples were made of a NiCr wire for the negative and a Ni wire for the positive pole.

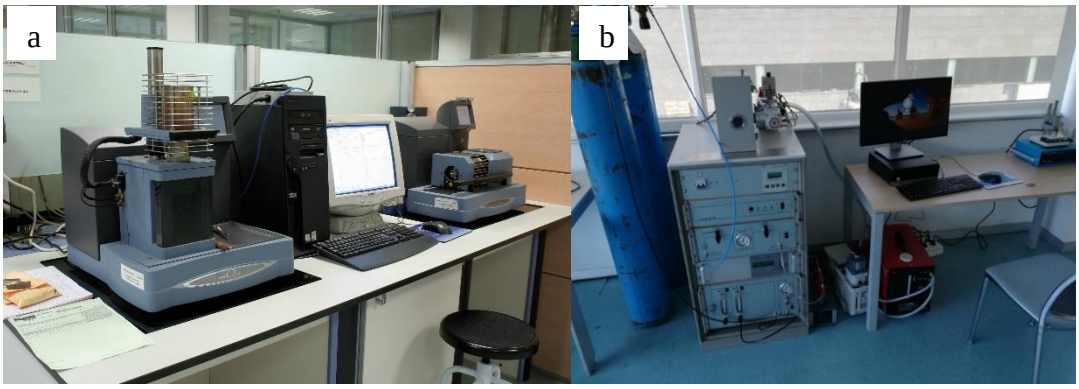

Figure 40. Images of the a) Thermomechanical analyser, b) Quenching dilatometer.

5.1. SAMPLE CHARACTERIZATION

Once the samples were poured and after applying the controlled cooling process, the results of the castings were studied as follows:

Tensile, impact and hardness specimens were machined from the bottom of each standard keel block (Figure 41).

A 10 mm diameter specimen was used for the tensile tests in case of the Y2 and Y3 blocks and a 8 mm diameter for the Y1 blocks due to geometrical reasons. The test was performed following the standard ISO 6892-1[35]. The mechanical parameters measured were the ultimate tensile strength (UTS.), the yield strength (YS), and the elongation (E).

Three unnotched and V notched samples (dimensions 10×10×55 mm^3) were prepared for the impact testing at different temperatures (room temperature, -20 and -40 ºC). The result of this test is the impact energy (Charpy) or the energy that a sample can absorb before breakage. These tests were performed following the standard ISO 148-1[49].

Brinell hardness (HBW) measurements were made on machined samples using a 10 mm diameter sphere and a load of 3000 kg, following the standard ISO 6506-1[48] .

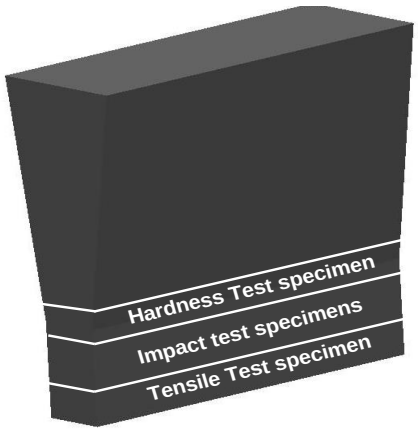

Figure 41. Test specimens machined from the Y blocks.

An image of the equipment used to carry out these tests is shown in Figure 42.

Figure 42. Image of a) Tensile test machine, b) Brinell hardness measurement, c) Charpy test machine.

Once tested, the tensile test specimens were prepared for a metallographic analysis on a cross section close to the fracture surface.

The dilatometry samples were metallographically analysed close to the surface.

The specimens were cut and prepared for metallographic examination using a sequence of SiC abrasives from 80 to 1200 grit paper. Nodularity and nodule count were determined using quantitative image analysis software. The microstructure was obtained after etching the samples with Nital 5 %.

With the aim of defining the phases that appear on the metallic matrix (AF, RA and M), the volume fraction of AF and M was defined using the point counting methodology described on the standard ASTM E562[177]. A square grid of 100 points per image, at 1000 magnifications to have a clear view of the different phases was considered and ten fields analysed per sample.

Light optical microscopy (LOM) and field emission gun scanning electron microscopy (SEM) were used for these evaluations. The LOM was a Leica-Reichert, MEF-4-35-M-1-DC-4 equipment, and the SEM was a Zeiss Ultraplus. This equipment is shown in Figure 43.

Figure 43. Microscopes for the characterization: a) LOM, b) SEM.

An example of a LOM micrograph used for the microstructure phases characterization is shown in Figure 44.

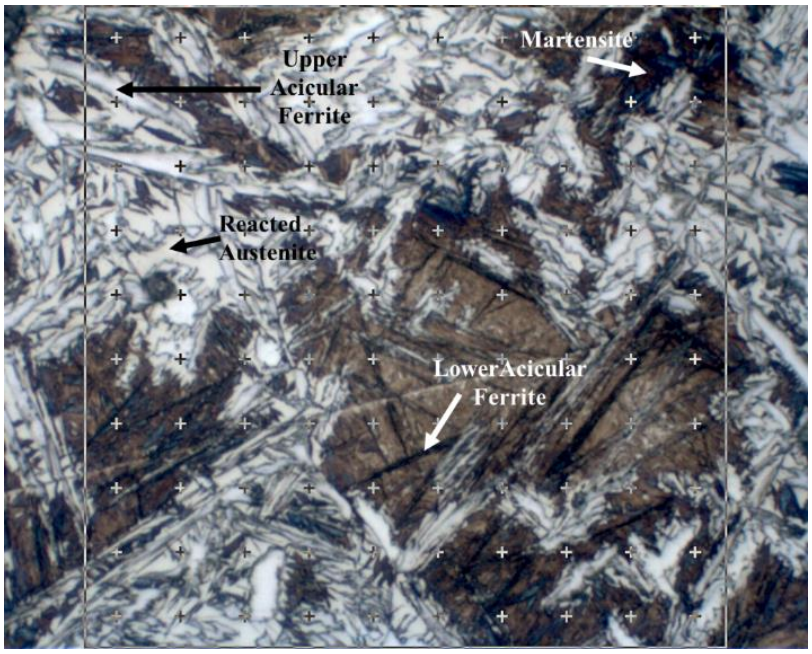

Figure 44. Micrograph showing the microstructure characterization methodology.

Considering the steering knuckles, tensile test samples (Ø 10 mm), impact samples (three V-notched 10x10x55 mm^3) as well as a Brinell hardness sample were machined from the castings as shown in Figure 45. The measured mechanical properties were the same than those obtained from the keel blocks. The metallographic analysis was carried out both from the tensile test samples and the impact strength samples (thin and thick sections respectively).

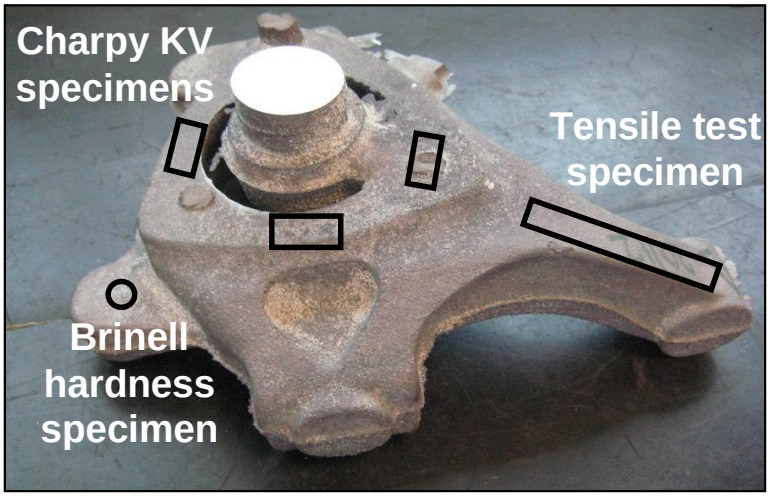

Figure 45. Samples to evaluate the mechanical properties taken from a steering knuckle.

6. ENGINEERED COOLED AUSFERRITIC SGI

The research activities performed to reach the contemplated objectives follow the next structure:

The first experimental data set comprises the activities to define the controlled cooling methodology that can guarantee the obtention of the desired ausferritic microstructure and the mechanical properties. Besides, the main variables that play a role in the final material properties are studied and their working ranges delimited.

These initial trials were designed to, on the one hand, proof the feasibility of the ausferritic as-cast methodology and on the other hand, define the optimal parameters from the point of view of achieving the desired microstructure and mechanical properties.

The main variables define the first three sub-sections, that are the, alloying elements definition, austempering technology and high temperature shakeout definition These results are shown on the first three sub-sections. The work carried out to define the proper engineered cooling methodology and the process parameters is gathered.

Moreover, on the fourth sub-section, the kinetics of an ausferritic transformation for an as-cast obtained ausferritic microstructure are deeply studied. The evolution of the microstructure with the austempering temperature and holding time is analysed, and their relationship with the mechanical properties studied.

Furthermore, once the technology and the process parameters are defined, an advanced characterization of the material is performed on the fifth sub-section. Dynamic mechanical properties, low temperature response of the material and the corrosion resistance is analysed. The aim of these tests is to corroborate that the as-cast ausferritic material presents the same characteristics as the heat-treated conventional ADI materials.

On the first five sub-sections the experimental data are obtained considering standard samples with a constant section size. For this reason, to be able to demonstrate the application of the methodology to real castings presenting different section sizes, technology demonstrator prototypes are produced in a laboratory scale. These prototypes are steering knuckles, and the results are shown on the sixth sub-section-

Finally, on the seventh sub-section, the industrial application of the technology is considered, trying to reproduce the laboratory scale results to an industrial environment. A mathematical model was developed to define the working window that the engineered cooling technology offers, determining on the one hand the application feasibility for a given casting and, on the other hand, stablishing the optimal alloy content and when the shakeout and isothermal transformation steps should be carried out, based on the desired mechanical properties.

6.1. ALLOY DEFINITION

As a first premise to define the methodology, air cooling was considered as the cooling media for the engineered cooling process. This decision was taken based on the simplicity of the methodology. For this reason, CCT diagrams were performed for different alloys to define the optimal alloy content that ensures the austemperability of the samples and castings cooled in air. Copper, nickel, and molybdenum were used as alloying elements since they are the main elements to increase the austemperability. The minimum cooling rate (CR) needed to avoid the pearlitic nose or to prevent the eutectoid transformation was calculated as a function of the alloy content. This was linked to the CR that a given thermal modulus (TM), or section size presents when air cooled.

The castings produced to develop these CCT diagrams were the different TM plates and cylinders (Figure 34) and the Y blocks and the TA cups (Figure 35). The alloying elements used to develop the CCT diagrams were Ni, Cu and Mo and they were on the following ranges: <0.03-5.05 % Ni, <0.02-0.22 % Mo, 0.09-1.09 % Cu.

To develop the CCT diagrams, two different cooling processes were followed. On the one hand, an early shakeout was applied to all the samples followed by air cooling. On the other hand, the cooling was performed in the mould. The target was, considering different TM and different cooling mediums, to achieve a wide range of CR for each studied alloy. The cooling curve of each casting was recorded by means of a thermocouple (type K) inserted in its thermal centre. With this information, the CR of the samples was experimentally calculated in the temperature range in which the eutectoid transformation takes place. This temperature range is normally above 600 ºC[84, 89]

Additionally, for the case of a low alloy content, due to the need of a high CR to avoid the pearlitic nose, quenching dilatometry (QDIL) samples were machined from the bottom of a Y2 block. The quenching dilatometry tests were performed applying a constant cooling rate in the temperature range that the eutectoid transformation takes place and below (500-800 ºC) after the austenization step. An example of the thermal evolution is shown in Figure 46.

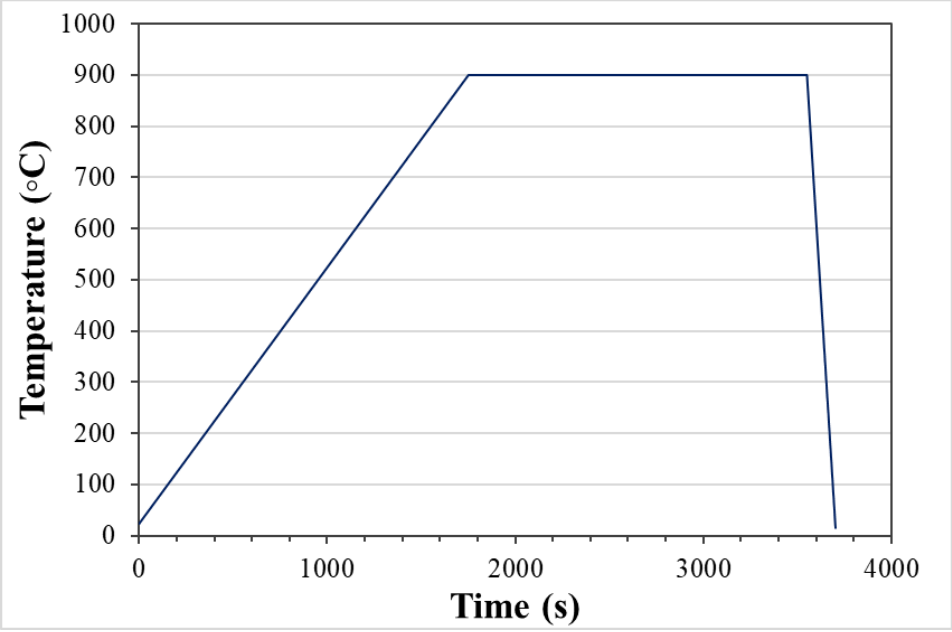

Figure 46. Thermal evolution of a sample in the quenching dilatometer.

The castings were then analysed by cutting one specimen from the centre and prepared for visual inspection by means of LOM. To reveal the microstructure, the metallographic samples were etched with Nital 5 %. This metallographic analysis was performed to define if pearlite apparition occurred. If no pearlite appeared in the microstructure of the castings, presenting then a martensitic and or an ausferritic microstructure, it was considered that the pearlitic nose was avoided. Consequently, the minimum CR needed to avoid the formation of pearlite as a function of the alloy composition was defined.

The range of chemical compositions in wt.% of the cast parts was as follows (Table 11):

Table 11. Chemical composition of the different trials (wt.%)

C	Si	Cu	Ni	Mo	Mg	Mn	S	P
3.56-3.75	2.00-2.31	0.09-1.09	0.027-5.05	0.01-0.22	0.038-0.049	0.18-0.25	0.003-0.009	0.007-0.010

The different trials were grouped in four different alloys, considering the ranges of the main alloying elements (nickel, molybdenum, and copper). This classification is shown in Table 12.

Table 12. Chemical composition of the alloys for which the CCT diagrams were developed (wt.%).

Alloy	C	Si	Mn	Mg	Ni	Mo	Cu
0.0 %Ni, 1.0 %Cu, 0.0 % Mo	3.56-3.58	2.20-2.31	0.20-0.25	0.040-0.044	<0.03	<0.02	1.00-1.09
3.0 %Ni, 1.0 %Cu, 0.0 %Mo	3.60-3.73	2.00-2.12	0.18-0.22	0.038-0.045	2.90-3.05	<0.02	0.94-1.01
5.0 %Ni, 1.0 %Cu, 0.0 %Mo	3.58-3.69	2.03-2.14	0.20-0.25	0.040-0.049	4.95-5.05	<0.02	0.97-1.04
3.0 %Ni, 0.0 %Cu, 0.2 %Mo	3.63-3.75	2.04-2.15	0.19-0.24	0.042-0.049	2.86-3.01	0.17-0.22	0.09-0.19

Next, an example of the trials with the cylinders is presented. In Figure 47, the cooling curves of the cylinders cooled in the mould with the chemical composition of 3.0 % Ni, 1.0 % Cu and 0.0 % Mo are shown. In Figure 48, the cooling curves of the cylinders shaken out at a high temperature and then air cooled, poured with the chemical composition 3.0 % Ni, 0.0 % Cu and 0.2 % Mo are shown.

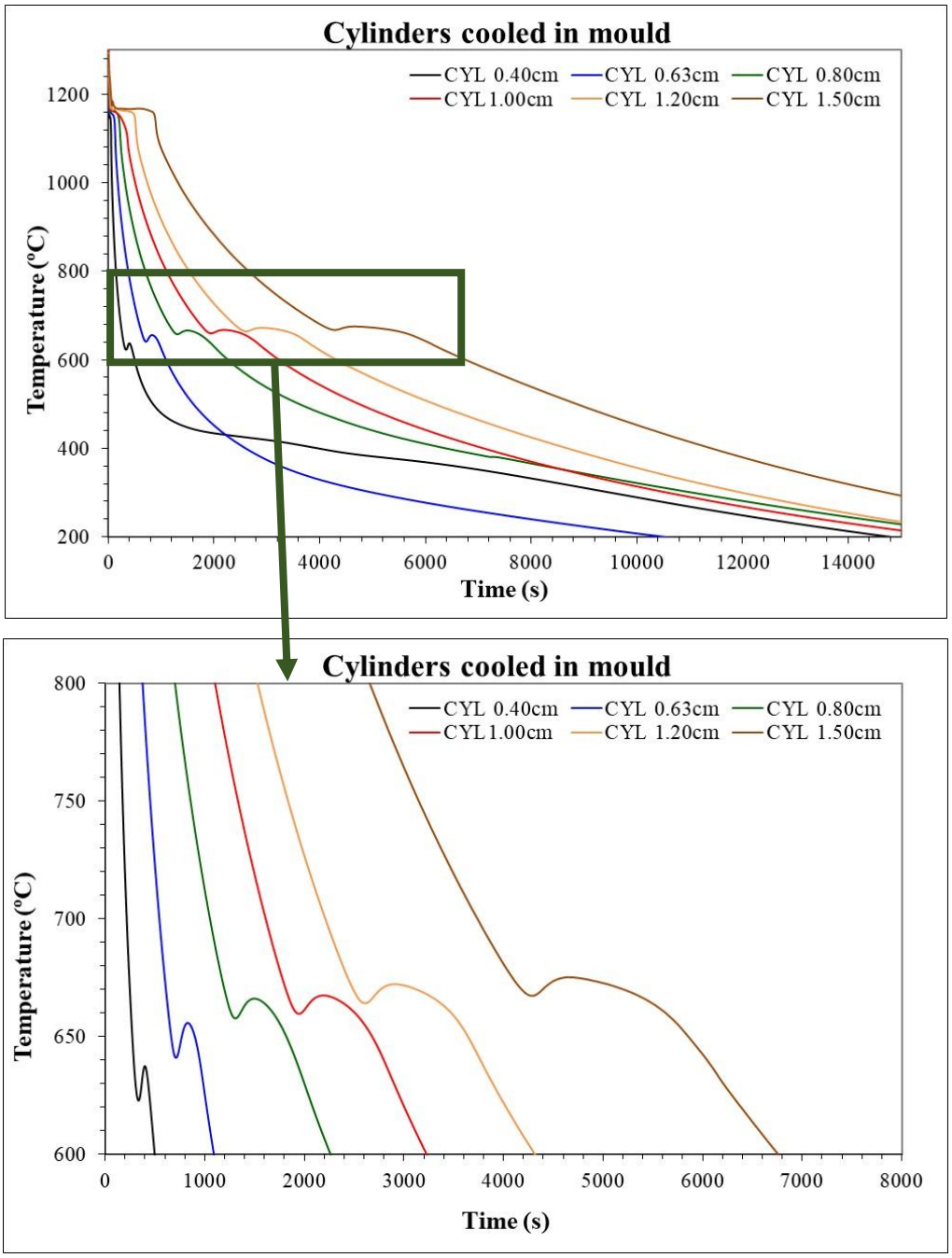

Figure 47. Cooling curves of the cylinders cooled in the mould with the chemical composition 3.0 %Ni, 1.0 %Cu and 0.0 %Mo.

It is seen that all the samples, during the cooling in the temperature range of the eutectoid transformation present a recalescence or a temperature increase. This is related to the pearlite formation as shown in Figure 49. In this figure, only the two smallest cylinders are shown, because, if the pearlitic nose was not avoided for the highest CR, it was not neither avoided for the highest ones. Thus, the microstructure remains pearlitic or ferritic/pearlitic in all the cases. It is important to point out the fact that the lower the TM, the lower the temperature at which the eutectoid transformation takes place.

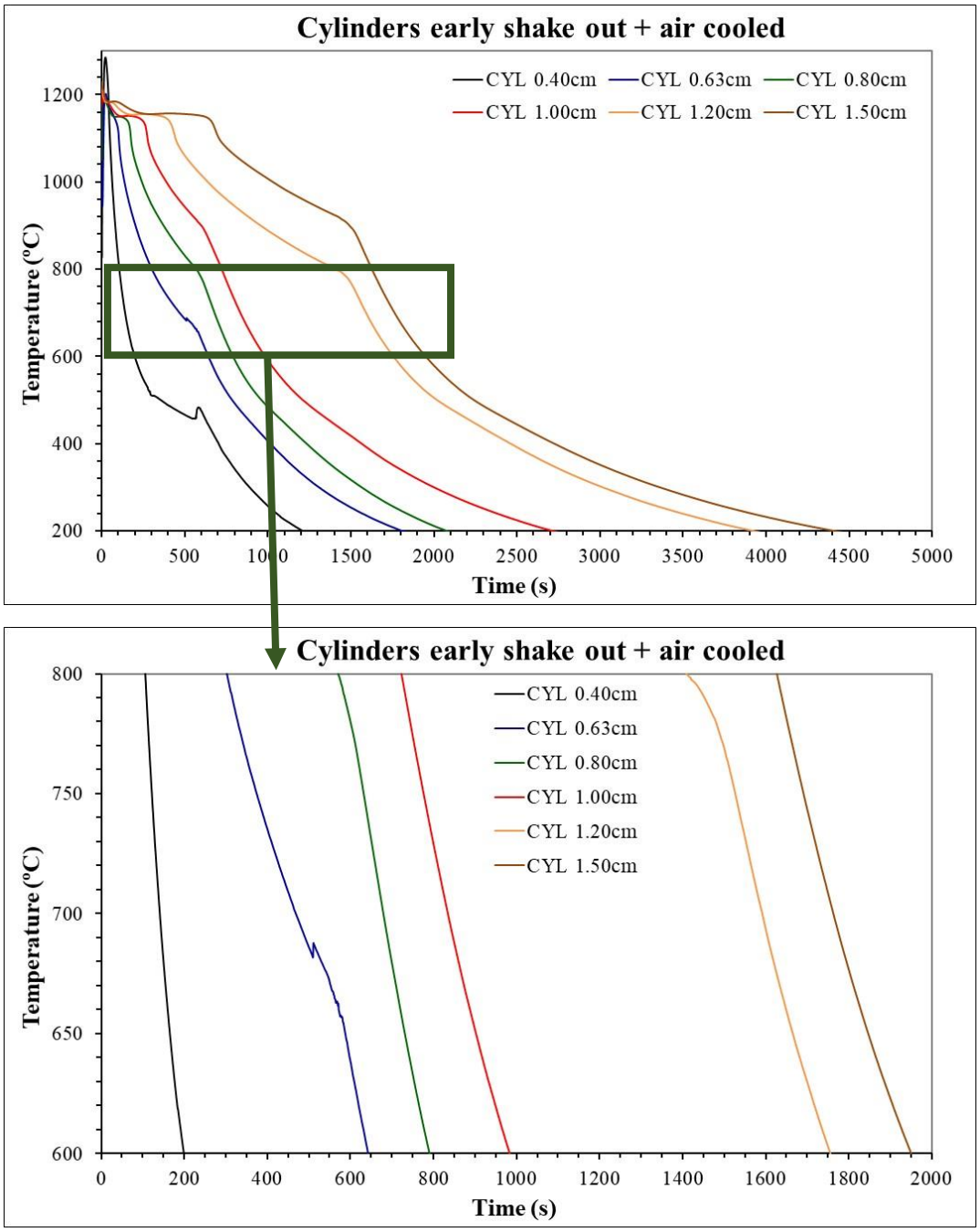

Figure 48. Cooling curves of the cylinders cooled in air with the chemical composition 3.0 %Ni, 0.0 %Cu and 0.2 %Mo.

It is seen, on the one hand, how the two highest TM cylinders are handled separately, so the shakeout moments for these cylinders and the other four are different. On the other hand, no eutectoid transformation is captured by the thermocouples. The recalescence that presents the smallest cylinder is linked to a registration problem during the handling of the mould for the shakeout. Studying the microstructure of the different cylinders shown in Figure 50, it is seen that neither of them present any pearlite. This means, that with the alloy content of 3.0 % Ni and 0.2 % Mo, the pearlitic nose is not touched even for a TM of 1.50 cm when cooled in the air. Consequently, there is no occurrence of the eutectoid transformation and thus, the microstructure of the different cylinders is made up of ausferrite, martensite and unreacted austenite.

CYLINDER TM 0.40 cm	CYLINDER TM 0.63 cm
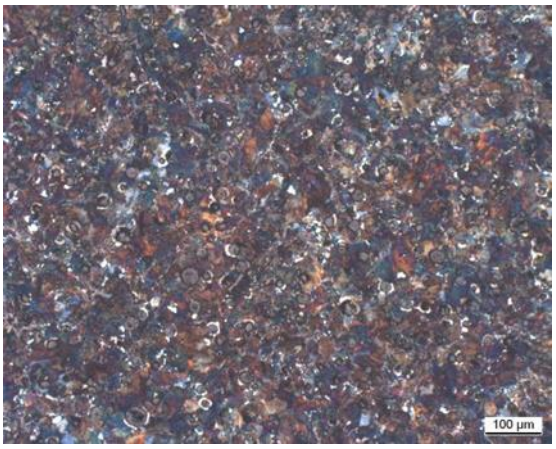	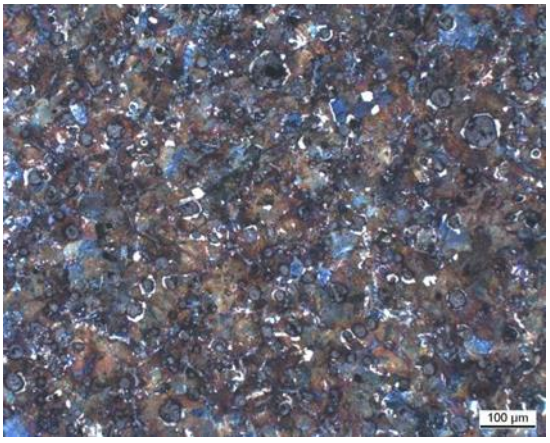
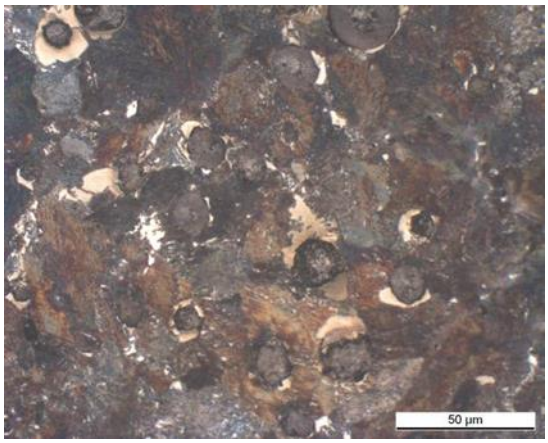	

Figure 49. Micrographs corresponding to the two smallest cylinders cooled in the mould with the chemical composition 3.0 %Ni, 1.0 %Cu and 0.0 %Mo. 100x on the upper row and 500x on the lower row.

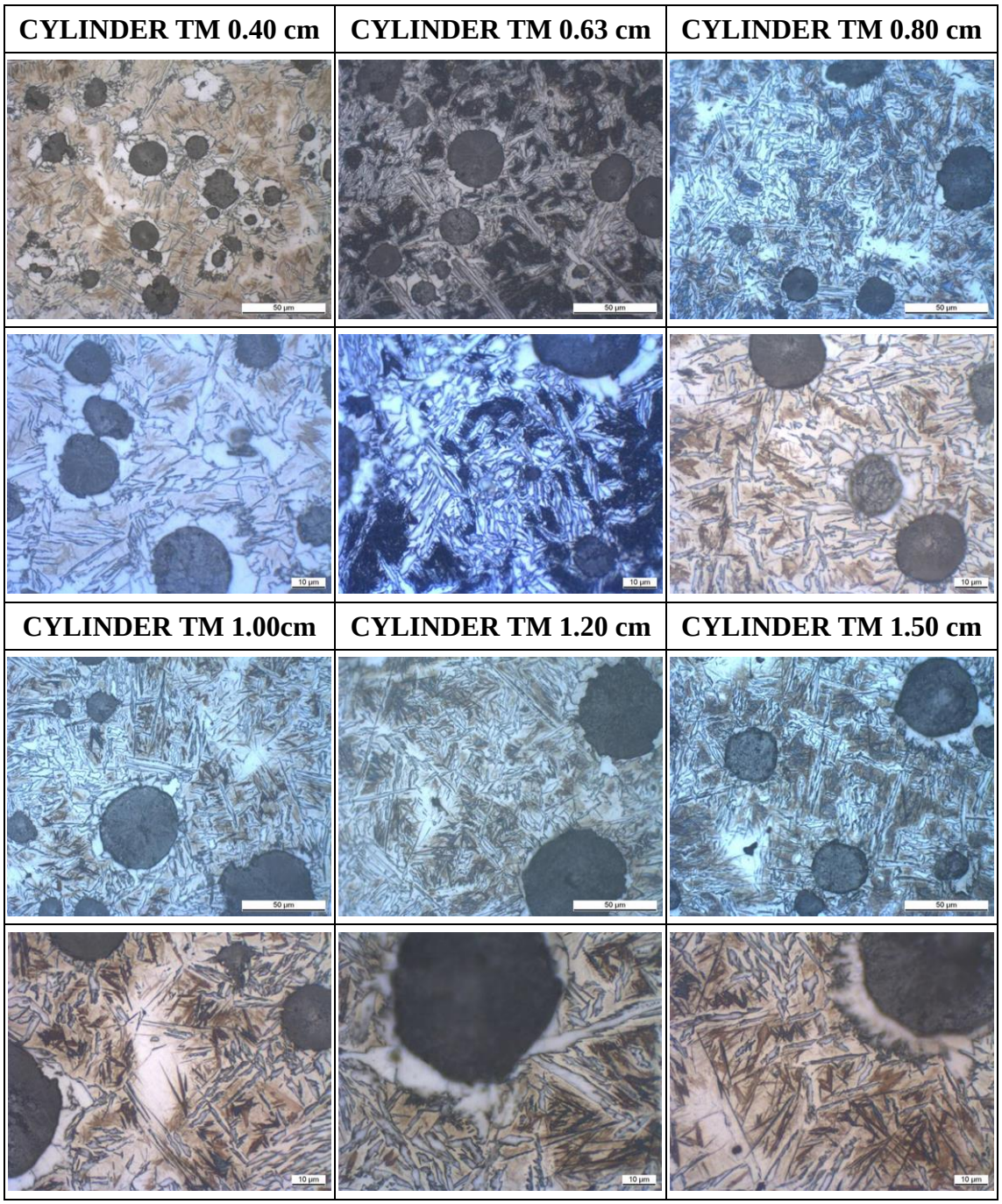

Figure 50. Micrographs corresponding to the cylinders early shaken out and air cooled with the chemical composition 3.0 %Ni, 0.0 %Cu and 0.2 %Mo. 500x on the upper row and 1000x on the lower row.

To establish the experimental CCT diagrams, each alloy was cooled with rates from 0.2 to 1.3 ºC/s in the temperature range between 800 and 500 ºC, except for the low alloy content treated in the quenching dilatometer, for which the CR was in the range 1.3-5.8 ºC/s. All the recorded cooling curves in this temperature range are shown in Figure 51. The formerly described methodology was followed in all the trials, that means, relating the microstructure with the cooling curves. In this manner, the pearlitic nose was defined for the four different alloys, as shown in Figure 52.

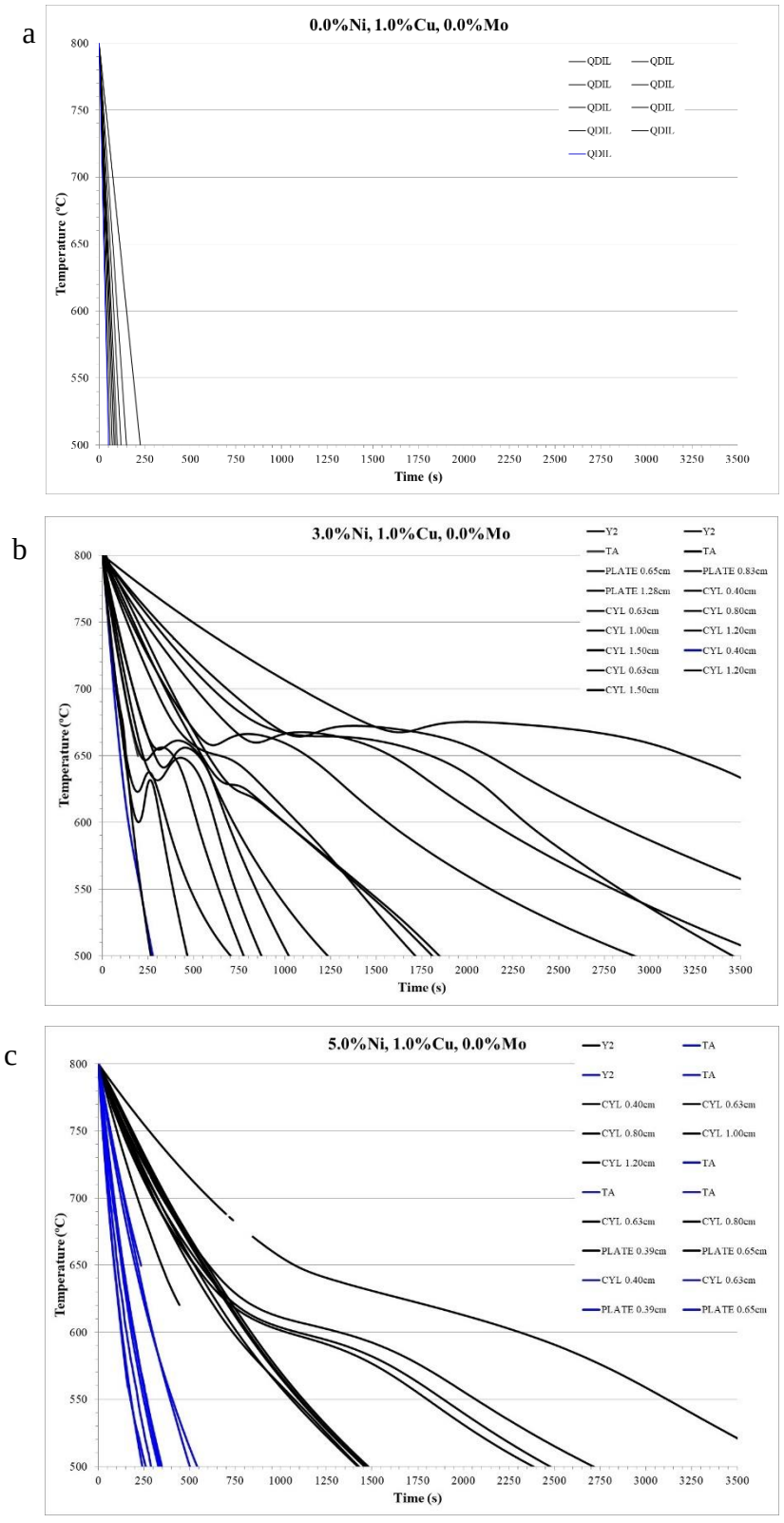

Figure 51. Studied cooling curves for the four analysed alloys. a) 0.0%Ni, 1.0%Cu, 0.0%Mo, b) 3.0%Ni, 1.0%Cu,0.0%Mo, c) 5.0%Ni, 1.0%Cu, 0.0%Mo, d) 3.0%Ni, 0.0%Cu, 0.2%Mo.

d

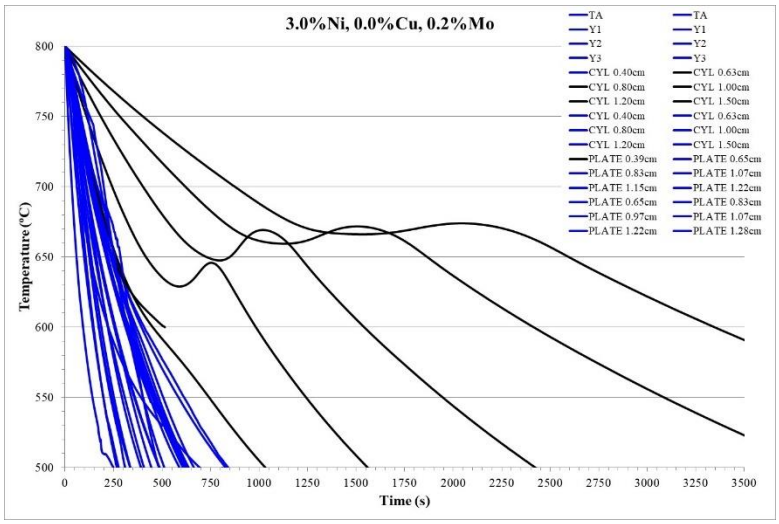

Figure 51 (Cont.) Studied cooling curves for the four analysed alloys. a) 0.0%Ni, 1.0%Cu, 0.0%Mo, b) 3.0%Ni, 1.0%Cu,0.0%Mo, c) 5.0%Ni, 1.0%Cu, 0.0%Mo, d) 3.0%Ni, 0.0%Cu, 0.2%Mo.

The cooling curves marked as blue do not present any pearlite. Thus, the blue curve with the slowest CR is the one that defines the tip of the pearlitic nose, or what is the same, the slowest CR needed to avoid the eutectoid transformation for a given alloy. This is more precisely shown in Figure 52. The pearlitic nose is marked in green.

a

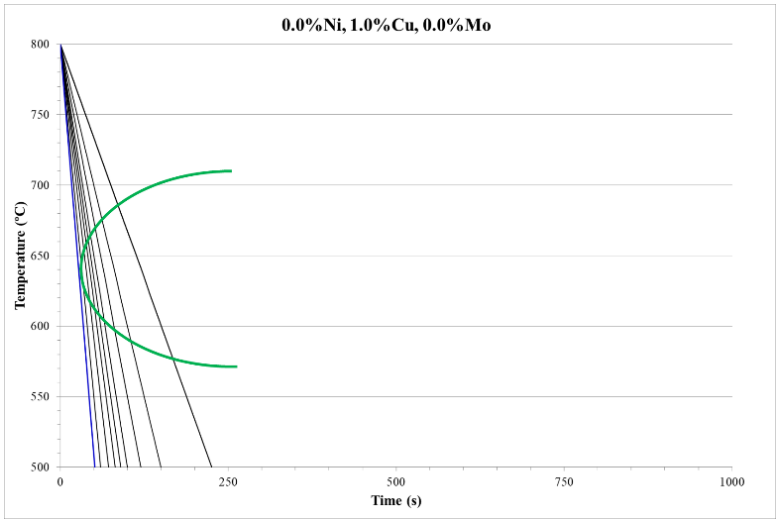

Figure 52. Pearlitic nose definition for the four studied alloys. a) 0.0%Ni, 1.0%Cu, 0.0%Mo, b) 3.0%Ni, 1.0%Cu,0.0%Mo, c) 5.0%Ni, 1.0%Cu, 0.0%Mo, d) 3.0%Ni, 0.0%Cu, 0.2%Mo.

b

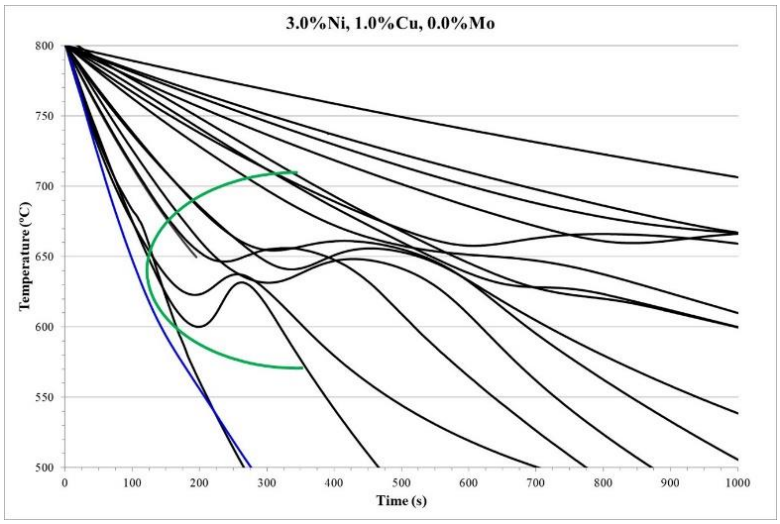

c

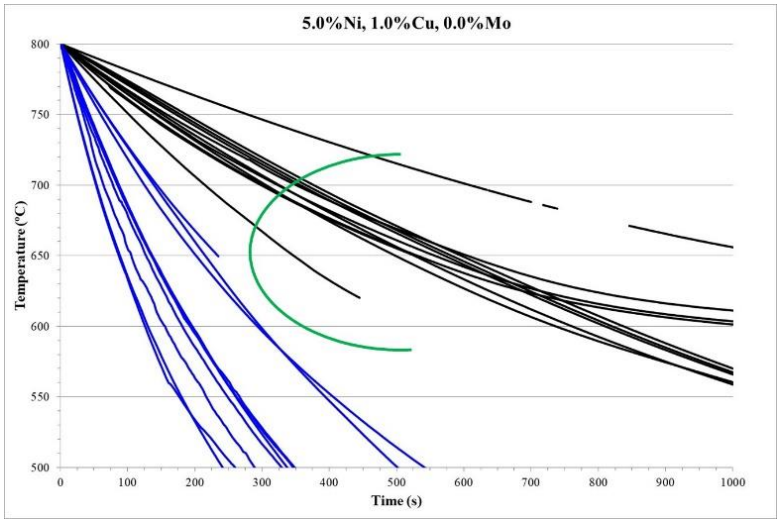

d

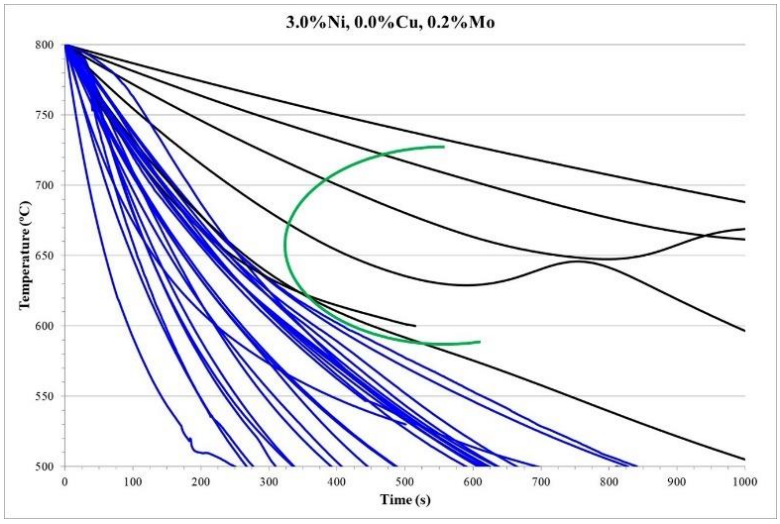

Figure 52 (Cont.) Pearlitic nose definition for the four studied alloys. a) 0.0%Ni, 1.0%Cu, 0.0%Mo, b) 3.0%Ni, 1.0%Cu,0.0%Mo, c) 5.0%Ni, 1.0%Cu, 0.0%Mo, d) 3.0%Ni, 0.0%Cu, 0.2%Mo.

The experimental minimum CR for each alloy to avoid the formation of pearlite is shown in Table 13. The minimum CR values were considered for the temperature range 600-700 ºC, since the lowest registered CR considering air cooling before the eutectoid transformation occurs on this range. In addition to this value, the maximum CR at which pearlite appears in the experimental trials is shown. CR values in between those numbers was not possible to obtain with the different TM and the different cooling processes (air cooling and cooling in the mould). To gain accuracy, intermediate values should be tested.

Table 13. Minimum CR to avoid the pearlite formation for the studied alloys in the 600-700 ºC temperature range.

Alloy	Minimum cooling rate without pearlite appearance (ºC/s)	Maximum cooling rate with pearlite appearance (ºC/s)
0.0 %Ni; 1.0 %Cu, 0.0 %Mo	5.83	5.00
3.0 %Ni; 1.0 %Cu, 0.0 %Mo	1.22	0.75
5.0 %Ni; 1.0 %Cu, 0.0 %Mo	0.60	0.54
3.0 %Ni; 0.0 %Cu, 0.2 %Mo	0.40	0.33

The strong effect of Ni and Mo on the austemperability is observed, which is in good accordance with the literature[143]. Without any addition of these two elements, the CR needed to avoid the pearlitic nose is too high for an air cooling.

This minimum CR must be maintained until the eutectoid transformation temperature is reached. In order to simplify the mathematical concepts, the cooling curves in this temperature interval were considered as straight lines, which is in good agreement with the experimental results as shown in Figure 53. In this plot, the cooling curves representing the minimum CR for which no pearlite was formed are represented for each studied alloy.

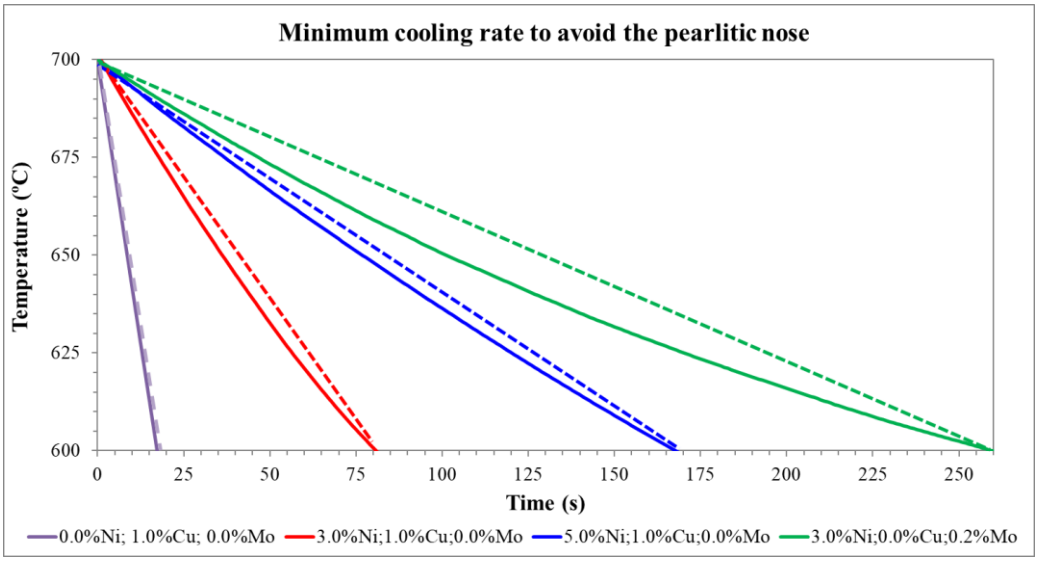

Figure 53. Experimentally obtained minimum CR to avoid the pearlitic nose as a function of the alloy (continuous lines) and the straight line approximation (dotted lines).

The minimum CR to avoid the pearlitic nose as a function of the alloying elements, was related to the CR that presents a certain TM when air cooled. Hence for each alloy can be defined which is the maximum TM that can be engineered cooled considering air cooling to avoid the pearlitic nose and thus to be in conditions to achieve a fully ausferritic microstructure.

To get the relationship between TM and CR for air cooled samples, the data that did not present any eutectoid transformation were considered. As seen in Figure 47, if the eutectoid transformation takes place, then the CR is influenced by the pearlite and/or ferrite formation. On the contrary, as seen in Figure 48, if the eutectoid transformation is avoided, then the CR can be considered as constant in the temperature range between 600-700 ºC (Figure 53).

The evolution of the CR with the TM in these trials is shown in Figure 54.

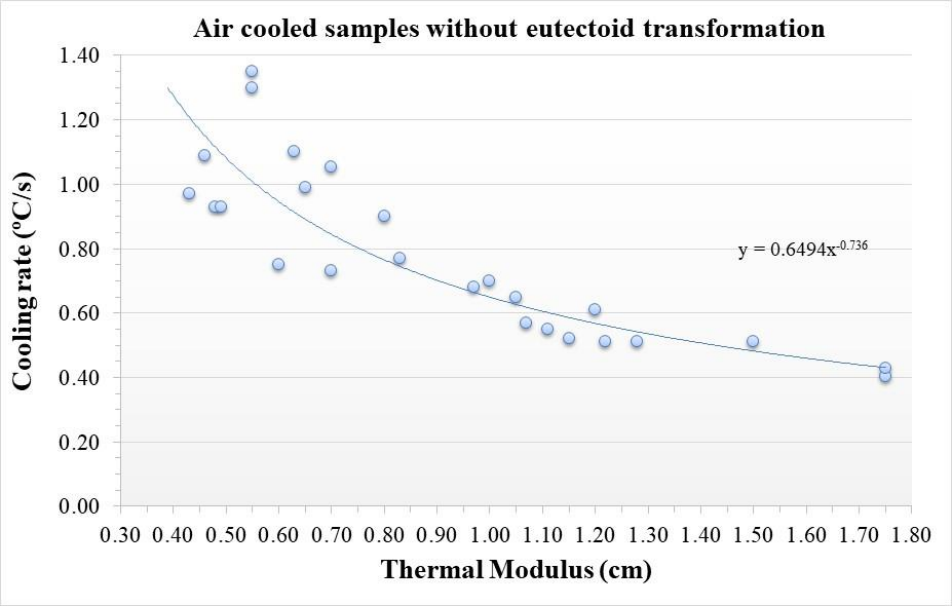

Figure 54. Relationship between the TM and the CR when the castings are air cooled.

With these results, the needed alloy for a given section size or TM can be defined, when the engineered cooling process considers air cooling after the high temperature shakeout. This is performed relating the CR of a given TM for an air-cooling process (Figure 54) to the values shown in Table 13.

Taking into consideration the studied highest TM of 1.75 cm, the CR in the temperature range between 600-700 ºC is of 0.40 ºC/s, so a minimum alloy content of 3.0 % Ni and 0.2 % Mo is needed to avoid the pearlitic nose (Table 13). For this reason, the optimal alloy content to obtain as-cast ausferritic castings considering air cooling and a TM of up to 1.75 cm is the defined in Table 14.

Table 14. Optimal alloy to produce ausferritic as-cast castings of TM up to 1.75 cm considering air cooling (wt.%).

C	Si	Cu	Ni	Mo	Mn
3.60-3.75	2.05-2.15	<0.20	2.90-3.10	0.18-0.22	<0.30

This is the alloy that is going to be considered in the next sections.

6.2. AUSTEMPERING TECHNOLOGY

As for the cooling process, the target during the austempering step on the proposed engineered cooling process, is to perform it as simply as possible and to avoid any energy consumption. To that aim, an insulating material (Table 10 and Figure 38-b) was used in the ausferrite formation temperature range to see if the temperature was maintained constant and this way allow the ausferritic reaction to evolve. In order to see if this technology is adequate, the temperature losses were analysed during the austempering phase. Moreover, the results were compared to an as-cast obtained ausferritic sample, in which the temperature was maintained constant using a heat treatment furnace (Figure 38-a).

On this series of experiments, keel blocks Y2 (as per the standard EN 1563[31]) were poured in order to analyse both the microstructure and the mechanical properties of the material. A type K thermocouple was inserted in the centre of the samples. The mechanical properties were measured as shown in Figure 41 and the microstructure analysed from the tensile test samples.

The targeted chemical composition of this series of experiments is the one defined on the former section of this work (Table 14). The obtained experimental results measured from a coin shape chill sample are shown in Table 15.

Table 15. Chemical composition of the trials analysing the austempering step (wt.%).

C	Si	Cu	Ni	Mo	Mn	Mg	S
3.42-3.62	2.02-2.09	0.12-0.19	2.77-2.92	0.17-0.20	0.17-0.22	0.039-0.051	0.008-0.013

The controlled cooling process was initially performed using a heat treatment furnace. On this case, after the end of solidification, once the samples reached 800 ºC, an early shakeout was applied, followed by air cooling to the isothermal transformation temperature. This temperature was defined in 350 ºC and the heat treatment furnace was heated to that temperature before the introduction of the castings. The samples were introduced in the heat treatment furnace below the eutectoid transformation temperature, but before the transformation temperature, so that the temperature did not drop below the desired temperature. Consequently, the samples were introduced in the heat treatment furnace when they reached the temperature of 550 ºC. The samples were maintained in the heat treatment furnace for 90 minutes and afterwards air cooled. The followed cooling process is shown in Figure 55.

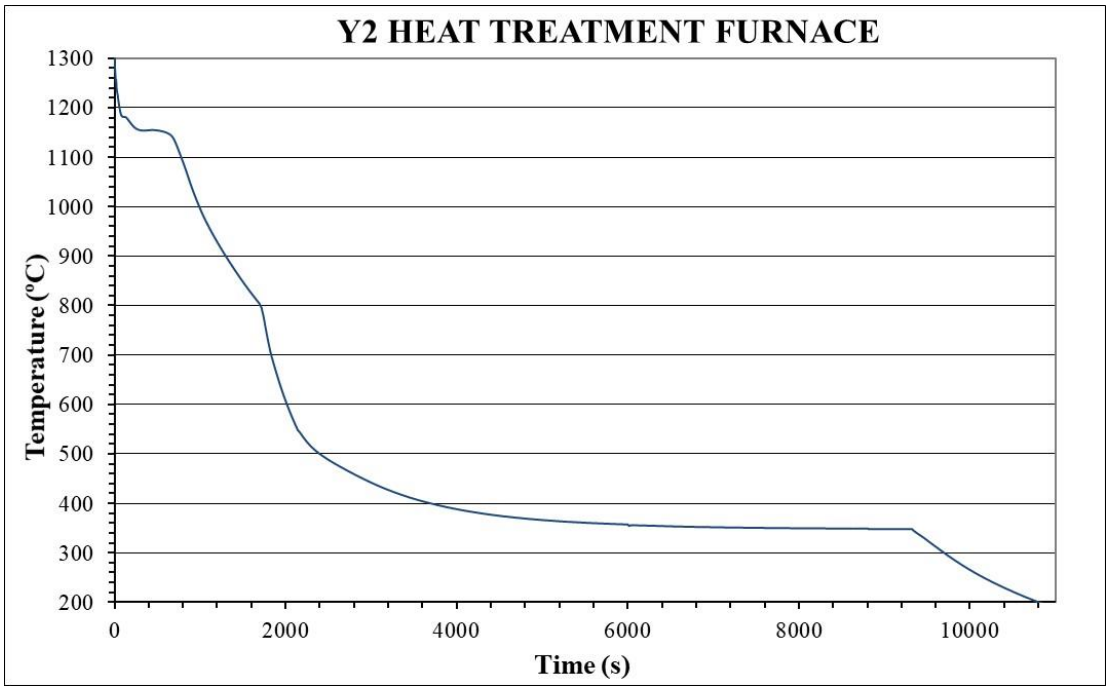

Figure 55. Engineered cooling process of a Y2 block using a heat treatment furnace for the austempering step.

On the other hand, the samples treated using the insulating medium, were also shaken out at the temperature of 800 ºC and then air cooled. The introduction into the insulating medium was carried out when the samples reached the temperature of 500 ºC. The castings were maintained in the insulating medium for 90 minutes and afterwards air cooled to room temperature. The followed cooling process is shown in Figure 56.

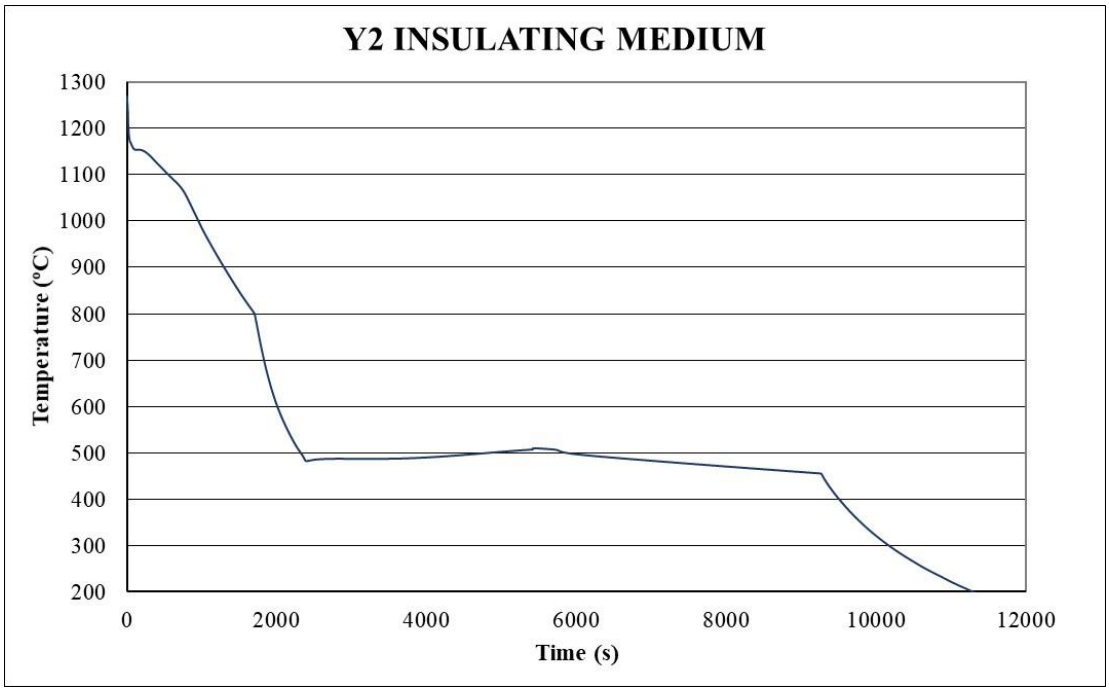

Figure 56. Engineered cooling process of a Y2 block using an insulating material for the austempering step. Introduction at 500 ºC.

The same methodology was followed for both technologies, expecting a temperature drop in the insulating medium. Nevertheless, it is seen, that the temperature is maintained in a very low range (460-505 ºC), and above the ausferrite formation temperature (250-450 ºC).

The mechanical properties of both samples are shown in Table 16.

Table 16. Mechanical properties of the samples treated in the heat treatment furnace and the insulating medium.

Sample	UTS (MPa)	YS (MPa)	E (%)	HBW
Furnace 350 ºC	859	574	16.0	263
Insulating medium 500 ºC	842	564	2.5	302

It is seen that the sample treated in the insulating medium presents a higher hardness, similar resistance, and a lower ductility. The sample treated in the furnace fulfil the requirement of the material EN GJS 800-8 from the standard EN 1564[32]. The sample treated in the insulating medium, however, presents a very low ductility. This is due to the high transformation temperature. In Figure 57 are shown the microstructure of both cases.

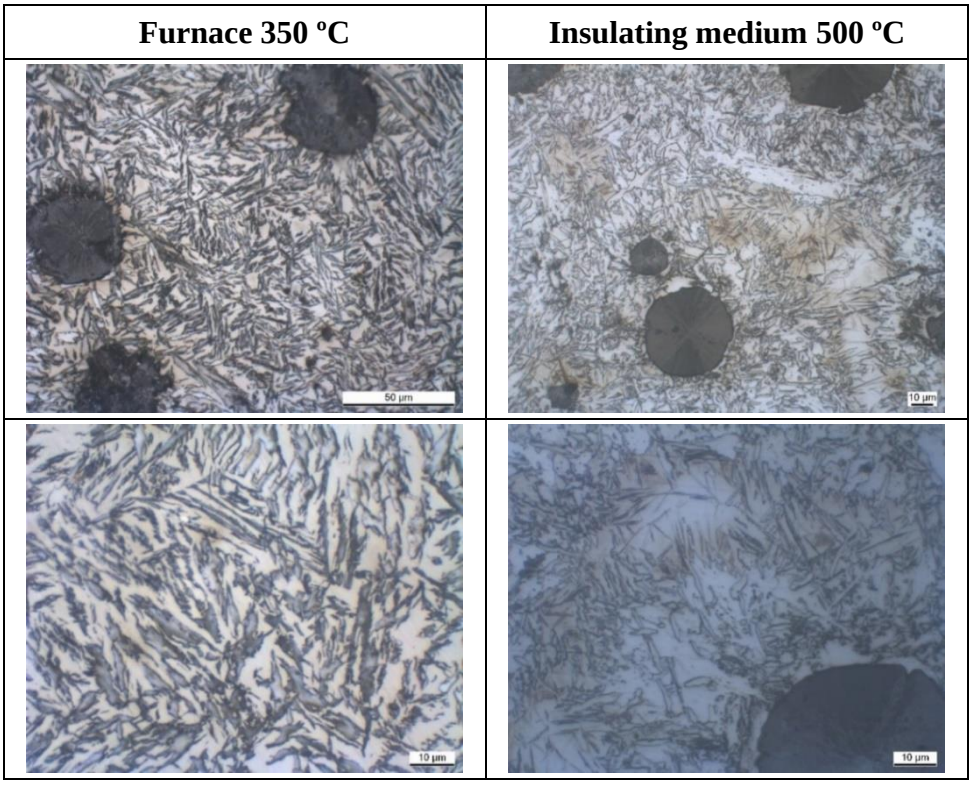

Figure 57. Microstructure of the samples treated in the heat treatment furnace at 350 ºC and in the insulating medium at 500 ºC. 500x on the upper row and 1000x on the lower row.

It is seen that the sample treated in the furnace presents an upper ausferritic microstructure, while the sample treated in the insulating medium, presents high amounts of blocky unreacted austenite. This austenite transforms partially to martensite during the cooling to room temperature, so that on the austenite pools, martensite needles are formed. This could be the reason for the low ductility.

In view of these results and seen that the insulating material is capable of maintaining the temperature constant, another trial was performed, repeating the same methodology but introducing the samples in the insulating medium at lower temperature. The temperatures of 350 and 400 ºC were chosen, so that they could be compared to the samples treated in the furnace. The previous steps were maintained the same, that is, shake out at 800 ºC and air cooling to the chosen transformation temperatures (350 and 400 ºC). The castings were maintained in the insulating medium for 90 minutes and afterwards air cooled to room temperature. The followed cooling process is shown in Figure 58.

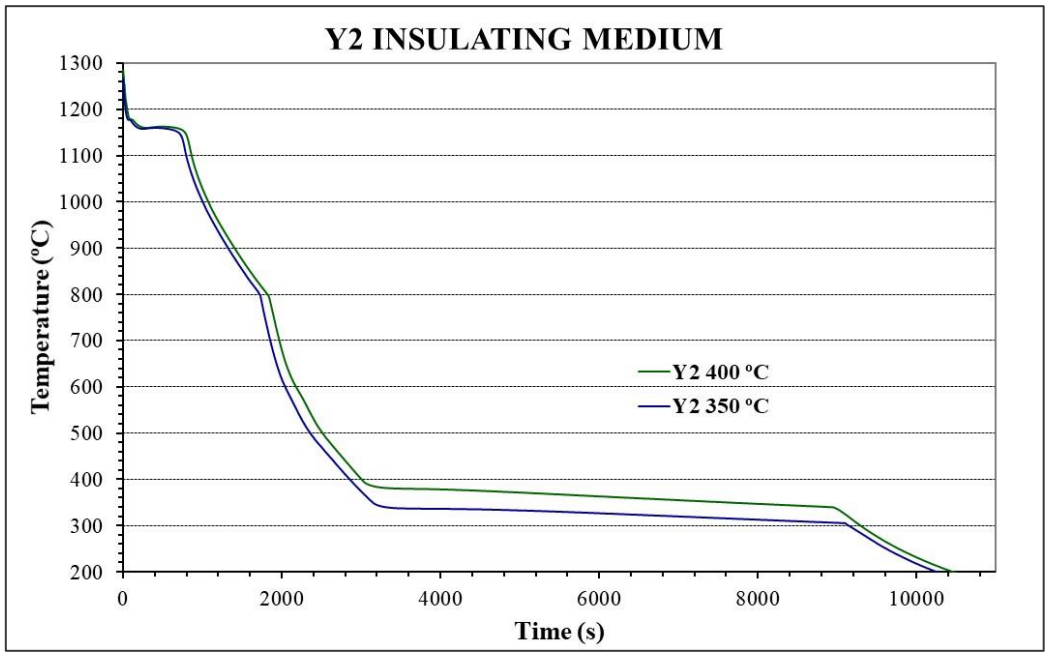

Figure 58. Engineered cooling process of Y2 blocks using an insulating material for the austempering step. Handling at 350 and 400 ºC.

The mechanical properties obtained in both cases are shown in Table 17. The mechanical properties of the sample treated in the furnace are shown for comparative purposes.

Table 17. Mechanical properties of the samples treated in the heat treatment furnace and the insulating medium at 350 and 400 ºC.

Sample	UTS (MPa)	YS (MPa)	E (%)	HBW
Furnace 350 ºC	859	574	16.0	263
Insulating medium 400 ºC	826	571	11.5	275
Insulating medium 350 ºC	911	630	9.4	286

Both samples treated at 350 and 400 ºC fulfil the requirements of the material EN GJS 800-8. Nevertheless, the sample treated at 350 ºC presents a higher hardness and resistance, together with a lower ductility. This is in good agreement with the transformation temperature literature for ADI [116, 124]. The sample treated in the insulating medium at 400 ºC is comparable with the one treated in the furnace, although with less elongation. The sample in the furnace was maintained at a lower temperature (350 ºC), but as it was introduced in the furnace at 550 ºC, during the cooling to 350 ºC, upper ausferrite had time to form, as seen in Figure 57. This could be the reason for the similar properties, despite the different austempering temperatures.

The microstructure of the samples treated in the insulating medium at 350 and 400 ºC is shown in Figure 59.

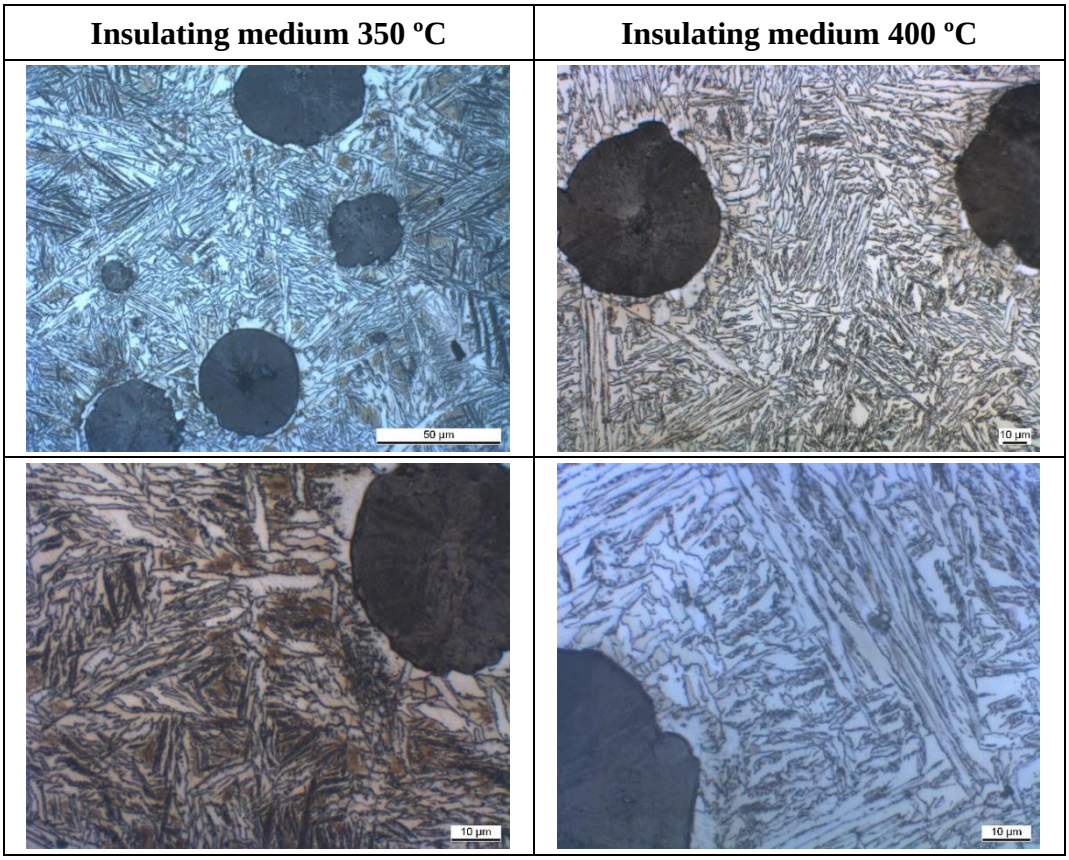

Figure 59. Microstructure of the samples treated in the insulating medium at 350 and 400 ºC. 500x on the upper row and 1000x on the lower row.

It is seen that the sample treated at 400 ºC presents an upper ausferritic microstructure, while the one treated at 350 ºC, presents a mixture of upper acicular ferrite (UAF) and lower acicular ferrite (LAF). UAF is thicker and coarser with a feathery morphology, while LAF is finer and presents a more acicular morphology. This is the reason for the mechanical properties difference, because LAF is stronger, while UAF more ductile[133, 138]. Additionally, the samples treated at a higher temperature present more reacted austenite, which also affects the mechanical properties, increasing the ductility[130].

Based on these results, the insulating medium as a technology to treat the samples during the ausferrite formation is considered feasible. Nevertheless, more trials were performed to see the influence of the temperature loss that takes place while the castings are in the insulating medium. On this case, different holding times and temperatures were used, so that, the influence of the temperature loss in the insulating medium could be studied. The castings were in all cases Y2 blocks.

The followed engineered cooling process was the same as before. The castings were shaken out at the temperature of 800 ºC and air cooled till the transformation temperature. The studied temperatures were 300, 350 and 400 ºC. When those temperatures were reached, the castings were introduced into the insulating material and held there for 30, 60 and 90 minutes. Afterwards they were air cooled to the room temperature. The recorded cooling curves are shown in Figure 60.

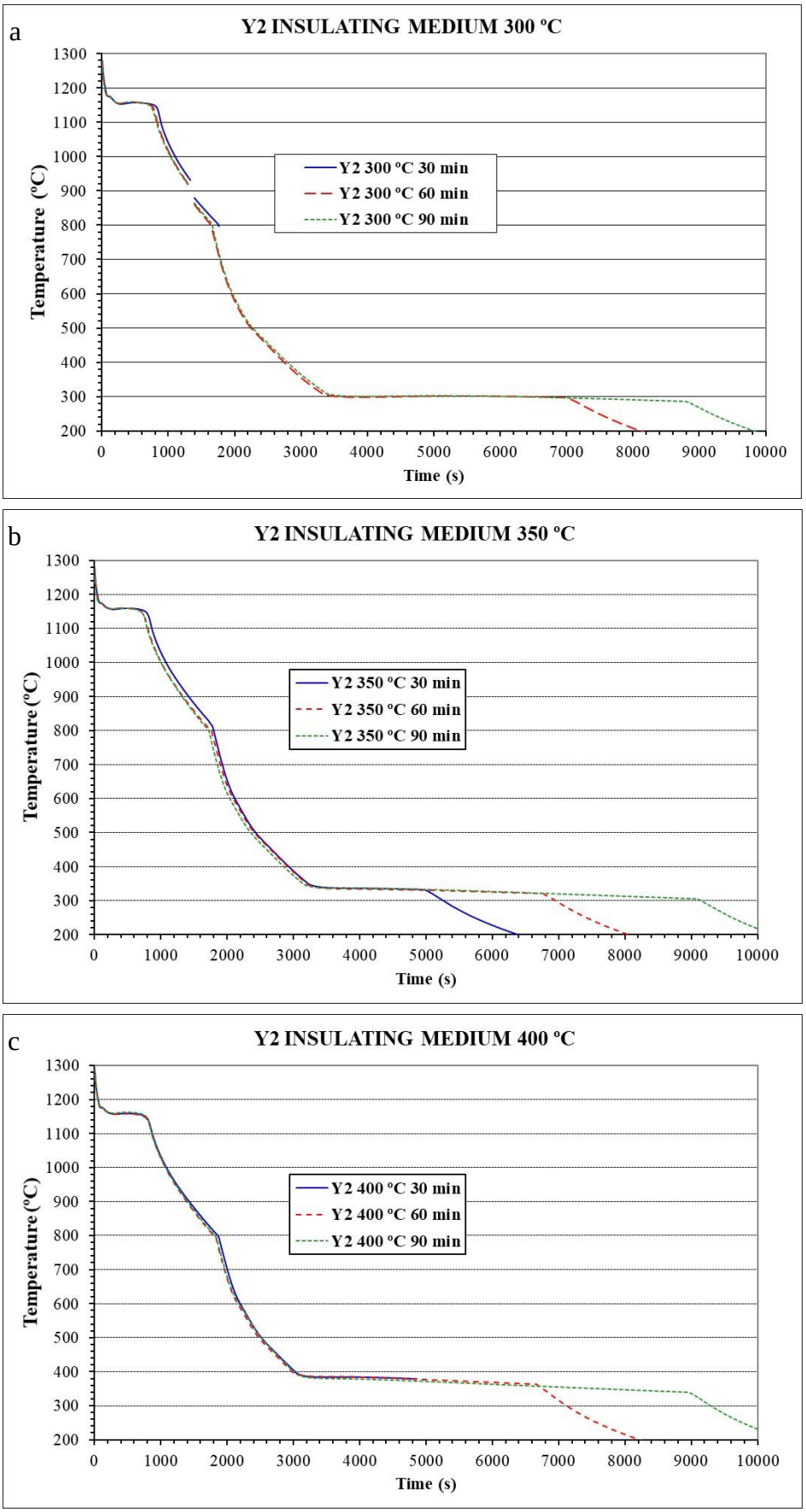

Figure 60. Cooling curves for the different treatment temperatures. a) 300 ºC, b) 350 ºC and c) 400 ºC.

The mechanical properties are shown in Table 18 and Figure 61. The results are presented with respect to the transformation temperature and holding time. The trial of the samples treated at 400 ºC was repeated to have more data.

Table 18. Mechanical properties of the experiments using an insulating medium for the austempering step.

Transformation Temperature (ºC)	Holding time (min.)	UTS. (MPa)	YS (MPa)	E (%)	HBW	Unnotched Charpy (J)
400	30	894	503	8.8	277	68/58/63
400	60	862	552	13.3	268	103/102/103
400	90	864	620	16.9	274	104/107/104
400	30	873	520	8.5	275	59/50/72
400	60	853	548	12.5	262	57/70/49
400	90	826	571	11.5	275	79/96/58
350	30	967	535	7.0	295	58/40/43
350	60	929	551	9.8	285	92/95/60
350	90	911	630	9.4	286	72/105/60
300	30	987	580	8.4	302	52/61/73
300	60	1036	626	9.7	311	88/70/93
300	90	1001	665	8.1	315	68/75/90

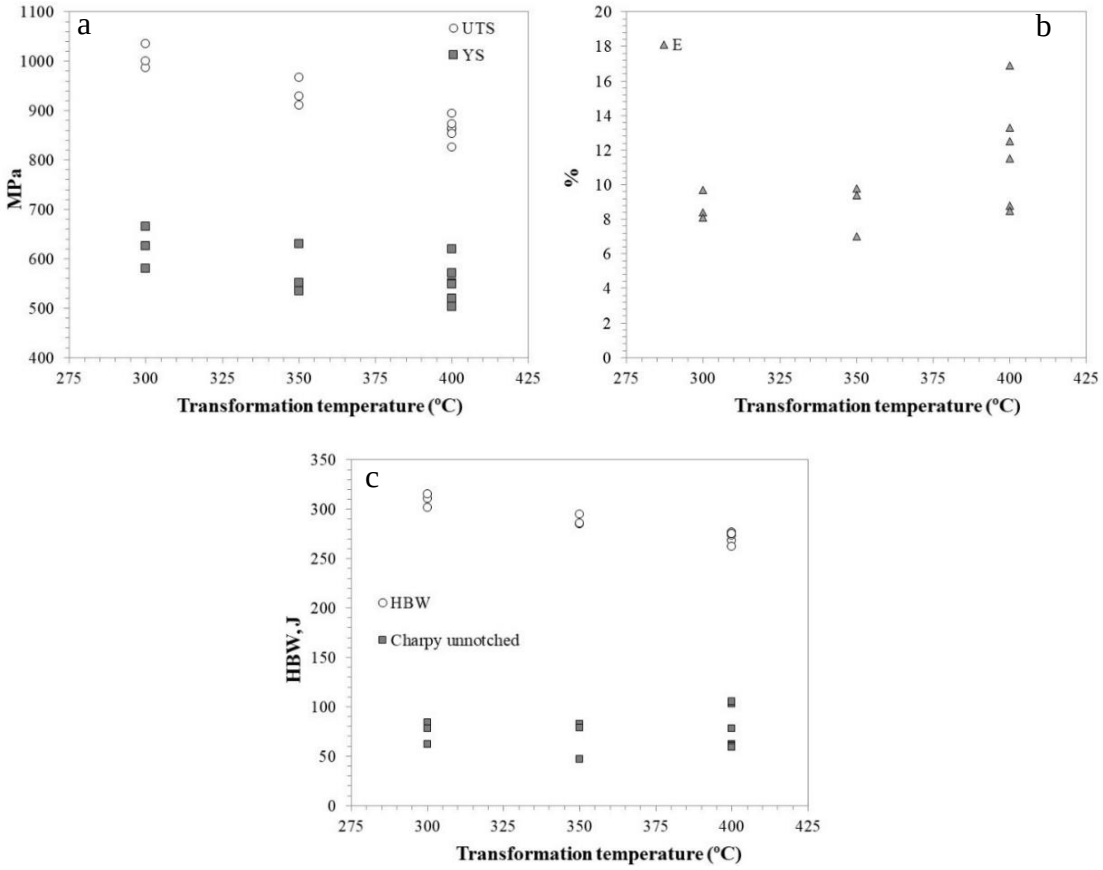

Figure 61. Evolution of the mechanical properties obtained from the Y2 blocks with respect to the transformation temperature. a) UTS and YS, b) E, c) HBW and Charpy unnotched room temperature.

As expected, for the low isothermal transformation temperatures, the strength and hardness are higher, while the elongation and impact resistance decrease[44]. The best strength /elongation ratios were achieved when the ausferritic transformation was carried out at 400 ºC. The mechanical properties of the samples treated at this temperature satisfy the EN 1564[32] standard for the low strength ADI grade (material EN-GJS 800-8).

The result of a metallographic analysis carried out close to the fracture surface of the tensile test samples is shown in Figure 62. When the transformation is performed at 400 ºC the matrix consisted of upper ausferrite. A mixture of LAF and UAF for the case of the transformation at 300 ºC. The samples maintained at a temperature of 350 ºC exhibited also a mixed microstructure of UAF and LAF, but more UAF than the samples treated at 300 ºC. The analysis of the phases as a function of the transformation temperature and holding time is deeper studied in the section "6.4. Kinetics of the ausferritic transformation".

Around 15 % of martensite is present in the samples treated for 30 minutes, which indicates that the ausferritic reaction has evolved to a large extent but was not complete. For longer holding times, the martensite apparition is reduced to 10 % at 60 minutes and 5 % at 90 minutes. The M evolution is shown later in Figure 65.

The evolution of the mechanical properties and the microstructure with the transformation temperature go hand in hand, since the lower ausferrite presents a higher resistance, but lower ductility than the upper ausferrite.

No pearlite was found in any of the samples. A small amount of ferrite was found around most of the graphite nodules. Because of the slower cooling rate as compared to those typical for the conventional austempering heat treatment where the samples are cooled in a salt bath, the carbon dissolved in the austenite surrounding the nodules has time to diffuse from the matrix to the graphite. Thus, the carbon content in the austenite decreases and ferrite halos are formed around the nodules. The presence of ferrite enhances the ductility of the material and decreases the resistance[178]. Nevertheless, the ferrite content is very small so as to influence the mechanical properties, as seen in Table 18 and Figure 61.

Transformation temperature (ºC)		
300	**350**	**400**
30 minutes	**30 minutes**	**30 minutes**
	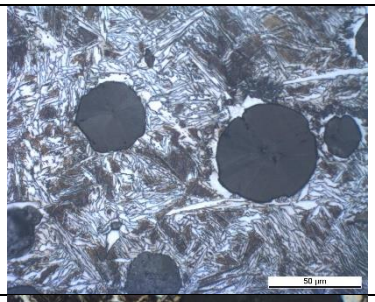	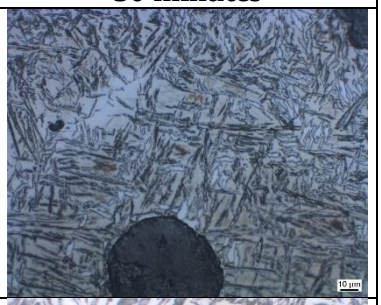
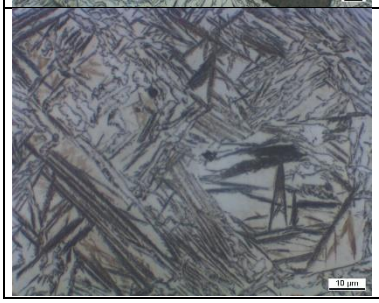	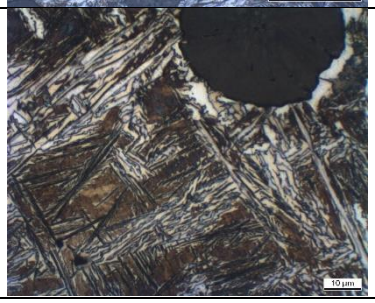	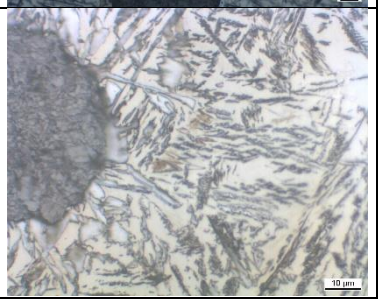

Figure 62. Micrographs for the different transformation temperatures and different holding times. 500x on the upper row and 1000x on the lower row.

Transformation temperature (ºC)		
300	**350**	**400**
60 minutes	**60 minutes**	**60 minutes**
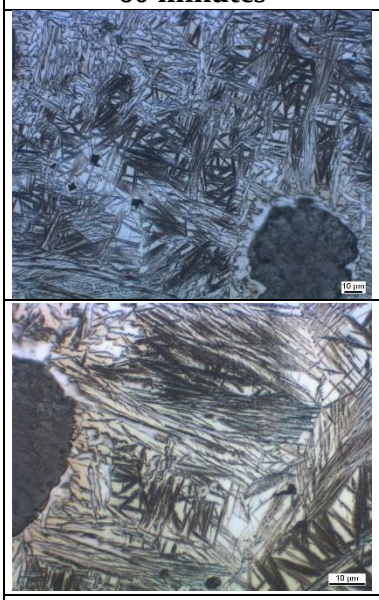	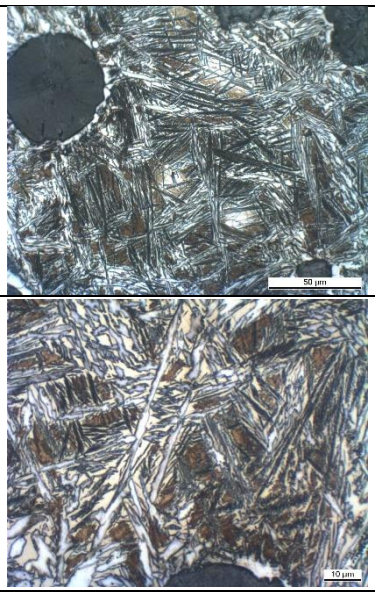	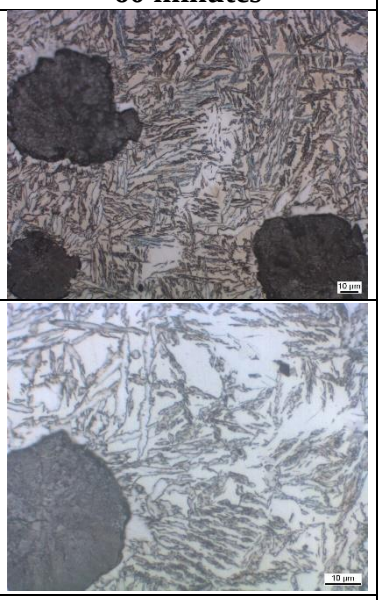
Transformation temperature (ºC)		
300	**350**	**400**
90 minutes	**90 minutes**	**90 minutes**
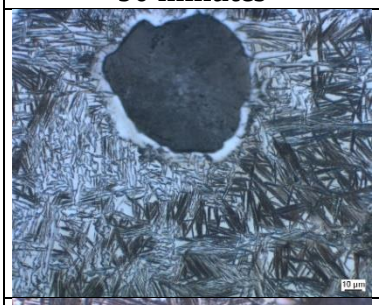	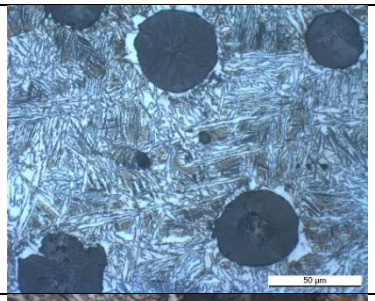	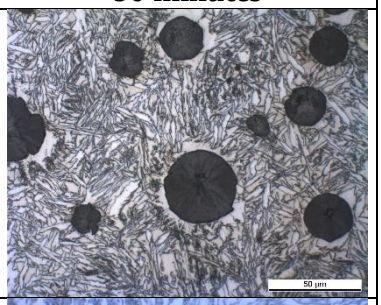
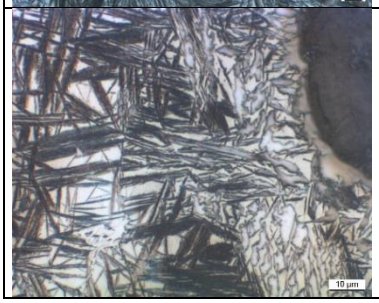	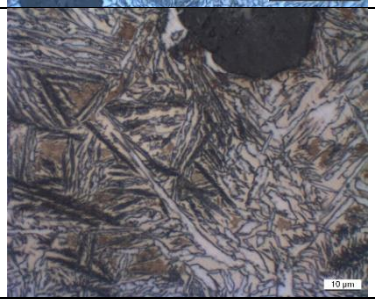	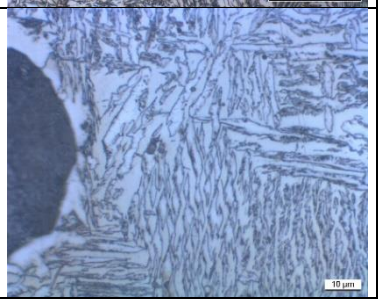

Figure 62 (Cont.) Micrographs for the different transformation temperatures and different holding times. 500x on the upper row and 1000x on the lower row.

As seen in Figure 56, Figure 58 and Figure 60, some temperature drop occurs during the transformation period, as the insulating material cannot completely prevent some heat loss.

As a consequence, some variations in the mechanical properties are expected. However, as can be seen in Figure 63, despite a temperature decrease of up to 60 ºC, no significant changes on the mechanical properties took place. The results are shown for the different austempering temperatures. It is seen that the transformation temperature has a stronger effect on the mechanical properties than the temperature loss.

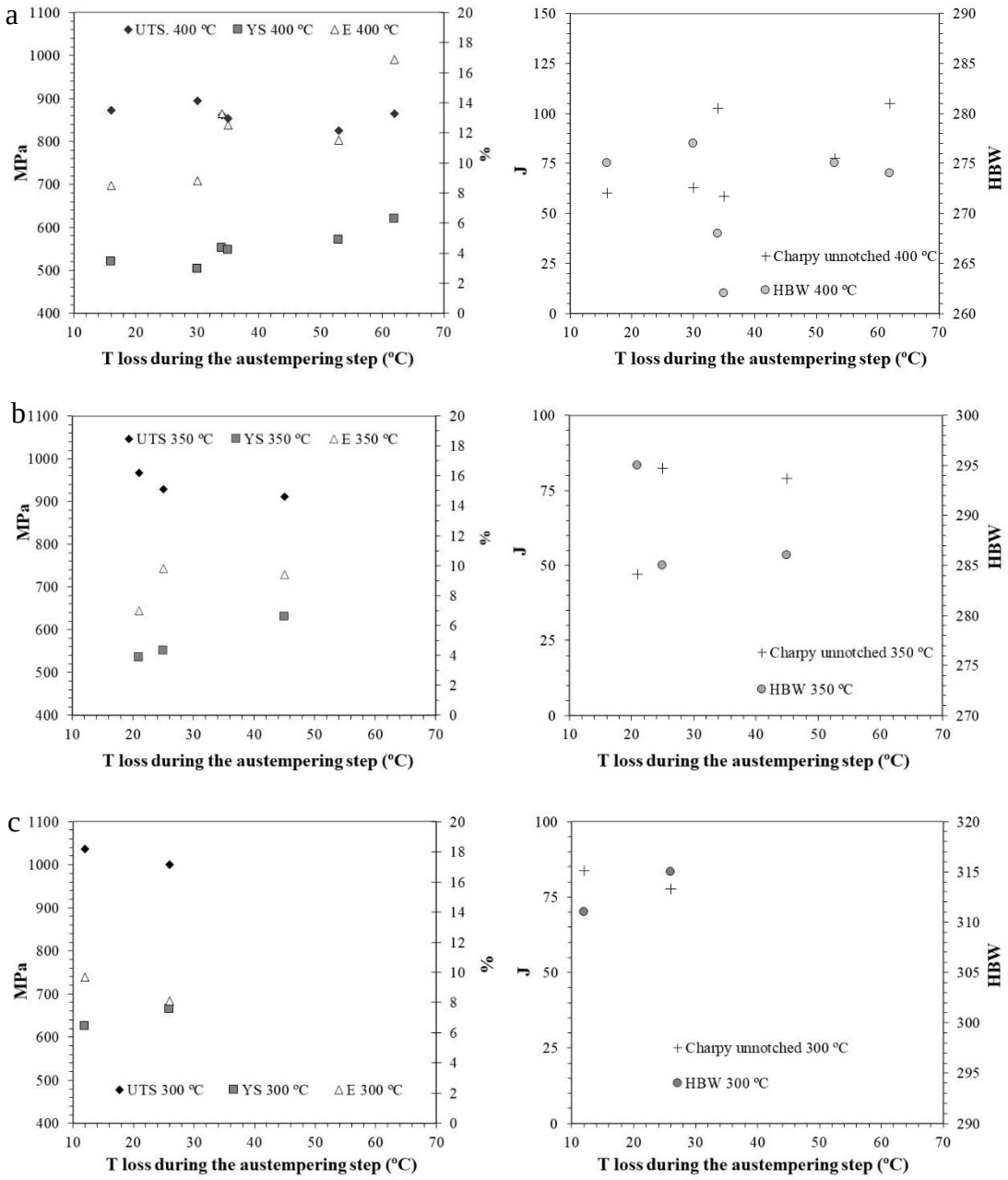

Figure 63. Evolution of the mechanical properties with the temperature loss during the austempering step in the insulating medium. a) 400 ºC, b) 350 ºC, c) 300 ºC.

The temperature loss increases as it does the holding time into the insulating material. For this reason, three different holding times were studied: 30, 60 and 90 minutes. Figure 64 presents the relationship between the mechanical properties and the holding time for each transformation temperature. It is seen that the UTS decreases when the holding time is increased, while the E and the YS increase. There is no clear relationship between the impact resistance and the holding time into the insulating medium. The hardness is maintained constant. This is in good agreement with the literature of conventional ADI, when the reaction has evolved to some rate, as it is the case (Figure 62)[140].

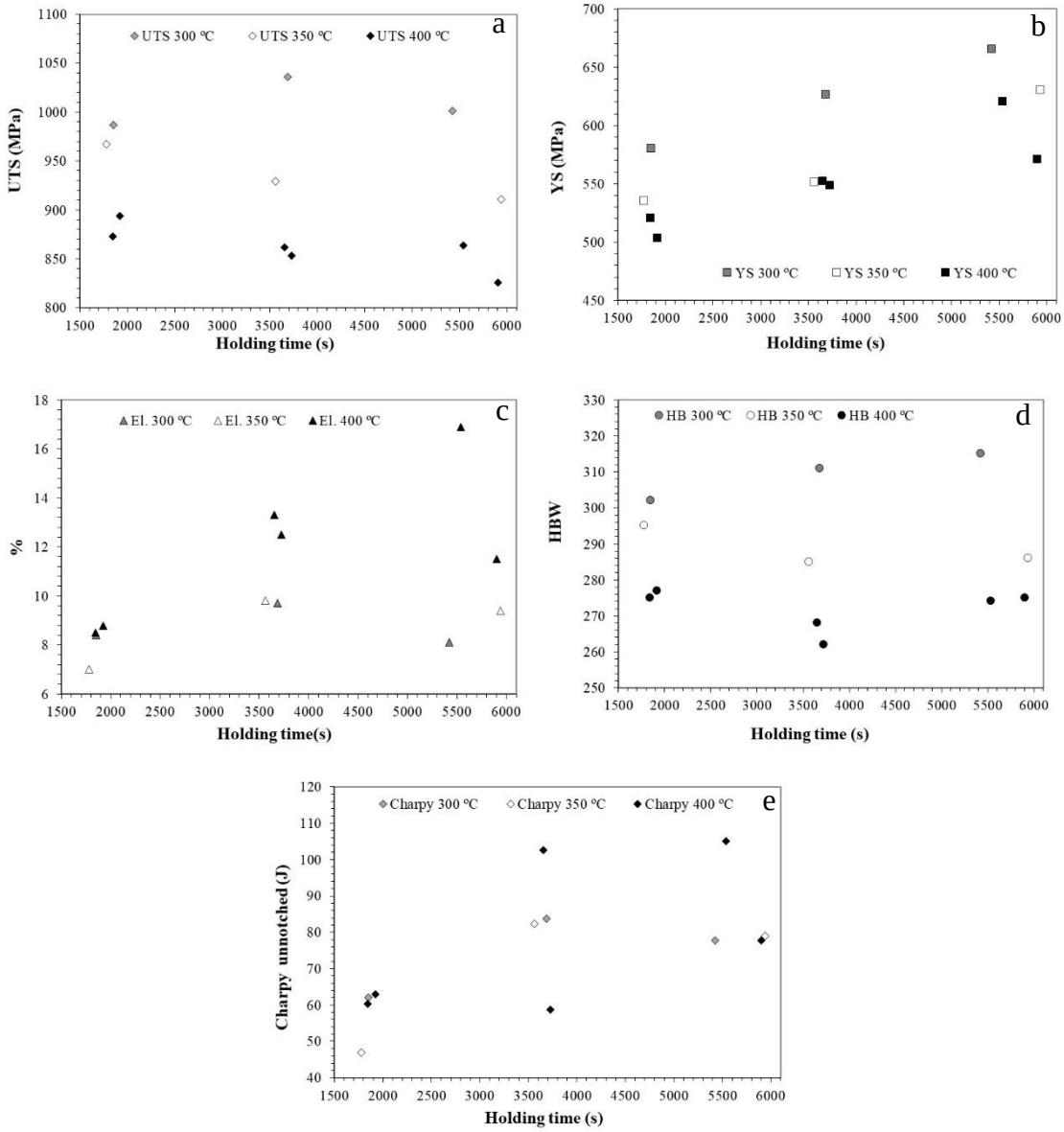

Figure 64. Evolution of the mechanical properties with the holding time into the insulating medium. a) UTS, b) YS, c) E, d) HBW, e) Charpy unnotched.

However, any influence of the temperature loss is not observed since the variation of the mechanical properties as a function of the holding time into the insulating medium could be explained through the microstructure evolution. The ausferrite formation starts with the nucleation of acicular ferrite (AF). The carbon that cannot be dissolved in the AF is partitioned into the austenite parent phase. Thus, the carbon content of the austenite increases, stabilising this phase and lowering the martensite formation start temperature (M_S) below room temperature. This fact prevents the formation of martensite during the last cooling to room temperature after the holding time into the insulating material. Martensite is a very hard phase that lowers drastically the ductility of the material. The ausferrite formation and consequently the absence of martensite, is a process that needs time to be carried out. As seen in Figure 62, on the studied samples, the holding time is not strongly affecting the mechanical properties, because after 30 minutes there is already a good part of the ausferritic reaction evolved.

Figure 65 shows the change in the amount of martensite as a function of the holding time into the insulating medium.

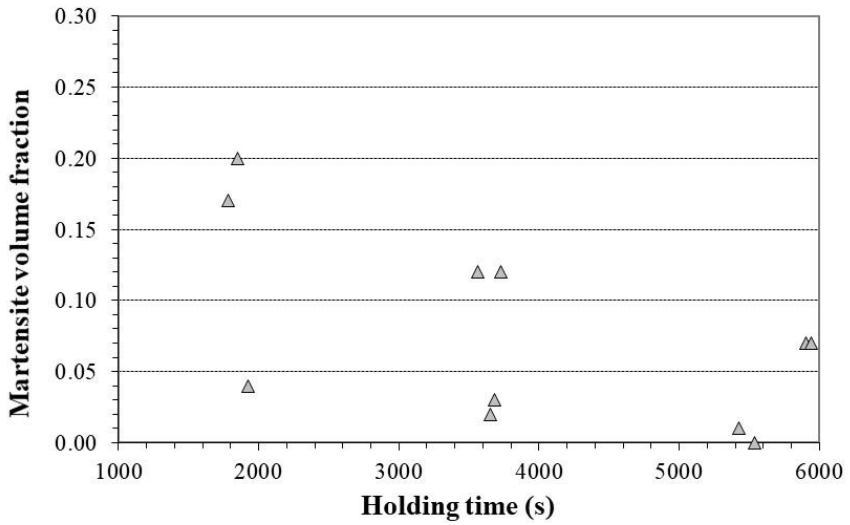

Figure 65. Martensite formation with the holding time in the insulating medium.

The amount of martensite decreases when increasing the holding time. The ausferrite formation kinetics are deeply studied in the section "6.4. Kinetics of the ausferritic transformation". Nevertheless, these results show that both the austempering temperature and holding time influence the final microstructure and consequently the mechanical properties. The effect seen on these experiment series could be related to these variables more than to the temperature loss in the insulating medium. Thus, the substitution of the furnace by an insulating medium seems to have little effect on the robustness of the process.

6.3. HIGH TEMPERATURE SHAKEOUT DEFINITION

Having defined the optimal alloy content to avoid pearlite formation considering air cooling, and the optimal technology to perform the austempering process, with no added energy consumption; on this section, the effect of the shakeout temperature is studied. On this case, the shakeout is carried out by mechanical means. All the cases were treated the same way. The target is to define which is the optimal shakeout temperature.

A series of experiments was performed using keel blocks Y2 (as per the standard EN 1563[31]). A type K thermocouple was inserted in the centre of the samples to record their cooling process. The mechanical properties of the material were measured as shown in Figure 41.

The targeted chemical composition of these series of experiments is the one defined on the former section of this work (Table 14). The obtained experimental results from a coin shape chill sample are shown in Table 19.

Table 19. Chemical composition of the trials analysing the shakeout step (wt.%).

C	Si	Cu	Ni	Mo	Mn	Mg	S
3.53-3.58	2.06-2.07	0.13-0.16	2.84-2.92	0.18-0.21	0.17-0.19	0.046-0.047	0.008-0.009

In order to analyse the effect of the shakeout temperature, the samples on this experiment series were shaken out at the temperatures of 1000 and 900 ºC and then introduced into the previously described insulating material (Table 10 and Figure 38-b) till they reached the temperature of 800 ºC. The aim of this step is to get an austenitic microstructure with a homogeneous carbon distribution trying to avoid the effect of the different solidification times.

When the samples were extracted from the insulating material at the temperature of 800 ºC, they were air cooled till the austempering temperature. The transformation temperature was defined at 350 and 400 ºC. The holding time was 30, 60 and 90 minutes. The austempering step was maintained as on the experiment series described on the former section, to be able to compare the results obtained on these trials to the ones described on the former section (6.2. Austempering technology).

An example of a sample shaken out at the temperature of 900 and another at 1000 ºC is shown in Figure 66.

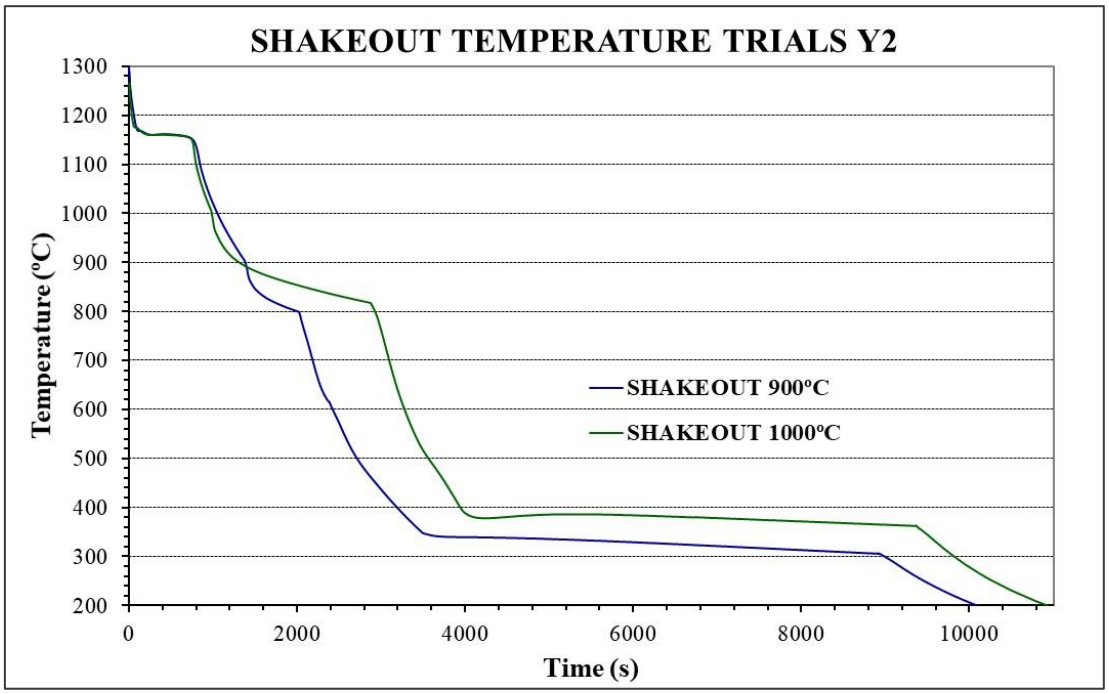

Figure 66. Engineered cooling process of Y2 blocks shaken out at 900 and 1000 ºC.

It is seen that when the samples are introduced at the shakeout temperature in the insulating medium, the insulating effect is lower than at the austempering temperature (Figure 58 and Figure 60), and consequently the temperature loss is higher and at a higher rate than at the ausferrite formation temperature range. This effect is linked to the higher temperature of the shakeout process.

The mechanical properties obtained in these experiments are shown in Table 20. The results are presented considering the shakeout temperature and the transformation temperature and holding time on the austempering step.

Table 20. Mechanical properties of the experiments using different shake out temperatures.

Shakeout temperature (ºC)	Transformation Temperature (ºC)	Holding time (min.)	UTS. (MPa)	YS (MPa)	E (%)	HBW
900	400	30	820	522	12.0	260
900	400	60	804	537	11.0	253
900	400	90	827	524	7.4	266
900	350	30	852	562	9.4	272
900	350	60	802	628	4.6	266
900	350	90	818	583	11.0	280
1000	400	30	743	545	4.4	278
1000	400	60	776	592	8.9	272
1000	400	90	812	569	12.0	268

It is seen that the samples shaken out at 900 ºC, satisfy the requirements of the material EN GJS 800-8[32], except the elongation of the samples treated at 400 ºC for 90 minutes and at 350 ºC for 60 minutes. The samples shaken out at 1000 ºC, present lower resistance and ductility than expected, even though, the sample treated for 90 minute fulfils the standard of the EN GJS 800-8 material.

The micrographs of these samples are shown in Figure 67.

Considering the castings shaken out at 900 ºC, the sample treated at 350 ºC for 60 minutes presents around 15 % of pearlite. This can be the reason for the low elongation that it presents. The pearlite apparition could be consequence of the cooling rate stop after the shakeout. As the samples are introduced after the shakeout into the insulating medium, when they are taken out, even though the castings are extracted at the temperature of 800 ºC, there is not enough time for the cooling rate to reach the limiting 0.40 ºC/s (Table 13) to avoid the pearlitic nose for the present alloy.

Regarding the samples shaken out at 1000 ºC, the sample treated at 400 ºC for 30 presents a nodularity of 60 %. The rest 40 % is Chunky graphite. This could be the origin of its low resistance and elongation since this graphite degeneration negatively affects the mechanical properties[74]. All the other samples present a nodularity ≥ 90 %.

Shakeout temperature 900 ºC	
Transformation temperature 350 ºC	**Transformation temperature 400 ºC**
30 minutes	**30 minutes**
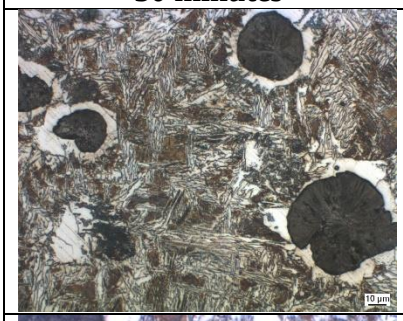	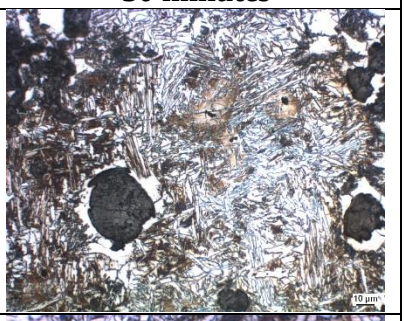
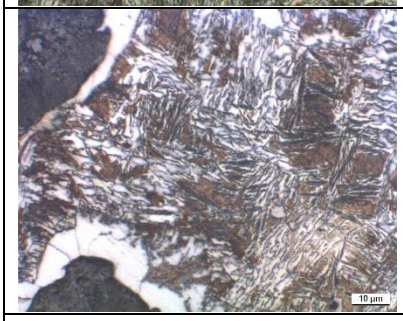	
Transformation temperature 350 ºC	**Transformation temperature 400 ºC**
60 minutes	**60 minutes**
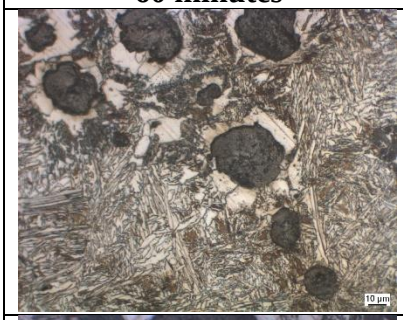	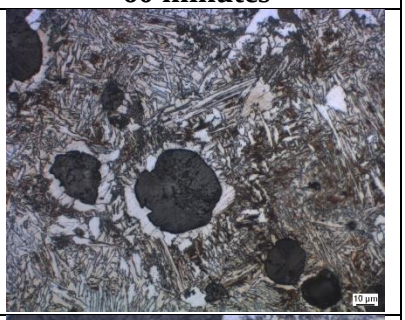
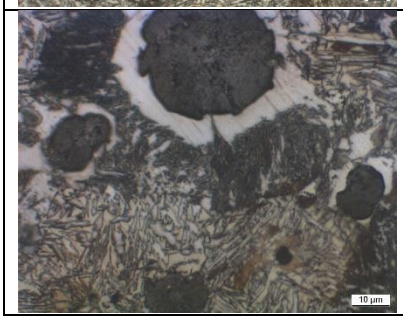	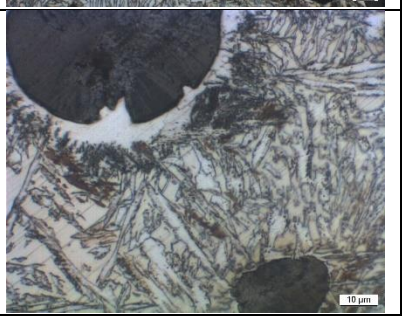

Figure 67. Micrographs for the different shake out temperature, transformation temperatures and different holding times. 500x on the upper row and 1000x on the lower row.

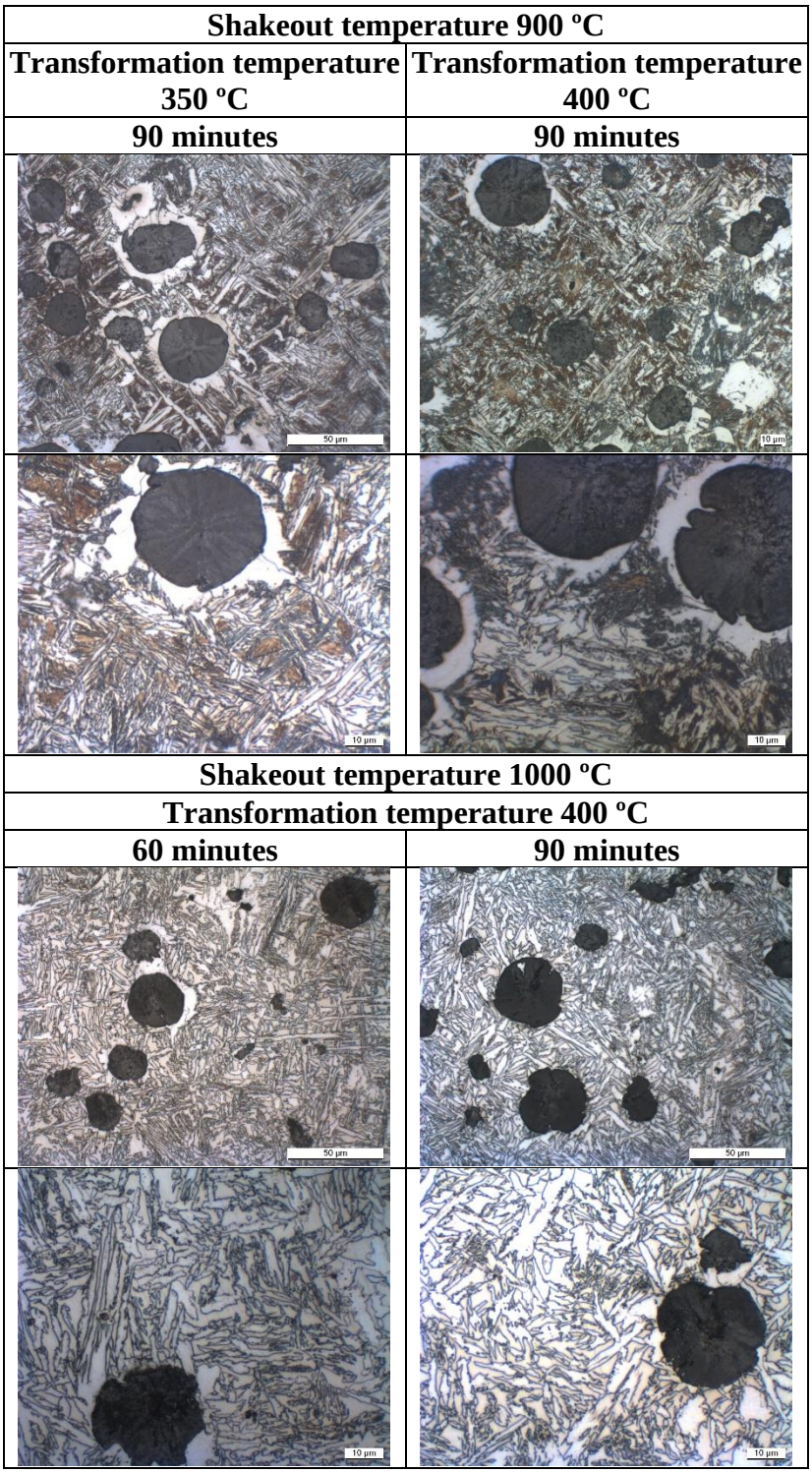

Figure 67. (Cont.) Micrographs for the different shake out temperature, transformation temperatures and different holding times. 500x on the upper row and 1000x on the lower row.

These results are compared in Figure 68, to the ones obtained on the former section (6.2. Austempering technology). The data are contrasted based on the transformation temperature, because it was seen that this is the main parameter that influences the mechanical properties for holding times equal or higher than 30 minutes, since the ausferritic reaction has had time to partially evolve.

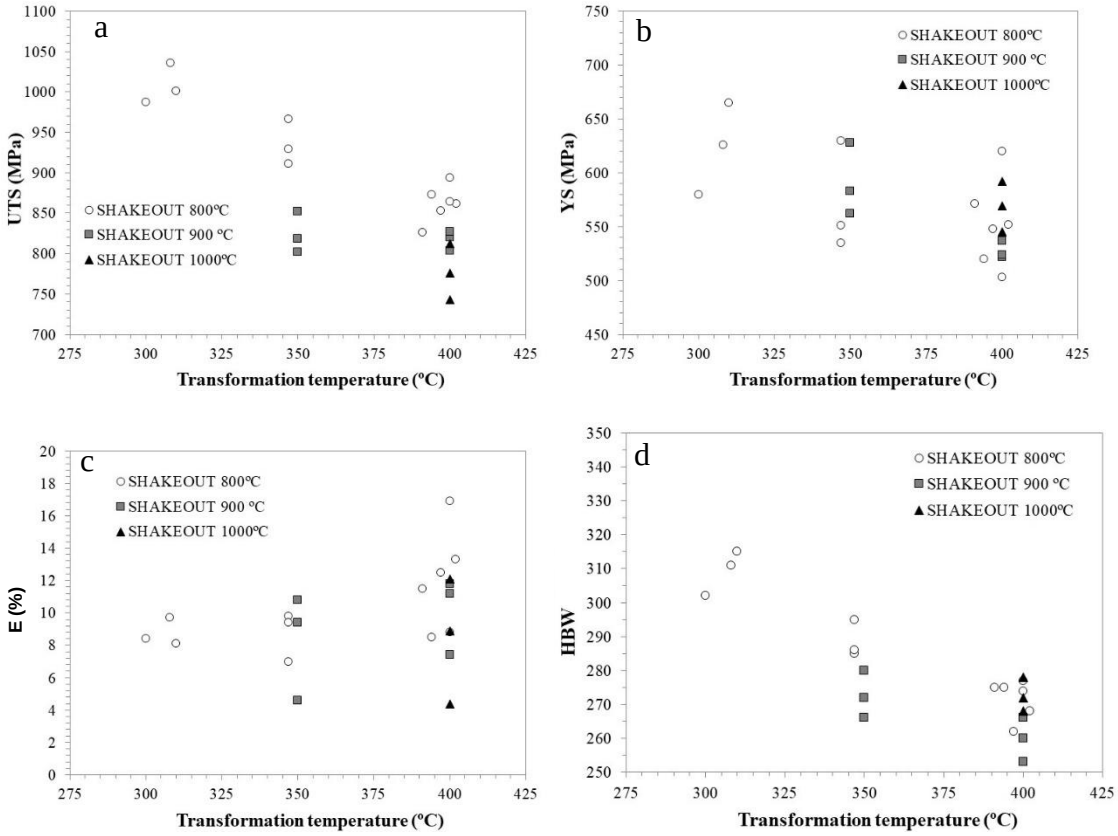

Figure 68. Evolution of the mechanical properties with the transformation temperature for different shakeout temperatures. a) UTS, b) YS, c) E, d) HBW.

It is observed that, the same as happened when the temperature loss in the insulating medium was studied, the main parameter that affects the mechanical properties is the transformation temperature. Independent of the shakeout temperature, the tendency is the same. When the transformation temperature increases, the UTS, YS and HBW decrease, while E increases, which is in good agreement with the literature for conventional ADI[130].

Based on these results and considering the fact that the latest the shakeout process is carried out, the longer the time to face it after pouring, which makes easier the application of this technology to an industrial process, the optimal shakeout temperature is defined at 800 ºC.

6.4. KINETICS OF THE AUSFERRITIC TRANSFORMATION

Once the technology to obtain an as-cast ausferritic microstructure was defined in the former sections (alloy content definition and shakeout and austempering parameters), in this section, the evolution of the ausferrite formation is studied. The target is, for different austempering temperatures, to define the kinetics of the ausferritic transformation by changing the holding time during the austempering step and this way, define the processing window for the ausferrite formation.

The experimental study was made following the premises defined in the previous sections and Y1, Y2 and Y3 blocks as per the standard EN 1563[31] were used together with TA samples and dilatometry samples (DIL) machined from the Y2 blocks. The idea is, using different section sizes, to have different thermal moduli (TM) represented and this way study if this parameter presents an influence on the ausferrite formation. The TM of these samples are shown in Table 9.

The targeted chemical composition is the one defined in Table 14. The experimental chemical composition obtained from a coin shape chill sample on the different trials is shown in Table 21.

Table 21. Chemical composition ranges considering the different trials to define the kinetics of the ausferritic transformation (wt.%).

C	Si	Cu	Ni	Mo	Mn	Mg	S
3.46-3.61	2.00-2.13	<0.06	2.81-3.05	0.19-0.20	0.13-0.21	0.042-0.059	0.005-0.010

The followed engineered cooling process is next explained and an example of the cooling curves for the different TM appears in Figure 69. As defined in the former sections, the cooling was performed on air, and the isothermal arrest carried out introducing the samples on a reusable insulating material.

After the solidification, early shake out was carried out at 800 ºC, as defined in the former section (6.3. High temperature shakeout definition). Afterwards, air cooling was applied till the isothermal temperature, so that the pearlitic nose was avoided. Two different austempering temperatures were tested: 300 and 400 °C. At those temperatures, the castings were introduced into a container containing an insulating material (Table 10 and Figure 38-b) with the aim of maintaining the temperature constant, so that the ausferritic reaction can occur. Different holding times were used: 10, 20, 30, 50, 60, 75, 90 and 180 minutes to evaluate the evolution of the transformation with the time. Finally, the samples were water quenched to room temperature.

Additionally, interrupted cooling experiments were performed with the Y1 and Y2 blocks following the same cooling process but quenching the samples in water once reached the temperatures: 550, 525, 500, 450, 400 and 300 °C. Y3 and TA samples were also quenched at the temperature of 400 and 300 ºC.

In the case of the dilatometry tests, the next thermal evolution was followed: heat up at 20 °C/min rate, an austenitizing step at 900 °C for 40 minutes, afterwards air cooled till the austempering temperature (300 and 400 ºC) and there maintained during 1, 2, 5, 10, 15, 20, 30, 50 and 180 minutes. Finally, air cooled to room temperature. On this case, due to the impossibility of performing an as-cast cycle, the air cooling was maintained in order to obtain equivalent cooling rates than for the Y blocks and the TA.

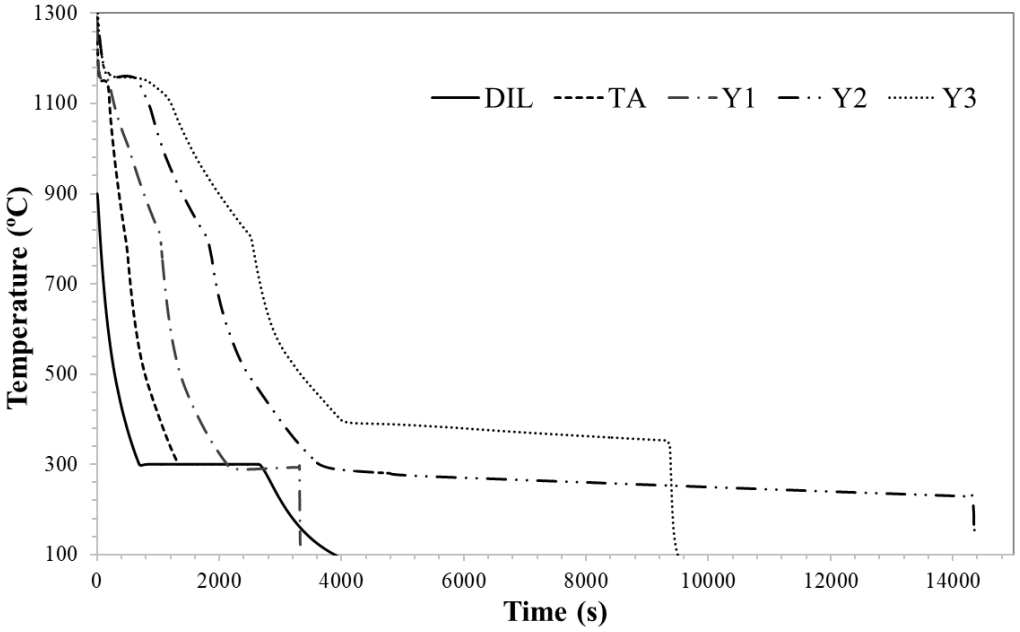

Figure 69. Thermal evolution of the controlled cooling process for the different castings.

The ausferrite formation kinetics were evaluated on the one hand, metallographically defining the phases that are present after the different controlled cooling processes and on the other hand, performing a tensile test and a hardness test. First, the microstructure development is described and afterwards, the evolution of the mechanical properties.

In Table 22 are shown the numerical results of all the samples studied on this series of experiments. TA and DIL samples have not mechanical properties values, because their target was only to define the microstructure evolution. Moreover, at 300 ºC, no Y3 and TA were poured, and the evaluation was made using Y1 and Y2 samples for the mechanical properties and those samples and DIL for the microstructure development.

Table 22. Microstructure and mechanical properties of all the studied samples.

Sample	Transformation Temperature (ºC)	Holding time (min)	UAF fraction	LAF fraction	Total AF	M fraction	UTS (MPa)	YS (MPa)	E (%)	HBW
TA	550	0	0.00	0.00	0.00	0.85	--	--	--	--
Y2	550	0	0.00	0.00	0.00	0.88	502*	--	--	587
TA	525	0	0.03	0.00	0.03	0.82	--	--	--	
Y1	525	0	0.05	0.00	0.05	0.84	698*	678	0.5	547
Y2	525	0	0.05	0.00	0.05	0.83	680*	--	--	569
Y1	500	0	0.13	0.00	0.13	0.63	856	642	1.0	448
Y2	500	0	0.17	0.00	0.17	0.58	672	619	0.3	440
Y2	450	0	0.17	0.00	0.17	0.48	823	570	0.8	383
TA	435	0	0.20	0.00	0.20	0.51	--	--	--	--

* Too brittle material.

Table 22 (Cont.). Microstructure and mechanical properties of all the studied samples.

Sample	Transformation Temperature (ºC)	Holding time (min)	UAF fraction	LAF fraction	Total AF	M fraction	UTS (MPa)	YS (MPa)	E (%)	HBW
TA	400	0	0.23	0.00	0.23	0.47	--	--	--	--
Y1	400	0	0.22	0.00	0.22	0.45	918	572	1.5	347
Y2	400	0	0.26	0.00	0.26	0.42	904	523	2.1	339
Y3	400	0	0.30	0.00	0.30	0.37	898	494	2.0	337
TA	300	0	0.29	0.00	0.29	0.38	--	--	--	--
Y1	300	0	0.26	0.01	0.28	0.41	786	594	0.8	378
Y2	300	0	0.30	0.03	0.33	0.32	956	513	4.1	319
Y3	300	0	0.32	0.02	0.34	0.34	940	485	4.7	311
DIL	400	1	0.18	0.00	0.18	0.40	--	--	--	--
DIL	400	2	0.25	0.00	0.25	0.35	--	--	--	--
DIL	400	5	0.28	0.00	0.28	0.51	--	--	--	--
Y2	400	5	0.33	0.00	0.33	0.32	937	505	3.9	328
DIL	400	10	0.25	0.00	0.25	0.38	--	--	--	--
TA	400	10	0.27	0.00	0.27	0.37	--	--	--	--
Y1	400	10	0.32	0.00	0.32	0.29	1004	543	5.6	311
Y3	400	10	0.39	0.00	0.39	0.26	950	488	4.9	300
Y2	400	10	0.33	0.00	0.33	0.31	964	513	5.7	301
DIL	400	15	0.36	0.00	0.36	0.23	--	--	--	--
DIL	400	20	0.44	0.00	0.44	0.18	--	--	--	--
TA	400	20	0.38	0.00	0.38	0.20	--	--	--	--
Y1	400	20	0.41	0.00	0.41	0.21	999	557	9.9	291
Y2	400	20	0.35	0.00	0.35	0.26	947	505	7.5	279
Y3	400	20	0.33	0.00	0.33	0.20	914	473	6.8	287
DIL	400	30	0.48	0.00	0.48	0.04	--	--	--	--
TA	400	30	0.43	0.00	0.43	0.08	--	--	--	--
Y1	400	30	0.46	0.00	0.46	0.14	939	551	11.8	283
Y2	400	30	0.51	0.00	0.51	0.09	896	505	9.0	275
Y3	400	30	0.43	0.00	0.43	0.20	860	499	9.1	272
DIL	400	50	0.55	0.00	0.55	0.02	--	--	--	--
TA	400	50	0.47	0.00	0.47	0.03	--	--	--	--
Y1	400	50	0.52	0.00	0.52	0.08	915	606	14.5	282
Y2	400	50	0.48	0.00	0.48	0.07	871	550	9.1	273
Y3	400	50	0.45	0.00	0.45	0.09	852	515	9.6	272
TA	400	60	0.50	0.00	0.50	0.03	--	--	--	--
Y1	400	60	0.53	0.00	0.53	0.07	884	611	14.7	272
Y2	400	60	0.53	0.00	0.53	0.03	865	550	12.9	267
Y3	400	60	0.51	0.00	0.51	0.05	841	553	11.7	266

Table 22 (Cont.). Microstructure and mechanical properties of all the studied samples.

Sample	Transformation Temperature (ºC)	Holding time (min)	UAF fraction	LAF fraction	Total AF	M fraction	UTS (MPa)	YS (MPa)	E (%)	HBW
Y1	400	75	0.55	0.00	0.55	0.03	894	608	15.1	276
Y2	400	75	0.50	0.00	0.50	0.09	889	557	12.4	270
Y3	400	75	0.50	0.00	0.50	0.06	852	545	13.7	269
TA	400	90	0.51	0.00	0.51	0.02	--	--	--	--
Y1	400	90	0.53	0.00	0.53	0.03	--	--	--	285
Y2	400	90	0.58	0.00	0.58	0.01	845	596	14.2	275
Y3	400	90	0.52	0.00	0.52	0.05	821	565	12.0	276
DIL	400	180	0.56	0.00	0.56	0.04	--	--	--	--
Y1	400	180	0.53	0.00	0.53	0.01	876	640	13.4	285
Y2	400	180	0.49	0.00	0.49	0.05	875	610	12.6	281
Y3	400	180	0.52	0.00	0.52	0.01	845	593	15.2	272
DIL	300	1	0.17	0.03	0.20	0.39	--	--	--	--
DIL	300	2	0.15	0.08	0.23	0.39	--	--	--	--
DIL	300	5	0.12	0.08	0.20	0.38	--	--	--	--
DIL	300	10	0.16	0.08	0.24	0.42	--	--	--	--
Y1	300	10	0.28	0.12	0.40	0.33	1033	576	2.7	361
Y2	300	10	0.26	0.06	0.32	0.30	999	518	5.8	317
DIL	300	15	0.19	0.21	0.40	0.36	--	--	--	--
DIL	300	20	0.16	0.24	0.40	0.33	--	--	--	--
Y1	300	20	0.29	0.20	0.49	0.22	1122	581	4.8	353
Y2	300	20	0.26	0.14	0.40	0.25	993	514	4.9	325
DIL	300	30	0.16	0.44	0.60	0.13	1059	578	5.7	333
Y1	300	30	0.28	0.22	0.50	0.18	1059	578	5.7	333
Y2	300	30	0.37	0.13	0.50	0.16	987	580	8.4	302
DIL	300	50	0.19	0.48	0.67	0.06	--	--	--	--
Y1	300	50	0.28	0.32	0.60	0.15	1059	611	9	341
Y2	300	50	0.28	0.24	0.52	0.13	986	544	7	306
Y1	300	60	0.30	0.39	0.69	0.03	1056	655	7.9	337
Y2	300	60	0.29	0.32	0.61	0.03	1036	626	9.7	311
Y1	300	75	0.29	0.40	0.69	0.04	1125	698	9.8	335
Y2	300	75	0.30	0.28	0.58	0.08	1017	560	8.5	293
Y1	300	90	0.29	0.42	0.71	0.01	995	692	4.8	339
Y2	300	90	0.35	0.23	0.58	0.08	1001	665	8.1	315
Y1	300	180	0.33	0.30	0.63	0.03	1033	692	9.5	343
Y2	300	180	0.25	0.47	0.72	0.02	881**	582	6.2	304
DIL	300	180	0.15	0.57	0.72	0.06	--	--	--	--

** 20 % Chunky graphite appearance.

6.4.1. Microstructure evolution

Regarding the quenching experiments, the evolution of the microstructure during the interrupted cooling experiments is shown in Figure 70 for the different quenching temperatures. The evolution of the phases acicular ferrite (AF) and martensite (M) is shown, being austenite the remaining amount to 1.

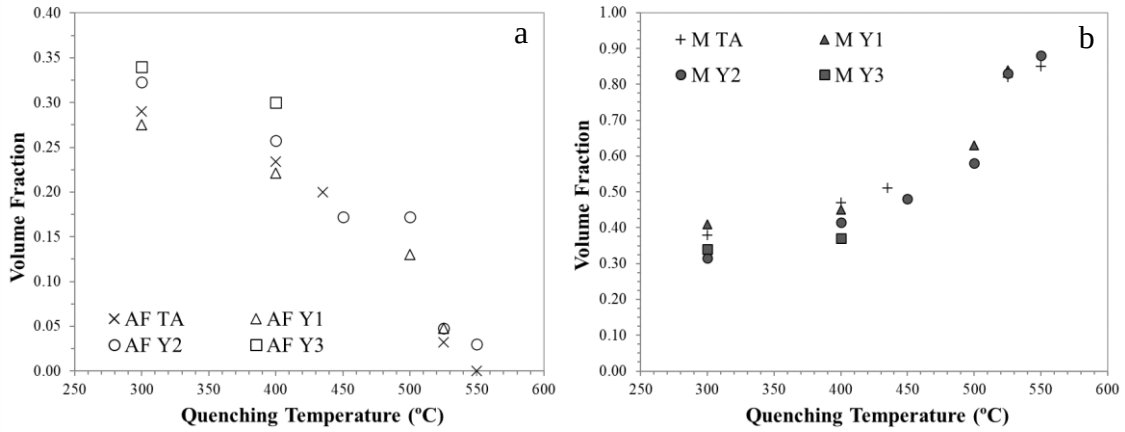

Figure 70. Evolution of the AF formation (a) and M evolution (b) with the quenching temperature.

It is seen, how when the quenching temperature decreases, the AF formation increases, and the M quantity decreases. For a given temperature, the higher the TM, the higher the AF precipitation and the lower the M amount.

The interrupted cooling experiments (Figure 70) show that around 550 °C AF starts to form, which could be considered as the AF formation start temperature (AF_S) for the studied cooling rate range and the present alloy (Table 21). When different TM were quenched at the same temperature, then it is seen that the higher the TM, the higher the AF precipitation and the less M formation. This is because augmenting the TM, the time needed to reach the quenching temperature after having touched the ausferritic nose increases (under the same cooling conditions, as it is the case), and thus longer time for the AF to precipitate. The unreacted parent austenite when reached the quenching temperature, transforms into M during the quenching process to room temperature. For this reason, the more the reaction has evolved, the lower M appearance.

At the beginning of the isothermal stage both at 400 and 300 °C, there is some AF already precipitated and the M content is below 0.50 as seen in Figure 70. This means, that the reaction has evolved before reaching the austempering temperature, that is, before the temperature arrest. This is due to the low cooling rate of the air cooling from the AF_S (around 550 °C) till the transformation temperature, that gives some time once in the ausferritic nose for the AF to precipitate. On this first stage of the reaction, before reaching the isothermal temperature, upper acicular ferrite (UAF) is formed, as seen in Figure 71. Only some lower acicular ferrite (LAF) is formed at the quenching temperature of 300 ºC (Table 22).

As an example of the evolution of the microstructure during the interrupted cooling experiments, in Figure 71 micrographs corresponding to the Y2 blocks and the quenching temperatures of 550, 525, 500, 450, 400 and 300 °C are shown.

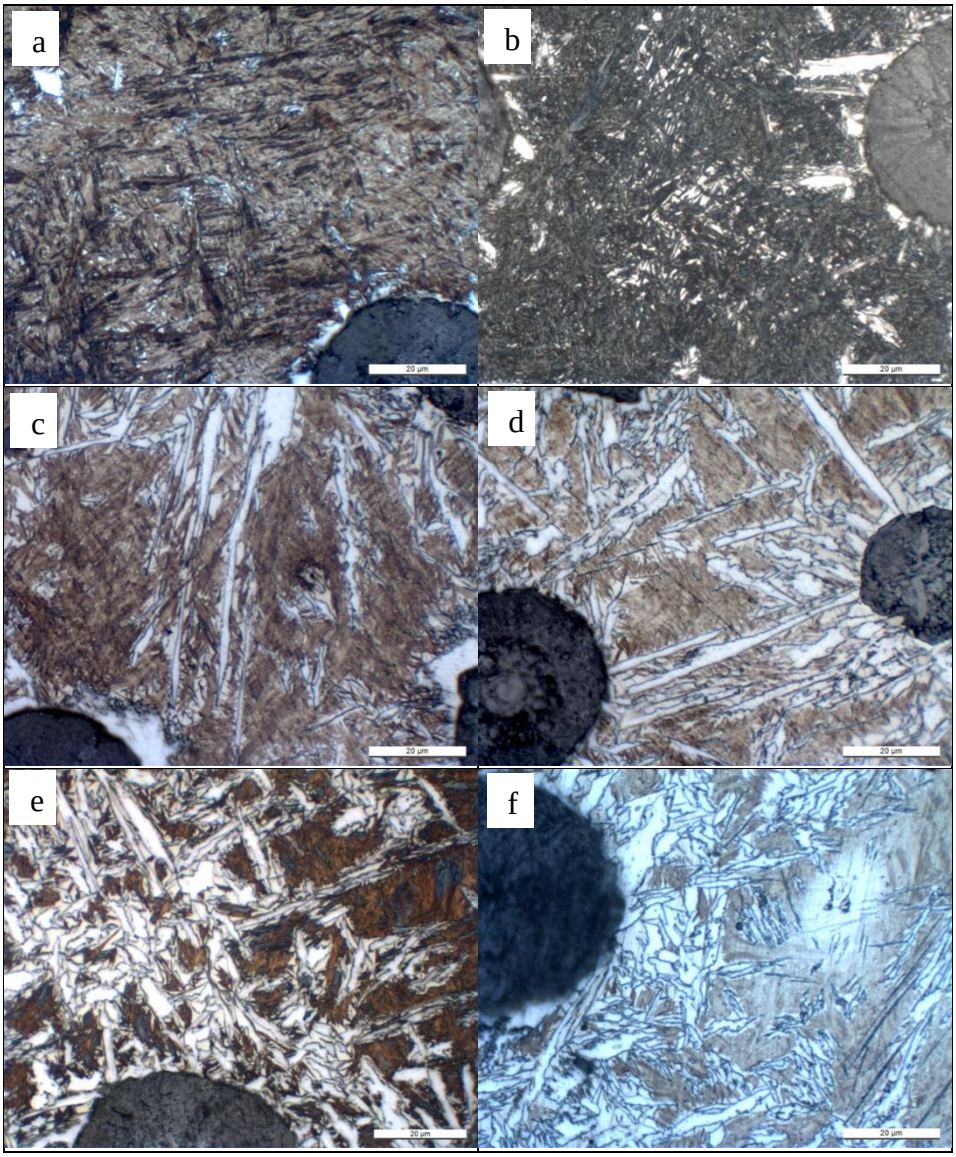

Figure 71. Examples of the microstructure for the Y2 blocks, at different quenching temperatures a) 550 ºC, b) 525 ºC, c) 500 ºC, d) 450 ºC, e) 400 ºC, f) 300 ºC. 1000x.

The cooling rate of the different TM is shown in Figure 72, from 600 to the 300 ºC, in which it is seen, how the higher TM, the lower the cooling rate.

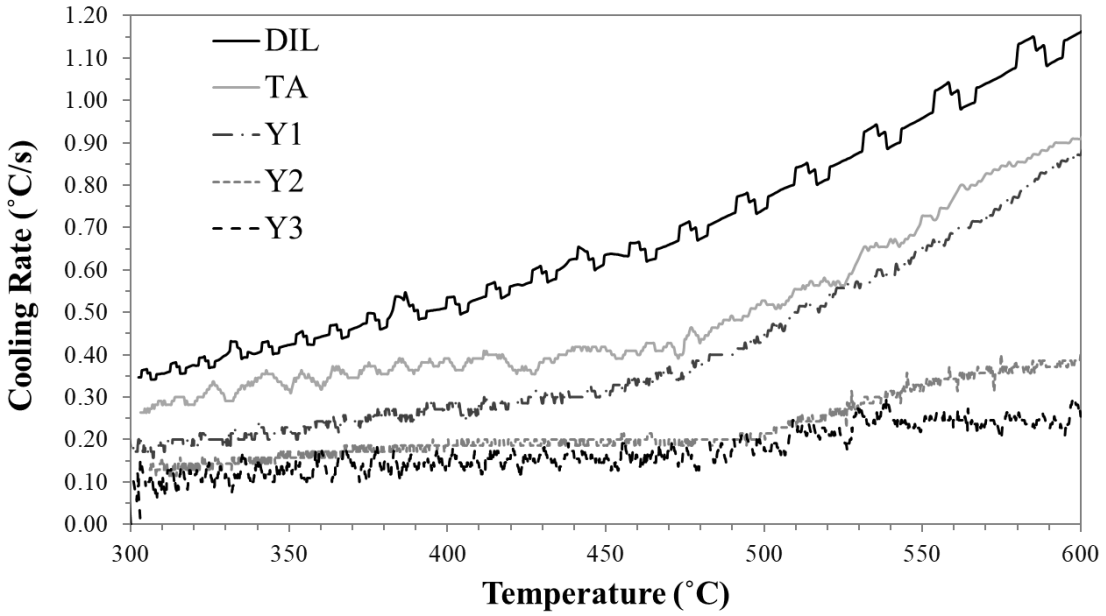

Figure 72. Cooling rate evolution with the temperature for the different TM.

Taking into account the cooling rate of the different TM (Figure 72), the longer the time needed to reach the isothermal temperature from the AF_S (higher TM), the more the transformation has evolved. Furthermore, on the range from 400 to 300 ºC, the reaction rate seems to slow down compared to the 550 to 400 ºC range (Figure 70). This contradicts the fact that, for a conventional austempering heat treatment, the lower the transformation temperature, the higher the driving force for the AF precipitation. However, on this case, the reaction has already started around 550 ºC and has been developing for a certain time. During this time, UAF has precipitated (Figure 71) and thus the remaining austenitic phase has been carbon enriched, which makes that the kinetics of the reaction slow down. Due to the higher carbon content of the austenite, its Gibbs free energy decreases and thus the driving force for the reaction is also decreased and hence the reaction rate is reduced as seen in Figure 22.

Considering 400 and 300 °C transformation temperatures, the microstructure evolution is shown in Figure 73 and Figure 74 respectively. The evolution of the phases AF and M is shown, being austenite the remaining amount to 1. As seen in Figure 70, the ausferritic transformation actually starts around 550 ºC, which could be considered as the AF formation start temperature (AF_S). For this reason, the time on the austempering or isothermal stage (t_{ISO}) as well as the time after reaching the AF_S temperature (t_{AUS}) are considered, that is, taking also into consideration the interrupted cooling experiment results.

t_{ISO} is the time that the samples were into the insulating material. t_{AUS} was calculated for each sample considering the initial moment, the one when the sample reached the AF_S temperature. This time was experimentally calculated using the recorded thermal evolution as seen in Figure 69 and Figure 72.

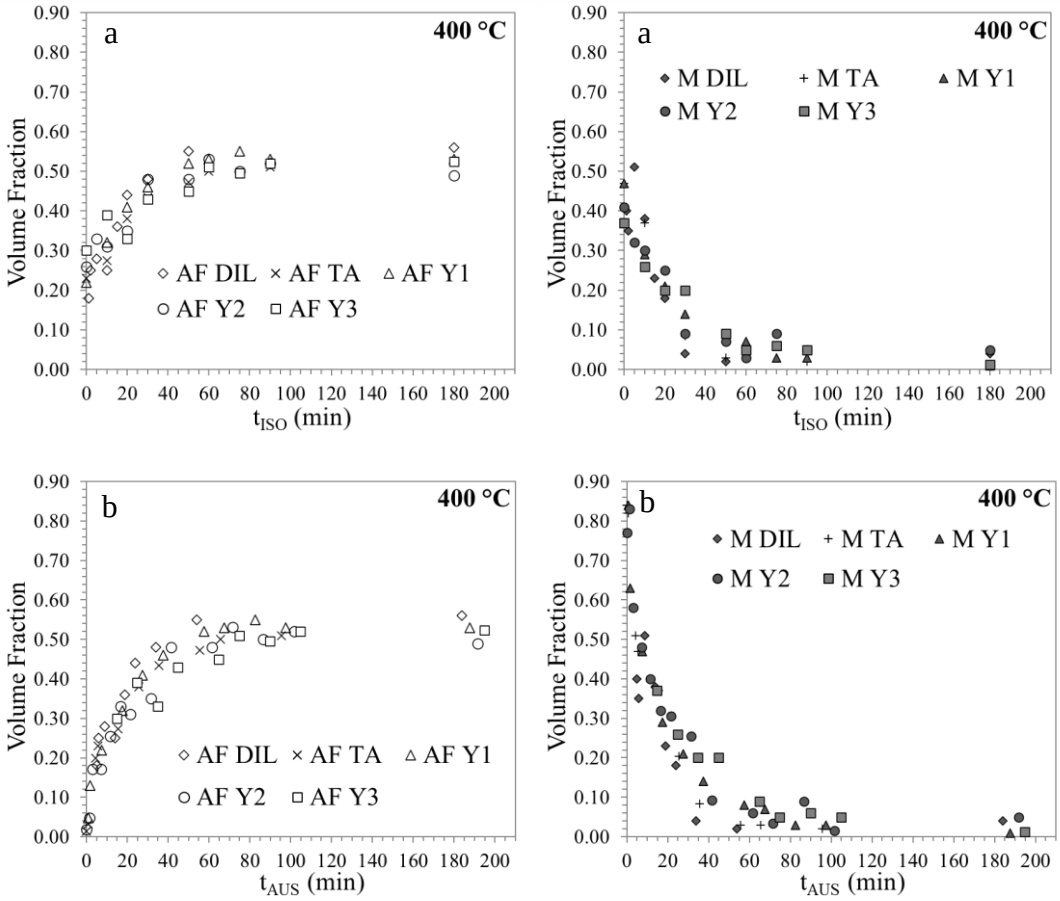

Figure 73 AF formation (left) and M evolution (right) for the different TM at 400 °C. a) t_{ISO}, b) t_{AUS}.

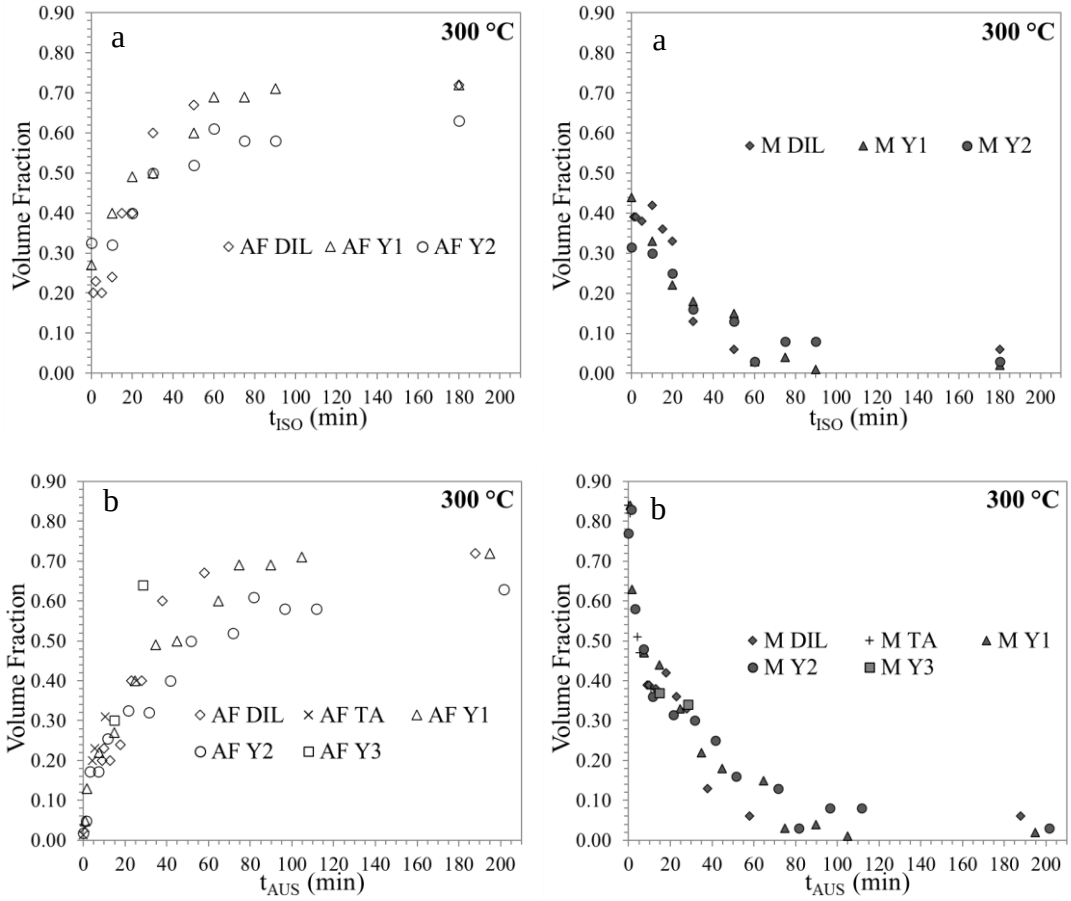

Figure 74. AF formation (left) and M evolution (right) for the different TM at 300 °C. a) t_{ISO}, b) t_{AUS}.

For both isothermal temperatures, it is seen, how when the time goes on, the AF precipitation increases, the M formation decreases and after a given time, the microstructure remains constant. The tendency is the same for the different TM.

Since the reaction has already started at the beginning of the austempering or isothermal stage (when the castings are introduced into the insulating medium), what does not occur for a conventional austempering heat treatment; instead of considering the time passed on the isothermal stage (t_{ISO}), the results considering the beginning of the transformation as the instant at which the temperature of 550 ºC (AF_S) was reached for each TM (t_{AUS}) are more representative of the analysed as-cast methodology. That is the moment at which for the studied cooling rates, the ausferritic reaction actually starts.

At 400 ºC austempering temperature, the transformation rate for the different TM is very similar (Figure 73), being the differences not considered on the scope of this work. This means that the TM has little effect on the reaction; independent of this value, the AF precipitation with the time is similar. This fact can be explained because the ausferritic transformation is not a diffusive phenomenon, but displacive[94, 99] and thus the TM has little influence because the reaction takes place on the different zones of the casting simultaneously.

The main difference between 400 and 300 °C austempering temperatures, is that at 400 °C all the AF is made up of UAF, while at 300 °C, both UAF as well as LAF are present. In Figure 75 is shown the evolution of the different AF types at 300°C, considering t_{ISO} and t_{AUS}.

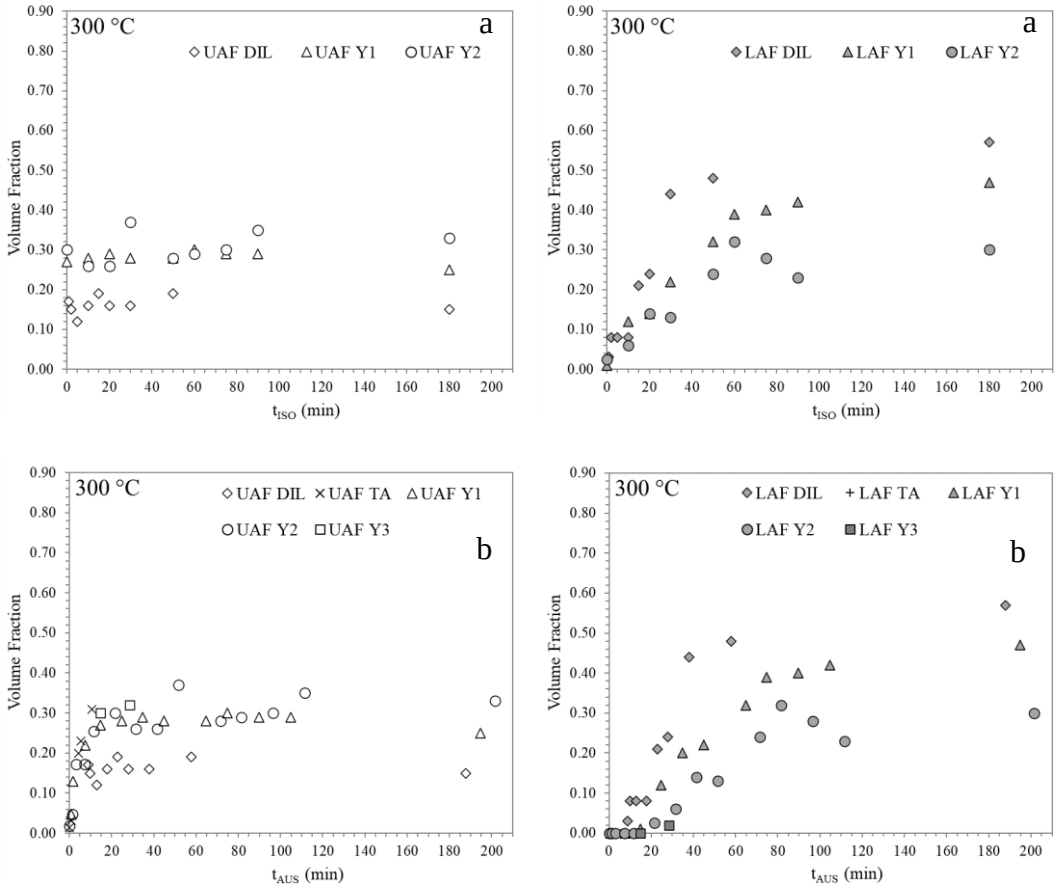

Figure 75. Different AF type's formation for the different TM at 300 °C, UAF (left) and LAF (right). a) t_{ISO}, b) t_{AUS}.

The evolution of both UAF and LFA is more clearly seen when t_{AUS} is considered, because this is the time at which the reaction actually starts.

It is observed how when the reaction starts (t_{AUS} = 0) UAF starts to form and the LAF remains zero and once the 300 ºC isothermal temperature is reached, LAF starts to form and the UAF remains constant. Till the end of the reaction during the isothermal arrest, LAF is formed.

As an example of the evolution of the microstructure, in Figure 76, micrographs corresponding to the Y2 blocks (TM of 1.11 cm) and the temperatures 400 and 300 °C, considering the isothermal transformation times of 10, 20 and 60 minutes are shown. A detail after 60 minutes t_{ISO} is pointed out to see the different morphology of UAF and LAF. UAF is thicker and coarser with a feathery morphology, while LAF is finer and presents an acicular morphology.

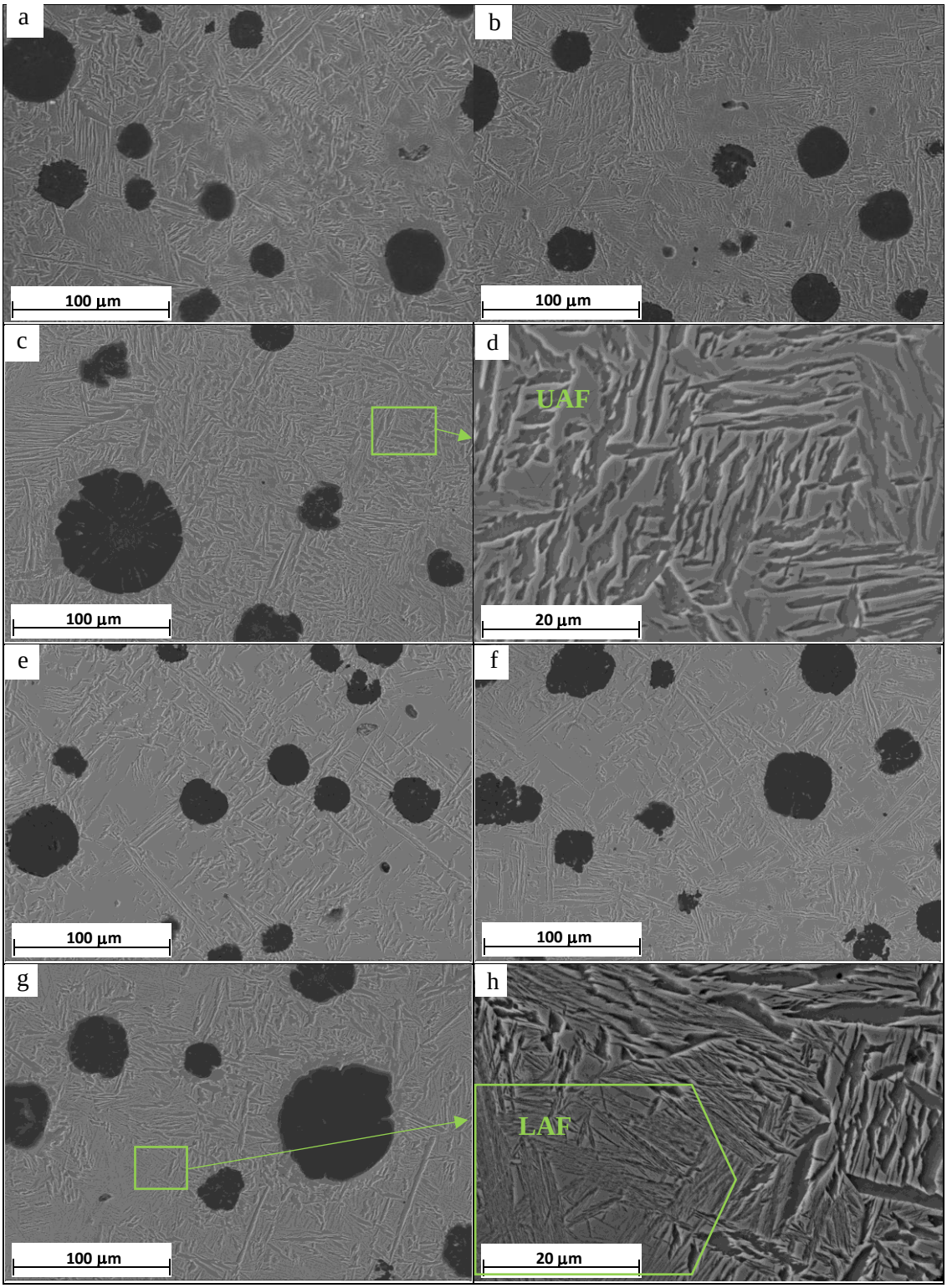

Figure 76. Examples of the microstructure for the TM 1.11 cm at 400 °C and 300 °C for different t_{ISO}. a) 400 ºC, 10 min; b) 400 ºC, 20 min; c) and d) 400 ºC 60 min; e) 300 ºC, 10 min; f) 300 ºC, 20 min; g) and h) 300 ºC 60 min.

On the other hand, it is seen that at 300 ºC (Figure 74 and Figure 75), the differences on the evolution of the reaction for the different TM are bigger, and not negligible. The main difference between the 300 and 400 °C transformation temperatures resides in the shape of the AF. At 400 °C only UAF is formed, while at 300 °C, a dual precipitation of UAF and LAF is observed (Figure 75). This is at the same time, the main divergence observed between the as-cast ausferritic material and the conventionally austempered ADI. The ADI samples treated at 300 °C, show only LAF[148]. The main feature of the LAF compared to the UAF, is that they present a higher resistance at the expense of a lower ductility, which consequently influences the mechanical properties as will next be shown. Additionally, the samples treated at 300 ºC, present a higher quantity of AF at the end of the reaction than the samples treated at 400 ºC. This is in good accordance with the incomplete reaction phenomenon, which defines that the reaction ceases when the austenite achieves the carbon content defined by the T_0 curve[102, 104]. This maximum carbon content increases when decreasing the isothermal temperature.

To explain the differences on the evolution of the reaction for the different TM at 300 ºC, in Figure 75 it is seen, how the higher the TM, the higher the quantity of UAF that is formed. This has been previously reasoned, because, increasing the TM, the cooling rate before the temperature arrest decreases and thus, the time needed to reach the isothermal temperature after AF_S increases, so that the AF has longer time to precipitate. During this period, mainly UAF is formed. Figure 75 shows, that the more the UAF that precipitates at the first stage of the reaction (before the austempering arrest), the less LAF is formed at the end of the transformation. Once the isothermal temperature is reached, then the AF formation becomes exclusively LAF.

These differences on the LAF content, can be explained by the incomplete reaction phenomenon, which assumes that a diffusionless reaction is not possible, if the austenite presents a higher carbon content than the T_0 curve[102, 104]. If at the beginning of the isothermal stage, the UAF quantity is higher, means that the dissolved carbon content in the austenite is higher and consequently, the smaller margin for LAF to precipitate before the austenite reaches the carbon content defined by the T_0 curve. The differences between the distinct TM, could then be attributed to the cooling rate before the temperature arrest and not to the evolution of the transformation itself during the isothermal stage.

To compare the reaction rate of the ausferritic transformation at 400 and 300 ºC austempering temperatures, in Figure 77, the AF and M evolution at both temperatures, considering t_{AUS} is shown. The different TM have not been differentiated, because the influence of this variable has been defined to have little influence on the ausferrite transformation kinetics. To have a clearer view, the first 100 minutes are only shown.

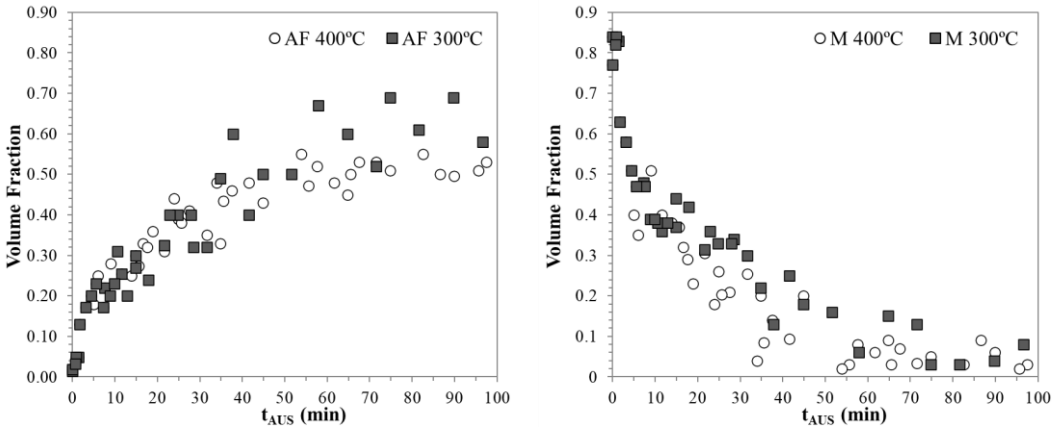

Figure 77. AF (left) and M (right) evolution considering t_{AUS} for 300 and 400 ºC isothermal temperatures.

A similar evolution is seen for both studied isothermal temperatures. As the AF formation at 300 ºC at the end of the reaction is higher than at 400 ºC, the time needed to reach a constant value of AF increases at 300 ºC. The M decrease is similar for both austempering temperatures.

The AF formation occurs at a similar rate both at 400 and 300 °C, which can be explained because on both cases, the reaction starts at around 550 ºC (AF_S) and thus the driving force is the same at the beginning of the transformation on both cases. On the other hand, considering that the AF quantity at the end of the reaction is higher at 300 °C, then the time needed to finish the transformation at 300 ºC is longer. At 400 ºC the reaction is finished 65 minutes after reaching the temperature of AF_S, while at 300 ºC, 80 minutes are needed.

At 180 minutes t_{ISO}, no carbides were observed. This suggests that the stage II of the ausferrite transformation was not started. For this reason, the processing window is at least beginning from the moment at which the ausferrite formation is complete, described in the paragraph above, till the 180 minutes t_{ISO}.

6.4.2. Mechanical properties evolution

The evolution of the mechanical properties corresponding to the Y1, Y2 and Y3 blocks is shown in Figure 78 at the austempering temperature of 400 ºC and corresponding to the Y1 and Y2 blocks at the austempering temperature of 300 ºC in Figure 79, considering both the time in the insulating material (t_{ISO}) and the time after reaching the AF_S (t_{AUS}).

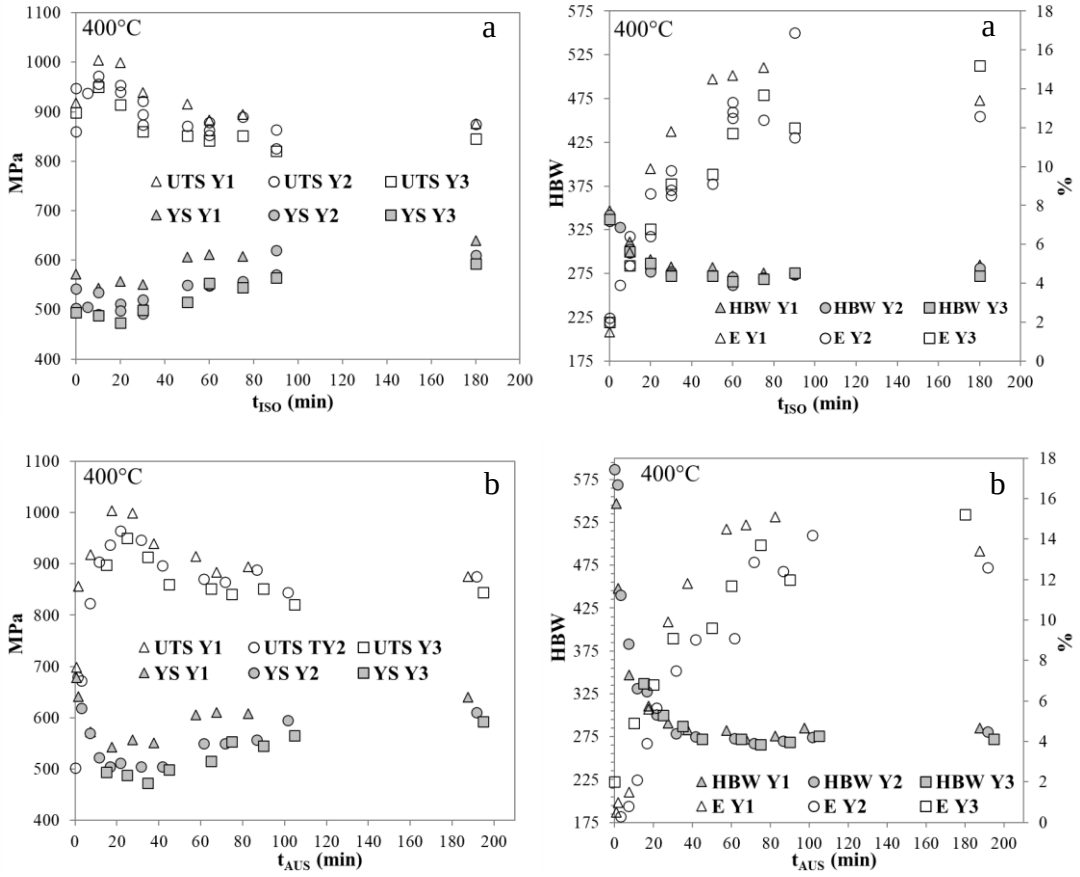

Figure 78. UTS and YS evolution (left) and HBW and E evolution (right) for the different TM at 400 °C considering a) t_{ISO} and b) t_{AUS}.

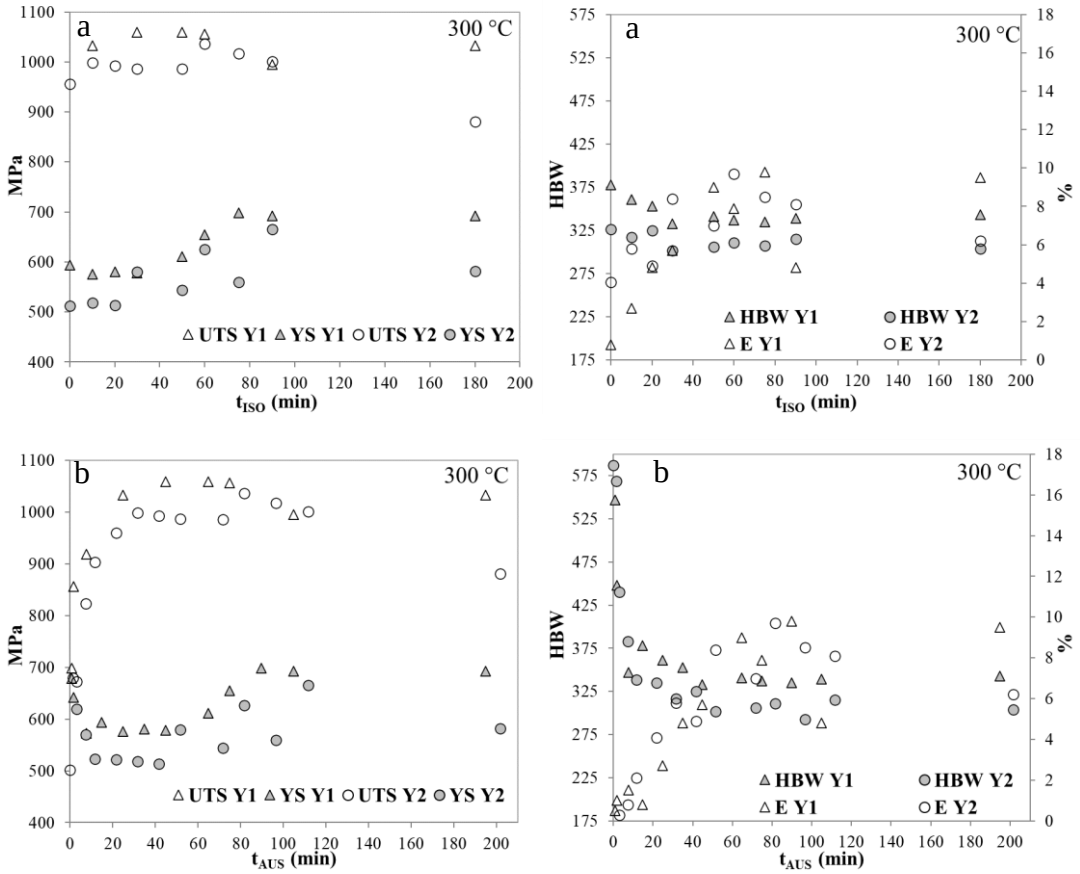

Figure 79. UTS and YS evolution (left) and HBW and E evolution (right) for the different TM at 300 °C considering a) t_{ISO} and b) t_{AUS}.

The same as happened for the microstructure, the evolution of the mechanical properties is more clearly seen when considering the beginning of the reaction (t_{AUS}). When the time in the insulating medium is considered (t_{ISO}), as the ausferrite formation has already started, the evolution of the mechanical properties is only partially considered. In addition, the higher the TM, the longer the t_{AUS}, but this does not happen with the t_{ISO}, which is the same for the different TM. For this reason, from now on, only the development of the mechanical properties considering t_{AUS} is going to be described.

For both isothermal temperatures, as the ausferritic reaction evolves, the HBW decreases, and the E grows. Regarding the UTS, at 300 and 400 ºC isothermal temperatures, at the beginning increases, and after achieving a maximum, it goes down to reach a constant value. On the other hand, the YS decreases at the beginning and afterwards increases to reach a constant value, for both studied isothermal temperatures.

The resistance and hardness values are higher for the 300 ºC austempering temperature, while the elongation is lower.

At the isothermal temperature of 400 °C (Figure 78), during the evolution of the reaction, as the AF content increases and the M decreases, the HBW decreases and the E increases, due to the microstructural evolution. The UTS increases at the beginning, and after reaching a maximum, it goes down to achieve a constant value. On the other hand, the YS decreases at the beginning and afterwards increases to reach a constant value. This initial fluctuation on the resistance values can be attributed to the high M content at the initial stages of the reaction. When the reaction is completed, the mechanical properties remain constant.

The ausferritic samples obtained by means of a controlled cooling at 400 ºC temperature arrest, present a necessary minimum t_{AUS} of 35 minutes to fulfil the standards of the ADI materials (EN 1564[32]) for the different TM tested. From 35 to 65 minutes, the mechanical properties improve and after 65 minutes remain constant. The UTS and E relationship defined on the standard for ADI materials EN 1564[32] is shown in Figure 80.

Considering the different TM studied, it is seen that the Y1 (TM 0.70 cm) presents in general slightly higher resistance and somewhat higher ductility than the Y2 (TM 1.11 cm) and at the same time, the Y2 slightly higher resistance and ductility than the Y3 (TM 1.75 cm). This fact could be attributed to the longer solidification time when increasing the TM, and thus a coarser grain size and even an increase of defects[81, 82]. This makes that for a higher TM, the mechanical properties in terms of resistance and ductility decrease. Furthermore, the hardness remains constant for the different TM, which also supports this explanation, since the microstructure of the different TM is similar as explained formerly. For these reasons, the slight differences are not attributed to the ausferritic reaction, but to the different solidification times.

At 300 °C isothermal temperature (Figure 79), as happens at 400 ºC, during the evolution of the reaction, as the AF content increases and the M decreases, the HBW decreases and the E increases, as a result of this evolution of the metallic matrix. The UTS and the YS follow the same trends as at 400 ºC, being the initial fluctuations also originated by a high M formation. When the reaction is completed, the mechanical properties remain constant.

As formerly explained, at 300 ºC, a dual matrix made up of UAF and LAF is observed. This makes that the resistance is higher than that for the samples which were austempered at 400 °C and the elongation decreases, because the LAF presents a higher resistance compared to the UAF, but less ductility. Compared to a conventional austempering heat treatment, performed at a low temperature (in this case at an equivalent temperature of 300 °C), in which the microstructure is made up completely of LAF[52], then the ductility decrease is minimized. On this case, there is a necessary minimum t_{AUS} of 80 minutes in order to fulfil the standards of the ADI.

Considering the different TM studied, it is seen that the differences are bigger than at 400 °C austempering temperature. The Y1 (TM 0.70 cm) presents higher resistance than the Y2 (TM 1.11 cm), while slightly lower ductility and higher hardness. These differences cannot be explained by the variable solidification time with the TM as happened at 400 ºC. The resistance decrease is not observed on the ductility when increasing the TM, and furthermore, the hardness decreases with the TM. These divergences are based on the microstructure differences that were explained formerly. The UAF increase and LAF decrease for a higher TM, makes that the resistance and hardness are decreased, and the ductility increased when the TM increases.

Average UTS vs E after 65 minutes t_{AUS} at 400 ºC and after 80 minutes t_{AUS} at 300 ºC (once the reaction is completed) for the different TM compared to the standard EN 1564[32] requirements are shown in Figure 80.

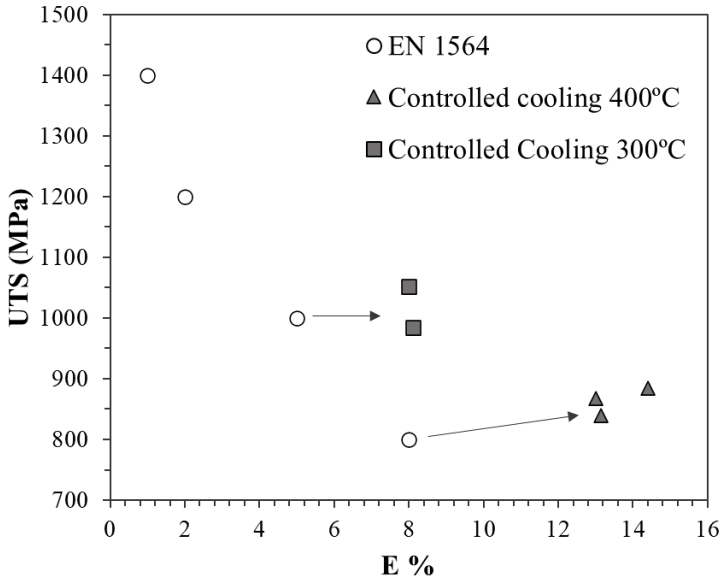

Figure 80. U.T.S. and elongation values of the controlled cooling process compared to the standard EN 1564[32].

It is observed, how for both austempering temperatures, the elongation is well above the standard. At 400 ºC, the resistance is also above the standard material EN GJS 800-8, while at 300 ºC, due to the dual matrix made up of UAF and LAF, the resistance values are on the same level as the requirements for the material EN GJS 1000-5.

As seen with the microstructure, at 180 minutes t_{ISO}, the mechanical properties are constant compared to the moment at which the ausferritic transformation is complete. This corroborates that the stage II of the ausferrite transformation was not started and consequently, the processing window is at least beginning from the moment at which the ausferrite formation is complete (65 minutes t_{AUS} at 400 ºC and after 80 minutes t_{AUS} at 300 ºC), till the 180 minutes t_{ISO}.

6.5. ADVANCED CHARACTERIZATION OF THE AUSFERRITIC AS-CAST MATERIALS

In the previous sections, the controlled cooling technology was defined, and corroborated that the tensile test, hardness and impact resistance values were in the same ranges as the conventionally obtained ADI materials.

In order to deeply analyse the mechanical properties of the as-cast obtained ausferritic ductile iron materials, in addition to the static mechanical tests, an advanced characterization of the material was conducted. These results are shown in this section.

A number of three ductile iron melts were prepared as previously defined. The obtained cast parts were standard keel blocks Y2 as per the standard EN 1563[31].

After solidification, once the samples reached 800 ºC, early shakeout was used, followed by air cooling to the austempering or isothermal transformation temperature. Then, the samples were introduced into a reusable insulating medium (Table 10 and Figure 38-b) in order to maintain a constant temperature for 90 minutes, so that a fully ausferritic transformation can take place. Three different isothermal transformation temperatures (400 – 350 – 300 ºC) were chosen to compare the properties achieved with upper and lower ausferritic microstructures.

An example of the registered cooling curves of the Y2 blocks treated at 300 and 400 ºC is shown in Figure 81.

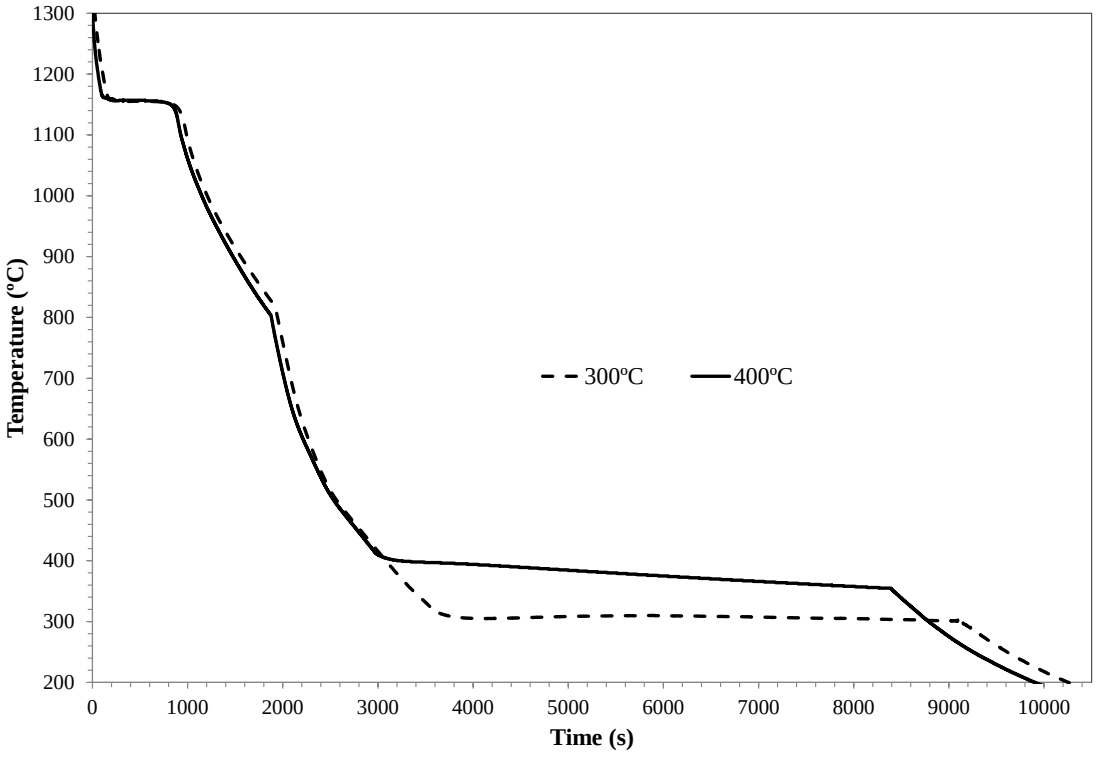

Figure 81. Cooling curves of Y2 keel blocks for 400 and 300 ºC austempering temperatures.

The targeted chemical composition was the one shown in Table 14. The experimentally obtained chemical composition is shown in Table 23, considering the austempering temperatures of 400, 350 and 300 ºC, denoted by AUS-40, AUS-35 and AUS-30 respectively. The chemical composition was analysed from a portion of the tensile bar by means of combustion methodology for C and S, gravimetric method for Si and inductively coupled plasma (ICP-OES) for the rest of the elements.

Table 23. Chemical composition of the trials to perform the advanced characterization of the engineered cooled ausferritic ductile iron (wt.%).

Test	C	Si	Cu	Ni	Mo	Mn	Mg	S
AUS-40	3.61	2.10	0.04	2.80	0.21	0.15	0.044	<0.005
AUS-35	3.61	2.02	0.03	2.84	0.33	0.16	0.054	<0.005
AUS-30	3.52	2.10	0.06	2.87	0.22	0.17	0.045	0.006

The following analysis were carried out:

Fatigue, tensile, impact and bending tests were made on a set of specimens machined from the bottom area of each standard Y2 block. A cylindrical specimen of 10 mm diameter was used for the tensile test and a group of three notched samples (KV_2 type following the standard ISO 148-1[49] with dimensions 10x10x55 mm^3 were prepared for the impact experiments at 20 and -20 ºC.

The three-point bending experiments were conducted on a universal testing machine MTS M.20 as shown in Figure 82 and following the standard ISO 7438[179]. Three specimens were tested at 20 and -20 ºC.

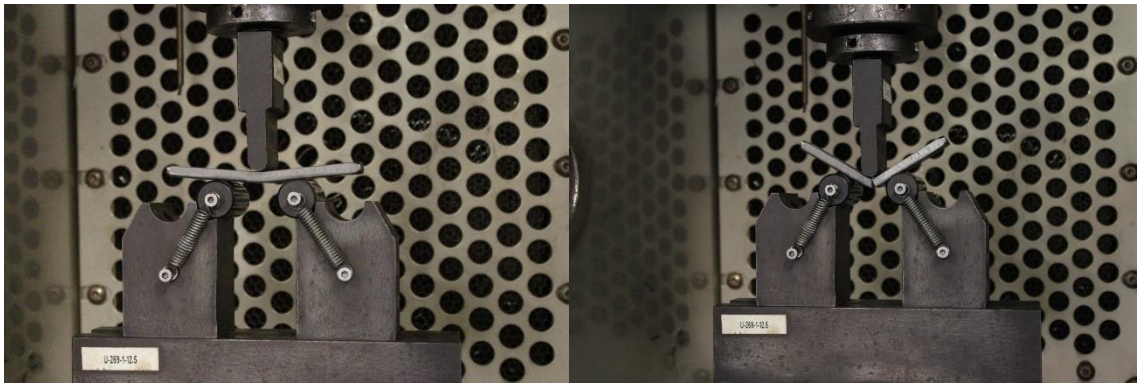

Figure 82. Image of the three-point bending test.

Fatigue tests were performed in specimens of 110 mm in length, 9 mm in minimum diameter and treaded ends. These specimens were machined from the bottom area of the Y2 blocks to build a Wohler diagram. A minimum (S_{min}) and a maximum (S_{max}) tensile stress were alternatively applied on the fatigue specimens with a ratio S_{min}/S_{max}=0.1 and 20 Hz in frequency. The S_{max} strength was in the range 450-610 MPa. The temperature was 21±2 ºC during all the experiments. The tests were stopped after breaking the specimen or after a total number of $4x10^6$ cycles. These tests were performed following the standard ISO 1099[54].

The static mechanical parameters measured were the ultimate tensile strength (UTS), yield strength (YS), elongation (E) and impact energy. Brinell hardness (HBW) measurements were also made on machined samples obtained from the bottom area of the Y2 keel blocks using a 10 mm diameter sphere and a load of 3000 kg.

After the tensile test, the specimens were cut and prepared for metallographic examination using a sequence of SiC abrasives from 80 to 1200 grit paper. Nodularity and nodule count were determined using quantitative image analysis software. The microstructure was obtained after etching the samples with Nital 5 %.

Corrosion behaviour of the specimens was evaluated using electrochemical and weight loss methods. Electrochemical tests were performed by means of an Autolab PGSTAT 302N potentiostat. 0.03M NaCl solution corrosive media were used to simulate the aggressive aqueous environment containing Cl^- ions.

A conventional three-electrode cell was used, where the working electrode was the specimen under study; saturated Ag/AgCl was used as the reference electrode and a spring platinum wire was used as the counter-electrode. In all cases, the contact area was approximately 1.20 cm^2. Samples were grinded to 1200 grit paper. The tests were carried out at room temperature and in triplicate. The electrode potential was scanned at a rate of 0.167 mV/s from an initial potential of -0.3 V (with respect to the open circuit potential), to a potential at which the specimen reached a current density of 0.25 mA/cm^2. Corrosion current density values were obtained by Tafel extrapolation method.

The samples for weight loss were prepared following ASTM G31-72[180] and the immersion solution was synthetic seawater (as per ASTM D1141[181] without heavy metals). The experiment was carried out at 25±2 ºC and the immersion time was defined at 480 h. The immersed area was in all the cases approximately 400 mm^2. The samples were polished to 1200 grit paper. The weight-loss method was used to confirm the electrochemical measurements and the corrosion rate was calculated using the following formula (Equation 8):

Equation 8. $\Delta W = (W_0 - W_1)/ (S * t)$

Where W_0 is the mass of the metal sample before corrosion (g); W_1 is the mass of the metal corrosion sample after clearing the corrosion products (g); S is the surface area of the metal sample (m^2); t is the immersion time (h).

An example of the microstructure of the samples treated at 300, 350 and 400 ºC austempering temperatures is shown in Figure 83. They consist of acicular ferrite (AF) and reacted or stabilised high carbon austenite (γ_{HC}) matrix (ausferritic microstructure) with nodular graphite. The microstructure reveals that samples with an isothermal transformation temperature of 400 ºC (AUS-40) have the typical broad ferrite needles of upper ausferritic microstructure (Figure 83-a). On the other hand, the samples with isothermal transformation temperature of 300 ºC (AUS-30) present a mix of upper and lower acicular ferrite (Figure 83-c). Samples treated at 350 ºC (Figure 83-b) present a slightly higher content of UAF than the samples treated at 300 ºC and a lower content of LAF, but the microstructure as well as for the austempering temperature of 300 ºC is a mixture of UAF and LAF.

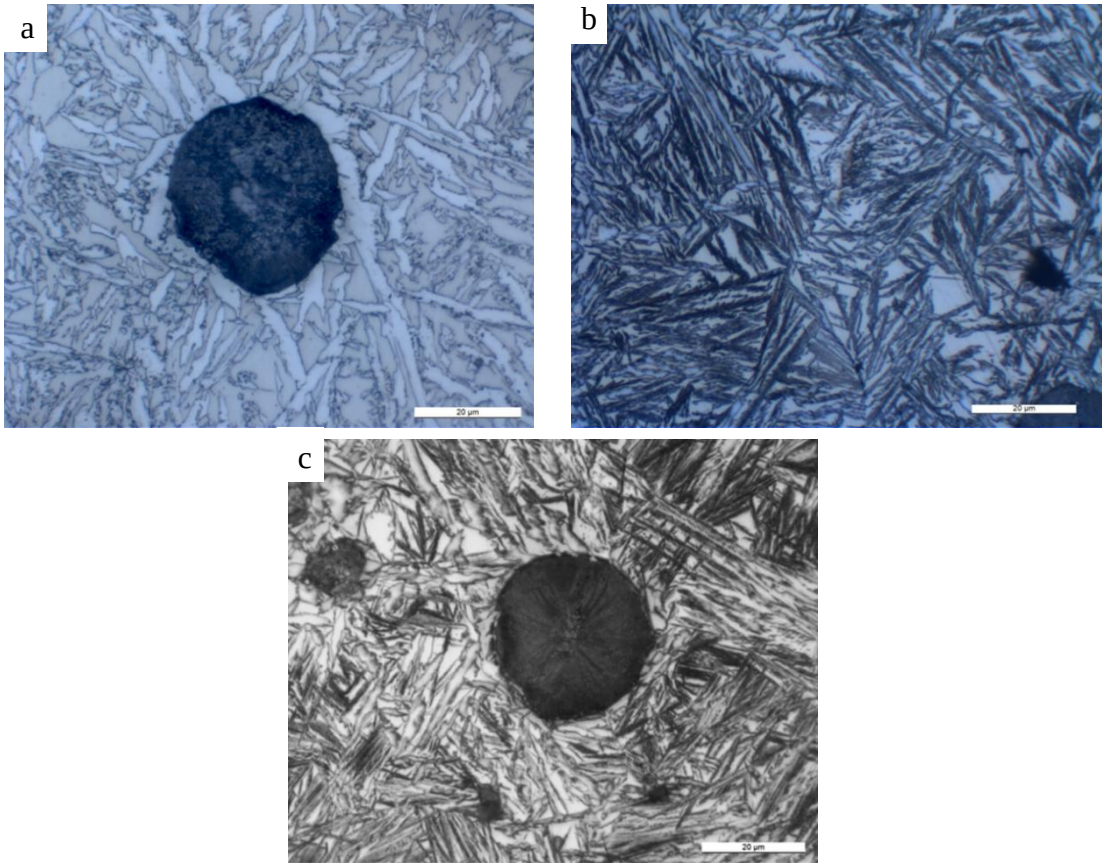

Figure 83. Microstructure of the samples treated at a) 400 ºC, b) 350 ºC and c) 300 ºC. 1000x.

The results of the metallographic analysis regarding the graphite morphology are shown in Figure 84.

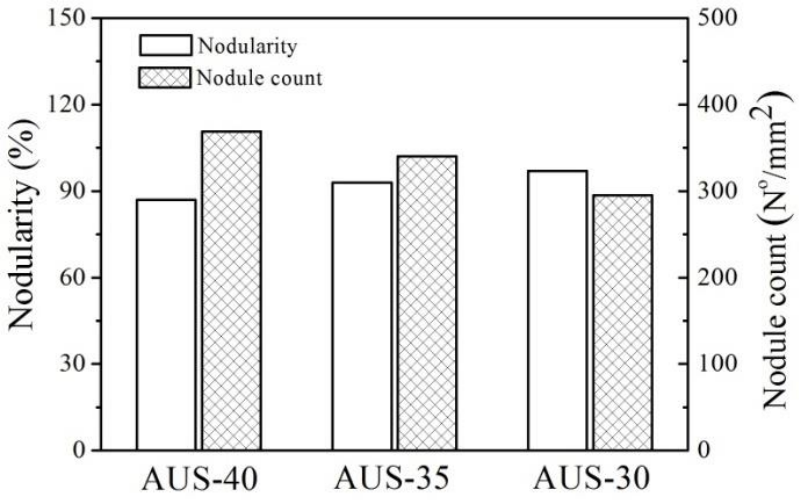

Figure 84. Nodularity and nodule count of the samples treated at 400 ºC (AUS-40), 350 ºC (AUS-35) and 300 ºC (AUS-30).

It is seen that the nodularity is always > 85 % and the nodule count > 250 N°/mm^2, which shows that the graphitization was correct and thus the mechanical properties are defined by the metallic matrix.

The values of the static mechanical properties are shown in Table 24.

Table 24. Static mechanical properties of the engineered cooled samples.

Property	Average values		
	AUS-40	AUS-35	AUS-30
YS(MPa)	573	666	676
UTS(MPa)	830	869	974
E (%)	10.6	6.2	6.4
HBW	273	289	312
Charpy KV at 20 ºC	12/10/11	12/13/13	9/9/12
Charpy KV at -20 ºC	7/8/8	8/8/8	9/9/8

The results of the tensile, impact and hardness tests agree with the previous results of this work. The resistance and hardness increase as the austempering temperature decreases. Nevertheless, the evolution of the elongation does not present a clear relationship. It is higher for the 400 ºC austempering temperature, but at lower temperatures remains constant.

The impact resistance test results at low temperature follow the same trend as presented on the literature[182]. Low temperature affects the impact test results in upper ausferritic structures more than in lower ausferrite. This could be due to the fact that the samples with higher isothermal transformation temperature present higher amount of austenite than the ones treated at lower temperatures, and austenite is the phase that becomes more rigid at low temperature.

6.5.1. Dynamic mechanical properties

Regarding the fatigue tests results, Figure 85 shows a Wohler diagram that was plotted comparing the results from the samples treated at 300 and 400 ºC. Only these two temperatures were tested as they represent the extremes of the tested transformation temperatures.

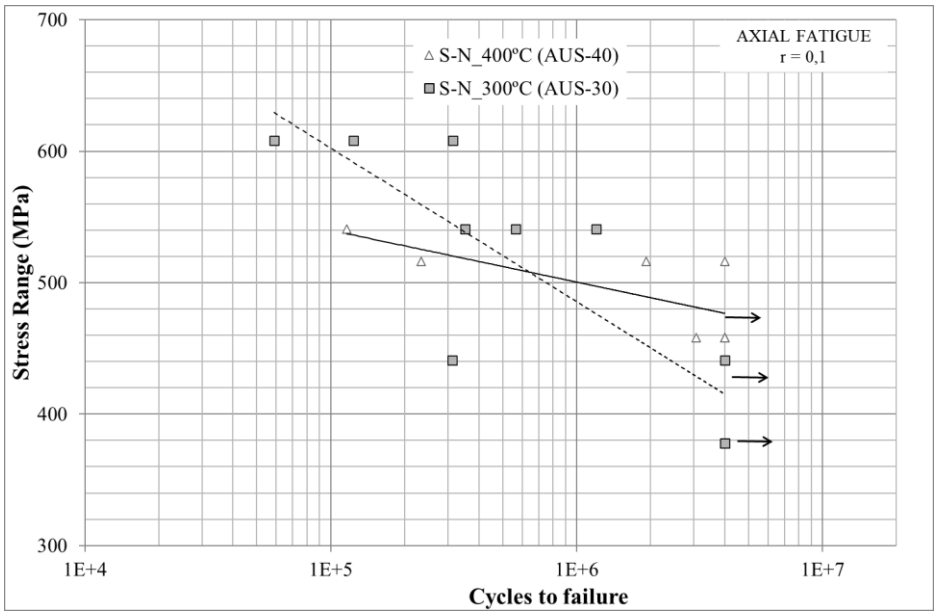

Figure 85. Fatigue response of AUS-40 and AUS-30 materials.

The fatigue limit obtained for the AUS-40 alloy (455 MPa) is higher than the one from the AUS-30 alloy (405 MPa). Considering the yield strength of both materials (Table 24), the AUS-40 alloy's fatigue limit is much higher in percent terms than for the AUS-30 (80 % against 60 % respectively). These results show that the AUS-40 material needs to be affected by higher stress efforts to nucleate cracks and to promote any kind of tearing when comparing to AUS-30 alloy. This fact could be due to the higher ductility that shows the AUS-40 alloy, which can provide this material with a higher resistance against periodically changing efforts. These values are in good agreement with the conventionally obtained ADI literature[57, 135].

The numerical results of these tests are shown in Table 25.

Table 25. Maximum stress and cycles to failure relationship of the fatigue tests.

AUS-40		**AUS-30**	
Maximum stress (MPa)	**Cycles to failure**	**Maximum stress (MPa)**	**Cycles to failure**
541	116,467	608	58,842
516	233,449	608	313,869
516	4 10^6 (No failure)	608	123,388
516	1,920,860	541	1,201,237
458	4 10^6 (No failure)	541	564,121
458	4 10^6 (No failure)	541	351,434
458	3,067,455	441	4 10^6 (No failure)
		441	311,787
		378	4 10^6 (No failure)
		378	4 10^6 (No failure)

The results of the bending tests are shown in Figure 86. In this case, the same as for the fatigue response, only 300 and 400 ºC temperatures were tested as they represent the extremes of the studied transformation temperatures. The performed three tests for each temperature are expressed by the numbers 1, 2 and 3.

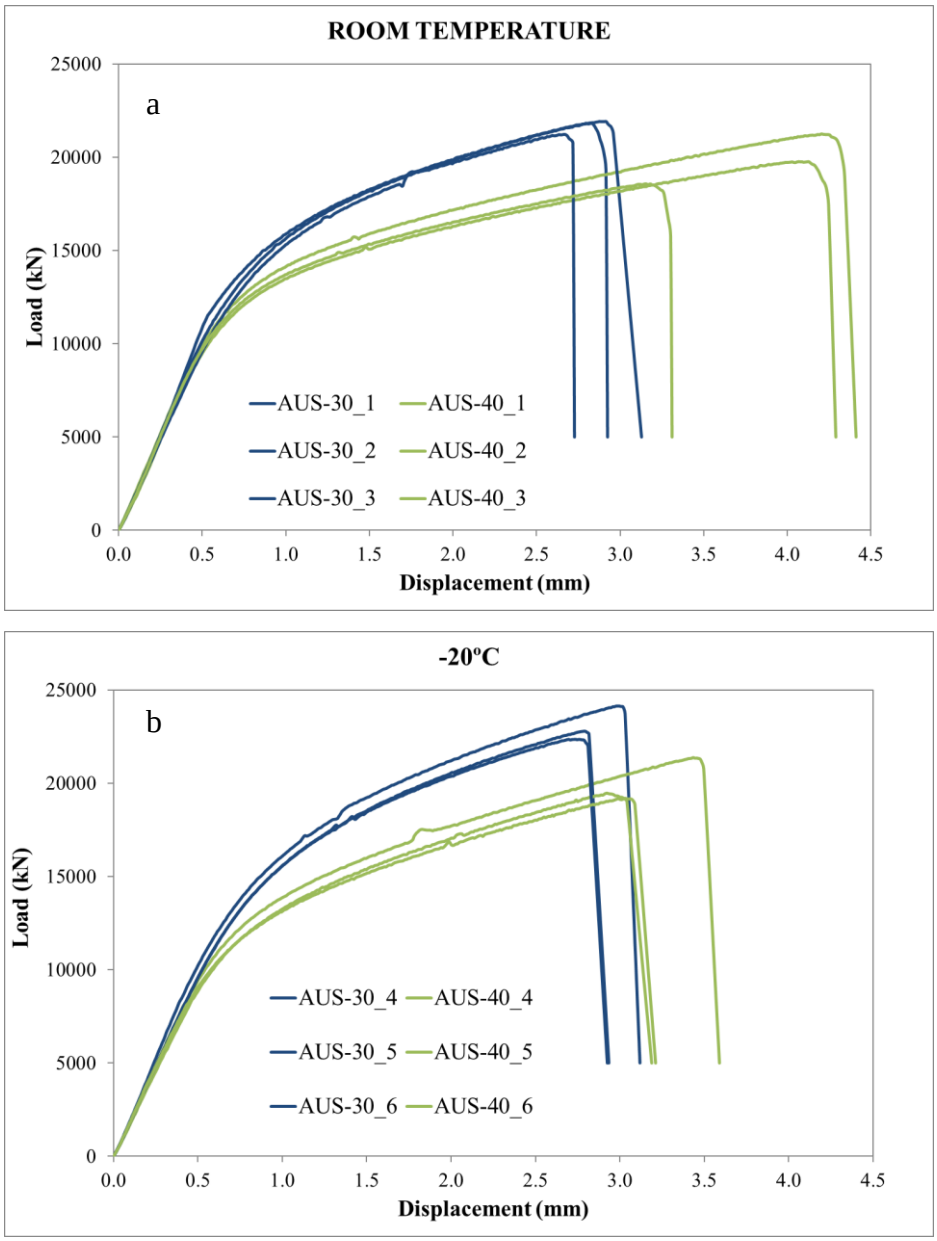

Figure 86. Load-displacement curves of the bending tests. a) Room temperature, b) -20 ºC.

All specimens present the same behaviour: the load reaches a maximum and then the sample breaks suddenly which indicates that the fracture initiation is of brittle nature.

The values of maximum load and displacement are presented in Table 26.

Table 26. Maximum load and displacement of the bending tests.

Reference	Temperature (ºC)	$Load_{max}$ (kN)	$Displacement_{max}$ (mm)
AUS-40_1	20	21.25	4.20
AUS-40_2	20	19.76	4.07
AUS-40_3	20	18.57	3.15
AUS-30_1	20	21.82	2.80
AUS-30_2	20	21.91	2.87
AUS-30_3	20	21.22	2.66
AUS-40_4	-20	21.37	3.43
AUS-40_5	-20	19.47	2.92
AUS-40_6	-20	19.19	3.03
AUS-30_4	-20-	24.14	2.99
AUS-30_5	-20	22.78	2.80
AUS-30_6	-20	22.35	2.70

At room temperature, the specimens tempered at 300 ºC present slightly higher values of $load_{max}$ than the specimens treated at 400º C. Nevertheless, for the same load, the AUS-40 samples have a much higher displacement. This behaviour follows the same tendency than the tensile and impact tests results, that is, the AUS-30 samples present higher resistance but lower toughness than the AUS-40. This tendency is also maintained at low temperature and as seen on the static tests, the influence of lowering the temperature is much more pronounced on the AUS-40 alloy.

6.5.2. Corrosion behaviour

The corrosion behaviour was tested for the 300 and 400 ºC austempering temperatures, to represent the extremes of the studied transformation temperatures. Figure 87 shows the variation of electrochemical potential (ECP) of samples against time, in terms of open circuit potential (OCP). Both samples have a very similar behaviour, remaining the OCP constant at around -650 mV.

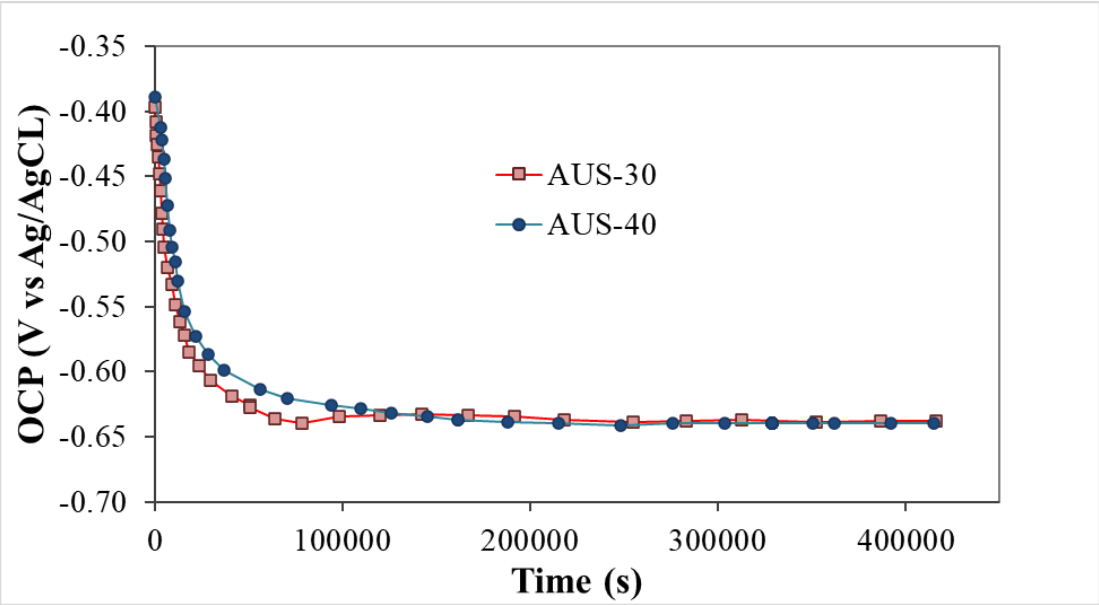

Figure 87. OCP evolution with time for the AUS-40 and AUS-30 samples.

Various corrosion parameters as corrosion potential (E_{corr}) and corrosion current density (I_{corr}) are calculated from the potentiodynamic polarization curves. The polarization curves are shown in Figure 88 and the E_{corr} and I_{corr} values are given in Table 27.

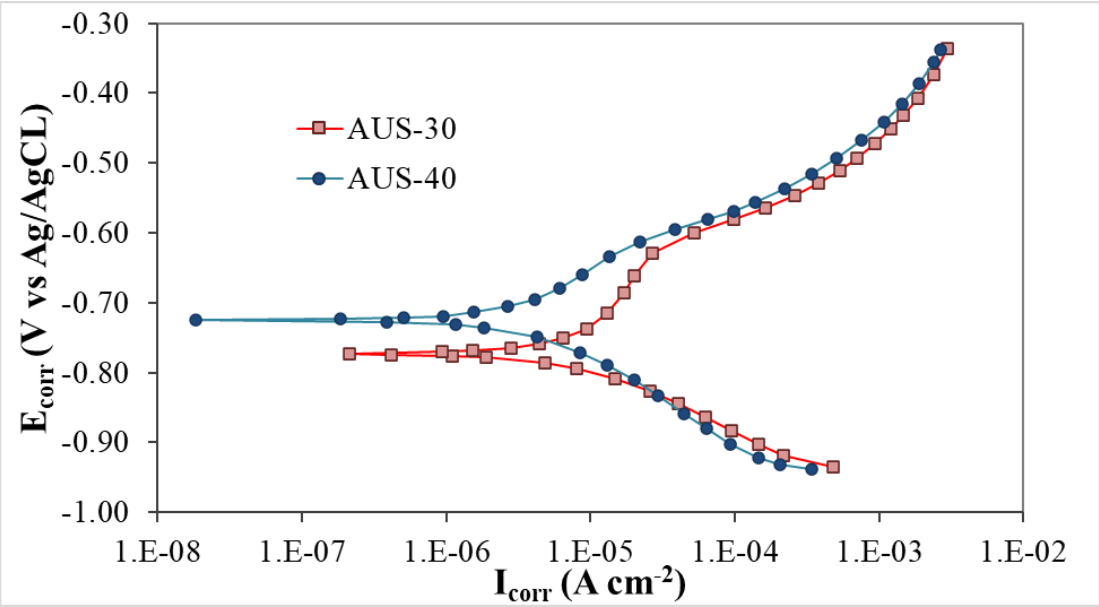

Figure 88. Polarization curves for the AUS-40 and AUS-30 samples.

Table 27. Corrosion parameters obtained from the polarization curves.

Material	E_{corr} (V)	I_{corr} ($A \cdot cm^{-2}$)
AUS-40	-0.7244	3.26×10^{-6}
AUS-30	-0.7705	9.91×10^{-6}

Higher E_{corr} value (-0.7244 $V_{Ag/AgCl}$ for AUS-40) implies more noble electrode potential. A higher austempering temperature shifts the corrosion potential to the anodic direction. This suggests that AUS-30 is more active than AUS-40.

The other parameter, I_{corr}, is used as an index to evaluate the kinetics of corrosion resistance. AUS-30 corrodes more quickly than AUS-40 due to its higher I_{corr} value.

This phenomenon could be attributed to the cathodic behaviour of austenite and the higher amounts of austenite when isothermal transformation temperature increases. Other factors reported by Krawiec et al.[183] as the good coarsening of the austenite grains and broad ferrite needless (less ferrite/austenite interfaces) when isothermal transformation temperature increases could also support this theory.

The behaviour of the weight loss test shown in Figure 89 of the samples AUS-30 and AUS-40 agrees with the results of the electrochemical results tendency shown above. It is seen that the sample treated at 300 ºC, corrodes faster than the sample treated at 400 ºC.

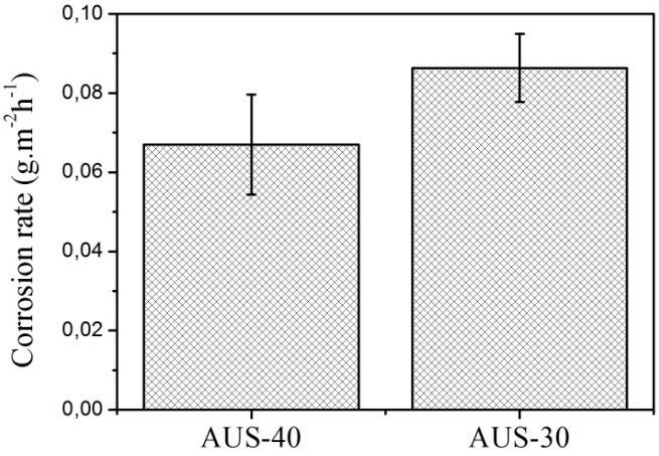

Figure 89. Weight loss tests results.

Corrosion in the studied ausferritic samples appears at graphite/matrix interfaces and at the ferrite needles. Small amounts of ferrite are usually placed at the graphite/matrix interfaces, and it is possible that ferrite acts as local anodes promoting corrosion process of this phase. This behaviour is similar to the ADI samples studied by Krawiec et al.[183.]

The cathodic behaviour of the graphite is shown in Figure 90, where the anodic matrix has been dissolved and led the graphite particles to fall down. Besides, the ferrite needles have an anodic behaviour against the austenitic matrix, and thus, they corrode easily.

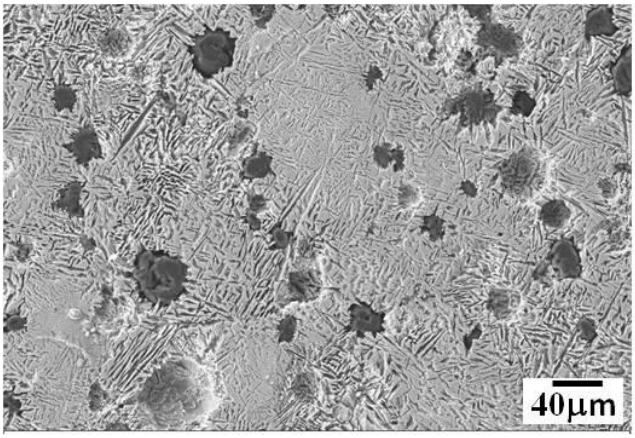

Figure 90. Cathodic behaviour of the graphite.

6.6. TECHNOLOGY DEMONSTRATOR PROTOTYPES

The technology developed on a laboratory scale and for standardized samples on the former sections of this work, was validated using a real casting of the automotive sector as a prototype. A steering knuckle shown in Figure 36 was chosen, due to its high-quality standards and its current ferritic matrix.

This casting is usually produced in an EN GJS 400-15 material, which presents a ferritic microstructure, because a high ductility is needed for the functionality of the component. The requirements of this material are shown in Table 1. It is seen that the current material of the steering knuckle presents a minimum UTS of 400 MPa, a minimum YS of 250 MPa and 15 % minimum elongation. If the YS of the material is increased, but maintaining a high ductility, the section size of the component could be reduced and consequently the weight of the casting. This is a key parameter for the automotive sector because a lighter vehicle needs less potency to be put in motion and thus less emissions to the atmosphere. Moreover, a lighter component involves a material saving, as well as less energy consumption needed to manufacture it. For these reasons and seen the advantages, a steering knuckle was chosen as a proper ausferritic as-cast technology demonstrator prototype.

The targeted chemical composition was the one shown in Table 14. The experimental chemical composition obtained from a coin chill sample is shown in Table 28.

Table 28. Chemical composition of the trials to produce the technology demonstrator prototypes (wt.%).

C	Si	Cu	Ni	Mo	Mn	Mg	S
3.48-3.58	2.03-2.07	0.14-0.16	2.91-2.97	0.20-0.21	0.17-0.21	0.046-0.051	0.008-0.010

The cooling curves were recorded in the sections shown in Figure 36, referenced as thin and thick sections. The problematic that presents a real casting, with different thermal moduli (TM) is that it is not possible to shakeout every TM at the same temperature, due to the distinct solidification times that implies a different section size.

On this case, the castings were shaken out when the thin section reached the temperature of 800 ºC and air cooled till the thin section reached the temperature of 400 ºC. At this time, they were introduced into the insulating medium (Table 10 and Figure 38-b) and held there for 90 minutes. Afterwards they were air cooled to room temperature. The thermal evolution of two castings is shown in Figure 91. The austempering temperature and holding time selection, was based on the preceding results and discussion. It is seen, that both castings follow a comparable temperature-time evolution, being the differences negligible. For this reason, the applied controlled cooling process is considered robust enough to be industrially implemented.

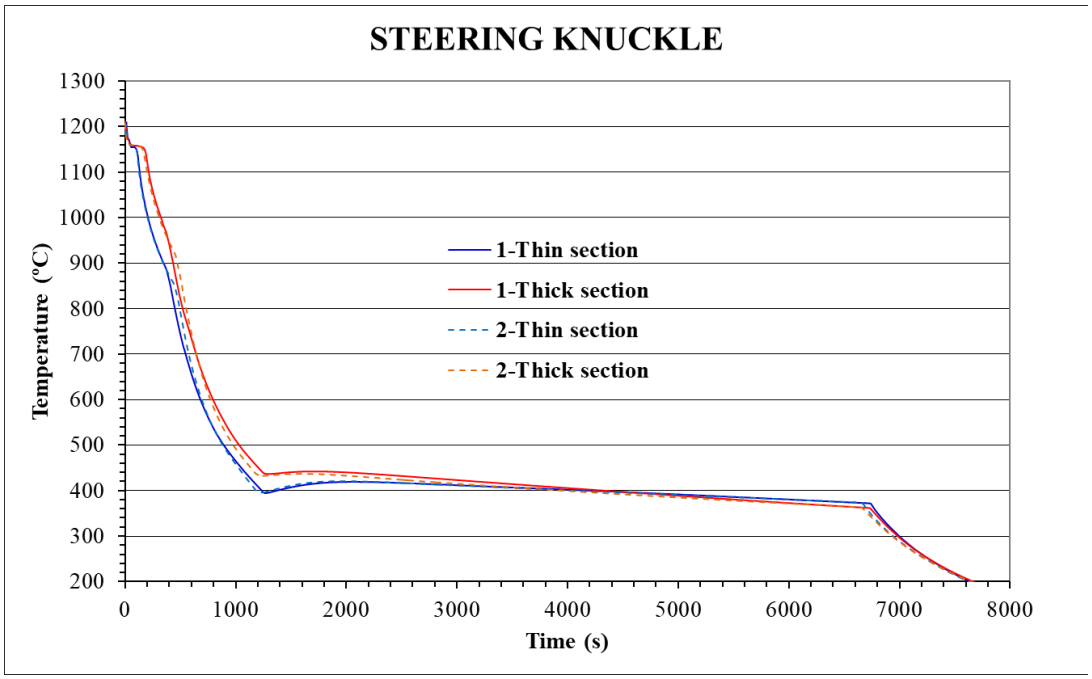

Figure 91. Cooling curves corresponding to a thin and a thick section of two steering knuckles.

There are two critical moments regarding the cooling process. The first one is the shakeout. This process was performed by mechanical means, breaking the mould. The target was to obtain a casting free of sand when the thin section reached the temperature of 800 ºC. The difficulty resides on the temperature of the thick section on that moment, since only the temperature of one section can be taken as a reference. In Figure 92 is shown a detail of the shakeout moment of the same two castings previously considered (Figure 91).

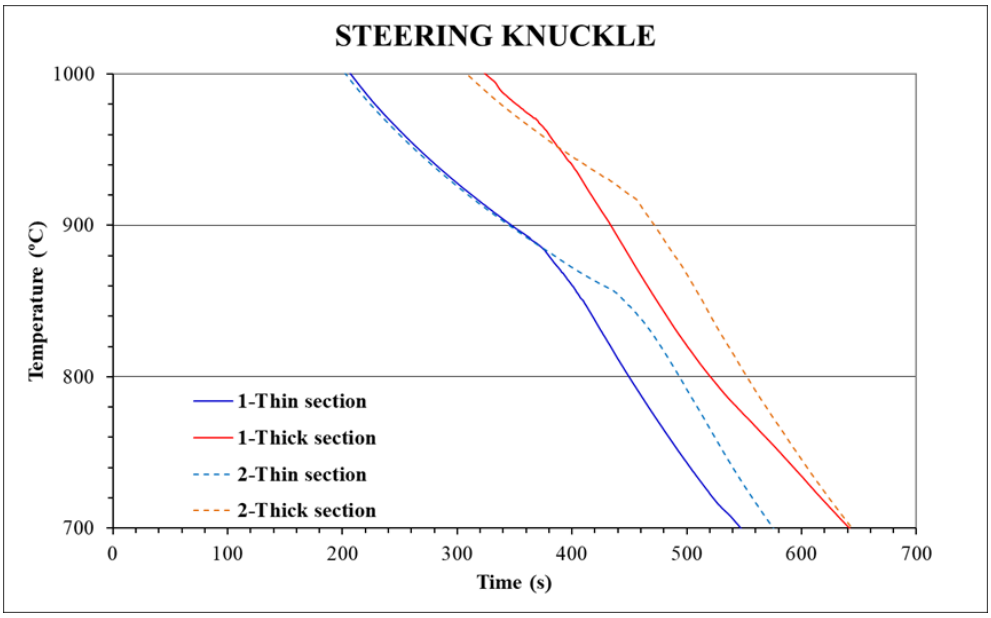

Figure 92. Detail of the shakeout moment corresponding to a thin and a thick section of two steering knuckles.

It is seen that one casting (1) was shaken out when the thin section reached the temperature of 880 ºC and the other one (2) when this section reached the temperature of 855 ºC. The thick section of both castings was at that moment at 965 and 920 ºC respectively. As said before, the target was to shakeout the thin area at 800 ºC, nevertheless, there was a divergence due to the mechanical shakeout process and that it is not immediate. With further experience this moment could be better controlled. However, one key point for the feasibility of the methodology for this casting is that at the shakeout moment, the thick section is already solid (temperature below 1050 ºC).

Another key moment of the cooling process is when the castings are introduced in the insulating medium. This moment was referenced taking into account the thin section, so that martensite formation can be avoided in that area, more precisely when it reached the temperature of 400 ºC. In Figure 93 is shown a detail of this moment. It is observed, that on the one hand, this moment is easier to control than the shakeout, since this is an immediate process, and both thin sections are at the temperature of 400 ºC when they are introduced in the insulating medium. On the other hand, the thick section is for both castings in the temperature range of 425-430 ºC.

During the austempering step into the insulating medium, the thin section is influenced by the thicker ones and consequently, its temperature in the insulating material increases at the beginning, before starting the temperature drop. This effect helps homogenising the microstructure of the different sections of a casting, as can be seen in Figure 94. Furthermore, for both castings, the cooling process is similar, so this reflects the robustness of the engineered cooling technology.

The temperature loss during the austempering step in the insulating medium is of 25 ºC for the thin section and 65-70 ºC for the thick section. These values are in a similar range as the temperature loses analysed in the section “6.2. Austempering technology” for the Y2 blocks. For this reason, this is not expected to have an influence on the final mechanical properties of the component.

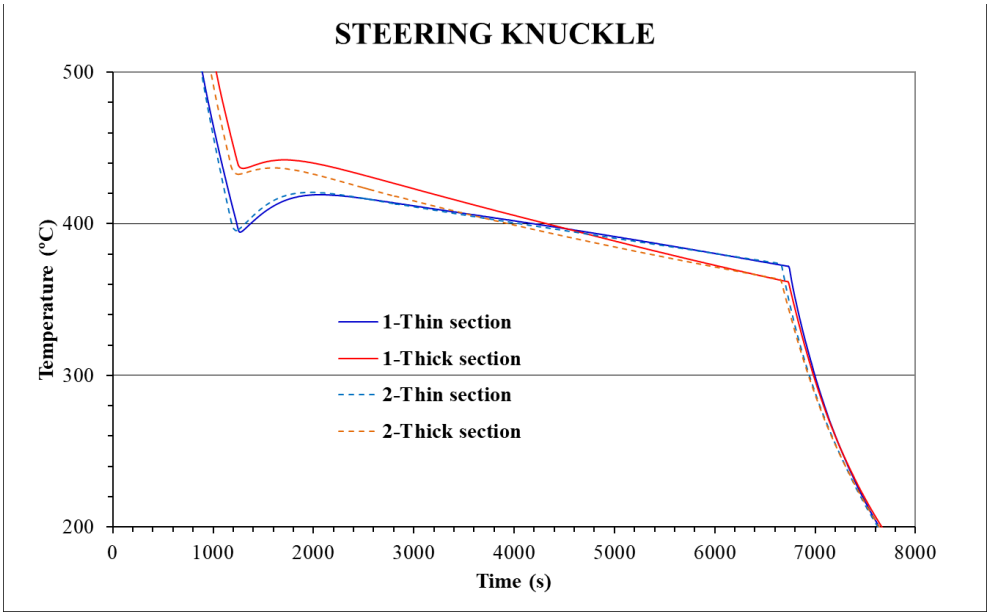

Figure 93. Detail of the austempering step corresponding to a thin and a thick section of two steering knuckles.

In Figure 94 micrographs representative of the thin and thick sections are shown. Both sections present an upper ausferritic microstructure. It is very important to point out, that even though both sections present different TM and consequently, the shakeout temperature and the temperature at which they were introduced into the insulating medium were different, the microstructure is similar. This is a key point for the as-cast technology feasibility.

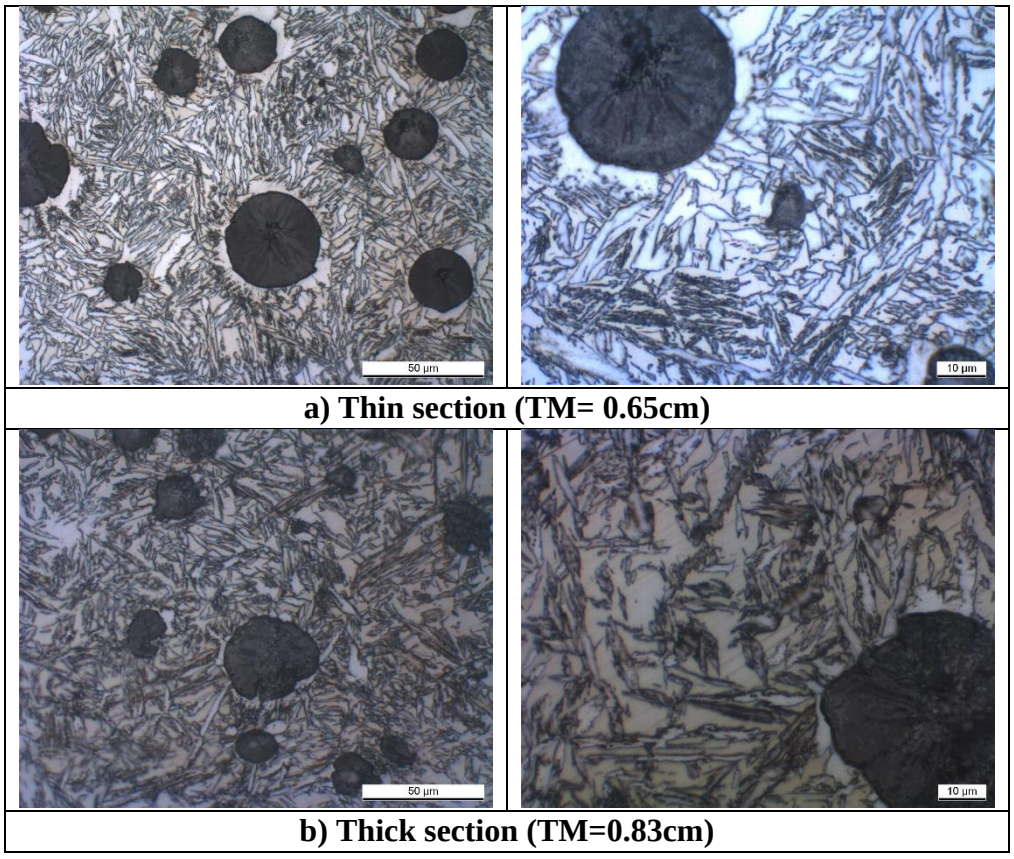

Figure 94. Micrographs of the two analysed sections of a steering knuckle. a) Thin section and b) thick section. 500x on the left column and 1000x on right column.

The mechanical properties were studied as detailed in Figure 45. The tensile test specimen was machined from the thin section and the impact resistance samples from the thick section due to space reasons. The Brinell hardness was measured from a section that presents a similar TM than the thin section (Figure 37 and Figure 45).

Table 29 presents the mechanical properties of the prototype castings.

Table 29. Mechanical properties obtained from samples machined from the steering knuckles.

UTS (MPa)	YS (MPa)	El (%)	HBW	Charpy KV room T (J)
822	589	9.2	271	13/9/12

The UTS, YS and E, as well as the hardness and impact resistance are in good accordance with the results obtained for the Y blocks shown in Table 17, Table 18, Table 20 and Table 22. They satisfy the requirements of the material EN GJS 800-8 of the standard EN 1564[32].

These results show that it is possible to obtain ausferritic ductile iron castings by means of a controlled cooling process that fulfil the requirements of the conventionally obtained ADI materials.

6.7. WORKING LIMITS MODELLING

Having defined the proper methodology to obtain as-cast ausferritic SGI microstructures, acting on the cooling process and without the need of a subsequent heat treatment on a laboratory scale, that meet the requirements of the ADI materials, the next step was to approach the industrial application of the technology. To that aim, a mathematical model was developed to make easier the several steps that are to be taken during the cooling process.

In the section “6.6. Technology demonstrator prototypes”, it was seen that for a casting presenting different TM, the shakeout temperature and the austempering temperature differ for the distinct sections, as seen in Figure 92 and Figure 93 respectively. For this reason, as a first approach for the industrial application of the controlled cooling technology, a model was developed, to define the working window in terms of TM differences that the engineered cooling technology offers, determining as a first step the applicability of the methodology for a given component and besides, stablishing when the shakeout and isothermal transformation steps should be carried out in order to get the desired mechanical properties.

The model defines the working limits of the controlled cooling technology. In the first place, it says if a given casting is feasible to be produced by the as-cast methodology that has been previously described in this work. The geometry and the TM range that it presents are the variables that can restrict the feasibility. If it is not feasible, then that is the output of the model. If it is feasible, then the model defines the minimum alloy content to avoid the pearlitic nose for the TM range of the casting that is being studied. In this case, the highest TM is considered, because this is the limiting for perlite apparition, since it presents the lowest cooling rate.

Once defined the alloying content, the model approaches the shakeout and the austempering steps. For the first one, it defines the optimal moment to carry it out, taking into account the temperature gradient inside the casting after the solidification, due to the distinct solidification times that present the different TM. For the second one, considering an air-cooling process, the model defines at which temperature are going to be the different sections of the casting, when they are to be introduced into the insulating medium. Depending on the desired mechanical properties, this temperature can be adjusted. When the austempering temperature is defined, then the model predicts the HBW and the UTS for the different sections of the casting. In Figure 95 is shown the architecture of the model.

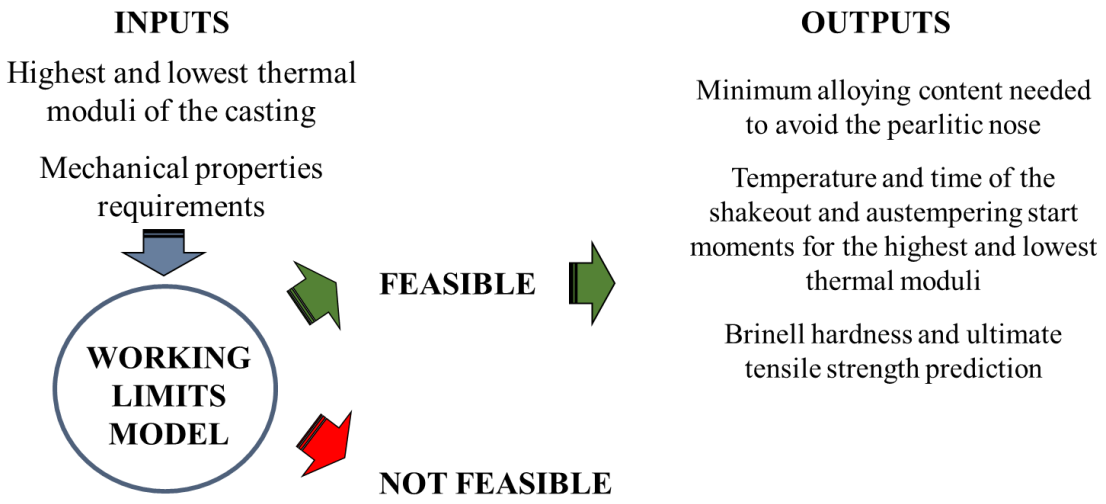

Figure 95. Architecture of the model for the industrial application of the engineered cooled technology.

To develop the model, the results of the trials described in the former sections of this work were used. The model is completely experimental.

The minimum alloying content was defined using the series of experiments described in the section "6.1. Alloy definition". The low alloyed chemical composition was not considered, since the cooling rate (CR) needed to avoid the pearlitic nose is too high so as to be reached by an air-cooling process. For this reason, the chemical composition range for which the model is valid is shown in Table 30.

Table 30. Chemical composition range for which the model was validated.

C	Si	Cu	Ni	Mo	Mn
3.60-3.75	2.05-2.15	0.09-1.04	2.86-5.05	0.01-0.22	<0.30

As a first step of the experimental model, an equation to calculate the minimum cooling rate (CR_{min}) needed to avoid the pearlitic nose as a function of the nickel, copper and molybdenum contents was developed for the studied chemical compositions. This is shown in Equation 9 and it was defined, relating the CR_{min} defined for the different alloy contents shown in Table 13, with the nickel, copper and molybdenum content of each alloy.

Equation 9 $CRmin = 2.35 - 0.33\ \%\ Ni - 0.10\ \%\ Cu - 4.0\ \%\ Mo$

The CR value that must be higher than the CR_{min} given by the Equation 9, is the CR defined by the highest TM of the casting that is being studied. To that aim, the TM is related to the CR when the cooling process is performed in air and no pearlite is present in the microstructure, as shown in Figure 54. This relationship is shown in Equation 10. This equation is valid for a TM range between 0.40-1.75 cm, since this was the studied range.

Equation 10 $CR = 0.6494\ TM^{-0.736}$

Considering the CR given by the Equation 10, then the alloy content must be high enough to guarantee that the CRmin obtained by the Equation 9 is equal or higher than that.

The second step of the experimental model deals with the definition of the thickness window in which this methodology is valid. The need to establish a thickness window is because a casting has different sections and consequently different TM. The higher the TM, the longer the solidification process and the lower the cooling rate. Thus, when the TM increases, the longer the time needed to reach the shakeout temperature and the austempering temperature. If a casting presents different TM, then, it is not possible to shakeout the distinct sections at the temperature of 800 ºC that was defined as optimum in the section "6.3. High temperature shakeout definition". Moreover, the austempering temperature will be different for the different TM, because they are introduced into the insulating medium at the same moment. For these reasons, the shakeout and austempering temperatures must be limited and outside those limits, the engineered cooling methodology is not considered feasible.

Considering the shakeout process, it cannot be carried out at any temperature. The upper limit is defined by the solidification process. A casting cannot be shaken out if it is still liquid, because then it would flow and loose its form. Additionally, shaking out a casting which is not completely solid can lead to casting defects such as microporosity or high thermal stress. For these reasons, the shakeout upper limit was defined as 1050 ºC, which is around 50 ºC below the solidus temperature for SGI materials[75, 83].

On the other hand, the lower limit is defined by the eutectoid transformation temperature. If the shakeout is performed once the eutectoid transformation temperature was reached, then the eutectoid transformation has taken place before the CR was increased enough to avoid the pearlite formation due to the air cooling. Consequently, pearlite forms. For this reason, the lower limit for the shakeout process was defined as the eutectoid temperature. This temperature is a function of the TM and the alloy content. Figure 96 shows the influence of the TM and the content of alloying elements on the eutectoid transformation temperature for the three alloys that were considered for the development of the model. This relationship is extracted from curves like the ones shown in Figure 47.

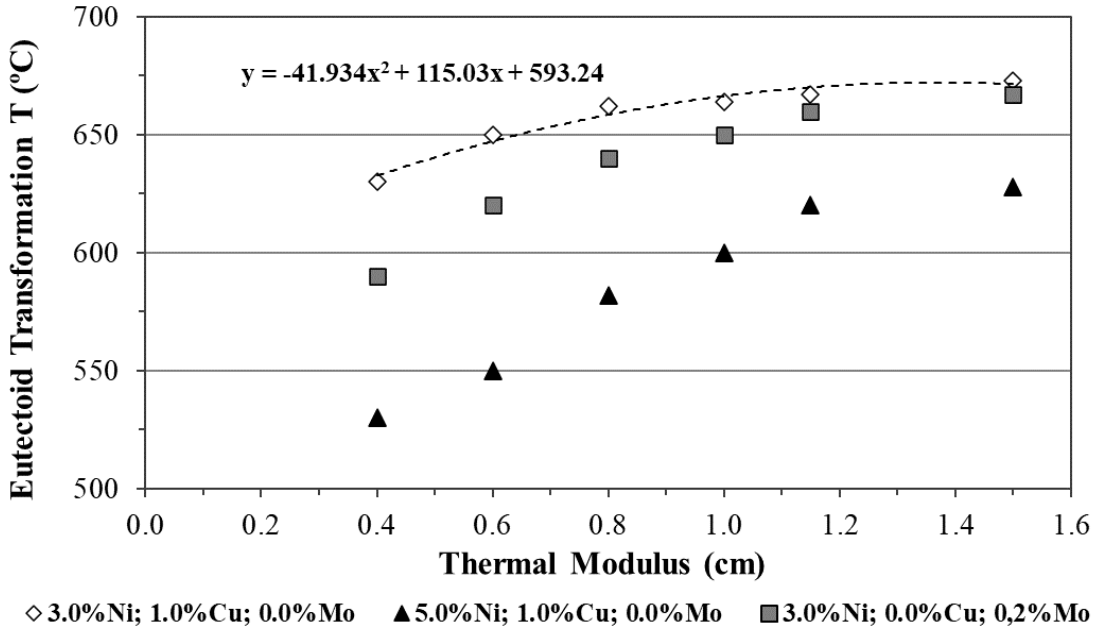

Figure 96. Influence of the content of alloying elements and of the thermal modulus on the eutectoid transformation temperature.

To define the lower limit of the shakeout temperature, the most restrictive of the curves, was considered. This corresponds to the 3.0 % Ni, 1.0 % Cu, 0.0 % Mo alloy. The Equation 11 fits the experimental results for this alloy and defines the eutectoid transformation temperature (T_{etd}) in ºC as a function of the TM. It represents the lower limit for the shakeout temperature to avoid the formation of pearlite.

Equation 11. $T_{etd} = - 41.93\ TM^2 + 115.03\ TM + 593.24$

Taking into account the experimental results with the castings of the cylinders and plates (Figure 34) with different TM, in which the solidification time and the subsequent cooling in the mould till the shakeout moment was recorded. The shakeout temperature was calculated as a function of the TM, considering that they are in the same mould. In Figure 97 is shown this relationship as the vertical dotted lines. At the same moment or time, this vertical line relates the temperature to the TM. This relationship is plotted in Figure 98. These data were gathered from the experiment series described in section "6.1. Alloy definition", an example shown in Figure 47 and in Figure 48.

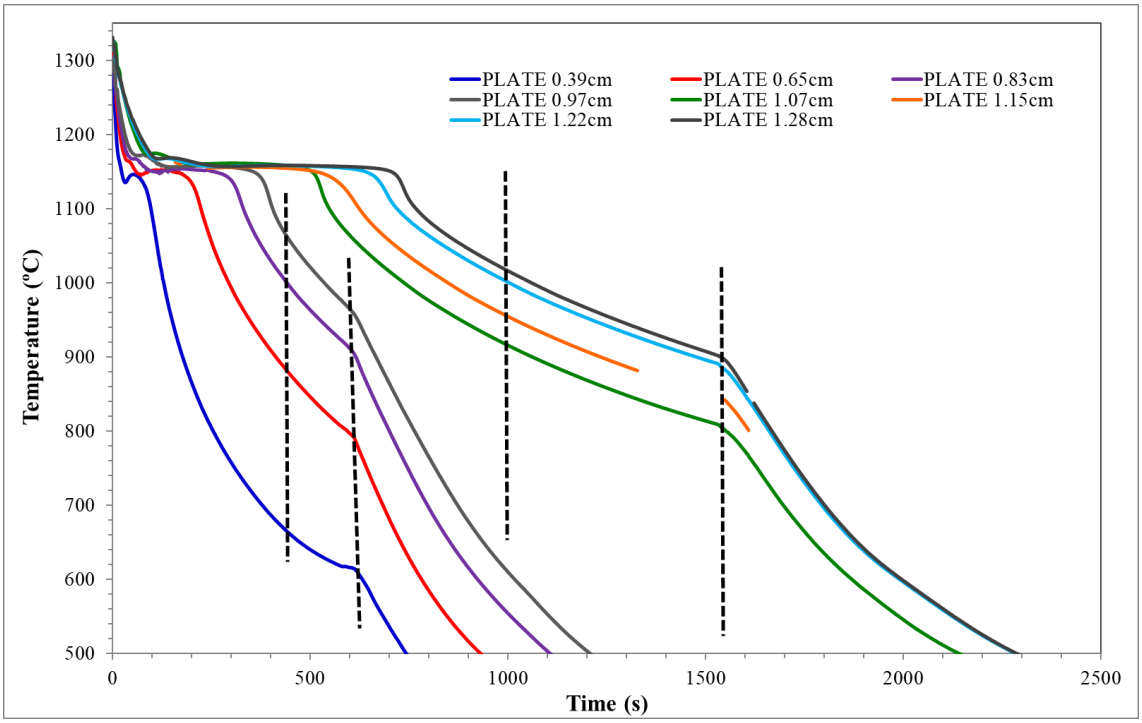

Figure 97. Shakeout temperature calculation for different TM of a casting.

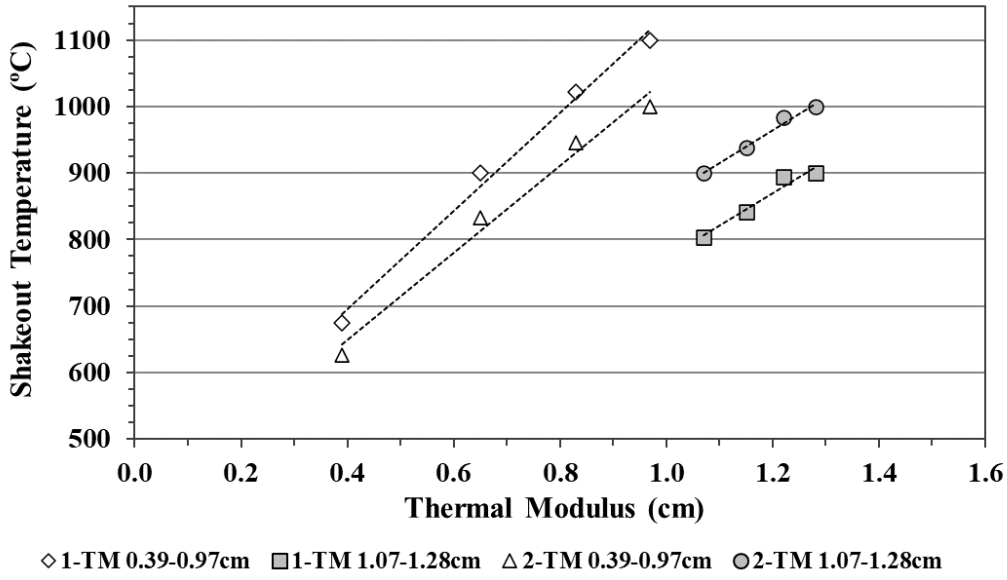

Figure 98. Relationship between temperature and TM when cooling in the mould.

It is seen that a straight line relates the shakeout temperature to the TM. Considering all the trials, the relationship shown in Equation 12 was obtained, as an average value. TM in the range between 0.4 and 1.3 cm were studied.

Equation 12 $T_{shkout\_TM} = 568.40\ TM - 341.04 + T_{shkout\_0.6cm}$

$T_{shkout\_0.6cm}$ is the shakeout temperature for a TM of 0.6 cm and T_{shkout_TM} is the shakeout temperature of the TM that is being studied.

In Figure 99 is shown the data used to develop the Equation 12 and how it fits the experimental results. It is seen that the experimental results are well fitted by the straight-line approach.

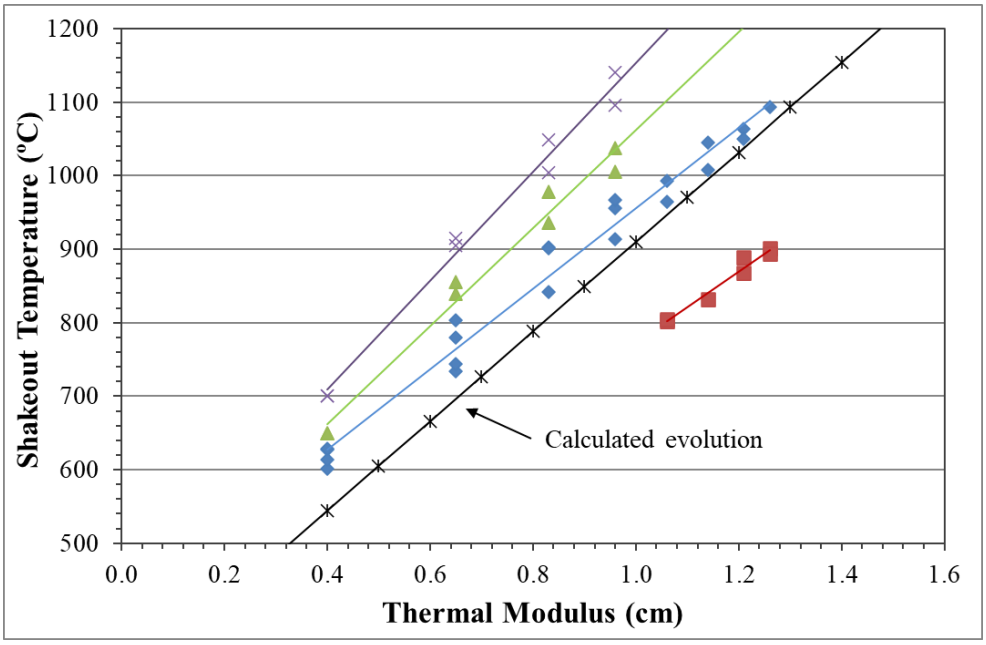

Figure 99. Fitting of the experimental results of the shakeout temperature calculation as a function of the TM.

In order to define the vertical positioning of the straight line defined by the Equation 12, the value of the shakeout temperature for a TM = 0.6 cm ($T_{shkout\_0.6cm}$) is considered as a reference for all the alloys. This reference value is needed to change the time of the shakeout, which enables to fit, for the different sections, the shakeout temperature into the range defined by the upper and lower limit (vertical positioning of the straight line). This is a constant determined by an iterative calculus method.

For a given casting, the model can calculate several shakeout times that make the process feasible. The iterative method chooses for the value of the TM = 0.6 cm, the one that gives the lower shakeout temperature, with the aim of reducing the thermal stress due to a high temperature shakeout, and for having a longer time to face the shakeout after the pouring process.

The result of this step is the shakeout temperature for the minimum and maximum TM of a casting.

The described calculation regarding the shakeout temperature is shown in Figure 100. It also shows the possibility to change the maximum and minimum TM of the casting.

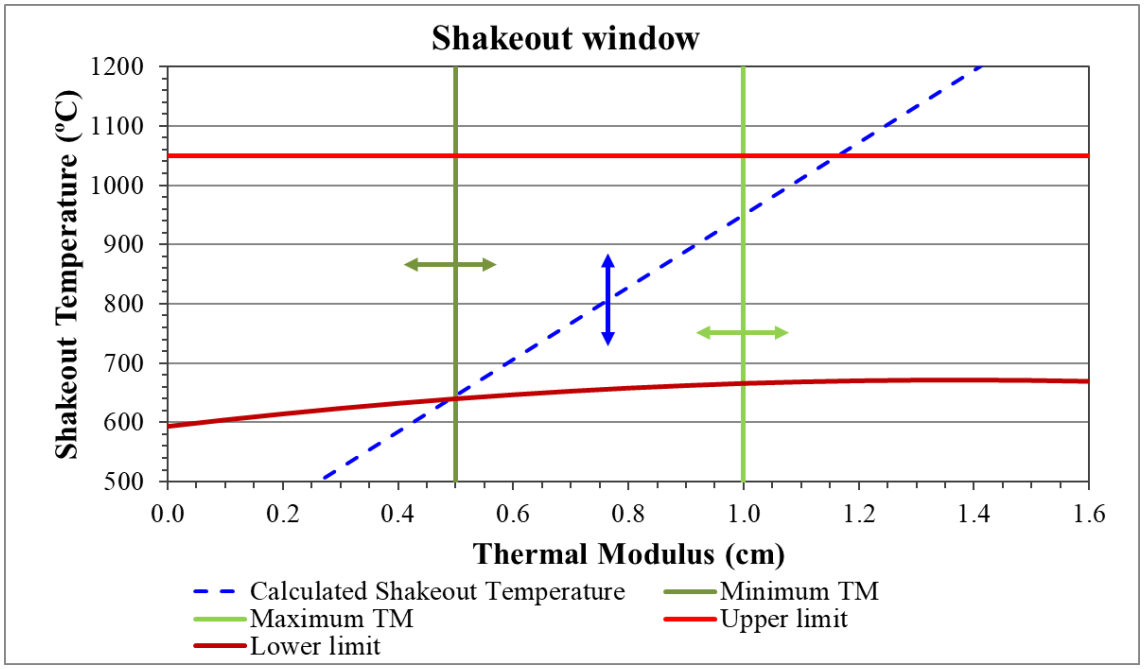

Figure 100. Graphical description of the calculation of the optimum shakeout temperature for the different TM of a casting.

The aim of the engineered cooling process is to obtain fully ausferritic microstructures. Therefore, once the composition to avoid the pearlitic nose is defined, as well as the shakeout temperature as a function of the different TM of a casting, the next step is to define the isothermal transformation or austempering temperature.

As happened for the shakeout temperature, the temperature at which the different TM of a casting are to be introduced into the insulating medium was calculated based on the experimental results shown in the previous sections. On this case, the effect of the cooling in the mould till the shakeout temperature was considered, together with the subsequent air cooling to the austempering temperature.

Taking into account the experimental results with the castings of the cylinders and plates (Figure 34) with different TM, early shaken out, in which the solidification time and the subsequent cooling in the mould till the shakeout moment and subsequent air cooling to the austempering temperature was recorded, the austempering temperature was calculated as a function of the TM. In Figure 101 is shown an example of this relationship as the vertical dotted lines. At the same moment or time, this vertical line relates the austempering temperature to the TM. This relationship is plotted in Figure 102. These data were gathered from the experiment series described in section "6.1. Alloy definition", an example shown in Figure 48.

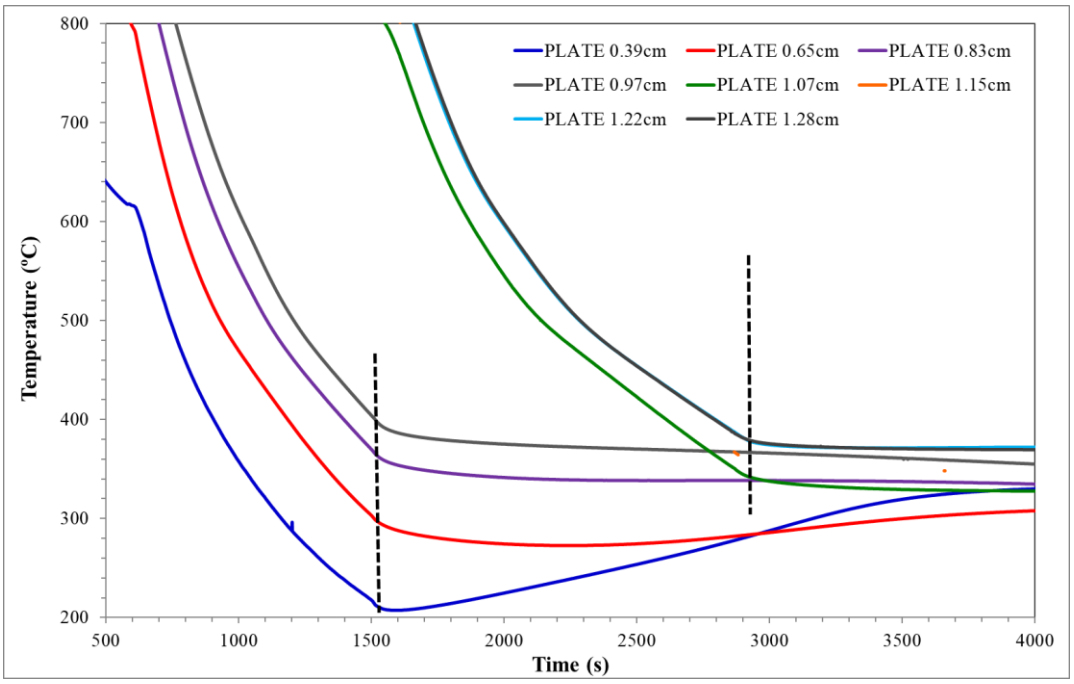

Figure 101. Austempering temperature calculation for the different TM of a casting.

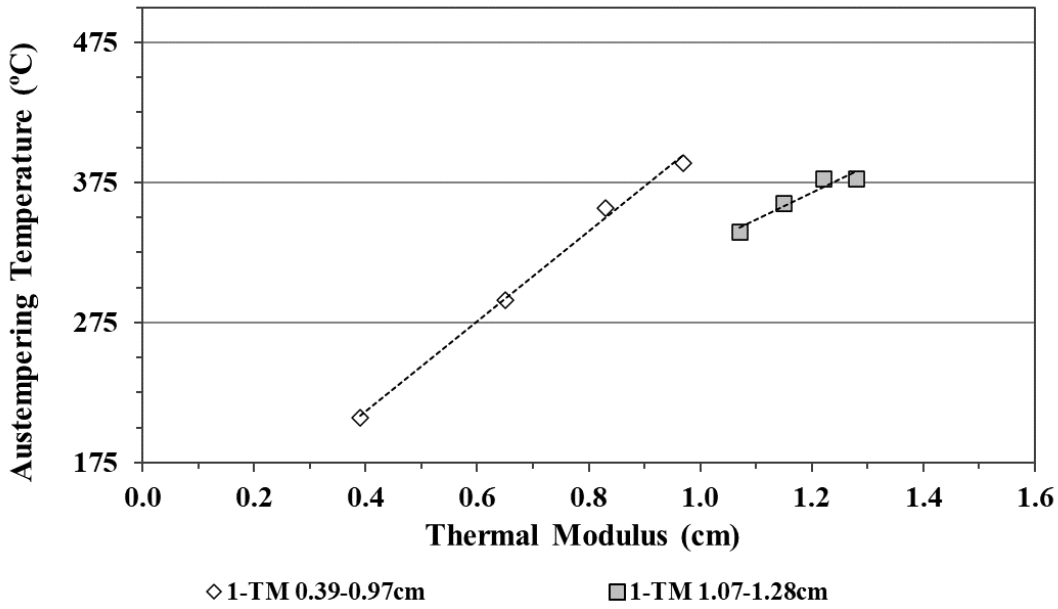

Figure 102. Relationship between the austempering temperature and TM when cooling in the mould.

Like in the former step, the model calculates the austempering temperature as a function of the TM as shown in Equation 13. This equation was obtained, as an average value. TM in the range between 0.4 and 1.3 cm were studied.

Equation 13. $T_{temp\_TM} = 293.39\ TM - 180 + T_{temp\_0.6cm}$

$T_{temp\_0.6cm}$ is the austempering temperature for a TM of 0.6 cm and T_{temp_TM} is the austempering temperature of the TM that is being studied.

Following the same methodology as for the shakeout temperature, the value of the austempering temperature for the TM = 0.6 cm ($T_{temp\_0.6cm}$) is taken as a reference value. This reference value adjusts the austempering temperature of the different TM into the defined range by an iterative method (vertical positioning of the straight line).

The results of the adjustment between the calculated austempering temperature and the experimental data is shown in Figure 103. It is seen that the experimental results are well fitted by the straight-line approach.

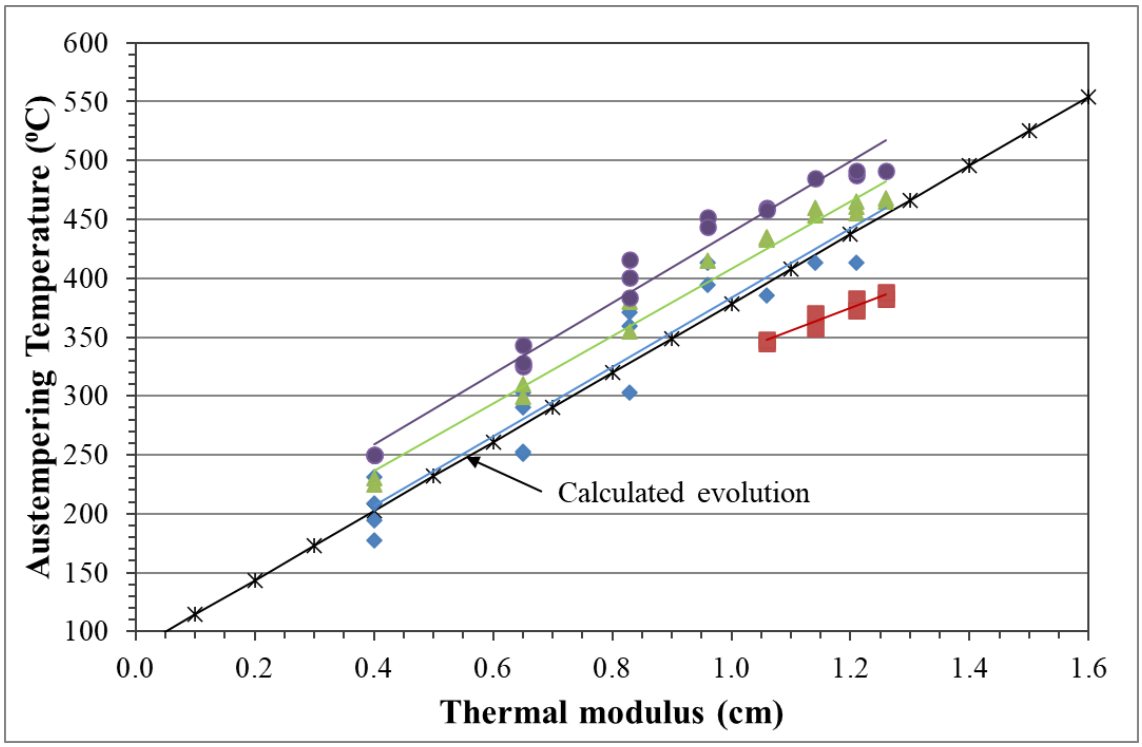

Figure 103. Fitting of the experimental results of the austempering temperature calculation as a function of the TM.

The isothermal transformation must take place within a temperature range to obtain the desired microstructure and thus the mechanical properties that satisfy the requirements of the ADI materials. For this reason, the austempering temperature window must be limited.

The upper limit was considered as 450 ºC. Above this temperature experimental evidence (Table 16) showed that the obtained ausferrite did not produce the desired mechanical properties, which is in good agreement with the literature[107].

The lower limit is defined by the martensite formation start temperature (M_s). For the alloy considered on this part of the work (Table 14), the M_s was defined by dilatometry tests. For the dilatometry tests, when the CR was high enough so as to avoid the pearlite and ausferrite formation, then the resulting microstructure is martensite. The M formation affects to the dimension of the sample, and consequently, the Ms can be defined by the dilatation effect that the M formation implies. An example is shown in Figure 104. The microstructure of this sample is shown in Figure 105. In this case, the M_s was defined as 170 ºC. For other alloys, further analysis should be carried out and relate this temperature to the content of alloying elements[141].

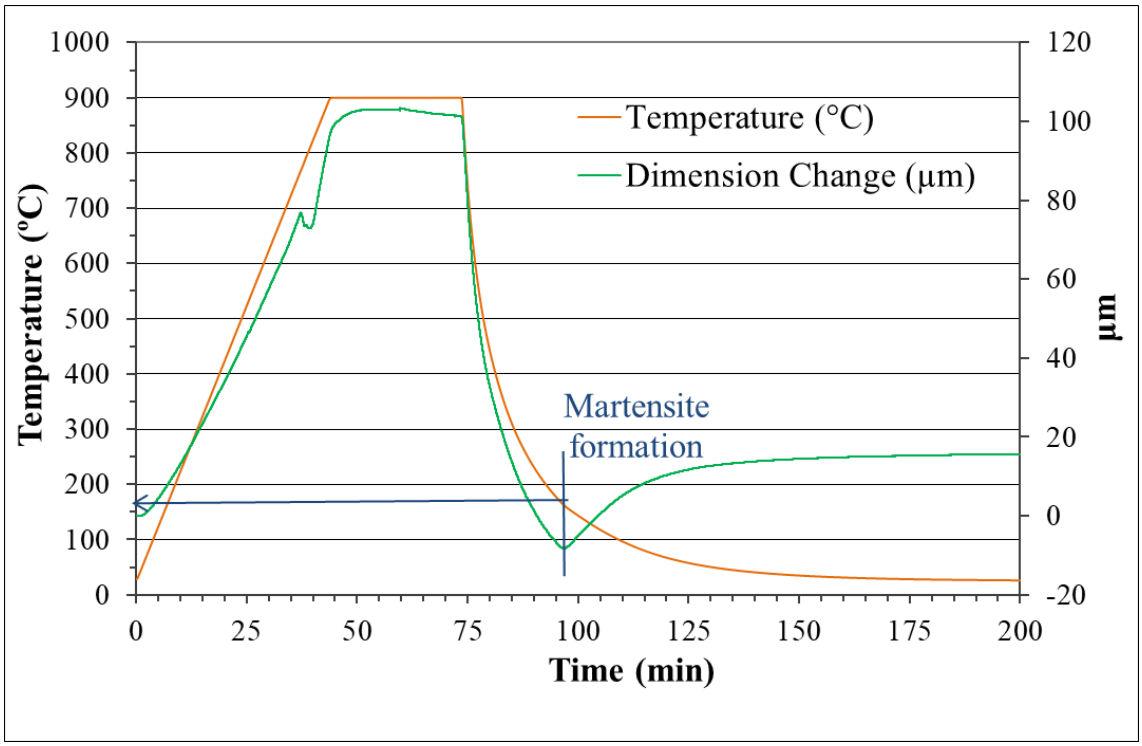

Figure 104. Martensite formation start temperature defined by dilatometry.

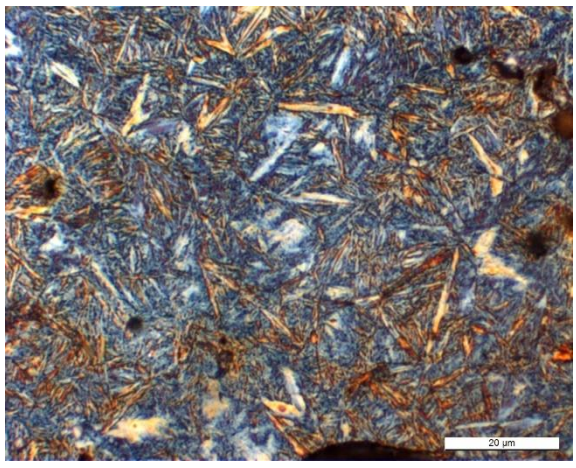

Figure 105. Martensitic microstructure obtained by dilatometry tests. 1000x.

Considering the Equation 13 and the limits for the ausferritic transformation, the model establishes if a particular casting can be produced following this methodology and when feasible, the temperature at which the different TM of the casting should be introduced into the insulating medium. This is shown in Figure 106.

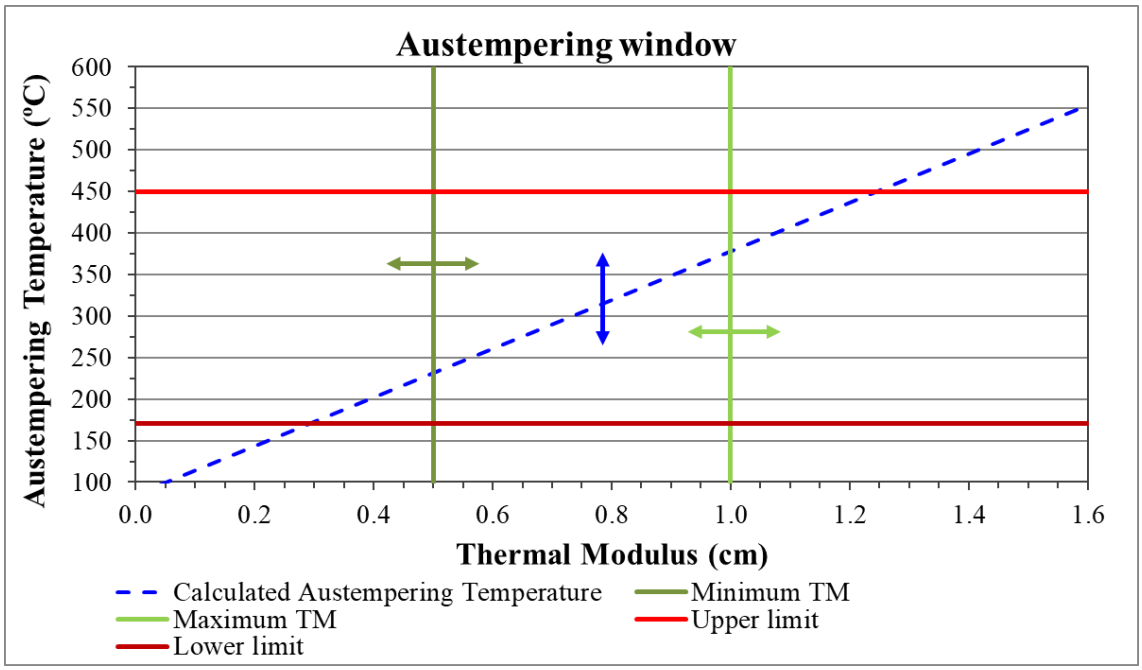

Figure 106. Graphical description of the calculation of the austempering temperature for the different TM of a casting.

From the different possibilities offered by the iterative calculation, the optimum solution is the one that enables to obtain the desired mechanical properties in terms of UTS and hardness. The value of the constant $T_{temp\_0.6cm}$ is defined consequently, based on the UTS and HBW requirements.

In order to define the optimal austempering temperature, the mechanical properties of the plates (Figure 34-b) were analysed by means of tensile and hardness tests. Table 31 shows the results obtained from these tests for the different TM. Additionally, the austempering temperature or the temperature at which the samples were introduced into the insulating medium is shown.

Table 31 Mechanical properties of the plates castings as a function of the austempering temperature.

TM (cm)	T_{temp} (ºC)	UTS (MPa)	YS (MPa)	E (%)	HBW
0.39	214	813	560	1.3	293
0.65	251	917	559	2.2	343
0.65	253	1020	569	2.4	356
0.65	290	938	670	6.5	319
0.83	303	1040	614	7.1	321
0.83	359	887	610	10.4	285
0.97	--	848	548	3.9*	308
0.97	394	839	595	6.9	265
1.07	385	846	627	7.9	288
1.07	345	889	682	6.3	295
1.15	413	822	552	11.3	280
1.15	358	879	630	9.0	288
1.22	413	760	552	7.9	263
1.22	383	815	629	4.9	285
1.28	--	775	573	7.0	266
1.28	383	829	623	7.3	286

* Microshrinkage on the surface of the specimen.

In Table 32 are shown the results of the metallographic analysis performed on an area close to the fracture surface of the tensile tests specimens.

Table 32. Microstructure volume fractions of the plates castings as a function of the austempering temperature.

TM (cm)	T_{temp} (ºC)	Upper acicular ferrite	Lower acicular ferrite	Total acicular ferrite	Reacted austenite	Pearlite	Martensite
0.39	214	0.10	0.38	0.48	0.27	0.25	0.00
0.65	251	0.24	0.36	0.60	0.35	0.00	0.05
0.65	253	0.18	0.45	0.63	0.34	0.00	0.03
0.65	290	0.23	0.45	0.68	0.30	0.00	0.02
0.83	303	0.33	0.30	0.63	0.35	0.00	0.02
0.83	359	0.39	0.15	0.54	0.46	0.00	0.00
0.97	--	0.39	0.19	0.58	0.39	0.00	0.03
0.97	394	0.51	0.05	0.56	0.44	0.00	0.00
1.07	385	0.51	0.00	0.51	0.49	0.00	0.00
1.07	345	0.40	0.18	0.58	0.38	0.02	0.02
1.15	413	0.51	0.00	0.51	0.48	0.00	0.01
1.15	358	0.50	0.03	0.53	0.44	0.03	0.00
1.22	413	0.53	0.00	0.53	0.47	0.00	0.00
1.22	383	0.54	0.00	0.54	0.41	0.03	0.02
1.28	--	0.51	0.00	0.51	0.45	0.00	0.04
1.28	383	0.53	0.00	0.53	0.43	0.04	0.00

Apart from the sample with a TM 0.39 cm, it is seen that only traces of pearlite or martensite appear (≤5 %) on the different samples, so it could be assumed, that the mechanical properties are not negatively influenced by these phases' precipitation. Therefore, the mechanical properties could be related to the austempering temperature and consequently to the UAF and LAF appearance.

As an example of the microstructure evolution with the TM, in Figure 107 are shown the microstructures obtained for the different TM in the same trials. It is observed that the lower TM is associated with a higher amount of lower ausferrite, due to the lower austempering temperature. This results in higher strength for the lower TM, but lower ductility.

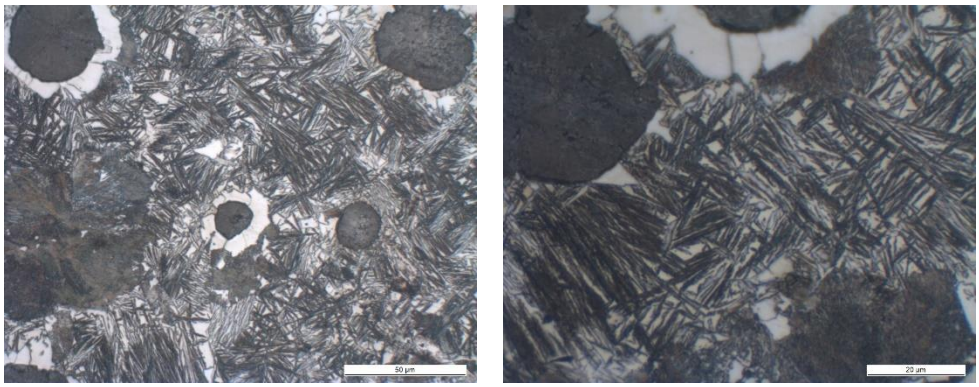

a) Microstructure for TM 0.39 cm and T_{temp} 214ºC

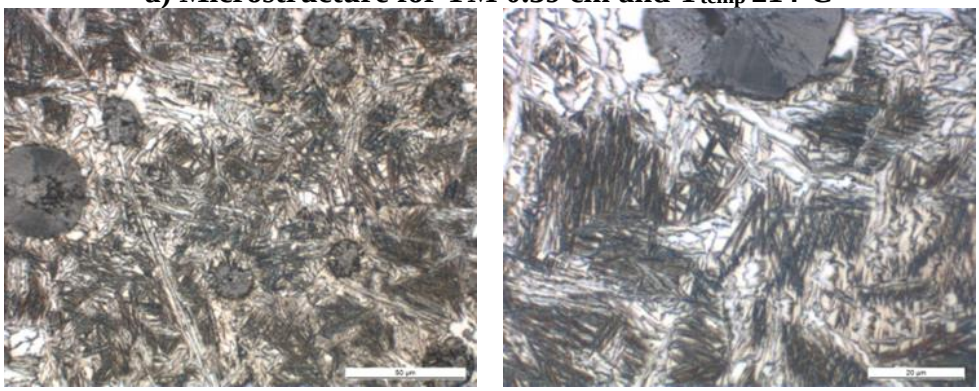

b) Microstructure for TM 0.65 cm and T_{temp} 251ºC

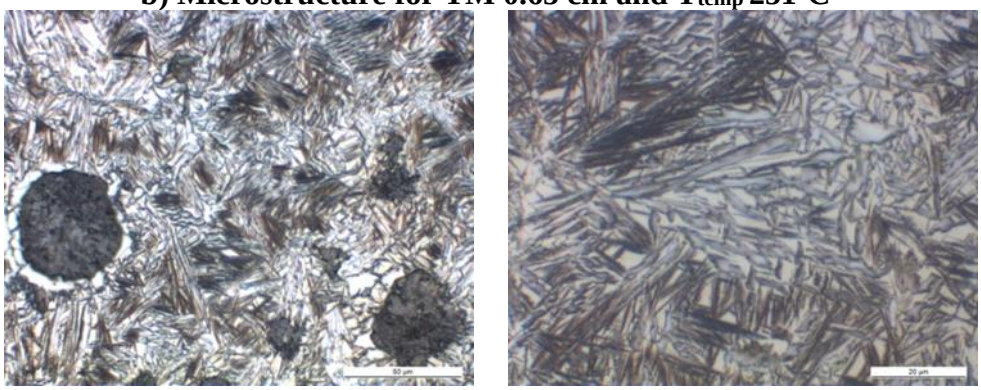

c) Microstructure TM 0.83 cm and T_{temp} 303 ºC

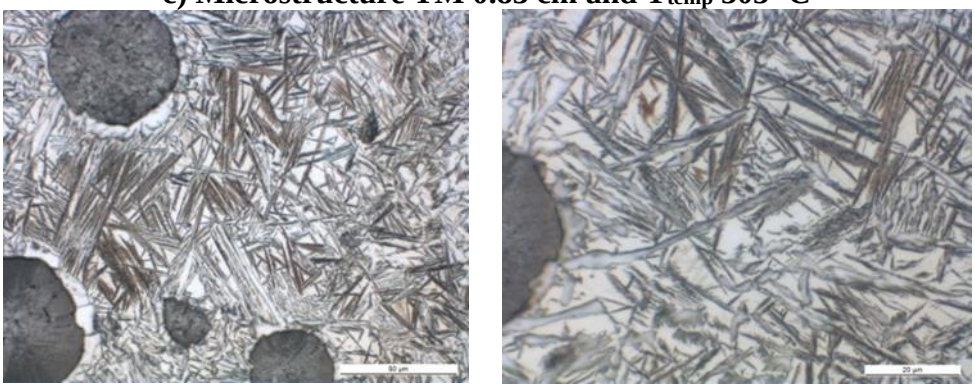

d) Microstructure TM 0.97 cm and T_{temp} -- ºC

Figure 107. Microstructure evolution with the TM for the plates castings. 500x on the left column and 1000x on the right column.

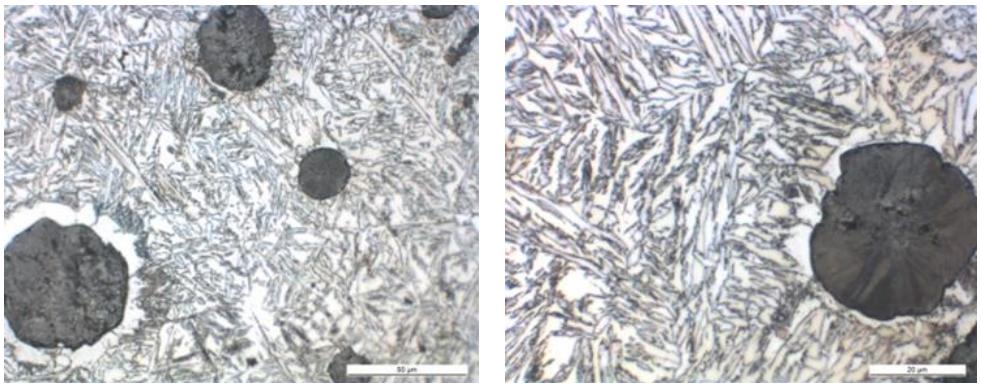

e) Microstructure TM 1.06 cm and T_{temp} 385 ºC

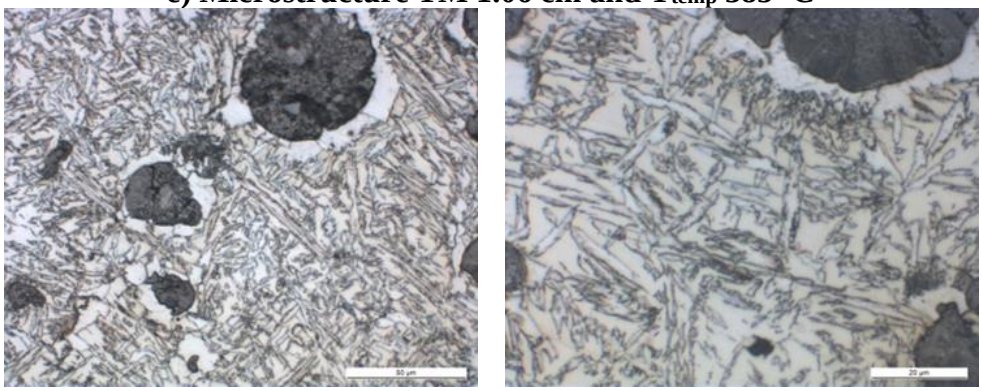

f) Microstructure TM 1.14 cm and T_{temp} 413 ºC

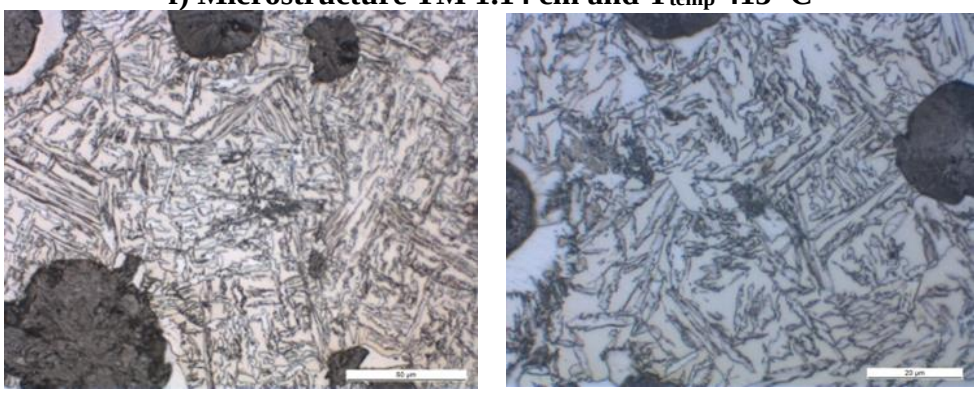

g) Microstructure TM 1.21 cm and T_{temp} 413 ºC

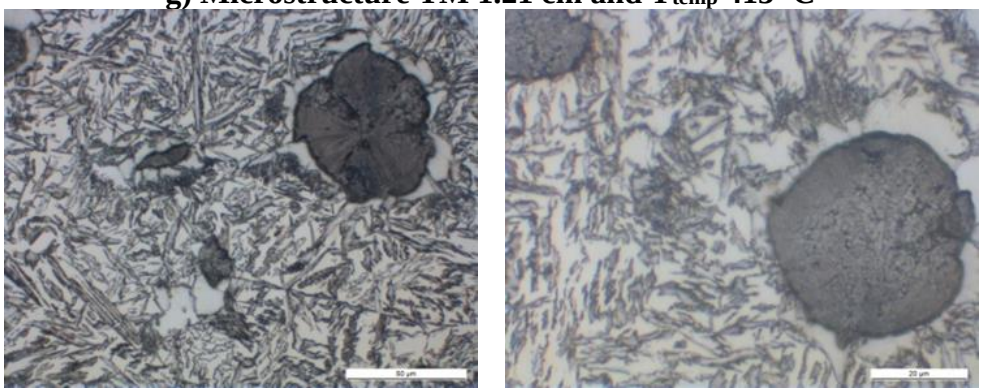

h) Microstructure TM 1.26 cm and T_{temp} -- ºC

Figure 107 (Cont.) Microstructure evolution with the TM for the plates castings. 500x on the left column and 1000x on the right column.

Depending on the TM, and consequently on the processing temperatures of the samples, different ADI grades were obtained (Table 31). The relationship between the mechanical properties and the austempering temperature is shown in Figure 108.

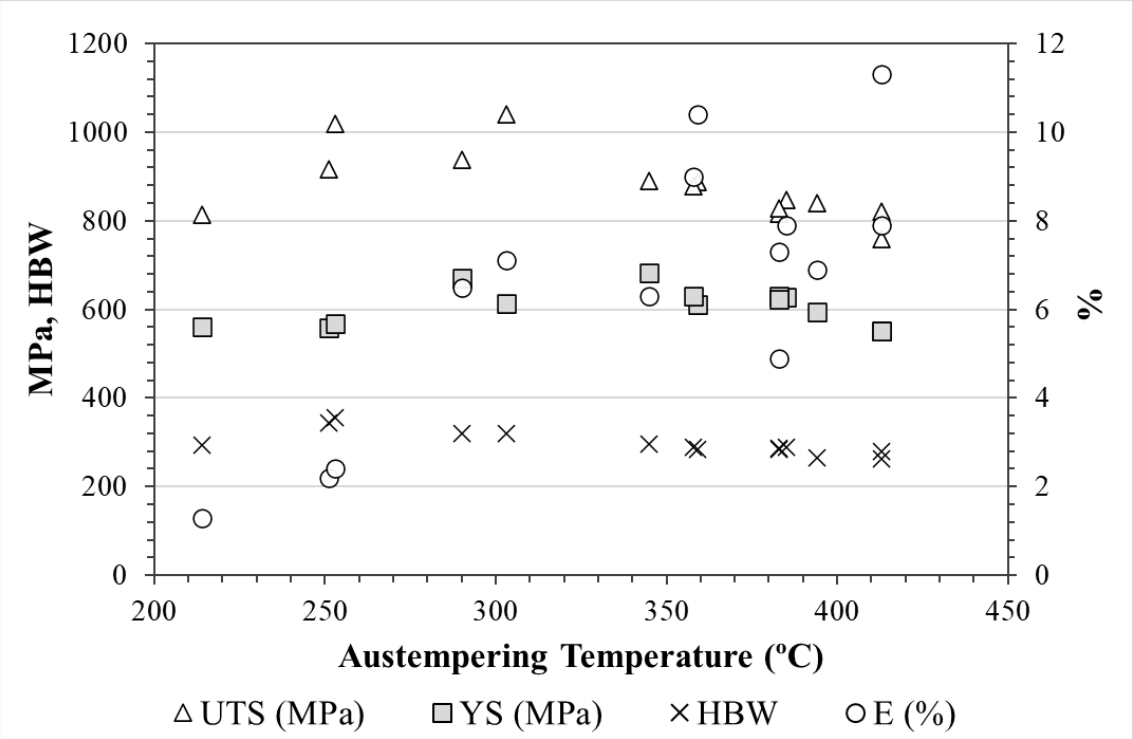

Figure 108. Evolution of the mechanical properties of the plates as a function of the austempering temperature.

The casting with the lowest austempering temperature should not be considered for the analysis due to the pearlite formation. Apart from that, as in former results, the E increases with the austempering temperature. Nevertheless, the scattering of the results is high. This could be due to the high sensitivity of this property on casting defects like microporosity and the tendency of these plates to present this kind of problematic. The YS, in contrast to the previous results, does not present any clear relationship. It seems to be more or less constant regardless of the isothermal transformation temperature. This could also be related to the nature of the plates. However, the UTS and HBW show a clear tendency linked to the isothermal transformation temperature. The higher this temperature the lower these properties. This leads to the assumption that, depending on the ADI grade that is being targeted, the optimum transformation temperature will be higher or lower, which is in good accordance with the formerly presented results.

A statistical analysis based on the Pearson correlation was carried out with all the experimental data shown in this work in order to relate the process parameters to the mechanical properties. These results are shown in Table 33. This correlation indicates the strength of a linear relationship between two variables.

Table 33. Results of the statistical analysis relating the mechanical properties and the processing temperatures.

	UTS	YS	E	HBW	Charpy	TM	T_{shkout} (ºC)	T_{temp} (ºC)	T_{loss} (ºC)	N	P	M
UTS	1.00	0.11	0.01	0.67	-0.01	-0.52	-0.33	-0.59	-0.46	-0.31	-0.59	-0.21
YS	0.11	1.00	-0.36	0.42	0.54	0.02	-0.03	-0.57	-0.02	0.05	0.11	-0.63
E	0.01	-0.36	1.00	-0.45	0.63	-0.07	-0.04	0.60	0.46	-0.44	-0.03	-0.29
HBW	0.67	0.42	-0.45	1.00	-0.07	-0.30	-0.21	-0.88	-0.56	0.10	-0.35	-0.19
Charpy	-0.01	0.54	0.63	-0.07	1.00	--	0.09	0.17	0.30	-0.54	--	-0.71
TM	-0.52	0.02	-0.07	-0.30	--	1.00	0.89	0.46	0.56	0.52	0.38	--
T_{shkout} (ºC)	-0.33	-0.03	-0.04	-0.21	0.09	0.89	1.00	0.46	0.49	0.39	0.23	-0.42
T_{temp} (ºC)	-0.59	-0.57	0.60	-0.88	0.17	0.46	0.46	1.00	0.60	-0.02	0.31	-0.01
T_{loss} (ºC)	-0.46	-0.02	0.46	-0.56	0.30	0.56	0.49	0.60	1.00	0.12	0.02	-0.23
N	-0.31	0.05	-0.44	0.10	-0.54	0.52	0.39	-0.02	0.12	1.00	0.05	0.73
P	-0.59	0.11	-0.03	-0.35	--	0.38	0.23	0.31	0.02	0.05	1.00	--
M	-0.21	-0.63	-0.29	-0.19	-0.71	--	-0.42	-0.01	-0.23	0.73	--	1.00

Being N nodule count, P pearlite and T_{loss} refers to the temperature loss in the insulating medium.

It is seen that the process parameter that has a greater influence on the mechanical properties (higher correlation values) is the isothermal transformation or austempering temperature.

With these data and seen that the UTS and HBW are the properties that seem to present the most robust tendency with the austempering temperature, it is possible to relate both properties to the temperature like expressed in Equation 14 and Equation 15. These equations are obtained from the results shown in Figure 108 and Table 31.

Equation 14 $UTS = - 1.2331\ T_{temp} + 1308.2$

Equation 15 $HBW = - 0.483\ T_{temp} + 466.34$

The relationship between the prediction of the UTS and HBW with the experimental results is shown in Figure 109. The results from the casting with a TM of 0.39 cm were removed due to the pearlite appearance. It is observed that the prediction fits properly the experimental results.

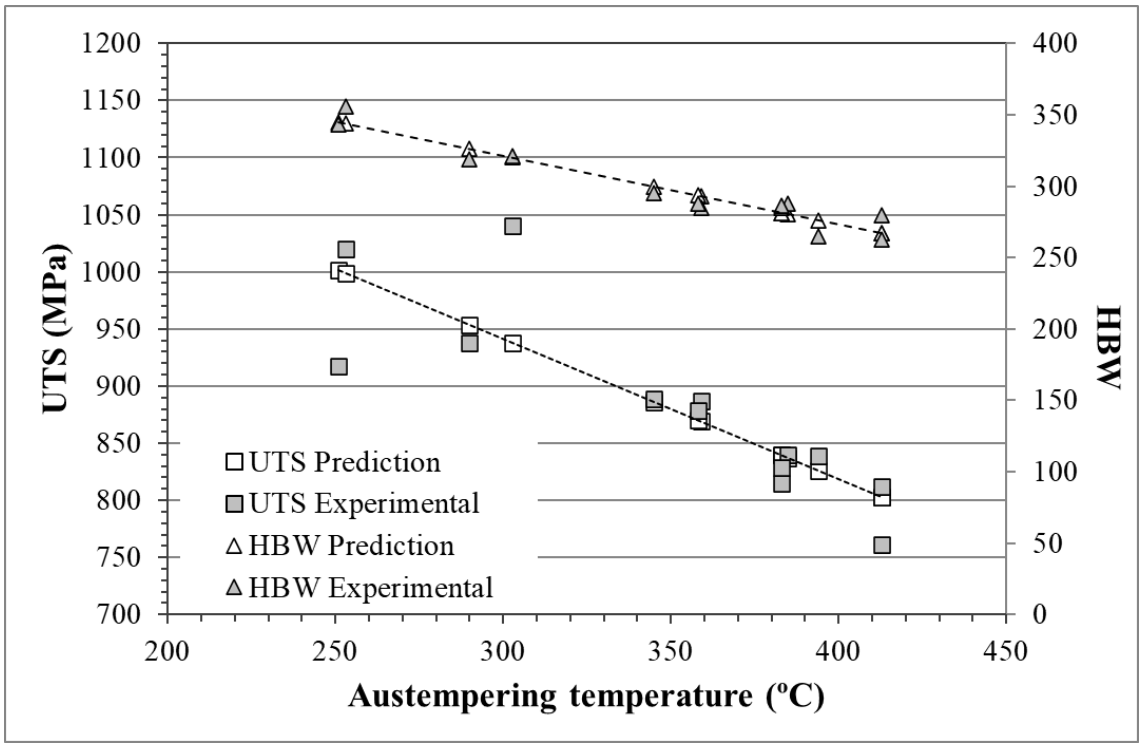

Figure 109. Relationship between the prediction of the UTS and HBW with the experimental results.

Based on the desired mechanical properties, combining Equation 13, Equation 14 and Equation 15, the model calculates the optimum austempering temperature for the different TM of the casting.

These steps define the different processing parameters needed to obtain fully ausferritic microstructures on all the sections of the casting, and the predicted mechanical properties, which are targeted to fulfil the requirements of the ADI materials.

6.7.1. Model summary

As explained previously, the developed model establishes if a specific casting, with specific thickness differences, can be produced through engineered cooling and if it is possible to obtain fully ausferritic microstructures on all its sections.

The inputs of the model are the minimum and maximum TM of the casting where an ausferritic microstructure must be guaranteed and where the mechanical properties requirements are stablished.

Taking into account these inputs, in the first step, the model analyses the as-cast production feasibility of the casting. For that, it considers if the shakeout and austempering temperature for the minimum and the maximum TM are in between the defined working limits. For the shakeout temperature, the upper limit is defined by the temperature of 1050 ºC (the solidification process is completed). The lower limit is defined by the eutectoid transformation temperature defined by the Equation 11, so that the formation of pearlite can be avoided. These limits are shown in Figure 100. For the austempering temperature, the upper limit is defined by the temperature of 450 ºC, above which the mechanical properties of the produced microstructure do not meet the requirements for the ADI materials. The lowest limit is defined by the M_s, that for the studied alloy (Table 14) was stablished in 170 ºC, so that the formation of martensite is avoided. These limits are shown in Figure 106.

To define if the shakeout temperature and the austempering temperature on the different sections of the casting are in between the defined limits, a relationship between the TM and the transformation temperature was obtained considering the first cooling in the mould for the shakeout temperature and posterior air cooling after the shakeout for the austempering temperature. This relationship is shown in Equation 12 for the T_{shkout} and in Equation 13 for the T_{temp}. These equations were validated for a TM range 0.4-1.3 cm.

If the obtention of fully ausferritic microstructures by the defined cooling technology is possible in the defined sections of the casting, then, the next step is to stablish the required alloying elements needed to avoid the pearlitic nose on the maximum TM. By means of an iterative method, the model calculates the minimum nickel, molybdenum and copper content to prevent the formation of pearlite. The CR_{min} of the alloy defined by the Equation 9 must be equal or higher to the CR corresponding to the maximum TM defined by Equation 10.

As several alloy combinations can be considered, different criteria like qualitative, economical or raw materials availability could be the decisive factor in selecting the proper alloy. The chemical composition range in which the model was developed is shown in Table 30.

In the third step, the model deals with the shakeout process. Based on the relation between the shakeout temperature and the TM described by Equation 12, the model determines the optimum shakeout temperature, considering it as the lowest temperature that maintains the different TM in the defined range (upper and lower limit shown in Figure 100).

The fourth step deals with the isothermal transformation temperature window. The model structure of this step is very similar to the precedent. For the same maximum and minimum TM, the model determines the austempering temperatures for the different TM using the Equation 13. On this case, the criteria to define the optimum austempering temperature is based on the required mechanical properties in terms of UTS and HBW. The relationship of these two properties with the austempering temperature is shown in Equation 14 for the UTS and in Equation 15 for the HBW. Combining these three equations (Equation 13, Equation 14 and Equation 15), the model calculates the optimum austempering temperature range to meet the desired mechanical properties.

7. CONCLUSIONS

In the present research work, a novel processing technology to obtain ausferritic microstructures in spheroidal graphite cast iron castings is described. Instead of the conventional austempering heat treatment to manufacture ADI materials, an engineered cooling process is proposed, which enables to meet the standards of these materials in an as-cast state, without any heat treatment.

The main conclusion we can draw, is that it is feasible to obtain ausferritic microstructures in a spheroidal graphite cast iron material, acting on the cooling process, without the need of a heat treatment to the as-cast product.

The actions taken on the cooling process that enable the obtention of as-cast ausferritic microstructures are the followings:

A high temperature shakeout followed by an accelerated cooling (compared to a cooling in the mould), with the purpose of avoiding the formation of pearlite and finally a temperature arrest in the ausferrite formation temperature range so that the ausferritic reaction can evolve.

During this development, the technology to carry out these steps was defined. Moreover, the optimal parameters working range was stablished for the most important process variables. Next are summarized and evaluated the obtained results:

The main target of the actions carried out during the cooling process was to perform them as simple as possible, trying to make easier their subsequent industrial application. A high temperature shakeout was carried out by mechanical means, and directly afterwards, air cooling was considered instead of a more complex cooling media like a salt bath or water quenching. Air cooling, on the one hand simplifies substantially the operability of the technology, but on the other hand, the cooling rate is not as high as it could be considering a quenching process. For this reason, the moderate cooling rate was compensated in this development with the addition of alloying elements that increase the austemperability of the material. Nickel, molybdenum, and copper additions were studied to that purpose.

CCT diagrams in the alloying range of 0.0-5.0 % nickel; 0.0-0.2 % molybdenum and 0.0-1.0 % copper were developed. This allowed defining the minimum cooling rate needed to avoid the pearlitic nose considering a given alloy content.

The air-cooling process, permitted at the same time relating the thermal modulus or section size of a casting with its cooling rate when cooled in the air.

Combining these both points (CCT diagrams and cooling rate as a function of the thermal modulus), it was possible to define the minimum alloying content to avoid the pearlitic nose for a certain casting.

Castings presenting a thermal modulus of up to 1.75 cm were studied, and in order to avoid the pearlitic nose considering an air-cooling process, for that thermal modulus the minimum alloying content was defined using 3.0 % nickel and 0.2 % molybdenum. No other alloying elements were added.

The optimal shakeout temperature was defined at 800 ºC, because it enables to obtain the accelerated cooling rate before the eutectoid transformation temperature takes place and compared to the other studied shakeout temperatures (900 and 1000 ºC), the shakeout process is carried out later after the pouring of the molds, so there is a longer time to face it after pouring, which makes easier the application of this technology to an industrial process.

Furthermore, a reusable insulating material was tested and corroborated as a feasible technology to maintain the temperature of the samples constant and this way allow the ausferritic reaction to take place. Results with samples treated in a furnace were compared to the samples treated in the insulating material and no remarkable differences were seen.

During the holding time into the insulating material, some temperature drop occurred. Temperature losses of up to 60 ºC were recorded. Nevertheless, their effect on the final microstructure and consequently on the mechanical properties was seen as negligible. Thus, the insulating material was stablished as a proper methodology to obtain ausferritic as-cast microstructures. This is a key point of the process from an environmental point of view, since the use of the insulating medium reduces the energy consumption of the process, and its reusability minimizes the waste of the process.

Regarding the optimal austempering temperature and holding time into the insulating material, a deep study of the ausferrite formation kinetics was performed for the transformation temperatures of 300 and 400 ºC.

On a first step, interrupted cooling experiments were performed to define the moment at which acicular ferrite starts to form considering an air-cooling process. These results showed that for the studied alloy (3.0 %Ni and 0.2 %Mo) and cooling rate's range (0.40-1.35 ºC/s on the 600-700 ºC temperature range), the acicular ferrite formation start temperature (AF_S) is defined at around 550 ºC.

Afterwards, different holding times into the insulating material (from 1 minute up to 180 minutes) were tested and the resultant microstructure and mechanical properties analysed. Considering the time at which the temperature of 550 ºC is reached as the starting point of the transformation, then the necessary time to achieve the complete transformation and thus the optimal mechanical properties is of 65 minutes at 400 ºC and 80 minutes at 300 ºC.

Holding times of up 180 minutes were tested and seen that both the microstructure and the mechanical properties are constant compared to the moment at which the ausferritic transformation is complete. This corroborates that the stage II of the ausferrite transformation was not started after that holding time and consequently, the processing window is at least beginning from the moment at which the ausferrite formation is complete, described in the paragraph above, till the 180 minutes holding time into the insulating material.

Taking into account that the ausferrite formation starts at the temperature of 550 ºC, during the cooling process from that temperature (AF_S) to the isothermal arrest, upper acicular ferrite is formed, even when the castings are introduced in the insulating material at 300 ºC. This is a peculiarity of this controlled cooling process compared to a conventional austempering heat treatment. For the austempering treatment and the high cooling rate achieved with the salt bath, no ausferrite is formed before the isothermal stage.

At 400 ºC, the microstructure evolution for different section sizes is similar and the final microstructure is made up of upper acicular ferrite and reacted austenite. The influence of the thermal modulus seems to be negligible.

At 300 ºC, the microstructure is made up of upper and lower acicular ferrite, and its evolution differs for the studied different thermal moduli. The higher the section size, the higher the upper acicular ferrite and the less lower acicular ferrite that is formed at the end of the reaction. The differences between the distinct thermal moduli are not negligible and could be attributed to the cooling rate before the temperature arrest, which has an impact on the final microstructure. As mentioned earlier, before the temperature arrest upper acicular ferrite is formed, so when the cooling rate decreases, then the upper acicular ferrite precipitation increases, due to a higher time from the AF_S to the 300 ºC and the lower acicular ferrite precipitation decreases.

The presence of upper acicular ferrite at 300 ºC is a discrepancy when compared to the conventionally austempered ADI samples. This occurs due to the cooling rate difference before the austempering stage and because of this effect, it is not possible to obtain the highest ADI grades in terms of resistance considering and engineered cooling process when the castings are air cooled.

The obtained as-cast ausferritic materials by means of the presented controlled cooling process fulfil the standards of the conventional ADI materials (EN 1564[32]).

As happens for the conventionally obtained ADI materials, there is a clear relationship between the resistance and the isothermal transformation or austempering temperature. Lowering the tempering temperature, the resistance increases. The fine ferrite needles of the lower ausferrite and broader ones of the upper ausferrite could be the origin of this difference, combined with the reacted austenite quantity variation. Together with the resistance evolution, the hardness also increases when lowering the austempering temperature and the ductility, decreases.

The as-cast obtained ausferritic materials transformed at a temperature of 400 ºC, fulfil the requirements of the ADI materials, 35 minutes after reaching the AF_S temperature. The mechanical properties keep improving up to 65 minutes and afterwards, they remain constant. The differences for the distinct thermal moduli are slight and possibly due to the different solidification times, not due to microstructure differences.

Considering the austempering temperature of 300 ºC, the mechanical properties keep improving up to 80 minutes after reaching the AF_S temperature and after that time, the requirements of the ADI materials are fulfilled. The mechanical properties obtained at 300 ºC, due to the dual matrix formed by upper acicular ferrite and lower acicular ferrite presents higher elongation than the conventional ADI treated at that temperature. The differences for the distinct section sizes tested are bigger than at 400 °C isothermal temperature. These variations are based on the microstructural disparities, which are caused by the different cooling rates before the temperature arrest.

The results of the ausferrite formation kinetics support the theory of the displacive nature of the ausferrite formation.

In addition to the static mechanical properties results at room temperature, the microstructure produced using different isothermal transformation temperatures (300, 350 and 400 ºC) was correlated with the dynamic mechanical properties at room and low temperature, static mechanical properties at low temperature and the corrosion behaviour.

Regarding, the dynamic mechanical properties, the material treated at 400 ºC presented a higher fatigue limit than the one treated at 300 ºC, in spite of the higher statical resistance of the latter. This fact could be due to the higher ductility that shows the upper ausferritic microstructure and the more reacted austenite content compared to a lower transformation temperature, which makes this material more resistant against periodically changing efforts. These results are in good agreement with the conventionally obtained ADI materials literature.

Bending tests showed that the material isothermally transformed at 400 ºC presented a higher displacement for the same applied load, but the maximum load was less than in the case of the material tempered at 300 ºC. These results follow the same trend as the tensile test results, the higher the austempering temperature, the more ductile material but less resistant.

Considering the low temperature properties in terms of impact and bending resistance, the effect of lowering the temperature is significant for the samples tempered at 400 ºC, while the ones tempered at 300 ºC are slightly affected. This could be because the upper ausferritic microstructure presents higher quantity of austenite and this phase becomes more rigid when lowering the temperature.

According to the electrochemical and weight loss tests results, upper ausferrite microstructure is shown less active than lower ausferrite in terms of corrosion behaviour in NaCl and both follow the same tendency than ADI microstructures. Higher contents of austenite in samples treated at higher temperatures show the cathodic nature of this phase. This fact is supported by lower corrosion rates obtained in structures with upper ausferrite. The fact that the structures don’t show any ferrite needle after being subjected to a corrosion test in NaCl reveals the anodic nature of the ferrite with respect to austenite.

The cathodic nature of the graphite against ferrite has also been shown after corrosion tests. Graphite nodules are kept suspended in the matrix during the corrosion process of the ferrite (more anodic phase) until the whole ferrite disappears and graphite particles are detached.

The formerly mentioned results were obtained for standard samples. As a further step for the validation of the methodology, steering knuckles were produced in a laboratory scale as a technology demonstrator prototype. A thin and a thick section were controlled, thermal moduli of 0.65 and 0.83 cm respectively. Both sections presented an upper ausferritic microstructure. In spite of the distinct thermal moduli of both sections, and consequently, different shakeout and austempering temperatures, the microstructure was similar. This is a key point for the as-cast technology applicability to real castings.

The steering knuckles produced following the engineered cooling technology satisfied the requirements of the material EN GJS 800-8 of the standard EN 1564[32] that defines the ADI materials.

These results showed that it is possible to obtain ausferritic ductile iron castings by means of a controlled cooling process that fulfil the requirements of the conventionally obtained ADI materials.

Nevertheless, the challenge of a controlled cooling methodology is the production feasibility of a casting that presents very distinct thermal moduli. For this reason, and in order to give a step forward on the industrial application of the technology, the processing window of the methodology was addressed.

To that aim, an experimental model was developed to determine in a simple way the process parameters capable of producing as-cast ausferritic parts with the desired mechanical properties. This model considers the different thicknesses of a specific casting and the cooling differences they present.

The model defines the optimal chemical composition and the two processing temperatures for the different sections (shakeout and austempering temperature).

These two critical temperatures have to be inside defined ranges that permit the formation of an ausferritic microstructure which meets the requirements of the ADI materials. Depending on the different thermal moduli of the casting, these temperatures will change. Based on these changes, the model calculates the thickness window in which this methodology is feasible and by extension, if a given casting could be produced with the engineered cooling process presented in this work.

The experimental model was validated with different geometries in a defined range of thermal moduli (0.4-1.5 cm) and for a specific range of chemical composition (3.0-5.0 %Ni; 0.0-0.2 %Mo; 0.1-1.0 %Cu by weight).

Taking into account the formerly described aspects, as a final conclusion, it can be claimed that the as-cast method to obtain an ausferritic matrix in spheroidal graphite cast iron castings was proved to be a valid method to produce cast parts as an alternative to the conventionally austempered ADI materials.

8. FUTURE WORK

An engineered cooling process to obtain ausferritic ductile iron castings in as-cast state was studied, defining the technology, the process parameters, and its limits. This technology is now ready to be industrially applied.

As a future work, the industrial application must be approached, so that the benefits of the developed technology can be energetically, environmentally, qualitatively and economically profited.

Currently, the production of a casting from the railway sector and another one from the automotive sector are being tested in an industrial environment, but on a pilot scale, that is, working mould by mould.

This application is being studied in horizontal moulding, considering a chemically bonded sand for the railway sector casting and green sand for the automotive sector casting. The chemically bonded sand production is approached mould by mould, while the green sand casting production is performed in an automatic moulding machine with a capacity of up to 150 moulds per hour.

These projects are ongoing, but so far, they have helped to see the necessity of a facility adaptation to be able to approach a secure and guaranteed application of this technology to the mass production of ductile iron castings.

Moulding lines for cast iron production are designed so that the cooling process takes place in the mould, at least till the eutectoid transformation has taken place. This way, the cooling is always the same and the eutectoid transformation occurs similarly and, consequently, the final microstructure is maintained on a narrow range. This fact significantly hinders the industrial application of a controlled cooling process.

The cooling in the mould approach is very valid for ferritic/pearlitic materials. Nevertheless, if a pearlitic material is being targeted, an accelerated cooling helps the obtention of this microstructure. The alloying elements addition could be minimized, and the mechanical properties enhanced. On the other hand, if a ferritic material is desired, a slower cooling rate that the one obtained in the mould is beneficial. This can be achieved introducing the castings after a high temperature shakeout into an insulating medium. The technology developed in the present work could be then extrapolated to other materials and microstructures.

There is, therefore, a need to deeply investigate a practical shakeout methodology that could help to take out the castings from the mould rapidly and to help, directly after, to remove the sand that can be stuck to the castings, so that the accelerated cooling can take place before the eutectoid transformation.

Furthermore, the utilization of an insulating medium on an industrial scale must be further studied, so that its application for a high mass production can be carried out. How to use the insulating material on a large scale and where its reusability ends are topics that need a further development.

All these aspects lead to a reconceptualization of the industrial automatic moulding lines and the main future work is thus on how they could be modified to fit the needs of a successful controlled cooling process.

Sensors to control the temperature and cooling rate should be implemented, as well as innovative mechanical means for the early shakeout and specifically designed spaces for the insulating medium.

In parallel to the industrial implantation of this technology, the effect of other cooling medias should be studied, like for instance, forced air, water or polymers. These cooling environments could complicate the applicability of the methodology, but on the other hand, they could help to minimize the addition of alloying elements. For these reasons, the rapid cooling with these medias should be further investigated and try to find a compromise between the applicability and the alloying elements addition.

REFERENCES

[1] Stefanescu, D. M., Classification and Basic Metallurgy of Cast Iron . Properties and Selection: Irons, Steels, and High-Performance Alloys, Vol 1, ASM Handbook, ASM International, pp 3-16, 1990. 10.31399/asm.hb.v01.a0009206.

[2] Campbell, F.C., Elements of Metallurgy and Engineering Alloys, ASM International, pp. 453-468, 2008.

[3] Berns, H., Theisen, W., Ferrous Materials: Steel and Cast Iron, Springer Science & Business Media, pp 9-14, 2008.

[4] Caesar, A.G., English: Iron-carbon phase diagram under atmospheric pressure, 2019. Wikimedia Commons. Available at: https://commons.wikimedia.org/wiki/File:Iron_carbon_phase_diagram.svg.

[5] Stefanescu, D.M., Classification and Basic Types of Cast Iron: Cast Iron Science and Technology, ASM Handbook, Vol 1, ASM International, pp 12-26, 2017. 10.31399/asm.hb.v01a.a0006294.

[6] Kubaschewski, O., Iron- Binary Phase Diagrams, Springer Science & Business Media, pp 23-26, 2013.

[7] González-Martínez, R., de la Torre, U., Ebel, A., Lacaze, J., Sertucha, J., Effects of High Silicon Sontents on Graphite Morphology and Room Temperature Mechanical Properties of As-Cast Ferritic Ductile Cast Irons. Part II – Mechanical Properties, Mat. Sci. & Eng. A, Vol 712, pp 803-811, 2018. 10.1016/j.msea.2017.11.051.

[8] Wayman, M.L., Cast Iron Metallurgy, CASTI Metals Black book, CASTI Publishing Inc., pp 26-30, 2003.

[9] Bazhenov V.E., Pikunov M.V., Determining the Carbon Equivalent of Cast Iron by the Thermo-Calc Program, Steel Transl.,Vol 41, pp 896–899, 2011. 10.3103/S0967091211110027.

[10] Castro M., Herrera M., Cisneros M.M., Lesoult G., Lacaze J., Simulation of Thermal Analysis Applied to the Description of the Solidificaction of Hypereutectic SG Cast irons, Int. J. of Cast Met. Res., Vol 11, pp 369-374, 1999. 10.1080/13640461.1999.11819301.

[11] Stefanescu D.M., Lacaze, J., Thermodynamics Principles as Applied to Cast Iron, ASM Handbook, Vol 1, Cast Iron Science and Technology, ASM International, pp 31-42, 2017. 10.31399/asm.hb.v01a.a0006294.

[12] Liu, J.H., Yan, J.S., Zhao, X.B, Fu, B.G., Xue, H.T., Zhang G.X., Yang P.H., Precipitation and Evolution of nodular Graphite During Solidification Process of Ductile Iron, China Foundry, Vol 17, pp 260-271, 2020. 10.1007/s41230-020-0042-2.

[13] Stefanescu D.M., Alonso, G., Larrañaga, P., Suarez, R., On the Stable Eutectic Solidification of Iron-Carbon alloys, Acta Mat., Vol 103, pp 103-114, 2016. 10.1016/j.actamat.2015.09.043.

[14] Walton C.F., Opar T.J., Iron Castings Handbook: Covering Data on Gray, Malleable, Ductile, White, alloy and Compacted Graphite Irons, Iron Castings Society, 1981.

[15] Stefanescu, D.M., Alonso, G., Larrañaga, P., De la Fuente, E., Suarez, R., A Comparative Study of Graphite Growth in Cast Iron and in Analogous Systems, Int. J. Met.Cat., Vol 12, pp 722-752, 2018. 10.1007/s40962-017-0204-1.

[16] International Organization for Standardization, Microstructure of Cast Irons- Part 1: Graphite Classification by Visual Analysis, ISO Standard 945-1, 2017.

[17] Sadocha, J.P., Gruzleski, J.E., The Mechanism of Graphite Spheroid Formation in Pure Fe-C-Si Alloys: The Metallurgy of Cast Iron, Georgi Publishing Co., 443-459, 1975.

[18] Ulewicz, R., Novy, F., Selejdak, J., Fatigue Strength of Ductile Iron in Ultra-High Cycle Regime, Adv. Mat. Res., vol 874, pp 43-48, 2014. 10.4028/www.scientific.net/AMR.874.43.

[19] International Organization for Standardization, Microstructure of Cast Irons-Part 4: Test Method for Evaluating Nodularity in Spheroidal Graphite Cast Irons, ISO Standard 945-4, 2019.

[20] Lekah, S.N., Qing, J., Richards V.L., Peaslee, K.D., Graphite Nodule Size Distribution in ductile Iron, Proc. 117th Metalcasting Congress, AFS, 2013.

[21] Sangame, B.B., Shinde, V.D., The Effect of Inoculation on Microstructure and Mechanical Properties of Ductile Iron, IOSR-JMCE, Vol 5, pp 17-23, 2013.

[22] Hecht, R.L., Dinwiddie, R.B., Wang, H., The Effect of Graphite Flake Morphology on the Thermal Diffusivity of Gray Cast Irons Used for Automotive Brake Discs, J. Mat. Sci., Vol 34, pp 4775-4781, 1999. 10.1023/A:1004643322951.

[23] Rundman, K.B., Microstructure and Mechanical Properties of Gray Cast Iron: Cast Iron, Encyclopaedia of Materials: Science and Technology, Elsevier, 2001, pp 1003-1010. 10.1016/B0-08-043152-6/00186-8.

[24] Lux, B., Minkoff, I., Mollard, F., Thury, E., Branching of Graphite Crystals Growing from Metallic Solution: The Metallurgy of Cast Iron, Georgi Publishing Co., pp. 495-508, 1975.

[25] Cooper, K., Loper, C.R., Some Properties of Compacted Graphite Cast Iron, AFS Trans., vol. 86, pp. 241-248, 1978.

[26] Regordosa, A., de la Torre, U., Sertucha, J., Lacaze, J., Quantitative Analysis of the Effect of Inoculation and Magnesium Content on compact Graphite Irons- Experimental Approach, J. Mat. Res. & Tech., Vol 9, pp 11332-11343, 2020. 10.1016/j.jmrt.2020.08.008.

[27] Dawson, S., Schroeder, T., Practical Applications for Compacted Graphite Iron, AFS Trans. Vol 112, pp 04-47, 2004.

[28] Abdel-Aziz, K., El-Shennawy, M., Omar, A.A., Microstructural Characteristics and Mechanical Properties of Heat Treated High-Cr White Cast Iron Alloys, Int. J. App. Eng. Res., Vol 12, pp 4675-4686, 2017.

[29] Stefanescu D.M., Mechanical Properties of Malleable Irons, ASM Handbook, Vol 1, Cast Iron Science and Technology, ASM International, pp 481-489, 2017. 10.31399/asm.hb.v01a.a0006347.

[30] Biswas, S., Monroe, C., Prucha, T., Analysis of Published Cast Iron Experimental Data, ICME, The Min., Met. & Mat. Soc., pp 293-303, 2015.

[31] European Committee for Standardization, Founding. Spheroidal Graphite Cast Irons, EN 1563, 2018.

[32] European Committee for Standardization, Founding. Ausferritic Spheroidal Graphite Cast Irons, EN 1564, 2011.

[33] European Committee for Standardization, Founding. Grey Graphite Cast Irons, EN 1561, 2011.

[34] International Organization for Standardization, Compacted (Vermicular) Cast Irons-Classification, ISO Standard 16112, 2016.

[35] International Organization for Standardization, Metallic Materials - Tensile Testing – Part 1: Method of Test at Room Temperature, ISO Standard 6892-1, 2019.

[36] Diószegi, A., Fourlakidis, V., Svensson, I.L., Microstructure and Tensile Properties of Grey Cast Iron, Research Report, School of Engineering, Jönköping University, 2004.

[37] Gregorutti, R.W., Grau, J.E., Mechanical Properties of Compacted Graphite Cast Iron with Different Microstructures, Int. J. Cast Met. Res., Vol 27, pp 275-281, 2014. 10.1179/1743133614Y.0000000118.

[38] Guo, X., Stefanescu, D.M., Chuzhoy, L., Pershing, M.A., Biltgen, G.L., A Mechanical Properties Model for Ductile Iron, AFS Trans. 105, pp 47-54, 1997.

[39] Hafiz, M., Mechanical Properties of SG-Iron with Different Matrix Structure, J. of Mat. Sci., Vol 36, pp 1293-1300, 2001. 10.1023/A:1004866817049.

[40] Riposan, I., Chisamera, M., Stan, S., Factors influencing Microstructure and Mechanical Properties of As-Cast and Heat Treated 400-18 Grade Ductile Cast Iron, Int. J. of Cast Met. Res., Vol 20, pp 64-67, 2007. 10.1179/136404607X239717.

[41] Lacaze, J., Sertucha, J., Effect of Cu, Mn and Sn on Pearlite Growth Kinetics in As-Cast Ductile Irons, Int. J. of Cast Met. Res., Vol 29, pp 74-78, 2016. 10.1080/13640461.2016.1142238.

[42] de la Torre, U., Loizaga, A., Lacaze, J., Sertucha, J., As Cast High Silicon Ductile Irons with Optimised Mechanical Properties and Remarkable Fatigue Properties, Mat. Sci. and Tech., Vol 30, pp 1425-1431, 2014. 10.1179/1743284713Y.0000000483.

[43] Stets, W., Löblich, H., Gassnre, G., Schumacher, P., Solution Strenghened Ferritic Ductile Cast Iron Properties, Production and Application, Int. J. of Metalcasting, Vol 8, pp 35-40, 2014. 10.1007/BF03355580.

[44] Kim, Y.J., Shin, H., Park, H., Lim, J.D., Investigation into Mechanical Properties of Austempered Ductile Cast Iron (ADI) in Accordance with Austempering Temperature, Mat. Let., Vol 62, pp 357-360, 2008. 10.1016/j.matlet.2007.05.028.

[45] Zhang, J., Zhang, N., Zhang, M., Lu, L., Zeng, D., Song, Q., Microstructure and Mechanical Properties of Austempered Ductile Iron with Different Strength Grades, Mat. Let., Vol 119, pp 47-50, 2014. 10.1016/j.matlet.2013.12.086.

[46] Polishetty, A., Singamneni, S., Littlefair, G., A Comparative Assessment of Austempered Ductile Iron as a Substitute in Weight Reduction Applications, MSEC_ICMP, pp 49-57, 2008. 10.1115/ msec_icmp2008-72091.

[47] Hayrynen, K.L., ADI: Another Avenue for Ductile Iron Foundries, Mod. Cast., Vol. 85, pp 35-37, 1995.

[48] International Organization for Standardization, Metallic Materials – Brinell Hardness Test – Part 1: Test Method, ISO Standard 6506-1, 2014.

[49] International Organization for Standardization, Metallic Materials – Charpy Pendulum Impact Test – Part 1: Test Method, ISO Standard 148-1, 2016.

[50] Hafiz, M.F., Tensile and Impact Properties of Conventional and Austempered SG-Cast Irons, AFS Trans., Vol 117, pp 445-452, 2009.

[51] Kobayashi, T., Yamamoto, H., Development of High Toughness in Austempered Type Ductile Iron and Evaluation of Its Properties, Met. Trans. A, Vol 19A, pp 319-327, 1988. 10.1007/BF02652541.

[52] Hsu, C.H., Lin, K.T., A Study on Microstructure and Toughness of Copper Alloyed and Austempered Ductile Irons, Mat. Sci. & Eng. A, Vol 528, pp 5706-5712, 2011. 10.1016/j.msea.2011.04.035.

[53] Sertucha, J., Lacaze, J., Serrallach, J., Suárez, R., Osuna, F., Effect of Alloying on Mechanical Properties of As Cast Ferritic Nodular Cast Irons, Mat. Sci. and Tech., Vol 28, pp 184-191, 20212. 10.1179/1743284711Y.0000000014.

[54] International Organization for Standardization, Metallic Materials-Fatigue Testing-Axial Force-Controlled Method, ISO Standard 1099, 2017.

[55] Fourlakidis, V., Schmidt, P., Jarfors, A.E.W., Svidro, P., Dioszegi, A., Fatigue Limit and Microstructure in Lamellar Graphite Iron, Mat. Sci. and Eng. A, Vol 802, pp 1-7, 2021. 10.1016/j.msea.2020.140617.

[56] Qiu, Y., Pang, J.C., Zou, C.L., Zhang, M.X., Li, S.X., Zhang, Z.F., Fatigue Strength Model Based on Microstructures and Damage Mechanism of Compacted Graphite Iron, Mat. Sci. and Eng. A, Vol 724, pp 324-329, 2018. 10.1016/j.msea.2018.03.110.

[57] Luo, J., Harding, R.A., Bowen, P., Evaluation of the Fatigue Behavior of Ductile Irons with Various Matrix Microstructures, Met. And Mat. Trans. A, Vol 33, pp 3719-3730, 2002.

[58] Rausch, T., Beiss, P., Broeckmann, C., Lindlohr, S., Weber, R., Application of Quantitative Image Analysis of Graphitic Structures for the Fatigue Strength Estimation of Cast Iron Materials, Proc. Eng., Vol 2, pp 1283-1290, 2010. 10.1016/j.proeng.2010.03.139.

[59] Shanmugam, P., Rao, P.P, Udupa, K.R., Venkataraman, N., Effect of Microstructure on the Fatigue Strength of an Austempered Ductile Iron, J. of Mat. Sci., vol 29, pp 4933-4940, 1994. 10.1007/BF00356546.

[60] Chapetti, M.D., High-Cycle Fatigue of Austempered Ductile Iron (ADI), Int. J. of Fat., Vol 29, pp 860-868, 2007. 10.1016/j.ijfatigue.2006.09.005.

[61] Buerger, M.J., Polymorphism and Phase Transformations, Fortschr. Miner., Vol 39, pp 9-24, 1961.

[62] Christian, J.W., Olson, G.B., Cohen, M., Classification of Displacive Transformations: What is a Martensitic Transformation?, J. de Phys. IV, Vol 05, pp 3-10, 1995. 10.1051/jp4:1995801.

[63] Campbell, F.C., Elements of Metallurgy and Engineering Alloys, ASM International, pp. 41-52, 2008.

[64] Bhadeshia, H.K.D.H., Bainite in Steels: Transformations, Microstructure and Properties, The Institute of Materials, pp 113-124, 1992.

[65] Lacaze, J., The Austenite to Pearlite/Ferrite Transfromation: Cast Iron Science and Technology, ASM Handbook, Vol 1, ASM International, pp 106-113, 2017. 10.31399/asm.hb.v01a.a0006300.

[66] Gazda, A., Determination of the Optimal Austempering Parameters of Ni-Cu (Mo, Mn) Ductile Iron Based on CCT and TTT Diagrams, Trans. Of Foundry Res. Inst., Vol 56, pp 133-145, 2016. 10.7356/iod.2016.11.

[67] Berns H., Theisen, W., Ferrous Materials: Steel and Cast Iron, Springer Science and Business Media, pp 9-52, 2008.

[68] Campbell, F.C., Elements of Metallurgy and Engineering Alloys, ASM International, pp 153-176, 2008.

[69] Tiedje, N.S., Solidification, Processing, and Properties of Ductile Cast Iron, Mat. Sci. and Tech., Vol 26, pp 505-514, 2010. 0.1179/026708310X12668415533649.

[70] Olawalw, J.O., Ibitoye, S.A., Oluwasegun, K.M., Processing Techniques and Productions of Ductile Iron: A Review, Int. J. of Sci. & Eng. Res., Vol 7, pp 397-423, 2016.

[71] Elliot, R., Cast Iron Technology, Butterowrth-Heinemann, pp 79-85, 1988.

[72] Lekakh, S., Robertson, D.G.C., Loper, C.R., Thermochemistry and Kinetics of Iron Melt Treatment, 67th World Foundry Congress Proceedings, ICME, Vol 2, pp 1003-1013, 2006.

[73] Riposan, I., Chisamera, M., Uta, V., Stan, S., Naro, R., Williams, D., The Importance of Rare Earth Contribution from Nodulizing Alloys and Their Subsequent Effect on the Inoculation of Ductile Iron, Int. J. of Met., Vol 8, pp 65-80, 2014. 10.1007/BF03355583.

[74] de la Torre, U., Lacaze, J., Sertucha, J., Chunky Graphite Formation in Ductile Cast Irons: Effect of Silicon, Carbon and Rare Earths, Int. J. of Mat. Res., Vol 107, pp 1041-1050, 2016. 10.3139/146.111434.

[75] Alonso, G., Larrañaga, P., de la Fuente, E., Stefanescu, D.M., Natxiondo, A., Suarez, R., Kinetics of Nucleation and Growth of Graphite at Different Stages of Solidification for Spheroidal Graphite Iron, Int. J. Met., Vol 11, pp 14-26, 2017. 10.1007/s40962-016-0094-7.

[76] Riposan, I., Skaland, T., Modification and Inoculation of Cast Iron, Cast Iron Science and Technology, ASM Handbook, Vol 1, ASM International, pp 160-176, 2017. 10.31399/asm.hb.v01a.a0006315.

[77] Alonso, G., Stefanescu, D.M., de la Fuente, E., Larrañaga, P., Suarez, R., The Influence of Trace Elements on the Nature of the Nuclei of the Graphite in Ductile Iron, Mat. Sci. Forum, Vol 925, pp 78-85, 2018. 10.4028/www.scientific.net/MSF.925.78.

[78] Rivera, G., Boeri, R., Sikora, J., Influence of the Inoculation Process, the Chemical Composition and the Cooling Rate, on the Solidification Macro and Microstructure of

Ductile Iron, Int. J. of Cast Met. Res., Vol 16, pp 23-28, 10.1080/13640461.2003.11819553.

[79] Chvorinov, N., Theorie der Starrung von Gussstücken (in German), Gieβerei 27, H 10 pp 177-186, H 11, pp 201-208, H 12, pp 222-225, 1940.

[80] Tiryakioğlu, M., Tiryakioğlu, E., Askeland, D.R., The Effect of Casting Shape and Size on Solidification Time: a New Approach, Int. J. of Cast Met. Res., Vol 9, pp 259-267, 1997. 10.1080/13640461.1997.11819667.

[81] River, G., Boeri, R., Sikora, J., Influence of the Solidification Microstructure on the Mechanical Properties of Ductile Iron, Int. J. Cast Met. Res., Vol 11, pp 533-538, 1999. 10.1080/13640461.1999.11819329.

[82] Shinde, V.D., Ravi, B., Narasimhan, K., Solidification Behaviour and Mechanical Properties of Ductile Iron Castings with Varying Thickness, Int. J. of Cast Met. Res., Vol 25, pp 364-373, 2012. 10.1179/1743133612Y.0000000024.

[83] Stefanescu, D.M., Solidification and Modeling of Cast Iron-A Short History of the Defining Moments, Mat. Sci. and Eng. A, Vol 413-414, pp 323-333, 2005. 10.1016/j.msea.2005.08.180.

[84] Gerval, V., Lacaze, J., Critical Temperature Range in Spheroidal Graphite Cast Irons, ISIJ Int., Vol 40, pp 386-392, 2000. 10.2355/isijinternational.40.386.

[85] Lacaze, J., Wilson, C., Bak, C., Experimental Study of the Eutectoid Transformation in Spheroidal Graphite Cast Iron, Scan. J. of Met., Vol 23, pp 151-163, 1994.

[86] Lacaze, J., Sertucha, J., Magnusson-Åberg, L., Microstructure of As-Cast Ferritic-Pearlitic Nodular Cast Irons, ISIJ INT, Iron & Steel Inst. Of Japan, Vol 56, pp 1606-1615, 2016. 10.2355/isijinternational.ISIJINT-2016-108.

[87] Carazo, F.D., García, L.N., Celentano, D.J., Metastable Eutectoid Transformation in Spheroidal Graphite Cast Iron : Modeling and Validation, Metals, Vol 8, pp 550-565, 2018. 10.3390/met8070550.

[88] Carazo, F.D., Dardati, P.M., Celentano, D.J., Godoy, L.A., Stable Eutectoid Transformation in Nodular Cast Iron: Modeling and Validation, The Min., Met. and Mat. Trans. A, Vol 48A, pp 63-75, 2017. 10.1007/s11661-016-3827-6.

[89] Sertucha, J., Larrañaga, P., Lacaze, J., Insausti, M., Experimental Investigation on the Effect of Copper Upon Eutectoid Transformation of As-Cast and Austenitized Spheroidal Graphite Cast Iron, Int. J. Mertalcasting, Winter 10, pp 51-58, 2010. 10.1007/BF03355486.

[90] Gumienny, G., Giętka, T., Continuous Cooling Transformation (CCT) Diagrams of Carbidic Nodular Cast Iron, Arch. of Met. And Mat., Vol 60, pp 705-710, 2015. 10.1515/amm-2015-0195.

[91] Vaško, A., Influence of Transformation Temperature on Structure and Mechanical Properties of Austempered Ductile Iron, Acta Met. Slo., Vol. 17, pp 45-50, 2011.

[92] Pereloma, E., Edmonds, D., Phase Transformations in Steels: Volume 1: Fundamentals and Diffusion-Controlled Transformations, Woodhead Publishing, pp 1-656, 2012.

[93] Bhadeshia, H.K.D.H., Bainite in Steels: Transformations, Microstructure and Properties, The Institute of Materials, pp 1-209, 1992.

[94] Thomson, R.C., James, J.S., Putman, D.C., Modelling Microstructural Evolution and Mechanical Properties of Austempered Ductile Iron, Mat. Sci. and Tech., Vol 16:11-12, pp 1412-1419, 2000. 10.1179/026708300101507370.

[95] Janowak, J.F., Gundlach, R.B., Development of a Ductile Iron for Commercial Austempering, AFS Trans., Vol 54, pp 377-388, 1983.

[96] Harding, R.A., The Production, Properties and Automotive Applications of Austempered Ductile Iron, Kovove Mater., Vol 45, pp 1-16, 2007.

[97] Rouns, T.N., Rundman, K.B., Moore, D.M., On the Structures and Properties of Austempered Ductile Cast Iron, AFS Trans., Vol 84, pp 815-840, 1984.

[98] Voigt, R.C., Loper, C.R., Austempered Ductile Iron-Process Control and Quality Assurance, J. Heat Treat., Vol 3, No 4, pp 291-309, 1984. 10.1007/BF02833124.

[99] Caballero, F.G., Miller, M.K., García-Mateo, C., Cornide J., New Experimental Evidence of the Diffusionless Transformation Nature of Bainite, J. Alloys Compd. Vol 577, pp 626–630, 2013. 10.1016/j.jallcom.2012.02.130.

[100] Boccardo, A.D., Dardati, P.M., Celentano, D.J., Godoy, L.A., A Microscale Model for Ausferritic Transformation of Austempered Ductile Irons, Metall. Mater. Trans. A, vol 48, pp 524-535, 2017. 10.1007/s11661-016-3816-9.

[101] Bermont, V.M, Sikora, J.A., Metallographic Study on the Influence of the Morphology and Distribution of Graphite on the Solid State Transformations of Grey and Ductile Cast Iron, Int. J. Cast. Met. Res., Vol 11, pp 51-61, 1998. 10.1080/13640461.1998.11819258.

[102] Aaronson, Reynolds, W.T., Purdy, G.R., The incomplete Transformation Phenomenon in Steel, Met. and Mat. Trans. A, Vol 37A, pp 1731-1745, 2006. 10.1007/s11661-006-0116-9.

[103] Kapturkiewicz, W., Burbelko, A.A., Lelito, J., Fras, E., Modelling of Ausferrite Growth in ADI, Int. J. of Cast Met. Res., Vol 16, pp 287-292, 2003. 10.1080/13640461.2003.11819597

[104] Yescas, M.A., Bhadeshia, H.K.D.H., Model for the Maximum Fraction of Retained Austenite in Austempered Ductile Cast Iron, Mat. Sci. and Eng. A, Vol 333, pp 60-66, 2002. 10.1016/S0921-5093(01)01840-8.

[105] Santofimia, M.J., Caballero, F.G., Capdevila, C., García-Mateo, C., García de Andrés, C., Evaluation of Displacive Models for Bainite Transformation Kinetics in Steels, Mat. Trans., Vol 47, No 6, pp 1492-1500, 2006. 10.2320/matertrans.47.1492.

[106] Prasad Rao, P., Putatunda, S.K., Comparative Study of Fracture Toughness of Austempered Ductile Irons with Upper and Lower Ausferrite Microstructures, Mat. Sci. and Tech., Vol 14, pp 1257-1265, 1998. 10.1179/mst.1998.14.12.1257.

[107] Kutsov, A., Taran, Y., Uzlov, K., Krimmel, A., Evsyukov, M., Formation of Bainite in Ductile Iron, Mater. Sci. Eng. A, Vol 273-275, pp 480–484, 1999. 10.1016/S0921-5093(99)00332-9.

[108] Rundman, K.B., Moore, D.J., Hayrynen, K.L., Dubensky, W.J., Rouns, T.N., The Microstructure and Mechanical Properties of Austempered Ductile Iron, J. Heat Treat, Vol 5, pp 79-95, 1988. 10.1007/BF02833175.

[109] Meier, L., Hofmann, M., Saal, P., Volk, W., Hoffman, H., In-situ Measurement of Phase Transformation Kinetics in Austempered Ductile Iron, Mat. Char., Vol 85, pp 124-133, 2013. 10.1016/j.matchar.2013.09.005.

[110] Aranzabal, J., Gutierrez, I., Rodriguez-Ibabe, J.M., Urcola, J.J., Influence of Heat Treatments on Microstructure and Toughness of Austempered Ductile Iron, Mater. Sc. Tech., Vol 8, pp 263-273, 1992. 10.1179/mst.1992.8.3.263.

[111] James, J.S., The Microstructural Modelling of Austempered Ductile Iron Camshafts, PhD Thesis, Loughborough University, 1999. https://dspace.lboro.ac.uk/.

[112] Darwish, N., Elliott, R., Austempering of Low Manganese Ductile Irons: Part 1. Processing Window, Mat. Sci. & Tech, Vol 9:7, pp 572-585, 1993. 10.1179/mst.1993.9.7.572.

[113] Ogi, K., Sawamoto, A., Jin, Y.C., Loper, C.R., A Study of Some Aspects of Austenization Process of Spheroidal Graphite Cast Iron, AFS Trans., Vol 2, pp 75-82, 1988.

[114] Batra, U., Ray, S., Prabhakar, S.R., Mathematical Model for Austenization Kinetics of Ductile Iron, JMEPEG, Vol 14, pp 574-581, 2005. 10.1361/105994905X64512

[115] Hayrynen, K., Heat Treating of Irons and Steels: Heat Treating and Properties of Ductile Iron, Vol 4D, ASM Handbook, ASM International, pp 508-521, 2014. 10.31399/asm.hb.v04d.a0005937.

[116] Darwish, N., Elliott, R., Austempering of Low Manganese Ductile Irons. Part 3: Variation of Mechanical Properties with Heat Treatment Conditions, Mat. Sci. & Tech, Vol 9:10, pp 882-889, 1993. 10.1179/mst.1993.9.10.882.

[117] Baud, J., Ferrier, A., Manenc, J., Bénard, J., The Oxidation and Decarburizing of Fe-C Alloys in air and the Influence of Relative Humidity, Oxid. Of Met., Vol 9, pp 69-97, 1975. 10.1007/BF00613495.

[118] Ramezani, M., Pasang, T., Chen, Z., Neitzert, T., Au, D., Evaluation of Carbon Diffusion in Heat Treatment of H13 Tool Steel under Different Atmospheric Conditions, J. of Mat. Res. And Tech., Vol 4, pp 114-125, 2015. 10.1016/j.jmrt.2014.10.014.

[119] Nemenyi, R., Controlled Atmospheres for Heat Treatment, Pergamon Press Ltd., pp 22-38, 1984.

[120] Totten, G.E., Bates, C.E., Clinton, N.A., Handbook of Quenchants and Quenching Technology, ASM International, pp 191-239,1993.

[121] Rassizadehghani, J., Raygan, S., Askari, M., Comparison of the Quenching Capacities of Hot Salt and Oil Baths, Met. Sci. and Heat Treat., Vol 48, pp 193-198, 2006. 10.1007/s11041-006-0069-z.

[122] Zahiri, S.H., Davies, C.H.J., Pereloma, E.V., Simultaneous Prediction of Austemperability and Processing Window for Austempered Ductile Iron, Mat Sci. and Tech., Vol 19, pp 1761-1770, 2003. 10.1179/174328413X13789824293867.

[123] Darwish, N., Elliot, R., Austempering of Low Manganese Ductile Irons. Part 2: Influence of Austenitising Temperature, Mat. Sci. and Tech., Vol 9, pp 568-602, 1993. 10.1179/mst.1993.9.7.586.

[124] Ali, A.S.H., Elliot, R., Influence of Austenitising Temperature on Austempering of an Mn-Mo-Cu Alloyed Ductile Iron. Part 2: Mechanical Properties, Mat. Sci. and Tech., Vol 13, pp 24-30, 1997. 10.1179/mst.1997.13.1.24.

[125] Ali, A.S.H., Elliot, R., Influence of Austenitising Temperature on Austempering of an Mn-Mo-Cu Alloyed Ductile Iron. Part 1: Austempering Kinetics and the Processing Window, Mat. Sci. and Tech., Vol 12, pp 1021-1031, 1996. 10.1080/02670836.1996.11665717.

[126] Górny, M., Angella, G., Tyrała, E., Kawalec, M., Paź, S., Kmita, A., Role of Austenitization Temperature on Structure Homogeneity and Transformation Kinetics in Austempered Ductile Iron, Met. and Mat. Int., Vol 25, pp 956-965, 2019. 10.1007/s12540-019-00245-y.

[127] Rao, P.P., Putatunda, S.K., Investigations on the Fracture Toughness of Austempered Ductile Irons Austenitized at Different Temperatures, Mat. Sci. ad Eng. A, Vol 349, pp 136-149, 2003. 10.1016/S0921-5093(02)00633-0.

[128] Wade, N., Ueda, Y., Isothermal Austenitizing of Spheroidal Graphite Cast Iron, Trans. ISIJ, Vol 20, pp 849-856, 1980. 10.2355/isijinternational1966.20.849.

[129] Radulovic, B., Bosnjak, B., Harding, R., Pop-Tonev, K., Asanovic, V., The Influence of Austenitising Temperature on the Mictostructure and Mechanical Properties of Low Alloyed Ni-Mo-Cu Austempered Ductile Iron, Mat. Teh., Vol 34, pp 207-212, 2000.

[130] Erić, O., Jovanović, M., Šiđanin, L., Rajnović, D., Zec, S., The Austempering Study of Alloyed Ductile Iron, Mat. & Des., Vol 27, pp 617-622, 2006. 10.1016/j.matdes.2004.11.028.

[131] Sohi, M. H., Ahmadabadi, M. N., Vahdat, A. B., The Role of Austempering Parameters on the Structure and Mechanical Properties of Heavy Section ADI, J. of Mat. Proc. Tech., Vol 153-154, pp 203-208, 2004. 10.1016/j.jmatprotec.2004.04.308.

[132] Kim, Y.J., Shin, H., Park, H., Lim, J.D., Investigation into Mechanical Properties of Austempered Ductile Cast Iron (ADI) in Accordance with Austempering Temperature, Mat. Lett., Vol 62, pp 357-360, 2008. 10.1016/j.matlet.2007.05.028.

[133] Hafiz, M., Mechanical Properties of SG-Iron Subjected to Variable and Isothermal Austempering Temperatures Heat Treatment, Mat. Sci. and Eng. A, Vol 340, pp 1-7, 2003. 10.1016/S0921-5093(02)00071-0.

[134] Putatunda, S.K., Gadicheria, P. K., Effect of Austempering Time on Mechanical Properties of a Low Manganese Austempered Ductile Iron, J. of Mat. Eng. And Perf., Vol 9, pp 193-203, 2000. 10.1361/105994900770346150.

[135] Salman, S., Findik, F., Topuz, P., Effects of Various Austempering Temperatures on Fatigue Properties in Ductile Iron, Mat. And Des., Vol 28, pp 2210-2214, 2007. 10.1016/j.matdes.2006.06.017.

[136] Bartosiewicz, L., Krause, A.R., Alberts, F.A., Singh, I., Putatunda, S.K., Influence of Microstructure on High-Cycle Fatigue Behavior of Austempered Ductile Cast Iron, Mat. Char., Vol 30, pp 221-234, 1993. 10.1016/1044-5803(93)90069-8.

[137] Takita, M., Ueda, Y., Effect of Retained Austenite on Properties of Austempered Ductile Iron, Cast Met., Vol 1, pp 147-155, 1988. 10.1080/09534962.1988.11818961.

[138] Bendikiene, R. Ciuplys, A., Cesnavicius, R., Jutas, A., Bahdanovich, A., Marmysh, D., Nasan, A., Shemet, L., Sherbakov, S., Influence of Austempering Temperatures on the Microstructure and Mechanical Properties of Austempered Ductile Cast Iron, Metals, Vol 11, pp 967-982, 2021. 10.3390/met11060967.

[139] Bayati, H., Elliot, R., The Concept of an Austempering Heat Treatment Processing Window, Int. J. of Cast Met. Res., Vol 11, pp 413-417, 1999. 10.1080/13640461.1999.11819309.

[140] Wen, D. C., Lei, T. S., The Mechanical Properties of a Low Alloyed Austempered Ductile Iron in the Upper Ausferrite Region, ISIJ Int. Vol 39, pp 493-500, 1999. 10.2355/isijinternational.39.493.

[141] Yang, H. S., Suh, D. W., Bhadeshia, H. K. D. H., More Complete Theory for the Calculation of the Martensite-Start Temperature in Steels, ISIJ Int., Vol 52, pp 164-166, 2012. 10.2355/isijinternational.52.164.

[142] Le, Y.H., Voigt, R.C., The Hardenability of Ductile Irons, AFS Trans., Vol 97, pp 915-938, 1989.

[143] Sadighzadeh Benam, A., Effect of Alloying Elements on Austempered Ductile Iron (ADI) Properties and its Process: Review, China Found., Vol 12, pp 54-70, 2015.

[144] Boeri, R., Weinberg, F., Microsegregation of Alloying Elements in Cast Iron, Cast Met., Vol 6, pp 153-158, 1993. 10.1080/09534962.1993.11819142.

[145] Yescas, M.A., Modelling the Microstructure and Mechanical Properties of Austempered Ductile Irons, PhD Thesis, University of Cambridge, 2002.

[146] Akbarzadeh Chiniforush, E., Iranipour, N., Yazdani, S., Effectof Nodule Count and Austempering Heat Treatment on Segregation Behavior of Alloying Elements in Ductile CAst Iron, China Found., Vol 13, pp 217-222, 2016. 10.1007/s41230-016-6034-6.

[147] Schissler, J.M., Saverna, J., Segregation Effects on the Formation of Austempered Ductile Iron, J. of Heat Treat., Vol 4, pp 167-176, 1985. 10.1007/BF02833136.

[148] Wang, B., Barber, G., He, M., Sun, X., Shaw, M., Slattery, B., Seaton, P., Study of the Ausferrite Transformation Kinetics for Austempered Ductile Irons with and without Ni, SAE Int., Tech Pap. 2016-01-0421, 2016. 10.4271/2016-01-0421.

[149] Landesberger, M., Koos, R., Hofmann, M., Li, X., Boll, T., Petry, W., Volk, W., Phase Transition Kinetics in Austempered Ductile Iron (ADI) with Regard to Mo content, Mat., Vol 13, pp 1-23, 2020. i:10.3390/ma13225266.

[150] Yazdani, S., Elliott, R., Influence of Molybdenum on Austempering Behaviour of Ductile Iron. Part 1: Austempering Kinetics and Mechanical Properties of Ductile Iron Containing 0.13 %Mo, Mat. Sci and Tech., Vol 15, pp 531-540, 1998. 10.1179/026708399101506247.

[151] Amran, Y., Katsman, A., Schaaf, P. Bamberger, M., Influence of Copper Addition and Temperature on the Kinetics of Austempering in Ductile Iron, Met. and Mat. Trans. B, Vol 41B, pp 1052-1058, 2010. 10.1007/s11663-010-9388-y.

[152] Rouns, T.N., Rundman, K.B., Constitution of Austempered Ductile Iron and Kinetics of Austempering, AFS Trans., Vol 95, pp 851-874, 1987.

[153] Bosnjak, B, Radulovic, B., Pop-Tonev, K., Asanovic, V., Influence of Microalloying and Heat Treatment on the Kinetics of Bainitic Reaction in Austempered Ductile Iron, J. of Mat. Eng. and Perf., Vol 10, pp 203-2011, 2001. 10.1361/105994901770345222.

[154] Rajnovic, D., Eric, O., Sidjanin, L., The Standard Processing Window of Alloyed ADI materials, Kovove Mat., Vol 50, pp 199-208, 2012. 10.4149/km 2012 3 199.

[155] Górny, M., Tyrala, E., Lopez, H., Effectof Copper and Nickel on the Transformation Kinetics of Austempered Ductile Iron, J. of Mat. Eng. and Perf., Vol 23, pp 3505-3510, 2014. 10.1007/s11665-014-1167-5.

[156] Bahmani, M., Elliott, R., Varahram, N., The Austempering Kinetics and Mechanical Properties of an Austempered Cu-Ni-Mo-Mn Alloyed Ductile Iron, J. of Mat. Sci., Vol 32, pp 4783-4791, 1997. 10.1023/A:1018687115732.

[157] Hayrynen, K.L., Keough, J.R., Austempered Ductile Iron-The State of the Industry in 2003, Keith Millis Symp., 2003.

[158] Polishetty, A., Singamneni, S., Littlefair, G., A Comparative Assessment of Austempered Ductile Iron as a Substitute in Weight Reduction Applications, Int. Manu. Sci. and Eng. Conf., MSEC_ICMP2008-7209, 2008. 0.1115/MSEC_ICMP2008-72091.

[159] Keough, J.R., Hayrynen, K.L., Automotive Applications of Austempered Ductile Iron (ADI): A Critical Review, SAE Int., Tech. Pap. 200-01-0764, 2000.

[160] Hayrynen, K.L., Brandenberg, K.R., Keough, K.R., Applications of Austempered Cast Irons, AFS Trans., 02-84, 2002.

[161] Kovacs, B.V., Development of Austempered Ductile Iron (ADI) for Automobile Crankshafts, J. Heat Treat., Vol 5, pp 55-60, 1987. 0.1007/BF02831620.

[162] Harding, R.A., The Production, Properties and Automotive Applications of Austempered Ductile Iron, Kovove Mat., Vol 45, pp 1-16, 2007.

[163] Brandenberg, K.., Ravesncroft, J., Rimmer, A., Hayrynen, K.L., An ADI Crankshaft Designed for High Performance in TVR's Tuscan Speed Six Sports Car, SAE Int., Tech. Pap. 2001-01-0408, 2001.

[164] Tanaka, Y., Kage, H., Development and Application of Austempered Spheroidal Graphite Cast Iron, Mat. Trans., Vol 6, pp 543-577, 1992. 10.2320/matertrans1989.33.543.

[165] Dündar, S., Application of Austempered Ductile Ironto Rail Wheel Sets, J. of Eng. Sci., Vol 9, pp 283-287, 2003.

[166] Kuna, M., Springmann, M., Mädler, K., Hübner, P., Pusch, G., Fracture Mechanics Based Design of a Railway Wheel Made of Austempered Ductile Iron, Eng. Frac. Mech., Vol 72, pp 241-253, 2005. 10.1016/j.engfracmech.2003.10.007.

[167] Nofal, A., Advances in the Metallurgy and Applications of ADI, J. of Mat. Eng., Vol 2, pp 1-18, 2013.

[168] Zimba, J., Simbi, D.J., Navara, E., Austempered Ductile Iron: an Alternative Material for Earth Moving Components, Cem. & Conc. Comp., Vol 25, pp 643-649, 2003. 10.1016/S0958-9465(02)00078-1.

[169] Lekakh, S.N., High Strength Ductile Iron Produced by Engineered Cooling: Process Concept, Int. J. Metalcast., Vol 9, pp 21-30, 2015. 10.1007/BF03355612.

[170] Lekakh, S.N., Hrebec, B., Scott, R., Schlobohm, J., High Strength Ductile Iron Produced by Engineered Cooling: Application for Different Casting Processes, Int. J. of. Met., Vol 9, pp 21-30, 2015. 10.1007/BF03355612.

[171] Sun, T., Song, R., Wang, X., Deng, P., Wu, C., Microstructure and Phase Transformation of Wear Resistance Ductile Iron Grinding Balls by Continuous Cooling Process, Mat. Sci. & Eng. A, Vol 626, pp 375-381, 2015. 10.1016/j.msea.2014.12.078.

[172] Murcia, S.C., Paniagua, M.A., Ossa, E.A., Development of As-cast dual Matrix Structure (DMS) Ductile Iron, Mat. Sci. & Eng., Vol 566, pp 8-15, 2013. 10.1016/j.msea.2012.12.033.

[173] Janowak, J.F., Gundlach, R.B., Approaching Austempered Ductile Iron Properties by Controlled Cooling in the Foundry, J. Heat Treat., Vol 4, pp 25-31, 1985. 10.1007/BF02835486

[174] Yoo, S.M., Moeinipour, K., Ludwig, A., Sahm, P.R., Numerical Simulation and Experimental Results of in Situ Heat Treated Austempered Ductile Iron, Int. J. of Cast Met. Res., Vol 11, pp 483-488, 1999. 10.1080/13640461.1999.11819321.

[175] Meena, A., El Mansori, M., Material Characterization of Austempered Ductile Iron (ADI) Produced by a Sustainable Continuous Casting-Heat Treatment Process, Met. and Mat. Trans. A, Vol 43A, pp 4755-4766, 2012. 10.1007/s11661-012-1271-9.

[176] Keough, J.R., Austempered Ductile Iron (ADI)- A Green Alternative, Applied Process Inc. Tech. Div., http://www.appliedprocess.com/library, 2010.

[177] ASTM E-562 Standard Test Method for Determining Volume Fraction by Systematic Manual Point Count, ASTM International, West Conshohocken, 2011.

[178] Basso, A.D., Martínez, R.A., Sikora, J.A., Influence of Austenitising and Austempering Temperatures on Microstructure and Properties of Dual Phase ADI, Mat. Sci. and Tech., Vol 23, pp 1321-1326, 2007. 10.1179/174328407X236544.

[179] International Organization for Standardization, Metallic Materials-Bend Test, ISO Standard 7438, 2020.

[180] ASTM G31-72 Standard Practice for Laboratory Immersion Corrosion Testing of Metals, ASTM International, West Conshohocken, 2004.

[181] ASTM D1141-98 Standard Practice for the Preparation of Substitute Ocean Water, West Conshohocken, 2013.

[182] Riabov, M.V., Lerner, Y.S., Fahmy, M.F., Effect of Low Temperatures on Charpy Impact Toughness of Austempered Ductile Irons, J. of Mat. Eng. and Perf., Vol 11, pp 496-503, 2002. 10.1361/105994902770343728.

[183] Krawiec, H., Lelito, J., Tyrala, E., Banaś, J., Relationship between Microstructure and Pitting Corrosion of ADI in Sodium Chloride Solution, J. Sol. Sta. Elect., Vol 13, pp 935-942, 2009. 10.1007/s10008-008-0636-x.

ANEX

The present research work has given as a result the following publications and patents:

- de la Torre, U., Stefanescu, D.M., Hartmann, D., Suárez, R., As-Cast Ausferritic Ductile Iron, Proceedings Keith Millis symposium, AFS pp 233-243, 2013. Presentation on the Keith Millis symposium 2013.
- Méndez, S., de la Torre, U., Suárez, R., Larrañaga, P., Stefanescu, D.M., Processing Thickness Window for As-Cast Ausferritic Castings, Trans Amer. Found. Soc., vol 123, pp 219-226, 2015. Presentation on the AFS congress 2015.
- Méndez, S., de la Torre, U., Gonzalez-Martinez, R., Suárez, R., Advanced Properties of Ausferritic Ductile Iron Obtained in As-Cast Conditions, Int. J. Metalcast., Vol 11, pp 116-122, 2017. 10.1007/s40962-016-0092-9. Presentation on the World Foundry Congress 2016.
- de la Torre, U., González-Martínez, R., Méndez, S., Effect of the Sections Size, Holding Temperature and Time on the Kinetics of the Ausferritic Transformation and Mechanical Properties of As-Cast Ausferritic Ductile Iron, Mat. Sci. and Eng. A, Vol 788, Article 139536, 2020. 10.1016/j.msea.2020.139536.
- European patent: A Method to Control Ausferritic As-Cast Microstructure in Ductile Iron Parts, EP3026128B1.